

Characterization of fracture behaviour of Indian
reduced activation Ferritic/Martensitic steel in
ductile to brittle transition region using master
curve approach

By

ABHISHEK TIWARI

ENROLMENT NO. ENGG01201304015

*A thesis submitted to the
Board of studies in engineering sciences
in partial fulfilment of requirements
for the degree of*

DOCTOR OF PHILOSOPHY

of

HOMI BHABHA NATIONAL INSTITUTE



Oct., 2017

Homi Bhabha National Institute

Recommendations of the Viva Voce Committee

As members of the Viva Voce Committee, we certify that we have read the dissertation prepared by **Abhishek Tiwari** entitled **Characterization of fracture behaviour of Indian reduced activation ferritic/martensitic steels in ductile to brittle transition region using master curve approach** and recommend that it may be accepted as fulfilling the thesis requirement for the award of Degree of Doctor of Philosophy.

Chairman	Dr. Dinesh Srivastava	Date:
Guide/convenor	Dr. R. N. Singh	Date:
Co-guide	Dr. J Chattopadhyay	Date:
Examiner		Date:
Member-1	Dr. K. B. Khan	Date:
Member-2	Dr. A. K. Arya	Date:

I/We hereby certify that I/we have read this thesis prepared under my/our direction and recommend that it may be accepted as fulfilling the thesis requirement.

Date:

Place :

Signature

Signature

Guide-1

Guide-2

STATEMENT BY AUTHOR

This dissertation has been submitted in partial fulfillment of requirements for an advanced degree at Homi Bhabha National Institute (HBNI) and is deposited in the Library to be made available to borrowers under rules of the HBNI.

Brief quotations from this dissertation are allowable without special permission, provided that accurate acknowledgement of source is made. Requests for permission for extended quotation from or reproduction of this manuscript in whole or in part may be granted by the Competent Authority of HBNI when in his or her judgment the proposed use of the material is in the interests of scholarship. In all other instances, however, permission must be obtained from the author.

(ABHISHEK TIWARI)

Declaration

I, hereby declare that the investigation presented in the thesis has been carried out by me. The work is original and has not been submitted earlier as a whole or in part for a degree / diploma at this or any other Institution / University.

(ABHISHEK TIWARI)

List of publications arising from the thesis

Journals/Published and under review

1. Tiwari, Abhishek, R. N. Singh, Per Ståhle, (2017) “Assessment of effect of ductile tearing on cleavage failure probability in ductile to brittle transition region” , International Journal of Fracture. pp. 1-24
2. Tiwari A, Gopalan A., Shokry A., Singh R. N., Ståhle P. (2017) “Fracture study of ferritic/ martensitic steels using weibull stress analysis at quasi-static and higher loading rates.” International Journal of Fracture pp. 17, DOI 10.1007/s10704-017-0184-4
3. “Determination of reference transition temperature of In-RAFMS in ductile brittle transition regime using numerically corrected Master Curve approach.” , Tiwari, Abhishek, G. Avinash, Saurav Sunil, R. N. Singh, Per Ståhle, J. Chattopadhyay, and J. K. Chakravartty, Engineering Fracture Mechanics 142 (2015): 79-92.
4. “Assessment of constraint difference in CT and SE(B) specimens using a novel Weibull triaxiality method on ferritic/martensitic steels in DBT region” , Tiwari, Abhishek, R. N. Singh, Per Ståhle, Fracture and Fatigue of Engineering Materials. Under review
5. “Fracture behaviour of ferritic/martensitic steels in DBT region characterized using CT and TPB specimen geometries” , Tiwari, A, R. N. Singh, International Journal of Fracture. Under review

Proceedings/International Conference

1. Tiwari, Abhishek, R. N. Singh, Per Ståhle, and J. K. Chakravartty. “A loss of constraint assessment using $\sigma^* - V^*$ approach to describe the effect of crack depth on reference transition temperature T_0 .” Procedia Structural Integrity 2 (2016): 690-696.

-
2. Tiwari, Abhishek, Ram Niwas Singh, Per Sthle, and J. K. Chakravartty. "Master curve in upper region of ductile brittle transition: a modification based on local damage approach." *Procedia Structural Integrity* 2 (2016): 1553-1560.

Dedication

to
my mom
and
my dear wife

Acknowledgement

This thesis is the final stamp on the ticket which has taken this me to different states of mind and when I look back at this point I find this thesis to be a memoir of all the stepping and stopping stones which shaped the work as well as myself. In the words of Robert Frost I can describe this journey as *"Two roads diverged from the woods and I, I took the one less travelled by.."* , however, any of two roads would have ended at some place giving me some character. So, the important part is the journey and therefore my greatest regards, and gratitude undoubtedly is to the work of this PhD.

Then I would like to thank my guide **Dr. R N Singh** and **Dr. J Chattopadhyay** for their continuous guidance and support. I remember the questions they asked to justify the results and to which I had no answer. Those questions turned to sleepless nights and pushed me toward understanding and seeing things beyond the results, interpreting the results and finding a reason which can explain it and then to prove that explanation further by repeating it. All this probably started when my guide Dr. R N Singh said *"..No matter how weird they look, results are the facts"*

Many a times, my guide **Dr. R N Singh** made me realize the importance of others' perspectives. Also his reply, when I shared my disgust towards Feudalistic behaviour of system, that "not all fingers in one's hand are of same length", made me think about the limitations of people scissored by their capabilities, social constraint, responsibility, and most importantly adaptability in a situation. I also learnt from him that every situation is a learning opportunity, irrespective of how ecstatic or painful it is.

I would also like to extend my gratitude to the doctoral committee members **Dr. Dinesh Srivastava**, **Dr. Ashok K Arya**, **Dr. K B Khan** and the ex committee members **Dr. R Tewari** and **Dr. R C Hubli**. Their constant reviews on the work expanded the understanding and troubleshot many problems.

I would also like to thank the reviewers of the journals who reviewed my manuscripts and asked questions which many a times changed the perspective of the work. They

helped not only in making the work presentable but also especially the negative ones which were adequate in amount, helped in giving the work altogether a different direction. I would like to especially acknowledge an anonymous reviewer who actually in one sentence described a function which opposed the ideas presented in my work. Without these reviewers this work would not have reached the conclusions it has.

The friendly and very supportive environment created by all the labmates especially, **Mr. Avinash Gopalan**, **Mr. Saurav Sunil** and **Mr. A K Bind** made the job easier and technical discussions with them improved the learning part. I would also like to thank **Mr. R K Choudhary** for helping me in the experimental analyses of dilatation strain analysis.

I am also very thankful to laboratories and researchers around the world who has previously worked on the subject especially **J Heerens** and **D Hellmann** from Institute of Materials Research, GKSS Research Centre Geesthacht and **Dr. Enrico Lucon** from Belgium Nuclear Research Centre, SCK-CEN, NMS, Mol, Belgium who made approximately 800 fracture data available for free which helped a lot in this research work. The work of **Dr. Kim Wallin** also inspired a great deal and helped when outcome of my work was not that great. It gave a sense of aspiration to know that Wallin started on the subject in 1964 pursued it till his method was standardized as ASTM E1921 which came to me as a readily available tool for analysis. Also the technical discussions online with very simple and extremely helpful expert of the subject of fracture mechanics **Dr. Robert O. Ritchie** helped me in improving my understanding of the subject and I shall always be grateful for his answers.

Another and perhaps most strong support in terms of technical understanding was offered by **Prof. Per Ståhle**. I am thankful for his kindness, teachings and support which not only helped this work but also taught me many fundamental concepts of fracture mechanics and finite element analysis.

I would also like to thank my friend **Dr. Dominic Olveda** from Technical University Darmstadt, Germany who taught me finite element analysis from scratch without any

expectation and I shall always be indebted for his kindness and the initiative taken by him to help me. I have been lucky to get friends like him.

I am also thankful to Bhabha Atomic Research Centre, Mumbai and Board of Research in Nuclear Sciences, India for my fellowship to make my PhD financially stable.

The biggest support without any doubt came from my wife **Dr. Sudha Bind** who has tolerated all the undocumented events of impatience, pressure, frustrations and yet held me together, supported and made me strong and motivated me by being strong while struggling in her own field. Last but surely not the least to be thanked is my mother **Mrs. Saroj Tiwari** who must be very proud of me for completing this work and who has always been supportive towards my studies. Without her it would not have been possible.

(ABHISHEK TIWARI)

Contents

Title	1
Front matter	i
List of publication	v
Dedication	vii
Acknowledgement	ix
Contents	xvii
Abstract	xvii
List of Figures	xix
List of Tables	xxvii
Abbreviation	xxix
List of Symbols	xxxii
Synopsis	19
1 Introduction	20
1.1 A brief history of fusion reactor & challenges to structural integrity . . .	20
1.2 Objectives	27
1.3 Structure of thesis	28
2 Literature Review	31
2.1 An Introduction to ductile to brittle transition of fracture mode	31
2.2 Probabilistic approach towards scatter in ductile to brittle transition . . .	32
2.2.1 Master curve: a global approach	35
2.2.2 Censoring of dataset for maximum likelihood analysis	39
2.2.3 Advanced master curve approaches: SINTAP, Bimodal and Multi- modal master curves	41
2.2.4 Modifications of master curve approach: Case studies	43
2.2.5 Cleavage fracture: local approaches	46
2.3 Reduced activation ferritic/martensitic steels: An Overview	49
3 Problem formulation	54
3.1 Test matrix	56
4 Material	58
4.1 Material: Ferritic/Martensitic steels	58

4.2	Microstructural characterization of In-RAFMS	59
4.2.1	Phase transformation and heat treatment	59
4.2.2	Microscopy: precipitates and micro-structure	65
4.3	Summary	69
5	Experimental and Numerical methods	70
5.1	Experimental set-up	70
5.1.1	Metallographic studies	76
5.1.2	Tensile and Charpy testing	77
5.1.3	Fracture toughness testing and measurement in DBT region	77
5.2	Finite element analysis	79
5.2.1	Continuum FEM	80
5.2.2	Ductile damage implementation	83
5.3	Solver, mesh and sensitivity analyses	84
6	In-RAFMS: Mechanical behaviour in DBT & conventional master curve	86
6.1	Impact toughness, damage in DBTT and Tensile properties	86
6.1.1	Brittle fracture in DBT region	87
6.1.2	Intermediate fracture in DBT region	89
6.1.3	Tensile properties	91
6.2	Conventional master curve analysis of In-RAFMS	96
6.2.1	Single and multi-temperature master curves	97
6.2.2	Strict censoring	100
6.3	Conclusions	101
7	Master curve: effect of out of plane constraint loss	103
7.1	Introduction	104
7.2	Fracture dataset	105
7.3	Numerical assessment of constraint loss	106
7.3.1	Numerical correction of Sokolov's Work	107
7.3.2	Pre processing	108
7.3.3	Post processing	109
7.3.4	Numerical correction on Euro dataset	113
7.3.5	Numerical Correction on In-RAFMS	115
7.3.6	Pre-processing	115
7.3.7	Post Processing	115
7.4	Results and Discussion	117
7.4.1	Master Curve from uncorrected experimental data	117
7.4.2	Numerical correction of In-RAFMS dataset	117
7.5	Conclusions	121
8	Master curve: effect of in plane constraint loss	122
8.1	Introduction	122
8.2	Experimental dataset	124
8.3	Numerical Analysis	124
8.4	Results	125

8.5	Discussion	127
8.6	Conclusions	134
9	Master curve: effect of specimen geometry (CT and SE(B))	135
9.1	Introduction	136
9.2	Material and Experimental Details	138
9.3	Cleavage failure probability, Weibull Triaxiality	138
9.3.1	Weibull Triaxiality	141
9.4	Finite element analysis	142
9.5	Results	143
9.6	Discussions	146
9.6.1	Effect of CT and SE(B) geometries on T_0	146
9.6.2	Constraint differences in CT and SE(B) and numerical prediction of cleavage failure probability	149
9.7	Conclusions	153
10	Master curve: effect of loading rate	155
10.1	Introduction	155
10.1.1	Master Curve Methodology and effect of loading rate	156
10.1.2	Cleavage failure probability, Weibull stress and loading rate	157
10.1.3	Calibration of Weibull parameters	157
10.2	Experimental dataset	162
10.3	Finite element analysis	163
10.3.1	Finite element analysis of In-RAFMS	164
10.3.2	Finite element analysis of F82H	166
10.3.3	Finite element analysis of Mod-9Cr-1Mo steels	167
10.4	Results	168
10.4.1	Calibration of Weibull slope:In-RAFMS	168
10.4.2	Calibration of Weibull slope:F82H	171
10.4.3	Calibration of Weibull slope:Mod-9Cr-1Mo	172
10.4.4	Master Curve analysis of In-RAFMS at different loading rates	172
10.5	Discussions	174
10.5.1	Calibrated cleavage failure probability distribution for ferritic/martensitic steels	174
10.5.2	Effect of loading rate on fracture behaviour	176
10.6	Conclusions	181
11	Master curve in upper region of DBT	183
11.1	Introduction	184
11.1.1	Cleavage fracture in upper region of ductile to brittle transition	184
11.2	Material datasets	188
11.3	Cleavage with prior DCG	189
11.3.1	Increasing active volume with DCG	189
11.3.2	Change in constraint with DCG	191
11.4	Numerical analyses	195
11.4.1	Ductile damage implementation	196

11.4.2	Calibration of GTN parameters	196
11.4.3	Finite element models of CT and TPB geometries	197
11.5	Results	202
11.5.1	Euro fracture data	204
11.5.2	In-RAFMS data	205
11.6	Discussion	208
11.6.1	Effect of plastic strain and embrittlement	211
11.7	Conclusions	213
12	Summary and conclusions	214
13	Future scope of work	218
A	Appendix-A	219
A.1	Maximum likelihood analysis: conventional master curve	219
A.2	Maximum likelihood analysis: Bimodal master curve master curve for upper DBT	221
A.3	Maximum likelihood analysis: Modified master curve for upper DBT	222
B	Appendix-B	223
B.1	Fracture data of 0.4T SEB specimen of In-RAFMS	224
B.2	Fracture data of 0.4T CT specimens of In-RAFMS	228
B.3	Fracture data of 0.4T SEB specimens of In-RAFMS at different loading rates	229
B.4	Fracture data of 0.2T SEB specimens of In-RAFMS at different crack depths	231
B.5	Fracture data of 1T CT specimens of P91 steel	235
B.6	Fracture data of 0.4T standard charpy specimens of P91 steel	236
C	Appendix-C	237
	Bibliography	251

Abstract

The ductile to brittle transition temperature of high Chromium ferritic/martensitic steel used in first wall blanket module in fusion reactor is prone to the damage imposed on the component by high energy neutrons (14.1 MeV) at high temperature (350-500°C). The structural material of fusion reactor, therefore, is designed to have better swelling resistance and creep strength. The structural material for first wall were derived from modified 9Cr-1Mo grade steels due to its proven creep and swelling strength. For the concerns related to radioactivity of the structural material, the transmutable elements of modified 9Cr-1Mo grade steels such as Mo, Nb were replaced by low activity elements such as W and Ta.

The He flow for heat extraction from the test blanket module provides a temperature window of 350-480°C. In this range of temperature with 14.1 MeV neutron irradiation, the possibility of transition of fracture mode from ductile to brittle is high. The irradiation causing structure defects and clusters of defects with added effect on dislocation loops density and mobility, results in hardening of the material. Studies have shown that an upward shift of 100°C and more can be realized in ferritic/martensitic steels in the mentioned temperature window at a dose of 2-2.5 dpa only [Kytka et al. \(2011\)](#). Further, the pulse mode operation of fusion reactor imposes the condition of higher loading rates on the blanket structure. The possibility of ductile to brittle transition in the operational condition and higher risk of catastrophic fracture due to higher loading rates, make it very important to study the fracture behaviour of blanket material in ductile to brittle transition range.

In the process of material development starting from Optifier and Manet grades, the first generation of candidate material was F82H steel developed by Japan Atomic Energy Association and JLF by Japan. The next grade was more advanced Eurofer97, which showed greater potential towards fracture resistance due to smaller carbides (100 μm) of Ta, which helped in grain size refinement, unlike oxides of Ta, which were found in F82H (30 μm) and showed detrimental behaviour by assisting in originating failure

nuclei (void and microcrack nuclei). In this lineage of material development extensive study of creep, tensile and fatigue properties helped in developing the first candidate structural material from India known as Indian Reduced Activation Ferritic Martensitic Steel (In-RAFMS).

To characterize the fracture behaviour of In-RAFMS, the probabilistic approach of master curve is used. The approach, however, have limitations on the test conditions to be applicable to statistical maximum likelihood analysis. Study the effect of irradiation on mechanical behaviour of ferritic/martensitic grade of steel requires small specimens to be tested for mechanical behaviour studies, which puts constraint loss as the major obstacle toward the fracture mechanics single parameter based approach of master curve.

In this work the master curve approach is corrected numerically by finite element method using $\sigma^* - V^*$ approach for both out of plane and in-plane constraint loss. The local approach of Weibull stress is applied using finite element method and the changes in reference transition temperatures occurring due to change in loading rates are examined. The Weibull stress based cleavage failure probability is calculated by calibrating Weibull modulus for In-RAFMS as well as mod-9Cr-1Mo steel. The calibration was carried out by generating datasets at two different constraint level and transforming the data at Small Scale Yielding (SSY) condition by modelling modified boundary layer formulation using finite element method.

The first novel outcome of this work is a finite element analysis based new constraint parameter named Weibull Triaxiality. The nomenclature is based on its mathematical expression, which is similar to Weibull stress. Second novel outcome is an analytical extension of master curve approach, which is applicable in upper region of DBT where so far no approach has shown potential to estimate a reference transition temperature, which can be compared with conventional master curve results.

The fracture toughness tests in DBT region were performed on In-RAFMS as well as modified 9Cr-1Mo steel, which is the reference material for all RAFM grades. The tests were carried out in the range of -150°C to -50°C on both Compact Tension (CT) and

Three Point Bend (TPB) geometries at three different loading rates. The parametric study of effect of crack depth in the range of $0.2 \leq a/W \leq 0.7$ was also performed. The effects of changing crack depths, loading rate, size and type of loading were studied and assisting numerical analyses for each subject were performed to better understand and interpret the experimental behaviour. Also, the numerical results helped in correcting the probabilistic master curve approach applicability. The results obtained for different studies (loading rate, size, crack depth) were similar to other popular grades of RAFMS.

The micro-structural studies on In-RAFMS were carried out to examine the phase transformation temperatures, which were supported by numerical predictions. The Scanning Electron Microscopy (SEM) micro-structural studies and fractographic studies helped in characterization of cleavage initiators and also in understanding the role of ductile tearing on cleavage fracture. The overall behaviour of In-RAFMS, for all affecting parameters, studied in this work were compared with the results of other popular RAFM grades and it was found that In-RAFMS is comparable to Eurofer97. Although, unlike for the case of Eurofer97, where a modification of master curve's athermal parameter was required, for In-RAFMS conventional master curve was found applicable with numerical corrections.

The applicability of master curve approach in upper region of DBT was an untouched field, which was explored in this work and a modified master curve approach was proposed, tested with existing and newly developed experimental dataset and justified.

Keywords *Master Curve, Ductile brittle transition, cleavage fracture, In-RAFMS*

List of Figures

1	(a) Active volume V^* versus K_{JC} and (b) master curve of In-RAFMS with untransformed and transformed datasets based on Active volume V^* versus K_{JC} behaviour under non-SSY condition with loss of constraint	11
2	Master curve of data transferred at a/W of 0.5 using $\sigma^* - V^*$ approach showing (a) Shift in T_0 with a/W and (b) K_{JC} transformed to $a/W = 0.5$	12
3	The Weibull triaxiality q_W compared for different specimens at -120°C with In-RAFMS tensile response as FEA input	13
4	Master curves at different loading rates and ΔT_0 of In-RAFMS with increasing loading rate	14
5	Numerical prediction and experimental rank probabilities for fracture tests performed at (a) 100 mm/min and (b) 1000 mm/min actuator speed.	14
6	(a) Modified master curve and conventional master curve comparison for <i>Euro 0.5TCT dataset</i> and (b) comparison of modified master curve results with one obtained from mean approximation of $K_{JC} - \Delta a$	16
1.1	Computer simulation of nuclear fusion reaction in a tokamak (a) D-T reaction (b) Plasma generation (Daniel, 2012)	23
1.2	Test blanket module	24
2.1	ASME K_{1C} Curve for SA533 steel base and weld datasets	33
2.2	ASME K_{1C} Curve for SA533 steel incoparison with master curve and RT_{10}	35
2.3	Schematic of fracture surface with shaded fatigue pre-cracked and cracked areas	37
2.4	Crack tip defining probability of cleavage failure according to Eq.(2.24)	48
2.5	Participation of alloying elements in (a) $M_{23}C_6$ carbides and in (b) MX precipitates in 10%Cr steel obtained from JMat-Pro	51
4.1	Dilatometer response of In-RAFMS and P91 steels (a) while solution-izing and aircooling and (b) tempering	61
4.2	Phase diagram of (a) In-RAFMS and (b) P91 calculated with chemical composition estimated from Optical Emission Spectroscopy	62
4.3	Optical Microstructure of In-RAFMS and P91 taken after etching the polished specimens with 5% Nital for 30 seconds	66
4.4	EDXS intensities and respective thresholds for image analysis	67
4.5	EDXs intensity threshold prediction of distribution of carbides	68
5.1	Engineering drawing of tensile specimens	71
5.2	Engineering drawings of fracture speicmens (a) 0.4T CT specimen drawing and (b) 0.4T TPB specimen drawing	72
5.3	0.4T CT specimen tested at sub-zero temperature in environmental chamber using UTM	73

5.4	0.4T TPB specimen tested at sub-zero temperature in environmental chamber using UTM	73
5.5	Schematic of Modified Boundary Layer model showing boundary conditions	82
6.1	Impact energy variation in DBT region for In-RAFMS and P91 steels	87
6.2	Fracture surface of broken charpy specimens of In-RAFMS in DBT region with ductile fracture at (a) -30°C (b) -50°C, (c) intermediate fracture at -85°C and (d) complete cleavage at -100°C	88
6.3	SEM image of near crack tip region of In-RAFMS broken specimen at -70°C showing ductile damage signatures along with microcracks	89
6.4	SEM image of near crack tip region of P91 broken specimen at -70°C showing ductile damage signatures along with micro-cracks	90
6.5	EDXs mapping of surface near micro-crack of In-RAFMS showing chemical composition	91
6.6	Engineering stress-plastic strain ($\epsilon_T - \sigma/E_0$) response of In-RAFMS in DBT region	92
6.7	Yield strength, UTS responses at (a) different temperatures and hardening behaviour in form of σ_0/σ_{UTS} at (b) different strain rates	94
6.8	Conventional master curve of In-RAFMS	98
6.9	Effect of single and multi-temperature analyses on conventional master curve of 0.2T TPB dataset of In-RAFMS	99
6.10	Effect of strict censoring on master curve of 0.4T TPB dataset of In-RAFMS	100
7.1	Extrapolated yield strengths for fracture toughness measurements in the range of test temperatures	106
7.2	Dimensions of CT specimen geometry	108
7.3	Boundary condition and mesh of 0.4T CT geometry of Sokolov's work (Sokolov and Tanigawa, 2007)	109
7.4	$K_{2D \approx SSY}$ and $K_{3D \approx non-SSY}$ obtained from FEA of Sokolov's geometry	110
7.5	Comparative master curve of Sokolov's dataset	112
7.6	Comparison of master curves obtained from Euro data transformed to SSY and untransformed conditions	114
7.7	Boundary conditions imposed and mesh of 0.2T TPB specimen of In-RAFMS	116
7.8	Active volume V^* under non-SSY condition with loss of constraint	117
7.9	Active volume V^* versus K_{JC} under non-SSY condition with loss of constraint	118
7.10	Master curve of In-RAFMS with untransformed and transformed datasets	119
8.1	Experimental analyses of Sumpter showing effect of crack depth on fracture toughness	123
8.2	Quarter symmetric charpy geometry with active volume at crack front	125
8.3	Master curves showing data outside tolerance bounds for shallower crack datasets and workable scatter for deeper crack datasets	126
8.4	Shift in transition temperatures with increasing crack depth	127

8.5	Curve fitting of active volume calculated according to Eq.(8.1)	128
8.6	Master curve plot of all K_{JC} transformed to $a/W = 0.5$	130
8.7	Correlation of fitting parameters of Eq.(8.1) with (a) change in constraint parameter ΔT_{stress} and (b) Tstress with a/W	132
9.1	Mesh of (a) side grooved 0.4T-CT specimen (RP represents a Reference Point which is kinematically coupled with the pin hole surface) and (b) 0.2T SE(B) specimen	143
9.2	Comparison of master curves for (a) In-RAFMS 0.4T-CT specimens with the TPB dataset (b) In-RAFMS 0.2T TPB specimens with 0.4T-CT datasets (c) P91 1T-CT specimens with 0.4T standard charpy dataset and (d) P91 0.4T standard charpy specimens with 1T-CT dataset for comparison	145
9.3	Master Curves of the combined dataset of P91 standard charpy specimens and 1T-CT specimens	148
9.4	(a) The stress field near crack tip in visualization mode of ABAQUS and the (b) normalized stress profile along crack front in 0.4T-CT geometry model	150
9.5	Weibull triaxiality q_W for P91 steel calculated at -60°C and -110°C for CT and SE(B) geometries	150
9.6	Weibull triaxiality q_W for In-RAFMS steel calculated at -120°C for CT and SE(B) geometries	150
9.7	Numerical and experimental cleavage failure probabilities comparison at -110°C for P91	151
9.8	Numerical and experimental cleavage failure probabilities comparison at -60°C for 1T CT dataset of P91 steel	152
9.9	Numerical and experimental cleavage failure probabilities comparison at -120°C for In-RAFMS	152
10.1	(a) Two dimensional MBL model quarter symmetric geometry mesh, (b) magnified crack tip root radius	165
10.2	Quarter symmetric models of (a) 0.4T CT geometry for LC condition and (b) CT 1T geometry modelled for F82H steel as HC condition	167
10.3	Tensile behaviour of In-RAFMS at -120°C , F82H at -100°C and P91 at -110°C extrapolated to 2.0 strain used for FE modelling. (The tensile property of F82H at -100°C is generated using the yield strength reported in literature and tensile property of In-RAFMS at -120°C .)	168
10.4	Rank probability of HC (0.4T CT side grooved) and LC (0.2T TPB) datasets of In-RAFMS	169
10.5	Error calculated using Eq.(10.5) for trial values of m and K_{min} used on fracture data of In-RAFMS	169
10.6	(a) The behaviour of g -function for HC and LC models at different m values and (b) σ_W behaviour for HC and LC dataset of In-RAFMS at $m = 9$	170
10.7	Rank probability of HC (1T CT) and LC (0.4T CT) dataset for F82H-IEA showing no constraint difference	171
10.8	Error values obtained for trial values of m and K_{min} for F82H-IEA	172

10.9 Rank probabilities of test data obtained on P91 steel for 10×10 standard charpy as HC and 0.16T CT as LC conditions	173
10.10 Error values obtained for trial values of m and K_{min} for Mod-9Cr-1Mo steel	173
10.11 Master curve of In-RAFMS with $T_0 = -120^{\circ}\text{C}$ with scatter of 0.2T TPB and 0.4T CT datasets	174
10.12 Master curves of 0.4T standard charpy specimens dataset of In-RAFMS tested at (a) 100 mm/min and (b) 1000 mm/min of actuator speed	175
10.13 Shift in reference transition temperature T_0 of In-RAFMS with increasing loading rate with the prediction of Wallin according to Eq.(10.1)	176
10.14 Cleavage failure probability with HC and LC datasets of (a) In-RAFMS (b) Mod-9Cr-1Mo and (c) F82H steels	178
10.15 Numerical prediction and experimental rank probabilities for fracture tests performed at (a) 100 mm/min and (b) 1000 mm/min actuator speed	179
11.1 Schematic of validity criteria of datasets used in master curve method	187
11.2 Schematic of increasing active volume with ductile tearing	189
11.3 Implementation of ductile damage in FEM using VUMAT subroutine; (a) Geometry of quarter symmetric tensile specimen (b) Calibration of GTN parameters (c) Comparison of calibrated VUMAT with Abaqus porous plasticity	197
11.4 Pseudo-randomly distributed elastic elements showing effect of constraint on criticality of carbides (a) Onset of DCG and carbides, (b) $\Delta a = 0.2\text{mm}$, (c) $\Delta a = 0.4\text{mm}$	200
11.5 True stress plastic strain response extrapolated to 2 for (a) 22NiMoCr37 and (b) In-RAFM steel	201
11.6 Triaxiality ratio q_f/q_i at different temperatures for (a) 0.5 T CT 22NiMoCr37 steel, (b) 0.4 T CT In-RAFM steel	202
11.7 Ductile tearing based on GTN ductile damage in 0.4T CT side grooved and 0.2T TPB geometries modelled with material parameters corresponding to -110°C for In-RAFMS	203
11.8 (a) Engineering Stress-strain response 22NiMoCr37 steel tensile specimens and (b) $K_{JC} - \Delta a$ response of 0.5T CT Euro data	205
11.9 (a) Modified master curve and conventional master curve for 0.5T CT Euro fracture dataset and (b) comparison with predictions obtained from Eq. (31)	206
11.10 (a) Engineering stress strain response In-RAFMS and (b) K_{JC} versus Δa behavior of In-RAFMS obtained from experimental CT and TPB datasets and finite element analyses	207
11.11 (a) Conventional and modified master curves 0.4T CT and (b) 0.2T TPB datasets of In-RAFM steel	208
11.12 Comparison of conventional, Wallin's and proposed formulation with rank probability obtained for 0.5T CT Euro fracture data at -40°C	209
11.13 Comparison of scaling of Active volume with conventional, Wallin's correction and proposed model of this work for (a) -110°C and (b) -130°C	210

C.1	Fabrication drawing of M6 tensile specimens)	238
C.2	Fabrication drawing of 0.5T-CT specimen)	239
C.3	Notch dimension of SE(B) 0.4T specimen)	240
C.4	Fabrication drawing of 0.4T SE(B) specimen	240
C.5	Fabrication drawing of 0.2T SE(B) specimen	240
C.6	Notch dimension of 0.4T SE(B) specimen	240

List of Tables

1	Experimental and numerical methodologies used in this work	5
3.1	Test matrix for fracture property assessment	57
4.1	Chemical composition of ferritic/martensitic steels investigated	60
4.2	Comparison of various ferritic/martensitic grade steels	64
5.1	Datasets generated for different parametric studies	75
5.2	All type of tests with experimental conditions performed in this work	76
6.1	Summary of microstructural and mechanical properties of In-RAFMS	95
6.2	Single and Multi-temperature analysis of 0.4T and 0.2T SEB datasets of In-RAFMS	99
7.1	Fracture toughness dataset obtained using 0.4T CT specimen at -100°C in Sokolov’s work used for validation of numerical modelling performed in this work (σ_o at -100°C = 575 MPa)	112
7.2	Comparison of reference transition temperatures of popular RAFM steels	120
8.1	Statistical details of MC analysis of grouped datasets	131
9.1	Statistical parameters of In-RAFMS and P91 Master Curve analysis ¹ n_i is the weight factor used according to ASTM E1921-13a for validity criteria	146
10.1	Dataset from Sokolov and Tanigawa (2007) used for Weibull calibration.	171
10.2	Numerical and statistical parameters of fracture test datasets.	180
11.1	Trials used for GTN parameter calibration for In-RAFMS tensile response at -110°C	198
11.2	Calibrated GTN parameters used for ductile crack growth modelling for In-RAFMS and 22NiMoCr37 steels	201
11.3	Comparison of T_0 obtained from modified and conventional MC for different datasets	213
B.1	Fracture data of 0.4T SEB specimen of In-RAFMS	224
B.2	Fracture data of 0.4T CT specimens of In-RAFMS	228
B.3	Fracture data at 100 mmpm actuator speed	229
B.4	Fracture data at 1000 mmpm actuator speed	230
B.5	Fracture data with a/W in range of 0.29 to 0.34	231
B.6	Fracture data with a/W in range of 0.35 to 0.44	232
B.7	Fracture data with a/W in range of 0.46 to 0.55	233
B.8	Fracture data with a/W in range of 0.56 to 0.69	234
B.9	Fracture data of 1T CT specimens of P91 steel	235
B.10	Fracture data of 0.4T standard charpy specimens of P91 steel	236

Abbreviation

Abbreviations	Full form
DBT	ductile to brittle transition
MC	Master Curve
WST	Wallin Saario Torregornen
MLE	maximum likelihood estimation
UTS	Ultimate tensile strength
YS	yield strength
GTN	Gurson Tvergaard Needleman
SDV4	state dependent variable number 4
CT	compact tension
TPB	three point bend
DCG	ductile crack growth
FEA	finite element analysis

List of Symbols

SYMBOL	Description
α	Threshold of colour in image analysis
β	constant in DCG modified cleavage failure probability by Wallin
γ_s	surface energy of material
γ_p	plastic work required for crack propagation
ψ	yield function in numerical analysis for an incremental plastic loading
ϕ	constant in DCG modified cleavage failure probability by Wallin
Ω	constant in DCG modified cleavage failure probability by Wallin
ω	an assumed constant resulting on integration of probability density of finding critical cleavage initiator in active volume ahead of crack tip
δ	Kronecker delta
ϵ_{eq}^p	equivalent plastic strain
$\dot{\epsilon}_{eq}^p$	equivalent plastic strain rate
$\dot{\epsilon}_{kk}^p$	volumetric plastic strain rate
λ	degree of Tstress function used for Master Curve modification
μ	mean of distribution of voids nucleation
τ	curve fitting parameter
ν	Poissons ratio
σ_{eq}	equivalent stress component
σ_h	hydrostatic stress component
σ_1	maximum principal stress

σ_{flow}	average of yield strength and ultimate tensile strength
σ_o	yield strength
σ_{yy}	stress applied normal to the crack plane
σ_{std}	Standard deviation of distribution of void nucleation sites
Θ	angle from the crack plane measured counter clock wise
a	crack length
Δa	ductile crack growth prior to cleavage in ductile to brittle transition region
f_i	probability density function of KJC
f^*	void volume fraction at current time increment in numerical analysis
f	cumulative void volume fraction
f_M	a constant in GTN theory
f_U^*	a constant in GTN theory
f_C	critical value of void volume fraction
\dot{f}_N	nucleation rate if voids
\dot{f}_G	growth rate if voids
r	radius of spherical cleavage initiator
r_C	radius of spherical cleavage initiator responsible for fracture
r_{flow}	radius of zone encompassed by flow stress locus ahead of crack tip
m	Constant in DCG modified cleavage failure probability by Wallin
n_T	thickness of specimen in terms of $n/25$ inch
q_1	a constant in GTN theory
q_2	a constant in GTN theory
A	Athermal toughness contribution in 100 MPa.m ^{1/2} toughness at reference transition temperature
B	thickness of fracture specimen
C	empirical constant in exponential variation of thermal part of 100 MPa.m ^{1/2} toughness at reference transition temperature
CT	compact tension

D	constant in DCG modified cleavage failure probability
E	elastic modulus
F	fraction of cleavage trigger sites taking part in fracture
K_0	fracture toughness at 63.2% cleavage probability
K_1	opening mode stress intensity factor
K_{JC}	elastic plastic fracture toughness based on J-integral
$K_{JC,1T}$	elastic plastic fracture toughness based on J-integral for specimen of thickness 1 inch
K_{min}	threshold fracture toughness below which cleavage cannot occur
$K_{JC,median}$	median of elastic plastic fracture toughness data generated in transition region
$K_{JC,nT}$	elastic plastic fracture toughness based on J-integral for specimen of thickness (n/25) inch
$K_{JC,limit}$	limit of fracture toughness defined in ASTM E1921-13a
$K_{JC,exp}$	elastic plastic fracture toughness value obtained by testing a sample

L	maximum likelihood parameter
M	constraint parameter in validity criteria of Master Curve approach
N	numbers of cleavage initiators' sites
P_f	probability of cleavage failure
Q	Non-dimensional parameter as a measure of distance under SSY condition
S_i	survival function of KJC
T_0	reference transition temperature defined by ASTM E1921-13a
$T_{0,est}$	estimated value of reference transition temperature from Charpy test data
T_{stress}	second term of Williams stress function
ΔT_{stress}	Change in Tstress as a function of increasing crack length
W	width of a fracture specimen defined in ASTM E1820
W_1	constant in DCG modified cleavage failure probability
X	distance from the crack tip
Z	parameter describing the nucleation rate multiplier in GTN model
Z'	power law fitting parameter of $\sigma^* - V^*$ approach



Homi Bhabha National Institute

SYNOPSIS OF Ph. D. THESIS

- | | |
|---|--|
| 1. Name of the Student: | Abhishek Tiwari |
| 2. Name of the Constituent Institution: | Bhabha Atomic Research Centre |
| 3. Enrolment No. : | ENGG01201304015 |
| 4. Title of the Thesis: | Characterization of fracture behaviour of In-RAFMS in DBT Region using master curve approach |
| 5. Board of Studies: | Engineering Sciences |

SYNOPSIS

Introduction

The Test Blanket Module (TBM) of thermo nuclear fusion reactor is the component which will face drastic irradiation by high energy (14.1 MeV) neutrons (IAEA, 2001a,b). The heat from the high energy neutron will be extracted by flowing Lead-Lithium eutectic and highly pressurized He separately passing through the Lithium titanate ceramic breeder. Flowing He for the heat extraction provides a temperature window of 350-480°C for the structural material.

The structural integrity of the test blanket module first wall material is decided by the material's performance under irradiation, at high temperature and in accidental conditions such as, loss of coolant and/or loss of flow (LOCA/LOFA). The irradiation induced safety measures impose further the condition of low activity on the material. The candidate structural material for the first wall of TBM is developed world wide. Extensively studied creep and irradiation induced mechanical properties put modified 9Cr-1Mo steel

as the reference material for the development of first wall material. The safety concern related to radioactive waste is ensured by replacement of transmutable long duration active elements from the precursor 9Cr-1Mo steel (P91) with low activity elements. The high activity Mo was replaced by W and Nb by Ta. The first generation of structural first wall material were MANET, OPTIFIER and F82H. The steel developed by Japan in this series of first generation to be the potential candidate for first wall TBM is known as F82H. This grade was extensively studied for creep, swelling resistance, irradiation damage and Ductile to Brittle Transition (DBT) behaviour. The second in this series of fusion grade structural material which became most popular is Eurofer97. A similar grade by examining for the better creep resistance was developed by India ([Laha et al., 2013](#); [Chaudhuri et al., 2012](#); [Jayakumar et al., 2013](#)) which is referred as Indian Reduced Activation Ferritic/Martensitic Steel (In-RAFMS).

Studies to assess structural integrity of RAFMS under high irradiation by [Kytka et al. \(2011\)](#) showed that the shift in Ductile to Brittle Transition Temperature (DBTT) results in an increase in DBTT by 100°C or more. It was also found that the maximum shift in DBTT for 2.43 dpa of irradiation occurred at 300°C. These and similar observations made the fracture behaviour of RAFMS in DBT region a major safety concern.

The existing method to characterize fracture behaviour in DBT region is more advanced in comparison to older yet in practise Impact and drop weight energy measurement methods. The master curve method ([E1921, 2013](#)) which statistically describes the fracture behaviour determines a material property known as reference transition temperature T_0 . This temperature can be obtained by testing smaller specimens and using the size adjustment method of master curve ([Donald E. McCabe, 2005](#); [E1921, 2013](#)), however, the basic assumption of master curve methodology which requires Small Scale Yielding (SSY) at the crack tip prohibits and also counters the size adjustment method. Additionally, irradiation studies demand smaller specimen characterization due to their ease in dosing the specimens with irradiation. The structure of the component i.e. TBM comprises many slots and channels for coolant passage where the thickness of the wall is smaller than the reference thickness of 1 inch (1T) used in master curve methodology. The smaller dimension structural components and ease in irradiation studies with smaller specimens require a method which can accurately transfer the fracture toughness from one dimension to another. In other words, the independence of master curve

method with parameters which may vary in application such as size, crack depth, loading rate is to be investigated extensively. Other major concern is the transferability of T_0 obtained from laboratory specimen to structural component. The master curve method as mentioned before may be affected by loss of constraint due to non self similarity of the stress field at the crack tip. Further the methodology of master curve used in analysing the fracture behaviour in DBT region suffers from a drawback of its inapplicability in the upper region of DBT. The true behaviour of fracture in the upper region of DBT is mostly censored by the master curve method due to significantly large ductile tearing preceding cleavage fracture. The censoring cuts off the true behaviour at maximum valid (i.e. fracture toughness without ductile tearing) K_{JC} . Moreover, for a dataset where all of the tests correspond to cleavage fracture with prior DCG cannot be used for T_0 estimation at all. The need to either extended or modified master curve method for its applicability in the upper region of DBT was realized. The approximation of master curve, mathematically modelled for lower region of DBT, cannot simply be extended in upper region of DBT due to significant amount of ductile tearing prior to cleavage. The real fracture behaviour in upper DBT is generally censored in master curve methodology due to the violation of its assumptions. Therefore, upper region of DBT where cleavage fracture is a possibility is yet to be investigated for accurate and complete assessment of fracture behaviour.

Objectives

The characterization of fracture behaviour of In-RAFMS in DBT region for the assessment of its structural integrity is the prime objective of this work. To understand the probability of catastrophic failure by cleavage fracture the statistical approach of master curve methodology is used as the tool to characterize the fracture behaviour of Indian RAFM steel in DBT region. The effect of both out of plane and in plane loss of constraint, effect of elevated loading rate and transferability of fracture toughness to different geometry are the domains explored in this work to meet the prime objective.

It is also a major concern of this work to analyse and include the cleavage fracture possibilities which occurs in the upper region of DBT and which is generally avoided with almost all the established fracture toughness characterizing methodologies.

TABLE 1: Experimental and numerical methodologies used in this work

Subject	Specimen Geometry	Loading rate	a/W	Material	Methodology
Conventional master curve	0.2T SE(B)	0.5 mmpm	0.5	In-RAFMS, P91	Conventional master curve
	0.4T SE(B)				
	0.4T CT				
	0.4T Charpy				
Loss of constraint	0.2T SE(B)	0.5	0.5	In-RAFMS, P91	$\sigma^* - V^*$ model
	0.4T SE(B)				
Loading rate	0.2T SE(B)	0.5 mmpm	0.5	In-RAFMS	Beremin's model
	0.4T Charpy	100 mmpm	0.5	In-RAFMS	
CT and TPB	0.4T Charpy	1000 mmpm	0.5	In-RAFMS	Weibull Triaxiality
	0.2T SE(B)	0.5 mmpm	0.5	In-RAFMS, P91	
	0.4T CT				
	0.4T Charpy				
1T CT					
Upper DBT	0.4T CT	0.5vmpm	0.5	In-RAFMS	Modified master curve
	0.2T SE(B)				

Methodology

To characterize the fracture behaviour of In-RAFMS steel in DBT region and to understand the effect of loss of constraint, type of specimen and loading rate, extensive fracture and tensile tests were performed on Compact Tension (CT), Single Edge Notched Bend (SENB/SE(B)), standard Charpy, Pre-cracked V Notch Charpy (PCVN) and sub-sized Charpy specimens in the range of -150°C to -50°C on In-RAFMS and P91 steels. The experimentally measured fracture toughness data were analysed using master curve approach which is described subsequently. The transferability of fracture toughness from one crack tip condition (level of constraint, loading rate, e.t.c.) to another, was examined by modified Ritchie Knott Rice (RKR) model. This methodology which is developed by [Bonadé et al. \(2008\)](#) is referred as $\sigma^* - V^*$ approach.

The numerical prediction of cleavage failure probability is generally determined by Beremin's model ([Beremin et al., 1983b](#)), which is also used in this work after calibration of Weibull parameters. The test matrix and analyses performed in this work are summarized in Table 1. The methodologies used and developed in this work are briefed below.

Master curve method

For ferritic steels, where the critical dislocation density for cleavage failure varies inversely with Peierls Nabarro stress; the toughness would show same type of correlation with temperature assuming Peierls Nabarro stress to be constant for ferritic steels (Wallin, 1993). The general form of fracture toughness distribution in DBT region for 1 inch (1T) thick specimens is expressed according to master curve methodology as,

$$K_{JC,1T} = A + (A_0 - A) \exp[C(T - T_0)]. \quad (1)$$

where $K_{JC(1T)}$ is the 1T thickness corrected elastic plastic fracture toughness, A_0 and T_0 are the reference values of fracture toughness and corresponding temperature. A and C are constants with T as temperature. The reference point of fracture toughness to describe DBT parameter is $100 \text{ MPa m}^{1/2}$ and the temperature corresponding to this value of median fracture toughness, is known as reference transition temperature, T_0 . The parameter C in Eq. (1) is the empirical constant defining correlation of fracture toughness with temperature. In conventional MC method, the values of A and C are $30 \text{ MPa m}^{1/2}$ and 0.019°C^{-1} , respectively. These values have been obtained by extensive studies on different grades of ferritic steels (Wallin, 1989a, 1993; Donald E. McCabe, 2005). The probability of cleavage failure P_f , in conventional MC is defined as,

$$P_f = 1 - \exp\left[-\frac{B_{nT}}{B_{1T}} \left(\frac{K_{JC} - K_{min}}{K_0 - K_{min}}\right)^4\right], \quad (2)$$

where K_{min} is the threshold below which cleavage cannot occur, B_{nT} is the thickness of the test specimen, B_{1T} is the reference thickness of 1 inch and K_0 is the scaling parameter of Weibull's fit which corresponds to K_{JC} at 63.2% cleavage failure probability.

 $\sigma^* - V^*$ approach

For the transferability of fracture toughness values obtained by testing specific specimen geometry to other geometry corresponding to different level of constraint, loading rate and stress field at the crack tip, the assumption that "same amount of deformed active volume corresponds to same probability of cleavage failure" can be used. The cleavage failure probability under the assumption of self similar stress field along the crack front is described with BK^4 scaling (Landes and Shaffer, 1980; Wallin, 2010a;

Donald E. McCabe, 2005) as,

$$P_f = 1 - \exp[-BK^4] . \quad (3)$$

For small specimen when self similarity of crack tip stress field is lost, one of the possible cleavage failure probability description is,

$$P_f = 1 - \exp[-BK^\lambda] . \quad (4)$$

The size adjustment of master curve methodology uses Eq.(3) for specimens of any thickness, however due to the break down of self-similarity of the stress field along the crack front the volume ahead of crack tip does not scale with a power 4 and therefore to find the true scaling a modified RKR model which utilizes the fact that cleavage occurs when a threshold tensile stress is reached at a characteristic distance from the crack tip. The characteristic distance may vary along the crack front as stress field may not be self similar and therefore, this criteria requires a volume to be considered which ends at the boundary where $\sigma_1 \geq \sigma_{th}$. The volume for a specimen geometry or for any crack front can be obtained by finite element analysis which then can be correlated to the fracture toughness K_{JC} or J to determine the true scaling parameter λ .

Beremin's model

A similar local approach of cleavage failure modelling numerically in DBT region started with the pioneer study of Beremin's group (Beremin et al., 1983b) on cleavage failure probability based on Weibull stress which is described as,

$$P_f = 1 - \exp[-(\frac{\sigma_W}{\sigma_u})^m], \quad (5)$$

where P_f is the numerical probability of cleavage failure, σ_u is the scaling parameter and m is the Weibull slope. σ_W is the Weibull stress defined as,

$$\sigma_W = [\frac{1}{V_0} \int_{V^*} \sigma_1^m dV]^{1/m}, \quad (6)$$

where V_0 is the reference volume not too big to have significant stress gradient nor too small to violate the characteristic length of RKR model (Ritchie et al., 1973) which is a few grains. Maximum principal stress, σ_1 , is integrated in the volume V^* . The volume

V^* is described to be the volume for which $\sigma_1 > \lambda \sigma_0$, where σ_0 is the yield strength of the material. Generally the value of λ is taken as 2 (Petti and Dodds Jr, 2005; Gao and Dodds Jr, 2005a; Wasiluk et al., 2006).

Weibull Triaxiality

For the described method of cleavage probability distribution estimation above, the Beremin's model has an implicit assumption that all the Reference Volume Elements (RVEs) for which the probability of failure is described by Eq.(5), should have the same stress levels. The Beremin's model therefore, is correct for a self-similar stress field. However, for a deviating condition from SSY condition needs a correction in the Beremin's formulation. This issue is addressed by assigning the ratio of triaxiality at the RVE, q_{RVE} , under consideration to the triaxiality level which is achieved at the centre or mid plane of the specimen geometry, q_{mid} as a weight factor to the probabilities of RVEs i.e. P of Eq.(6).

With above description where q is the triaxiality factor defined as the ratio of hydrostatic, σ_H , and equivalent σ_{eq} , stress components, Eq.(6) is re-written for modified Weibull stress σ_{Wm} as,

$$\sigma_{Wm}^m = \frac{1}{NV_0} \sum_{i=1}^N \sigma_{1,i}^m V_i \frac{q_{RVE}}{q_{mid}}, \quad (7)$$

where, there are N RVEs in the active volume V^* , each corresponding to a volume of V_i . The division by N is to make the quantity independent of finite number of RVEs involved in a Finite Element (FE) post processing calculation. Using Eq.(6) the σ_{Wm} can be expressed as,

$$\sigma_{Wm} = \sigma_W \left\{ \frac{1}{N} \sum_{i=1}^N \frac{q_{RVE}}{q_{mid}} \right\}^{1/m}. \quad (8)$$

The extra terms in Eq.(8) is defined as Weibull Triaxiality and denoted as q_W as,

$$q_W = \left\{ \frac{1}{N} \sum_{i=1}^N \frac{q_{RVE}}{q_{mid}} \right\}^{1/m}. \quad (9)$$

This new parameter is a measurement of deviation of self-similarity of stresses in the active volume of a specimen geometry and therefore, it also measures the constraint in a geometry with a reference frame set at SSY condition. The reference point is SSY condition as for a self-similar stress field the q_W is always 1. Therefore, q_W calculation avoids the modified boundary layer modelling for assessments of constraint deviation.

Due to the modifications described here, the probability of cleavage failure can be re-defined as,

$$P_f = 1 - \exp\left[-\left(\frac{\sigma_{Wm}^{m/4} - \sigma_{Wm-min}^{m/4}}{\sigma_{Um}^{m/4} - \sigma_{Wm-min}^{m/4}}\right)^4\right], \quad (10)$$

where σ_{Wm-min} and σ_{Um} are the minimum modified Weibull stress and modified scaling parameter. The values of σ_{Wm-min} and σ_{Um} are obtained from the history of $\sigma_{Wm} - K_{JC}$.

Structure of the thesis and results

The thesis starts by highlighting the challenges of fusion reactor technology with a motivation towards cheaper, safer and cleaner energy source. The history of the concept and the practical aspects of the ITER program and its design activities are outlined in brief in Chapter 1, which converges towards the development of structural component of fusion reactor, especially first wall blanket component. With In-RAFMS developed in our country this work of investigation finds its objective to examine the fracture behaviour of In-RAFMS in DBT region and to investigate, extend and possibly correct the existing probabilistic approach of master curve to the domains of practical/operational importances but beyond the scope of conventional master curve methodology in Chapter 1.

The methodology is reviewed in depth and its applicability on similar grades of materials are documented in Chapter 2, which helps in formulating the test matrix and numerical program for understanding and characterizing the fracture behaviour in DBT region. The detailed formulation of the problem addressed in this work and proposed test matrix is described in Chapter 3.

The details of microstructure, phase transformation and precipitates in In-RAFMS and mod-9Cr-1Mo steels with comparison to other popular grades of ferritic/martensitic steels are provides in Chapter 4.

The experimental set-up, standards, test specimen geometries, temperature set up, procedure of fracture toughness measurements along with details of impact energy measurement, microstructural examinations are described in the first part of Chapter 5. The

finite element analyses pre and post processing methods with formulation and meshing schemes used for standard calculations such as modified boundary layer model are provided in second part of Chapter 5.

Chapter 6 titled "In-RAFMS mechanical behaviour in DBT & conventional master curve" describes the impact toughness and uniaxial tensile behaviour in DBT region. The second part of the chapter comprises conventional master curve, comparison of single and multi-temperature methods, and the effect of valid data/censoring on uncertainty in estimation of reference transition temperature.

Chapter 7 & 8 describe loss of constraint both out of plane and In-plane, respectively. The chapter on Out of plane constraint loss details the conventional master curve analysis of 0.2T TPB specimens of In-RAFMS which resulted in a T_0 of -123°C . In this analysis the small specimen do not show a self similar stress field at crack front and therefore the master curve assumption of BK^4 scaling does not work. This violation of SSY condition is corrected numerically by transforming the volume deformed under a non-SSY condition to an equivalent SSY condition which is described as $\sigma^* - V^*$ approach. The numerical correction based on $\sigma^* - V^*$ approach resulted in a T_0 of -109°C .

The active volume V^* dependencies on $K_{JC,2D}$ obtained by integrating the area under maximum principal stress at mid plane along thickness and on $K_{JC,3D}$ by calculating the volume with non-self similarity of stress field are shown in Figure 1(a) and the SSY corrected master curve obtained by testing 0.2T SE(B) specimens is shown in Figure 1(b).

Chapter 8 describes in-plane constraint loss by analysing the results obtained by testing specimen of same dimension as for out of plane constraint loss study in chapter 7, with varying crack depths showed an expected behaviour of increasing T_0 from lowest value of -125°C for crack depth of 0.3 to 0.44 to highest of -99°C for crack depth of 0.65 to 0.7. The approach of $\sigma^* - V^*$ again showed good potential to scale the differently constrained conditions to SSY condition and a T_0 of -100°C was obtained for all data transformed to a/W of 0.5. The in plane change in constraint also showed that the standard deviation increased for shallower crack depths which indicated that as the dataset

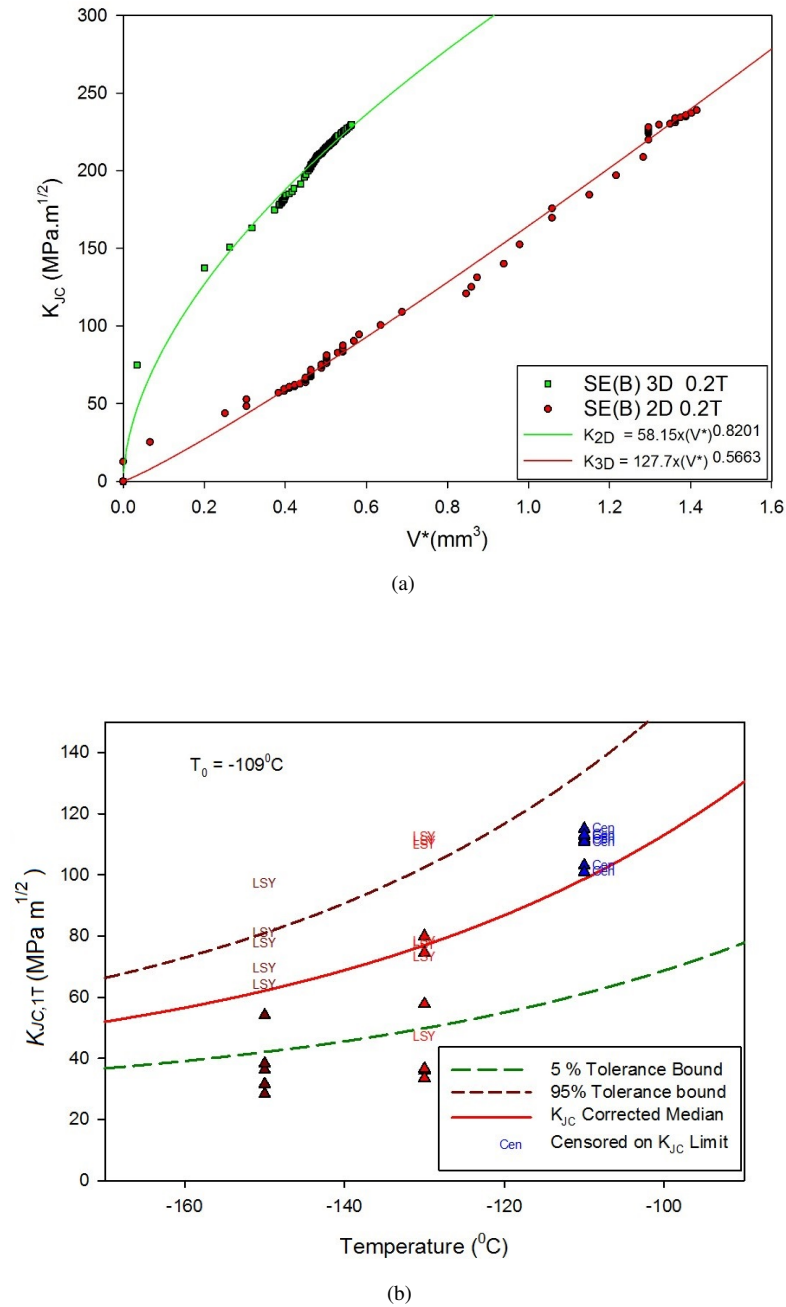


FIGURE 1: (a) Active volume V^* versus K_{JC} and (b) master curve of In-RAFMS with untransformed and transformed datasets based on Active volume V^* versus K_{JC} behaviour under non-SSY condition with loss of constraint

moves away from high constraint condition more uncertainty is induced in the estimation of T_0 . The T_0 obtained with $K_{JC,med}$ and master curve obtained by transferring all the data to an a/W of 0.5 is shown in Figure 2.

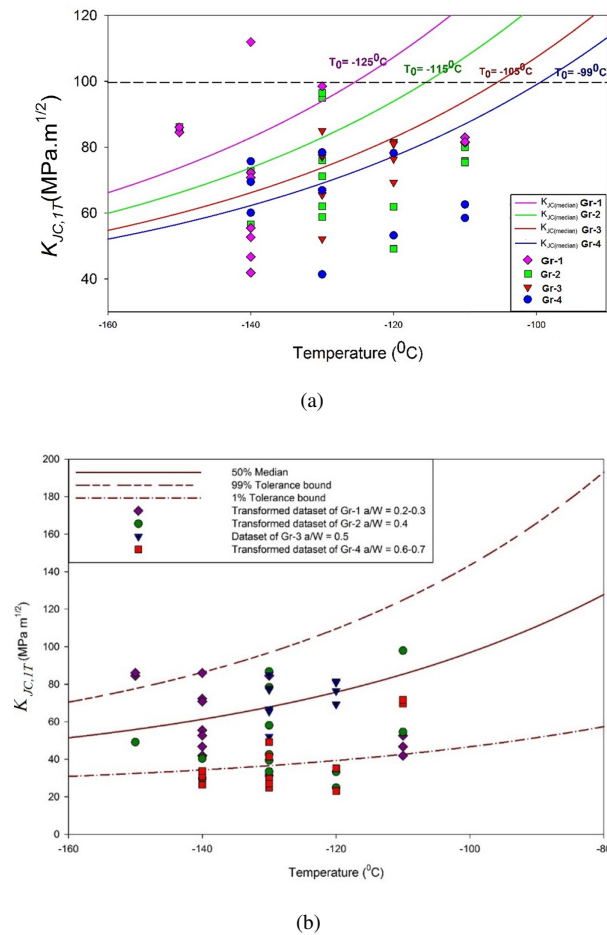


FIGURE 2: Master curve of data transferred at a/W of 0.5 using $\sigma^* - V^*$ approach showing (a) Shift in T_0 with a/W and (b) K_{Jc} transformed to $a/W = 0.5$

Chapter 9 describes the two popular loading schemes of fracture mechanics which impose different amount of triaxiality along the crack front. The effect is further complicated with the in plane and/or out of plane constraint effects as discussed above. CT and TPB specimens of In-RAFMS as well as P91 steels re-confirmed the effect and proved once again that CT specimens should be preferred for T_0 estimation as it always shows more triaxiality in comparison to bending for identical a/W and thickness. The bending scheme may have other benefits such as quick setting up while testing and advantage of using load line displacement for K_{Jc} measurement but it also induces errors associated with the misalignment while fixing the specimens. The side grooved specimens of In-RAFMS showed the constraint level reaches high enough to ensure self similarity of stress field. The Weibull Triaxiality developed as an independent constraint assessment parameter is shown in Figure 3 comparing different specimens tested for T_0 determination of In-RAFMS and P91 steels.

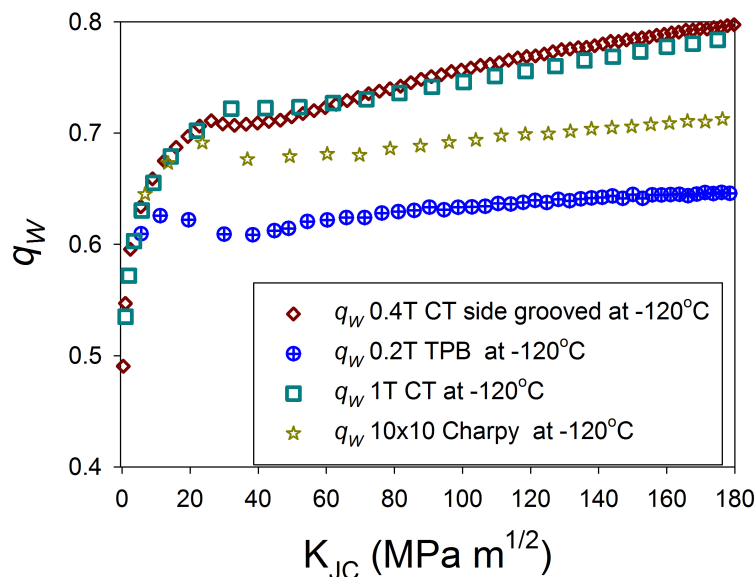


FIGURE 3: The Weibull triaxiality q_w compared for different specimens at -120°C with In-RAFMS tensile response as FEA input

The effect of loading rate on reference transition temperature is described in Chapter 10. The experimental results on the dataset of In-RAFMS at three different loading rates showed an expected systematic increase in T_0 with increasing loading rate. The Weibull stress analysis was used to predict the cleavage failure probability numerically. This method required a numerical parameter which is also a material property to be calibrated. For In-RAFMS this material property known as Weibull modulus was found to be 9. The Weibull modulus for P91 was also calibrated for the first time and was found to be 15. The numerical prediction of Weibull stress analysis does not show very good agreement with the experimental results. This behaviour is attributed to the effect of plastic strain which causes violation of constant numbers of cleavage initiators in the active volume. The reasoning is in support of experimental results as for higher loading rate datasets the Weibull stress based numerical predictions were better than that for quasi-static condition. As higher strain rate imposes more triaxiality, the possibility of cleavage initiators turning into void nucleation sites decreases. The master curves at different loading rates and the comparison of shift in T_0 with Wallin's correlation is shown in Figure 4. The Beremin's model used for numerical predictions of cleavage failure probability at different loading rates are shown in Figure 5.

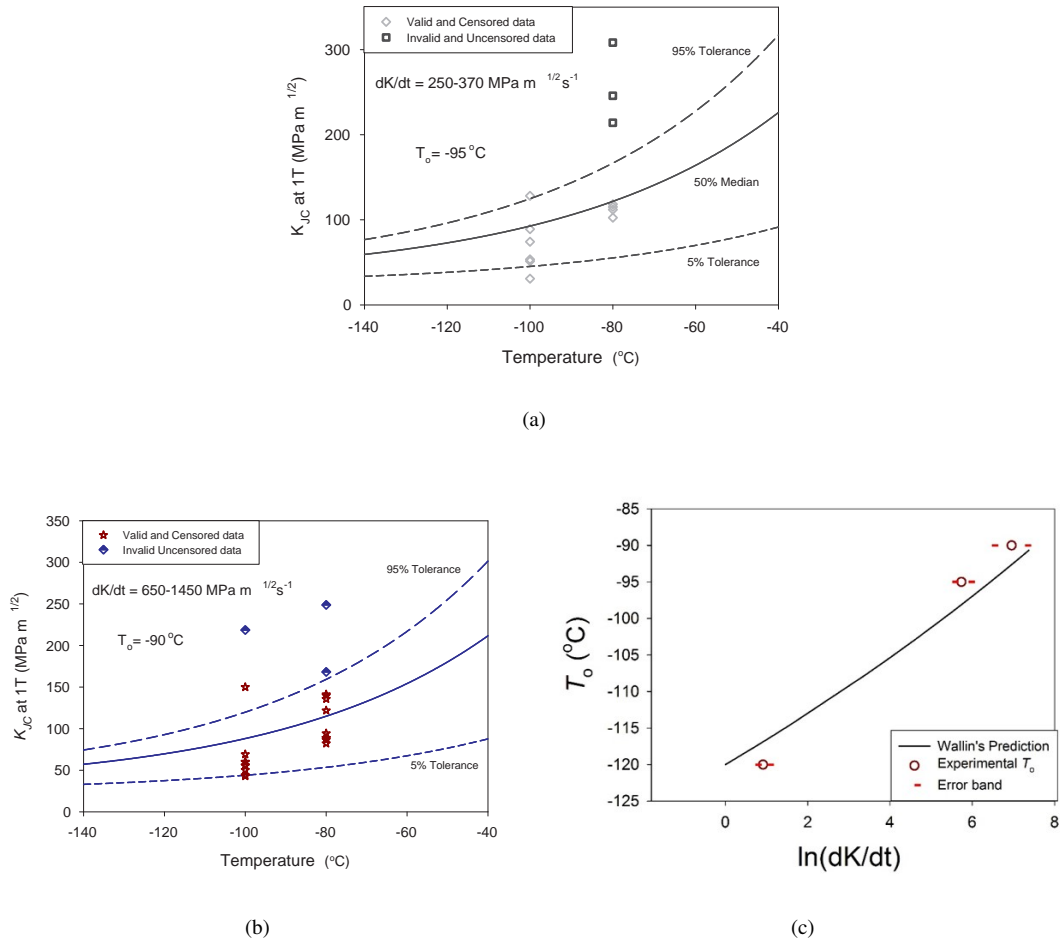


FIGURE 4: Master curves at different loading rates and ΔT_0 of In-RAFMS with increasing loading rate

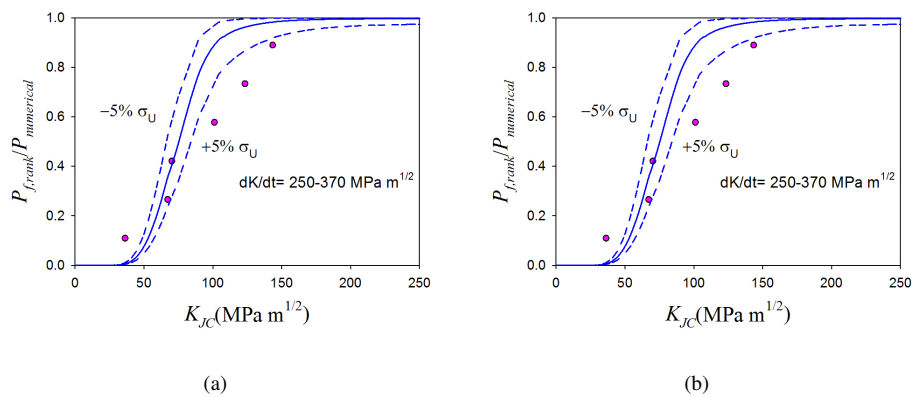


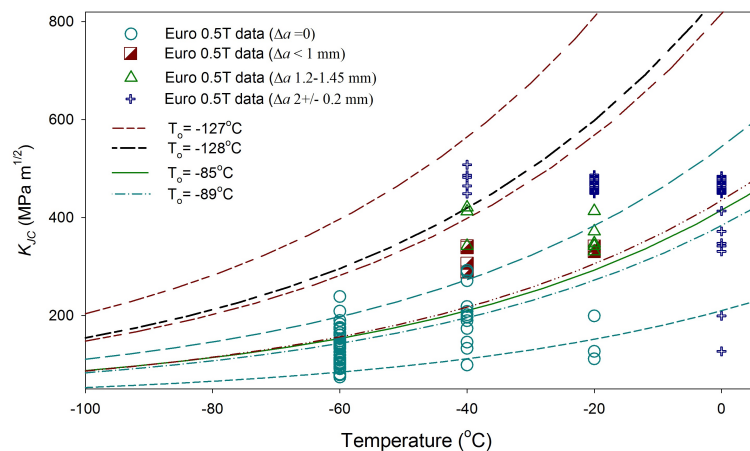
FIGURE 5: Numerical prediction and experimental rank probabilities for fracture tests performed at (a) 100 mm/min and (b) 1000 mm/min actuator speed.

Chapter 11 describes the effect of ductile tearing on cleavage fracture. The event of cleavage fracture preceded by ductile tearing is analytically modelled and a contribution due to change in constraint with ductile tearing which was mostly ignored by previous researchers is considered in the mathematical model. The change in triaxiality measured as q_f/q_o where q is the ratio of hydrostatic and Mises stress components for final and initial conditions, when incorporated with correction of increasing active volume with ductile tearing, the probability of cleavage failure resulted in a form shown as,

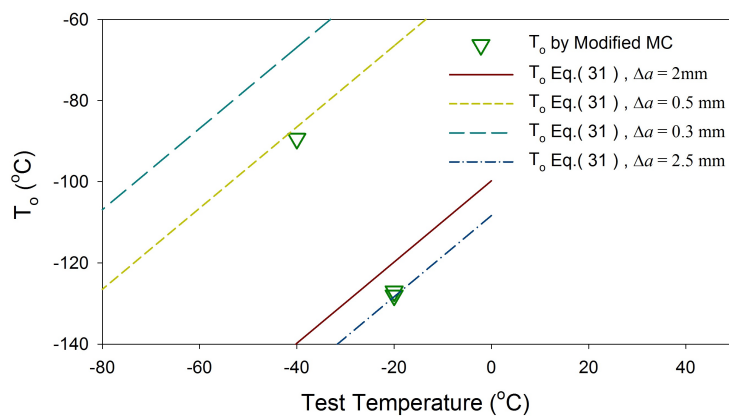
$$\ln\left(\frac{1}{1-P_f}\right) = \left(\frac{B_{nT}}{B_{1T}}\right)\left(\frac{q_f}{q_i}\right) \cdot \left(\frac{K - K_{min}}{K_o - K_{min}}\right)^4 \cdot \left[1 + 2\frac{(\Delta K)^2}{K^2}\right], \quad (11)$$

where ΔK is the change in K_{JC} with amount of ductile tearing Δa . The triaxiality and active volume were calculated by modelling ductile crack growth using GTN model with VUMAT subroutine.

It was found that this modification expands the validity window of master curve approach and predicts T_o in very close range to one obtained by conventional method when the dataset contains only few cleavage fracture events with prior ductile tearing. Moreover, the T_o was also obtained for the dataset where no valid data according ASTM E1921 was available and no T_o could have been obtained by using conventional master curve method. The modified method was used and justified on Euro fracture data (Heerens and Hellmann, 1999), and on the dataset CT and SE(B) geometries of In-RAFMS. The modified master curve in comparison with conventional master curve for Euro 0.5T CT dataset is shown in Figure 6 (a). The prediction based on mean approximation of $K_{JC} - \Delta a$ is compared with the results obtained by using modified master curve in Figure 6 (b)



(a)



(b)

FIGURE 6: (a) Modified master curve and conventional master curve comparison for *Euro 0.5TCT* dataset and (b) comparison of modified master curve results with one obtained from mean approximation of $K_{JC} - \Delta a$

Conclusions

- The conventional master curve was used for the determination of T_0 of fusion reactor test blanket structural In-RAFMS steel using smaller CT and Bend specimens. The T_0 for In-RAFMS was -120°C . The loss of constraint for smaller specimens was studied using $\sigma^* - V^*$ approach extensively for both in plane and out of plane

loss of constraint. The $\sigma^* - V^*$ approach was found accurate enough for transferring the fracture toughness to SSY condition and estimated conservative T_0 for smaller In-RAFMS specimens was found to be -109°C .

- The in plane constraint loss study using test specimens with crack depth from a/W of 0.3 to 0.7, showed that in this range of crack depth, T_0 shows consistent correlation with constraint and $\sigma^* - V^*$ approach can be used for estimation of T_0 for any a/W in the investigated range.
- The differences of constraint between CT and TPB geometries were analysed using a novel Weibull Triaxiality method which was found to correct Beremin's model for constraint. The numerical predictions based on corrected Beremin's model shows the potential of Weibull Triaxiality.
- The assessment of loading rate effect on T_0 was found to follow Wallin's correlation based on Zener-Holomon strain rate parameter. The numerical prediction based on Beremin's model showed good accuracy and Weibull slopes were calibrated for the first time for In-RAFMS, P91 and F82H steels which were 9, 15 and 11, respectively.
- The master curve validity window was expanded by modifying the cleavage failure probability when cleavage is preceded by significant amount of ductile tearing. The increasing active volume, increasing triaxiality and criticality of carbides were taken care of in the modified master curve with the help of constraint assessment by triaxiality factor q and re-derivation of increasing active volume. The modified master curve was found to estimate T_0 for a dataset where no T_0 estimation was possible using conventional master curve approach. This modification was found applicable in upper region of DBT where cleavage is followed by significantly large amount of ductile tearing of the order of 2.5 mm.

References

- ASTM E. (1921) E 1921 standard test method for determination of reference temperature. T₀, for ferritic steels in the transition range
- Beremin F. M., Pineau A., Mudry F., Devaux J.-C., D'Escatha Y., Ledermann P. (1983) A local criterion for cleavage fracture of a nuclear pressure vessel steel. *Metallurgical Transactions A* 14(11):2277–2287, doi10.1007/BF02663302
- Bonadé R., Mueller P., Spätig P. (2008) Fracture toughness behavior in the ductile–brittle transition region of the tempered martensitic eurofer97 steel: Experiments and modeling. *Engineering fracture mechanics* 75(13):3985–4000
- Chaudhuri P., Kumar E. R., Sircar A., Ranjithkumar S., Chaudhari V., Danani C., Yadav B., Bhattacharyay R., Mehta V., Patel R., Vyas K., Singh R., Sarkar M., Srivastava R., Mohan S., Bhanja K., Suri A. (2012) Status and progress of indian {LLCB} test blanket systems for {ITER}. *Fusion Engineering and Design* 87(78):1009 – 1013, doihttp://dx.doi.org/10.1016/j.fusengdes.2012.02.062,
- Donald E. McCabe K. W. John G. Merkle (2005) An Introduction to the Development and Use of the Master Curve Method.
- Gao X., Dodds Jr R. H. (2005) Loading rate effects on parameters of the weibull stress model for ferritic steels. *Engineering Fracture Mechanics* 72(15):2416 – 2425, doihttp://dx.doi.org/10.1016/j.engfracmech.2005.03.001
- Heerens J., Hellmann D. (1999) Fracture toughness of steel in the ductile to brittle transition regime. Final Report, Measurement and Testing Programme Contract MAT1-CT-940080
- IAEA (2001a) Final Report of the ITER EDA. No. 21 in ITER EDA Documentation Series, INTERNATIONAL ATOMIC ENERGY AGENCY, Vienna,
- IAEA (2001b) Summary of the ITER Final Design Report. No. 22 in ITER EDA Documentation Series, INTERNATIONAL ATOMIC ENERGY AGENCY, Vienna,
- Jayakumar T., Mathew M., Laha K. (2013) High temperature materials for nuclear fast fission and fusion reactors and advanced fossil power plants. *Procedia Engineering* 55:259 – 270, doihttp://dx.doi.org/10.1016/j.proeng.2013.03.252,
- Kytka M., Brumovsky M., Falcnik M. (2011) Irradiation embrittlement characterization of the eurofer 97 material. *Journal of Nuclear Materials* 409(2):147–152
- Laha K., Saroja S., Moitra A., Sandhya R., Mathew M., Jayakumar T., Kumar E. R. (2013) Development of india-specific RAFM steel through optimization of tungsten and tantalum contents for better combination of impact, tensile, low cycle fatigue and creep properties. *Journal of Nuclear Materials* 439(13):41 – 50, doihttp://dx.doi.org/10.1016/j.jnucmat.2013.03.073
- Landes J., Shaffer D. (1980) Statistical characterization of fracture in the transition region. In: *Fracture Mechanics*, ASTM International

- Petti J. P., Dodds Jr R. H. (2005) Calibration of the weibull stress scale parameter, u , using the master curve. *Engineering Fracture Mechanics* 72(1):91 – 120, doi-<http://dx.doi.org/10.1016/j.engfracmech.2004.03.009>
- Ritchie R. O., Knott J. F., Rice J. (1973) On the relationship between critical tensile stress and fracture toughness in mild steel. *Journal of the Mechanics and Physics of Solids* 21(6):395–410
- Tagawa T., Kayamori Y., Hira H. (2010) Statistical scatter of fracture toughness in the ductile–brittle transition of a structural steel. *Engineering Fracture Mechanics* 77(16):3077–3086
- Wallin K. (1989) The effect of ductile tearing on cleavage fracture probability in fracture toughness testing. *Engineering Fracture Mechanics* 32(4):523–531
- Wallin K. (1993) Irradiation damage effects on the fracture toughness transition curve shape for reactor pressure vessel steels. *International journal of pressure vessels and piping* 55(1):61–79
- Wallin K. (2010) Structural integrity assessment aspects of the master curve methodology. *Engineering Fracture Mechanics* 77(2):285 – 292, doi-<http://dx.doi.org/10.1016/j.engfracmech.2009.02.010>
- Wasiluk B., Petti J. P., Jr. R. H. D. (2006) Temperature dependence of weibull stress parameters: Studies using the euro-material. *Engineering Fracture Mechanics* 73(8):1046 – 1069, doi<http://dx.doi.org/10.1016/j.engfracmech.2005.11.006>

Chapter 1

Introduction

In this chapter, the background of fusion reactor technology is briefed and motivations are drawn for the dissertation work. The objectives of the work is followed subsequently.

1.1 A brief history of fusion reactor & challenges to structural integrity

The worldwide energy demand with an estimated increase of electricity production by at least a factor of two in the second half of this century, fading resources of raw materials and a growing concern about global warming require innovative solutions (Kytka et al., 2011). The concept of producing efficient energy at low cost to make energy available for everything and everyone gave motivation for the nuclear power production and resulted in large scale power production units through nuclear fission reactors world wide. The technology of fission reactor is well established, in-depth studied, and worked upon. However, the huge radioactive waste and nuclear accidents such as, Three miles island, Chernobyl and Fukushima raise concerns regarding the safety and environmental effects of nuclear power (Oughton, 2016). With the added benefit of being even cheaper and non-fossil source of power, fusion power production is highly appreciated by the world and the first largest international collaboration currently including India, Russian Federation, China, South Korea, Japan, European Union and USA came under the umbrella of International Thermonuclear Experimental Reactor (ITER) program to establish this technology.

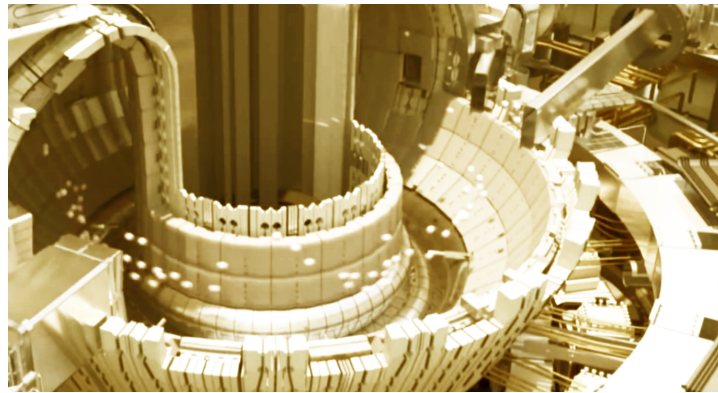
The power production from fusion of two light elements such as Deuterium (D) and Tritium (T) is not practically very easy. The first device to magnetically confine plasma as a pre-requisite for this reactor started in 1950 with the *tokamak* creation credited

to Andrei Sakharov and Igor Kurchatov ([Bromberg, 1982](#); [Wikipedia, 2004](#)). For the fusion reaction i.e. the fusion of D and T, it requires a very high temperature (gas temperature approx. 5×10^7 K) for the fusion reaction rate to attain its peak ([Bromberg, 1982](#); [Stacey, 2010](#)). Other possibilities such as fusion of D-D and D-He require further higher temperatures. To generate this amount of temperature the concept of Z-pinch is used ([Miernik et al., 2013](#)). The first nuclear fusion registered in 1948 was also the first detailed examination of this concept which was patented by the United Kingdom Atomic Energy Authority. The invention of this reactor with Z-pinch is credited to Sir George Paget Thomson and Moses Blackman.

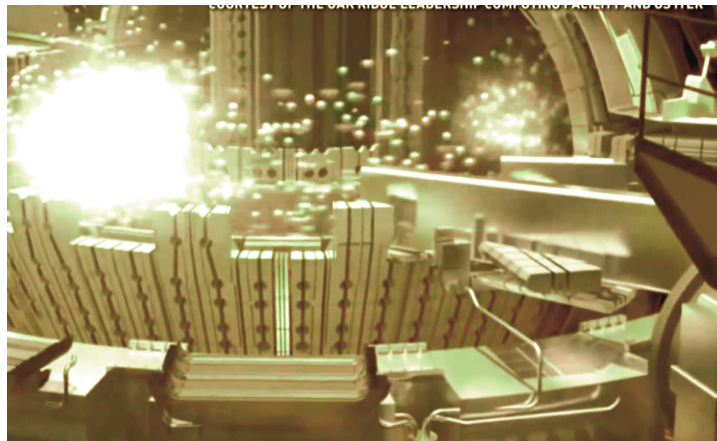
The principle of Z-pinch is that a current passing through plasma generates a magnetic field around it which according to Lenz's law causes an inward force for plasma to collapse in. This results in a dense plasma, which further increases the inward force. This chain reaction in controlled manner can reach the density and temperature required for D-T reaction to occur. However, the challenge is to have an electrode which can pass current to this plasma at the temperature of as high as million K. The possibility is explored by inducing current by magnetic fields around plasma. Because the plasma is charged and thus reacts to electrical and magnetic field the plasma is also controlled by these fields. The practicality of the idea of harnessing energy with a safer and cheaper means motivated towards the first international project in 1985 when European community, Soviet Union, Japan and United States were invited to conceptualize by IAEA the terms and conditions of engineering and design activities of an International Thermonuclear Experimental Reactor (ITER). The acceptance of IAEA invitation was realized in 1988 and in 1990 first conceptual design activity was completed. Further progress in terms and conditions of Engineering Design and Activity (EDA) resulted in IAEA-EDA agreement in 1992. In 1998, at the end of the six years of joint work originally foreseen under the ITER EDA agreement, a design for ITER was developed which fulfilled the overall programmatic objectives and complied with the detailed technical objectives, technical approaches, and the cost target adopted by the ITER Parties in 1992 at the start of the EDA ([IAEA, 2001a](#))

Due to huge financial requirements, safety concerns and challenges of practicality, the formation of Special Working Group (SWG) lead to divide the full-fledged reactor establishment to smaller steps or phases of fusion reactor technology (IAEA, 2001b).

- **H-phase** This is a non-nuclear phase using only hydrogen or helium plasmas, planned mainly for complete commissioning of the tokamak system in a non-nuclear environment where remote handling maintenance is not mandatory.
- **D-phase** The characteristics of deuterium plasma are very similar to those of DT plasma except for the amount of alpha heating. Therefore, the reference DT operational scenarios, i.e., high Q, inductive operation and non-inductive steady state operation, can be simulated further. Since some tritium will be generated in the plasma, fusion power production for short periods of time without fully implementing the cooling and tritium-recycle systems could therefore also be demonstrated. By using limited amounts of tritium in a deuterium plasma, the integrated nuclear commissioning of the device will be possible. In particular, the shielding performance will be tested.
- **D-T Phase** During the first phase of DT operation the fusion power and burn pulse length will be gradually increased until the inductive operational goal is reached. Non-inductive, steady state operation will also be developed. DEMO reactor relevant test blanket modules will also be tested whenever significant neutron fluxes will be available, and a reference mode of operation for that testing will be established. The second phase of full DT operation, beginning after a total of about ten years of previous operation, will emphasise improvement of the overall performance and the testing of components and materials with a higher neutron fluence. This phase will address the issues of higher availability and further improved modes of plasma operation. The implementation and the programme for this phase will be decided following a review of the results from the preceding three operational phases and an assessment of the merits and priorities of programmatic proposals. A decision on incorporating in the vessel a tritium breeding blanket during the course of the second D-T phase will be taken on the basis of



(a)



(b)

FIGURE 1.1: Computer simulation of nuclear fusion reaction in a tokamak (a) D-T reaction (b) Plasma generation (Daniel, 2012)

the availability of this fuel from external sources, its relative cost, the results of breeder blanket module testing, and acquired experience with plasma and machine performance.

This basic idea of controlled production of plasma resulting in D-T reaction with further challenges such as maximizing the energy efficiency and structural components which can withstand the high temperatures resulted in the design of ITER -tokamak; the world's largest nuclear fusion device which is based in France. The D-T reaction generating plasma in toroidal and poloidal magnetic fields are shown in Figure 1.1. The shielding blanket is divided into two parts as shown in Figure 1.2.

The part at the front that may be separated from a back one. The back part with a radial thickness of around 30 cm is a pure shield made of steel. The front part, the

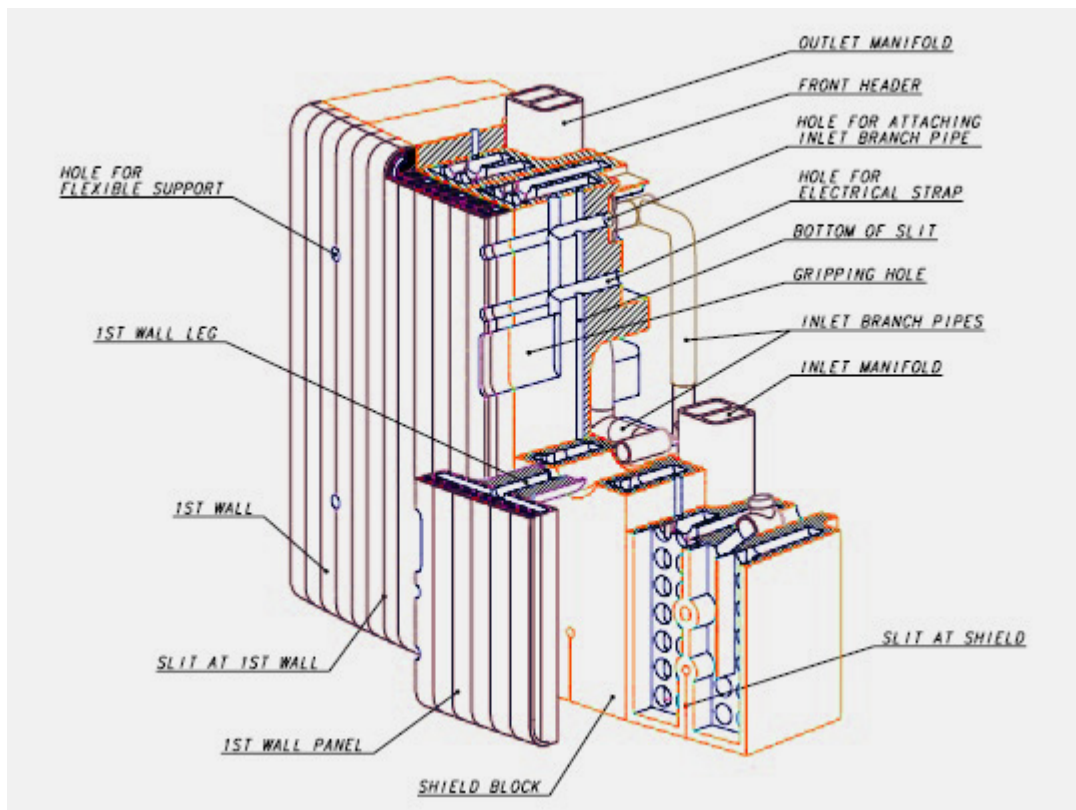


FIGURE 1.2: Test blanket module

first wall, includes various different class of materials which are 1 cm thick Beryllium armour protection, 1 cm thick copper to diffuse the heat load as much as possible, and around 10 cm of steel structure. *This component will become the most activated and tritium-contaminated component in the entire ITER device.* It could be in contact with the plasma in off normal conditions, and thus can suffer damage from the large heat locally deposited, and may have to be repaired or possibly changed.

The operational pulsating mode due to non-availability of longer duration plasma, high temperature and high energy neutrons demand the first wall blanket material to have enough structural strength to withstand these conditions. The first wall blanket is also the component which is used for flowing lead-lithium eutectic which works as Tritium breeder and coolant. Due to such operational conditions the first reference taken for structural material came from the extensively researched fission reactor. The initial studies for fast breeder reactors conditions showed that the austenitic stainless steels were prone to swelling resulting from irradiation induced vacancy-interstitial creations. The fusion reactor condition therefore would magnify this effect due to even higher

energy irradiation caused by 14MeV neutrons in comparison to 2MeV neutrons of fission reactors. The tempered martensitic steels showed good swelling resistance and therefore the reference material for fusion reactor test blanket material converged on modified 9%Cr–1%Mo steels ([Banerjee, 2014](#); [Mathew et al., 2011](#); [Jayakumar et al., 2013](#)).

Due to the high energy irradiation the safe waste management of radioactive materials requires the activity of nuclear components to be controlled. The low activity therefore was achieved by replacing the active elements of modified 9%Cr–1%Mo steels with low activity W, Ta and Mn.

In the process of establishing fusion reactor technology, Pb-Li eutectic is to be used as tritium breeder (Lead-lithium ceramic breeder/LLCB) and helium to be used for cooling. The test blanket module which consists of U-shaped first wall with helium cooling system has inlet at 350°C and outlet at 480°C, helium pressure of 8 MPa and pressure drop of 0.3 MPa. With 9%Cr–1%Mo steels as reference material the proposed material for U-shaped first wall structure evolved as Reduced Activation Ferritic Martensitic steel (RAFMs). Many such steels such as EUROFER-97, F82H, JLF, Optifier and In-RAFMs are proposed by different parts of world. First generation of RAFMS, however, were OPTIFIER, MANET and F82H. The more improved version of Eurofer97 was developed after F82H which was followed by other grades from different part of the world. Research activities on the future generation of RAFMS which is oxide strengthened grades mainly by oxides of Yttrium has also started world wide ([Banerjee, 2014](#); [Jayakumar et al., 2013](#)).

Being a ferritic martensitic steel, RAFMs undergoes a transition from ductile to brittle failure at lower temperature. Transition temperature of steels, also known as reference temperature (T_0) shifts upward under the influence of irradiation. Both for quasi-static and dynamic loading rates the transition temperature can shift by 100°C with an irradiation dose of 2dpa ([Kytka et al., 2011](#)). The irradiation studies, on various grades of RAFMs, further show that for damage induced at 250-300°C the shift in transition temperature is maximum. Therefore, in order to assure the structural safety and integrity

of the test blanket module, it becomes utmost important to understand the behaviour of fracture toughness in DBT region for RAFM grade steels and effect if irradiation on it.

At present, the transition temperatures of steels are characterized by impact toughness, RT_{NDT} ASME approach and recently developed Master Curve approach (Wallin, 1984; Yoon et al., 2001a). Out of these, impact test method suffers with huge scatter and requires large number of samples. Additionally for testing and measurement of mechanical responses of nuclear grade materials, the conventional standard size impact specimens are too big and sub-sized and miniature specimens which are best for irradiation studied do not show a single correlation with standard size specimens.

On the other hand RT_{NDT} approach of ASME uses the data from impact tests and drop weight tear tests and takes the lowest values to determine reference temperature. This approach does not deal with the scatter of data and results in an over-conservative estimate in many cases.

Master Curve (MC) approach is the only approach which works on the concept of stochastic nature of cleavage initiators' distribution in DBT regime; making it the most efficient method for transition behaviour characterization (Slatcher, 1986).

The extensive research on Indian RAFMS started with reference composition of Eurofer97 and four different compositional variation were studied exhaustively for creep deformation strength, low cycle fatigue properties, tensile and impact properties. The chemical composition of elements driving these properties in steels i.e. W and Ta were studied with four basic variation in compositions of W and Ta. The four alloys comprises 1%W-0.06%, 1.4%W-0.06%, 2%W-0.06% and 1%W-0.14% Laha et al. (2013).

The higher activity elements such as Mo, Nb, B, Cu, Ni, Al, Co, Ti and embrittling elements such as S, P, As, Sb, Sn, Zr and O are kept in ppm levels. After the extensive studies on mechanical behaviour the second composition was declared as In-RAFMS Laha et al. (2013), with the understanding that 1.4%W results in the best creep rupture strength and creep deformation resistance and 0.06%Ta with 9%Cr gives the lowest possible Ductile to Brittle Transition Temperature (DBTT) obtained from 68 Joule criteria

of impact toughness. The heat treatment of In-RAFMS is fixed to be solutionized at $1263\pm 10\text{K}$ for 30 minutes per 25 mm. After solutionizing and normalizing the plates are to be tempered at $1038\pm 5\text{K}$ for 90 minutes per 25 mm thickness.

1.2 Objectives

The structural material for the fusion reactor test blanket developed in India which is designated as Indian reduced activation ferritic martensitic steel (In-RAFMS) is designed by its creep and fatigue properties with swelling resistance against irradiation. Further understanding of effect of irradiation on transition behaviour and mechanical behaviour under liquid metal embrittling environment of Pb-Li eutectic is required. The objective of work presented here is to study extensively the fracture behaviour of Indian RAFMS in DBT region with the help of probabilistic master curve approach.

With the broad objective to characterize the fracture behaviour of In-RAFMS in DBT region following objectives were derived.

- To determine the conventional reference transition temperature for In-RAFM and modified 9Cr-1Mo steels and also to examine the effect of censoring of dataset and censoring parameter.
- To establish a method of transforming the fracture toughness obtained from smaller specimen to SSY and other non-SSY scales.
- To understand the effect of size and specimen geometries, such as CT and SE(B) on reference transition temperature.
- To understand the effect of loading rate on reference transition temperature.
- To establish numerical methods of predicting cleavage fracture probability for different sizes and loading rates.
- To determine reference transition temperature from cleavage fracture with prior ductile tearing.

The scope of the work, therefore, includes the parametric study of loading rate, specimen geometry type (CT and SE(B)), and the fracture behaviour in full domain of DBT. To attain this material based understanding, the scope of this work also includes the modification in the existing methodology of master curve in the DBT region where applicable.

1.3 Structure of thesis

The thesis starts by highlighting the challenges of fusion reactor technology with a motivation towards cheaper, safer and cleaner energy source. The history of the concept and the practical aspects of the ITER program and its design activities are outlined in brief in Chapter 1. With In-RAFMS developed in our country as structural first wall blanket material, this work of investigation finds its objective to examine the fracture behaviour of In-RAFMS in DBT region and to investigate, extend and possibly correct the existing probabilistic approach of master curve to the domains of practical/operational importances but beyond the scope of conventional master curve methodology in Chapter 1.

The methodology is reviewed in depth and its applicability on similar grades of materials are documented in Chapter 2 which helps in formulating the test matrix and numerical program for understanding and characterizing the fracture behaviour in DBT region. The detailed formulation of the problem addressed in this work and proposed test matrix is described in Chapter 3.

The details of microstructure, phase transformation and precipitates in In-RAFMS and mod-9Cr-1Mo steels with comparison to other popular grades of ferritic/martensitic steels are provides in Chapter 4.

The experimental set-up, standards, test specimen geometries, temperature set up, procedure of fracture toughness measurements along with details of impact energy measurement, microstructural examinations are described in the first part of Chapter 5. The

finite element analyses pre and post processing methods with formulation and meshing schemes used for standard calculations such as modified boundary layer model are provided in second part of Chapter 5.

Chapter 6 titled "In-RAFMS mechanical behaviour in DBT & conventional master curve" describes the impact toughness and uniaxial tensile behaviour in DBT region. The second part of the chapter comprises conventional master curve, comparison of single and multi-temperature methods, and the effect of valid data/censoring on uncertainty in estimation of reference transition temperature.

The loss of constraint occurring due to out of plane dimension is dealt in Chapter 7, where the effect is analysed and corrected numerically with a thickness scaling or constraint transformation method developed as an outcome of this work. The same approach was proven to be applicable to solve the problem of loss of constraint resulting from in-plane changes in crack tip stresses due to different crack depths. The approach also is claimed and justified as a tool of constraint measurement as detailed in Chapter 8.

The persistent problem of bending and tension loading in fracture mechanics is taken care off in Chapter 9. The problem is analysed using the dataset generated on CT and TPB geometries of P91 and In-RAFM steels and a novel method of constraint measurement is developed. The importance of simple side-grooving method which appears to solve the large scale yielding problem for smaller specimens is discussed in this chapter.

The effect of loading rate at three different actuator speeds is studied in Chapter 10. To examine this aspect a numerical property which is presumably a signature of material and also known as Weibull modulus is calculated for In-RAFMS in this Chapter by calibrating it on the dataset created for high constraint and low constraint conditions which is analysed in previous chapters.

The master curve methodology is re-defined for its application to the region of DBT which has been more or less untouched so far by the fracture mechanics community.

The modified method is assessed numerically and on the existing as well as newly developed dataset of In-RAFMS in Chapter 11.

The different aspects of aforementioned parameters are collectively interpreted and critically summarized in Chapter 12 and the outcome of the work are concluded.

The fracture dataset created in this work is tabulated in Appendix-A. The maximum likelihood estimation method for conventional and modified master curve methodologies are explained mathematically in Appendix-B. The different types of test specimens used to generate the fracture, tensile and impact toughness dataset are detailed in Appendix-C. The complete bibliography is provided on page numbers 240 to 250. The list of figures, tables and symbols are provided on page number xxi to xxxiii.

Chapter 2

Literature Review

In this chapter, various problems, shortcomings and existing methodologies of mechanical behaviour in ductile to brittle transition region are briefed. The developments of probabilistic approach to solve the scatter of DBT region is then explained subsequently. The global as well as local approaches to model cleavage fracture, their applicability and developments of master curve method, which is used in the work of dissertation is explained. Later, the modifications in master curve method, advanced master curve methods to study inhomogeneities and case studied on ferritic martensitic steels are discussed.

2.1 An Introduction to ductile to brittle transition of fracture mode

Nuclear fusion reactor is one promising future solution to replace fossil fuel for power production. In the process of establishing fusion reactor technology, Pb-Li eutectic is to be used as tritium breeder (Lead-lithium ceramic breeder/LLCB) and helium to be used for cooling. The test blanket module, which consists of U-shaped first wall with helium cooling system has inlet outlet at 350-480°C, helium pressure of 8 MPa and pressure drop of 0.3 MPa. The proposed material for U-shaped first wall structure is Reduced Activation Ferritic Martensitic steel (RAFMs). The RAFMs has been derived from Mod-9Cr-1Mo steel with elements having half life more than 100 years replaced with those having less than 100 years, for instance Mo is replaced by W and Nb by Tantalum. Properties, which make RAFMs challenging candidate material for structure are its low swelling property and improved creep resistance. Many such steels such as

EUROFER-97, F82H, JLF, Optifier and In-RAFMs are proposed by different parts of world.

Being a ferritic martensitic steel, RAFMs undergoes a transition from ductile to brittle failure at lower temperature. Transition temperature of steels, also known as reference temperature (T_o) shifts upward under the influence of irradiation. Therefore, it becomes important to investigate the fracture behaviour of Indian RAFMs (In-RAFMs) in DBT regime. At present, the transition temperatures of steels are characterized by impact toughness, RT_{NDT} ASME approach and Master Curve approach. Out of these, impact test method suffers with huge scatter and requires large number of samples (Wallin, 1984). On the other hand RT_{NDT} approach uses the data from impact tests and drop weight tear tests and takes the lowest values to determine reference temperature. This approach does not deal with the scatter of data and results in an over-conservative estimate in many cases. Master Curve (MC) approach is the only approach utilizing the fact of stochastic nature of cleavage initiators' distribution in DBT regime; making it the most efficient method for transition behaviour characterization. Master curve method was established initially for Reactor Pressure Vessel steels, which was ferritic in nature. The approach is discussed in detail in following section.

2.2 Probabilistic approach towards scatter in ductile to brittle transition

The ductile to brittle transition region is usually characterized industrially by Charpy test (ASTM E23). The specimens used in this method are $10 \times 10 \times 55$ mm³ rectangular bars with V notch. There are generally three parameters resulting from Charpy tests, which are used for indexing the ductile to brittle transition. The first parameter is the impact energy (in Joules). There are several reference points to define a transition temperature such as 28 J, 41J and 68J reference points. The second parameter is the fracture surface showing a mixture of flat and rough surfaces in correspondence to brittle and ductile fracture zones, respectively. The percentage area on fracture surface is defined

as Fracture Appearance Transition Temperature (FATT) where 50% area is rough and rest is flat. The third parameter is the lateral strain measured in perpendicular to the plane of notch. Despite of aforementioned criteria huge scatter in DBT region makes the result only useful for qualitative purpose.

To deal with the problem of scatter the ASME provided a method known as RT_{NDT} approach and was given in form of ASME K_{1C} Curve in ASME Pressure Vessel Code Section III. The Japanese Research Program , which re-analysed the dataset including 655 static fracture toughness data of SA533 steel including data from Weld specimens, also compared the results of ASME K_{1C} Curve with a statistical approach of master curve. The details of the categorical datasets used in the analysis is provided in (Yoon et al., 2001b). The temperature axis normalized with RT_{NDT} for the datasets are shown in Figure 2.1.

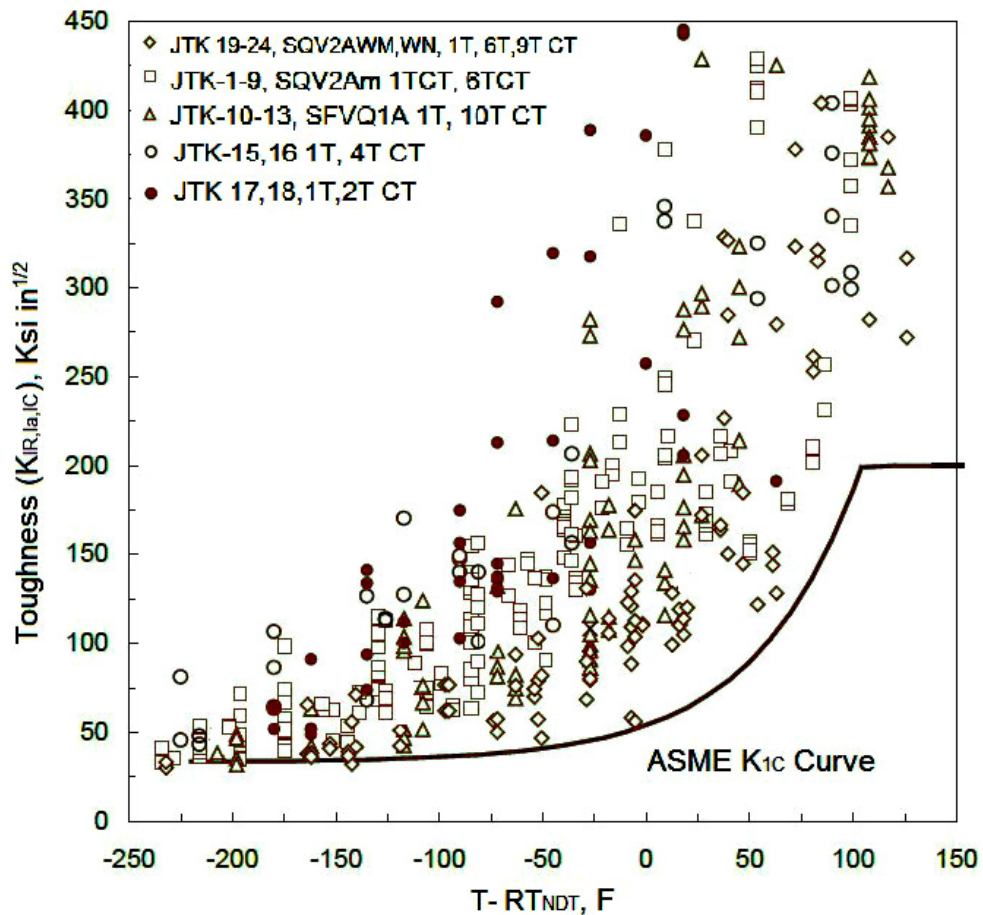


FIGURE 2.1: ASME K_{1C} Curve for SA533 steel base and weld datasets

It is evident from Figure 2.1 that the RT_{NDT} is a lower bound curve, which is over conservative to the true fracture behaviour of material, as it can be realized that the RT_{NDT} for weld as well as base metal shows same profile in form of ASME K_{1C} Curve, even after scaling the temperature axis to $T - RT_{NDT}$. The RT_{NDT} temperature is obtained by analysing Charpy and drop weight test data following the rules given below.

- Charpy and Drop Weight tests are performed on the material with the intention that a conservative value from either of the test is obtained.
- The crack plane in the test specimen is oriented to coincide with the plane of maximum primary membrane stress.
- The Nil Ductility Temperature (T_{NDT}) is obtained by following ASTM E208 at quarter thickness (0.25T) location.
- At least three Charpy V Notch (CVN) at $T_{NDT} + 33.3^{\circ}\text{C}$ using specimens from quarter thickness location.
- If all three of the CVN tests show a lateral strain of 1mm or more then $RT_{NDT} = T_{NDT}$.
- If above criteria is not met then find the temperature T_{40} , where lateral strain is 40 mils (1mm) and then $RT_{NDT} = T_{40} + 33.3^{\circ}\text{C}$.

A modification in ASME K_{1C} Curve was performed in Code Case 610 by analysis the data generated by performing Drop Weight tests on specimens made by one-pass welding unlike double pass. Further, in Code case - 629, the RT_{NDT} is referred as RT_{10} , which is $T_0 - 33.3^{\circ}\text{C}$. The dataset analysed using master curve method is compared with ASME K_{1C} Curve and RT_{10} in Figure 2.2. The potential of master curve is evident from Figure 2.2 and the motivation to use master curve approach for characterization of fracture behaviour is realized.

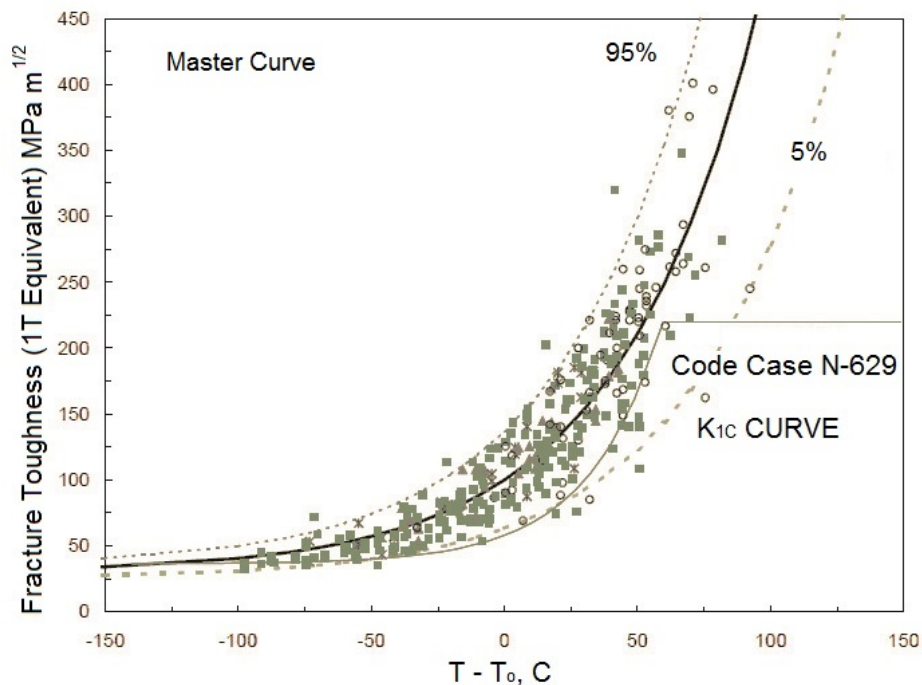


FIGURE 2.2: ASME K_{1C} Curve for SA533 steel in comparison with master curve and RT_{10}

2.2.1 Master curve: a global approach

The fracture behaviour of ferritic steels in the Ductile to Brittle Transition (DBT) region is known for its inherent huge scatter (Wallin, 1984). There have been various methodologies developed to assess this scatter ranging from impact energy measurement to elasto-plastic fracture toughness correlation with temperature known as Master Curve approach. The development of master curve, which takes probabilistic behaviour of cleavage fracture into consideration exploits the weakest link theory of Weibull (Weibull, 1951). It is unsure about the time the terms of master curve equations started emerging in engineering fracture mechanics but it won't be wrong to say that the most important tool to analyse DBT regime started with the Weibull's model of weakest link in 1951, which is described in brief here.

Weakest Link Theory

A chain made by joining n number of links will fail if one link fails, thus the weakest of all links will describe the failure probability of the chain, which is expressed as,

$$P = 1 - \exp^{-\phi(x)} , \quad (2.1)$$

where P defines the probability of failure of one link in the sense that it can be written as probability of x having a value less than a property of link , which in this case is failure. Extending the concept, for n links the failure probability of a chain can be written as,

$$1 - (1 - P)^n = 1 - \exp^{-n\phi(x)} . \quad (2.2)$$

Weibull in his theory (Weibull, 1951) also gave the simplest function $\phi(x)$ in the form as,

$$\phi(x) = \frac{(x - x_U)^m}{x_o} , \quad (2.3)$$

considering the necessary conditions of the function to be positive, non-decreasing and vanishing at a value x_U . The value x_o is called the scaling parameter and m is known as Weibull's coefficient or Weibull slope. Weibull also demonstrated by giving examples for the application of the theory of weakest link in variety of fields, such as yield strength of Bofors, Fiber strength of Indian cotton, fatigue behaviour and few more.

In the field of fracture mechanics, especially in DBT regime one can realize the effect of Weibull's equation together with probabilistic fracture mechanics analysis of Stephan Slatcher (Slatcher, 1986). Slatcher not only explored the probabilistic approach in DBT regime but also found theoretically the Weibull's slope parameter to be 4. Slatcher in his theoretical model, assumed that the elemental initiation can be considered as the event to define fracture in DBT regime , which depends on the proportion of crack front in elements ahead of crack tip and the probability of failure can be described as,

$$P_f = 1 - \exp(-B\phi J^2) , \quad (2.4)$$

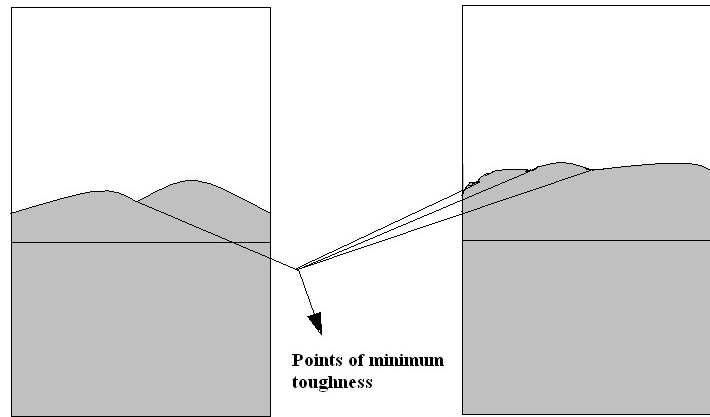


FIGURE 2.3: Schematic of fracture surface with shaded fatigue pre-cracked and cracked areas

where B is the thickness of specimen and φ is defined as,

$$\varphi = \int_{\theta=-\pi}^{\theta=\pi} \int_{u=g(\theta)}^{u=h(\theta)} u f(u, \theta, \eta_1, \eta_2 \dots) du \cdot d\theta . \quad (2.5)$$

In his first assumption, the elemental homogeneity is of crucial importance and for a material where the elemental homogeneity is questionable, the model cannot be beneficial. The second assumption considers the stresses and strains to be dependent on J/r ratio, which comes from the assumption that the stress strain ahead of crack front is fully characterized by J value. The functions $g(\theta)$ and $h(\theta)$ describe the annular domain that uses r to define the element area under consideration. In Eq.(2.5), parameter u is a function of J/r ratio. In the review of Slatcher the master curve equation was already clear but before going any further, a briefing of the classic work of Landes and Shaffer is necessary. [Landes and Shaffer \(1980\)](#) in their work in DBT regime found a characteristic microstructural feature shown in Figure 2.3. The figure schematically shows the initiation points ahead of pre-cracked region, from where the specimen cleaved. Sometimes, there were more than one initiation points, and this feature reported by Landes and Shaffer was documented to be the evidence of materials following weakest link theory in DBT regime by Wallin ([Donald E. McCabe, 2005](#)). Landes and Shaffer brought an important aspect of cleavage fracture that it was dependent on the points of minimum toughness across the crack tip and the scatter in smaller specimens were found to be lower due to the scarcity of these points of minimum toughness, which are also

referred to as cleavage triggers. Since then, it was concluded that the cleavage failure in DBT regime is a stochastic process and should be treated with probabilistic approach.

For ferritic steels, where the critical dislocation density for cleavage failure varies inversely with Peierls Nabarro stress; the toughness would show same type of correlation with temperature assuming Peierls Nabarro stress to be constant for ferritic steels (Wallin, 1993). The general form of fracture toughness distribution in DBT region for 1 inch (1T) thick specimens is expressed according to master curve methodology as,

$$K_{JC,1T} = A + (A_0 - A) \exp[C(T - T_0)]. \quad (2.6)$$

where $K_{JC(1T)}$ is the 1 inch (1T) thickness corrected elastic plastic fracture toughness, A_0 and T_0 are the reference values of fracture toughness and corresponding temperature. A and C are constants with T as temperature. The reference point of fracture toughness to describe DBT parameter is $100 \text{ MPa m}^{1/2}$ and the temperature corresponding to this value of median fracture toughness, is known as reference transition temperature, T_0 . The parameter C in Eq. (2.6) is the empirical constant defining correlation of fracture toughness with temperature. In conventional MC method, the values of A and C are $30 \text{ MPa m}^{1/2}$ and 0.019°C^{-1} , respectively. These values have been obtained by extensive studies on different grades of ferritic steels (Wallin, 1989a, 1993; Donald E. McCabe, 2005). The probability of cleavage failure P_f , in conventional MC is defined as,

$$P_f = 1 - \exp\left[-\frac{B_{nT}}{B_{1T}} \left(\frac{K_{JC} - K_{min}}{K_0 - K_{min}}\right)^4\right], \quad (2.7)$$

where K_{min} is the threshold below, which cleavage cannot occur, B_{nT} is the thickness of the test specimen, B_{1T} is the reference thickness of 1 inch and K_0 is the scaling parameter of Weibull's fit, which corresponds to K_{JC} at 63.2% cleavage failure probability.

The fracture data obtained by testing the specimens in DBT region undergo Maximum Likelihood (ML) analysis after size adjusting the dataset to 1 inch thickness. The ML

parameter L is defined by finding the probability density function (f_i) and survival function (S_i)

$$f_i = \frac{dP_f}{dK_{JC}} , \quad (2.8)$$

$$S_i = \exp\left[-\left(\frac{K_{JC(i)} - K_{min}}{K_o - K_{min}}\right)^{1/4}\right] , \quad (2.9)$$

where index i refers to the individual data analysed at each test temperature. The maximum likelihood parameter is described as

$$L = \prod_{i=1}^N f_i^{\delta_i} \cdot S_i^{1-\delta_i} . \quad (2.10)$$

The maximization of ML parameter is carried out for master curve method by satisfying set of equations,

$$\frac{\partial L}{\partial A} = \frac{\partial L}{\partial C} = \frac{\partial L}{\partial T_o} = 0 . \quad (2.11)$$

Apart from aforementioned three equations, the ML analysis is solved by using the relation of K_o with reference transition temperature T_o described as

$$K_o = K_{min} + \frac{1}{(\ln 2)^{1/4}} (A - K_{min}) + (A_o - A) \exp[C(T - T_o)] . \quad (2.12)$$

The relation in Eq.(2.12) is obtained using the fact that K_o is K_{JC} at 63.2% probability of cleavage failure.

2.2.2 Censoring of dataset for maximum likelihood analysis

The reference transition temperature can be obtained by two methods; one of which utilizes experimental fracture toughness values at different temperatures to create the sample space (multi-temperature master curve), whereas other simplifies the method by using experimental data at single temperature (Single temperature master curve method). The fracture dataset , which is used for maximum likelihood analyses is right censored

before analyses. There are various levels of censoring in master curve methodology , which are,

- Any fracture toughness value $K_{JC} > K_{JC,limit}$ is replaced with the $K_{JC,limit}$ value where $K_{JC,limit}$ is obtained by measuring initial ligament length b_0 , Elastic modulus, E , constraint parameter M , which is generally = 30, yield strength σ_0 and Poisson's ratio ν as,

$$K_{JC,limit} = \sqrt{\frac{Eb_0\sigma_0}{M(1-\nu^2)}} \cdot \quad (2.13)$$

- Any fracture toughness value K_{JC} , which is accompanied by ductile tearing $>$ minimum of $5\%b_0$ and 1 mm, is replaced by the maximum value of valid K_{JC} according to first validity criteria obtained experimentally or K_{J1C} at same test temperature.

The aforementioned are the two censoring criteria according to ASTM E1921. Apart from these, there are few validity requirements , which put further constraint on usage of experimental dataset for maximum likelihood analyses according to master curve approach , which are,

- The crack depth for the all the fracture toughness dataset should be in the range of $0.45 \leq (a/W) \leq 0.55$. This criteria is imposed to ensure homogeneity of the dataset as much variation in crack depth may cause difference in stress field at the crack tips , which may not be adjusted by the homogeneity assumption of master curve methodology.
- The product of statistical validity factor r_i and the number of valid tests n_i should always be greater than 1.
- If $K_{JC,median}$ of a data set is lower than $58 \text{ MPa m}^{1/2}$, then the maximum likelihood analyses using that dataset is not allowed. This criteria eliminates the chances of increased uncertainty , which may be imparted due to nearing lower shelf for smaller specimens where nucleation controlled cleavage based master curve is not valid.

- The rate of loading defined in terms of rate of change of stress intensity factor $\frac{dK}{dT}$ should be in the range of $0.2 \leq \frac{dK}{dT} \leq 2\text{MPa m}^{1/2}$. This criteria justifies the quasi-static assumption of master curve micro-mechanics (Wallin et al., 1986; Wallin and Laukkanen, 2008).
- The test temperature should be in the range of $T_0 \pm 50$. However, this range is changed to mitigate the effect of nearing lower shelf by redefining it as $-14 \leq (T - T_0) \leq +50$.

2.2.3 Advanced master curve approaches: SINTAP, Bimodal and Multi-modal master curves

The datasets, which do not respond accurately to conventional master curve methodology can be analysed by advanced statistical algorithms of inhomogeneity analysis methods. There are three different approaches, which are SINTAP, Bi-modal and Multi-modal master curve approaches. The Bi-modal master curve, which is generally used for dissimilar welded materials and materials showing clear evidence of two types of distribution in the fracture dataset. The details of Bi-modal master curve is described in next section with the example of Sokolov and Tanigawa (2007)'s work on F82H steel.

The inhomogeneity in a dataset is expected when the cleavage triggering sites show segregation or the initial conditions of few of the data in the dataset are different. For example if some of the specimens had different crack depths or suffered from prior DCG. Two differently sized specimen's dataset can also show bi-modality to certain extent, if the difference of the size is huge and one shows loss of constraint while other complies with the thickness scaling of conventional master curve method. The approaches of dealing with inhomogeneous datasets are described below.

SINTAP lower tail estimation

The SINTAP method takes its name from Structural INTEGRity Assessment Procedure, which was proposed in 1999 (SINTAP, 1999; Wallin, 2010b). The procedure works for

a smaller datasets unlike Bi-modal or Multi-modal master curves for , which a minimum of 15 valid data are required (SINTAP, 1999; Wallin, 2010b; Wallin et al., 2004). This procedure not only gives a lower bound T_0 but also works as an algorithm to check the inhomogeneity of a dataset.

The SINTAP lower tail estimation method has three steps of analysis , which are

- **STEP-1** The first step is the conventional master curve approach where first estimate of T_0 or $K_{JC,median}$ is found using Eq.(2.8) to Eq.(2.11) with conventional censoring.
- **STEP-2** In the second step all the data with $K_{JC,1T} > K_{JC,median}$ are censored with $\delta = 0$ in Eq.(2.10). The T_0 obtained after this is referred here as $T_{0,2}$ and the first estimate as $T_{0,1}$. The method concludes the $T_{0,SINTAP} = T_{0,1}$ if $T_{0,1} > T_{0,2}$, otherwise when $T_{0,1} < T_{0,2}$, $T_{0,2}$ is used as $T_{0,1}$ and Step-2 is repeated until a constant estimate of $T_{0,adjusted}$ is obtained. The only condition is that minimum valid data should not be less than 10 at any point of calculation.
- **STEP-3** If valid data are less than 10 then in step-3 each K_{JC} value is converted to corresponding T_0 , i.e. $T_{0,i}$. The maximum value of $T_{0,i}$ is designated as $T_{0,max}$. If $T_{0,max} > T_{0,adjusted} + 8^\circ\text{C}$ then *the dataset is inhomogeneous* and the lower tail estimate i.e. $T_{0,SINTAP} = T_{0,max}$, otherwise $T_{0,SINTAP} = T_{0,adjusted}$

Random inhomogeneity analysis: Multi-modality

To analyse a dataset where inhomogeneity is observed but Bi-modality cannot describe it accurately; a random inhomogeneity is assumed in the form of Gaussian distribution of T_0 , with T_{0MML} as the mean of the distribution and σ_{0MML} as standard deviation. The distribution of T_0 in a dataset, then, can be described as,

$$f_T = \frac{1}{\sigma_{0MML}\sqrt{2\pi}} \exp\left[-\frac{(T_0 - T_{0MML})^2}{2\sigma_{0MML}^2}\right]. \quad (2.14)$$

The probability density function obtained by using Eq.(2.8) is referred here as f_{T_o} and the total survival factor S_{MML} and probability density f_{MML} is then obtained as,

$$S_{MML} = \int_{-\infty}^{\infty} f_T \cdot S_{T_o} dT_o , \quad (2.15)$$

and

$$f_{MML} = \int_{-\infty}^{\infty} f_T \cdot f_{T_o} dT_o . \quad (2.16)$$

2.2.4 Modifications of master curve approach: Case studies

The conventional master curve methodology has been proven accurate by using extensively on many huge datasets (Wallin, 1993) such as, Euro fracture data on reactor pressure vessel steel. The method however is rarely used on tempered martensitic steels, which is the material of investigation in this work. There have been, however, several studies after master curve standardization on tempered martensitic fusion reactor grade steels such as Eurofer97 and F82H. The master curve application on these materials have shown some differences from conventional approach, which are discussed in brief, subsequently.

Case 1: Master curve analyses of Eurofer97: strict censoring

The approach however for the first time was used for the analysis of ferritic martensitic steels, which are micro-structurally tempered martensite with precipitates of chromium, by Odette's group (Mueller et al., 2009; Lucas et al., 2007; Spätig et al., 2007). In their work, it was found that the fracture dataset obtained from 0.5T CT and 0.25T CT specimens were not following the trend of conventional master curve. The important fact to note is that in conventional master curve methodology the maximum likelihood analysis is performed by maximizing the ML parameter only with respect to T_o , which means that only last part of Eq.(2.11) is used. However, it has been suggested in many studies on constraint effect on fracture behaviour that the basic assumption of self-similar stress field along the crack front is violated for smaller specimens. The same was

suspected in the work of Odette's group and the constraint based censoring was made more strict for the Eurofer97 dataset by using a value of 80 for constraint parameter M instead of 30, which is used by conventional master curve method (E1921, 2013).

After censoring the dataset with strict constraint parameter, the dataset was re-analysed with maximization of ML parameter for two variables of Eq.(2.6), i.e. with respect to A and T_o . The values of A and T_o obtained with the analysis was 12 MPa and -77°C , respectively. The conventional master curve method estimates the T_o for similar grade of steel as low as -133°C (Wallin et al., 2001). This work pushes toward an interpretation that ferritic martensitic steels have lower contribution from athermal component of fracture toughness and major part of fracture toughness in DBT region is temperature dependent. This would also mean that a temperature shift will cause more drastic effects and will be further magnified under irradiation damage. However, no physical reason behind less athermal contribution in comparison to conventional steels, is provided for Eurofer97.

Case 2: Master curve analyses of inhomogeneous datasets: Advanced master curves

For a homogeneous material, the assumption that the probability of cleavage failure follows the distribution as described in section 2.2.1 by Eq(2.7) is accurate, However when the material shows inhomogeneity, which may be interpreted as one or more separate distribution functions are required to describe the cleavage failure probability, the conventional master curve approach is extended to describe bi or multi-modality. In cleavage failure probability to follow bi-modal behaviour the probability of cleavage failure is assumed to be a combination of two distributions as,

$$P_f = 1 - p_a \exp\left[-\left(\frac{K_{JC} - K_{min}}{K_{0,1} - K_{min}}\right)^4\right] - (1 - p_a) \exp\left[-\left(\frac{K_{JC} - K_{min}}{K_{0,2} - K_{min}}\right)^4\right], \quad (2.17)$$

where p_a is the fraction describing contribution from first distribution. The master curve approach applied with the kind of distribution described by Eq.(2.17) is referred to as Bi-modal Master Curve (BMMC). Unlike conventional MC, BMMC has two more

unknown parameters in comparison to conventional MC , which are the respective K_{0s} corresponding to 63.2% probabilities of respective distributions, namely, $K_{0,1}$ and $K_{0,2}$. These two parameters are changed in terms of temperatures, $T_{0,1}$ and $T_{0,2}$, which are the respective reference transition temperatures. The relation describing the dependencies of scaling parameters with reference transition temperatures are described as,

$$K_{0,1} = \frac{1}{\ln(2)^{1/4}} (A + (100 - A) \exp[C(T - T_{0,1})]) , \quad (2.18)$$

$$K_{0,2} = \frac{1}{\ln(2)^{1/4}} (A + (100 - A) \exp[C(T - T_{0,2})]) . \quad (2.19)$$

For BMMC analyses, there are 5 unknown parameters to be solved for , which are $T_{0,1}$ or $K_{0,1}$, $T_{0,2}$ or $K_{0,2}$, p_a , C and A .

The multi-model master curve or random inhomogeneity approach was applied on Euro fracture dataset as well as ferritic/martensitic grade steel known as F82H by [Lucon and Scibetta \(2011\)](#) and [Sokolov and Tanigawa \(2007\)](#). For F82H dataset of [Sokolov and Tanigawa \(2007\)](#) the 50% median K_{JC} predicted from conventional master curve method did not describe the experimental fracture behaviour at lower temperatures for the dataset of F82H , which resulted in inhomogeneity analysis of the dataset. However, instead of bimodal a multi-modal approach was applied by [Sokolov and Tanigawa \(2007\)](#) , which then was found to be reciprocating the dataset behaviour accurately.

It was noticed, in both the cases presented here, that the deviation from the conventional method , which was suspected, and also justified for both the datasets comprised two or more differently sized specimens. In case of F82H ([Sokolov and Tanigawa, 2007](#)), the 0.25T CT specimens were fabricated from 0.5T CT tested specimens and in Euro fracture data the dataset contained 0.5T CT to 1T CT datasets.

In the case of Eurofer97 (Case 1), the loss of constraint was given importance and the criteria of validity was made more strict with M of 80 and in case of F82H this was ignored and inhomogeneity appeared to solve the problem. This observation suggests that a dataset with a large thickness specimen having higher constraint and a very small

thickness specimen with greater loss of constraint may behave as two different materials, if proper constraint corrections are not applied, and therefore any non-identical condition in a dataset may be statistically dealt by assuming different probability distribution assigned to those datasets. However, this kind of approach does not guarantee any physical reasoning of the results, neither it ensures reproducibility and repeatability of the results.

Similar material effect on dataset inhomogeneity was found in the analyses of Euro fracture data, where a set of specimens made from a block (plate SX9) , which had a different material history than other parts of the ring segment of RPV steel supplied by Siemens from which the whole Euro fracture data was created. It was found that the degree of inhomogeneity was more, if the dataset of SX9 was included in the master curve analysis. The dataset was analysed by SINTAP, conventional Bimodal as well as multi-modal methods and its was found that the overall variation in estimated T_0 was 6°C and the scatter increased by including the dataset of SX9. The inhomogeneity was confirmed by the fact that BMCC analysis resulted in p_a of 0.91 , which was also the percentage share of the data not coming from SX9 dataset (the ratio of numbers of data after excluding SX9 , which is 698 and complete dataset of 734 tests gives a ratio of 0.95 , which is close to p_a).

2.2.5 Cleavage fracture: local approaches

The cleavage fracture event is modelled micro-mechanically by taking into consideration the micro-crack generation in the vicinity of the volume ahead of the crack tip and unstable propagation of the same. The micro-cracks, generated under opening mode, may be parallel to the crack plane and therefore can have an angular distribution associated with the distribution of micro-cracks. The probability of non-failure event, P_{nf} for a unit volume can be described as,

$$P_{nf} = \int_V P(a)g(\theta)dad\theta . \quad (2.20)$$

where $P(a)da$ describes the probability of finding a micro-crack oriented in single direction of size between a and $(a + da)$ in the volume V , which has suitable stress conditions to be eligible to influence cleavage fracture directly. The function $g(\theta)d\theta$ together with $P(a)da$ describes this probability for micro-cracks in all possible orientations. The definition of this volume, sometimes referred as active volume or critical volume or V^* (Bonadé et al., 2008; Ritchie et al., 1973; Tiwari et al., 2015), is a function of maximum principal stresses both first and second (Mudry, 1987). If micro-cracks are assumed to nucleate only at carbides for specific case of a steel such as low impurity ferritic steel most micro-cracks will nucleate parallel to principal loading direction (Smith, 1966). Additionally, assuming the volume V^* to be divided into smaller volumes independent of each other, the P_{nf} can be described as,

$$P_{nf} = \exp[-\phi(\sigma_1) \cdot V] , \quad (2.21)$$

where $\phi(\sigma_1)$ is the function of first principal stress. The effect of second principal stress is neglected assuming planar micro-crack nucleation. The effect of second principal stress is dominant for an angular distribution of micro-cracks and become more predominant under pre-straining on both tensile and compressive kinds (Smith, 1966; Beremin et al., 1983a; Mudry, 1987).

With Eq.(2.21) describing non failure event, the probability of cleavage fracture can be described as,

$$P_f = 1 - \exp[-\phi(\sigma_1) \cdot V] . \quad (2.22)$$

The cleavage failure probability model as described by the probabilistic local approach of WST (Wallin et al., 1986; Wallin and Laukkanen, 2008) assumes the Small Scale Yielding (SSY) condition at the crack tip, , which in fact is also the basic assumption of MC approach developed with active volume responsible for cleavage to be scaling with BK^4 . The critical size of cleavage initiators (assumed to be spherical) responsible for unstable failure in DBT region is assessed from Griffith's instability criteria described as,

$$r_C = \frac{\pi E(\gamma_S + \gamma_P)}{2(1 - \nu^2)\sigma_{yy}^2} , \quad (2.23)$$

where, E is elastic modulus, ν is Poisson's ratio, γ_s is the surface energy of the matrix, γ_p is the plastic work required for crack propagation and σ_{yy} is the applied mode-I stress ahead of the crack tip. The probability of cleavage failure is then defined as,

$$P_f = 1 - \prod_{X=0}^{X=r_{pl}} (1 - P(r \geq r_C))^{NFBdXX \sin \theta} , \quad (2.24)$$

where X is the distance ahead of crack tip, r is the radius of a cleavage crack initiator, r_{pl} is the distance from the crack tip to the elasto-plastic interface, N is the number of cleavage initiators, F is the fraction of N taking part in fracture process and θ is the angle measured counter clockwise from the crack plane and $P(r \geq r_C)$ is the probability of in-homogeneities such as carbides being critical in size to initiate cleavage. The variables can be visualized in Figure 2.4.

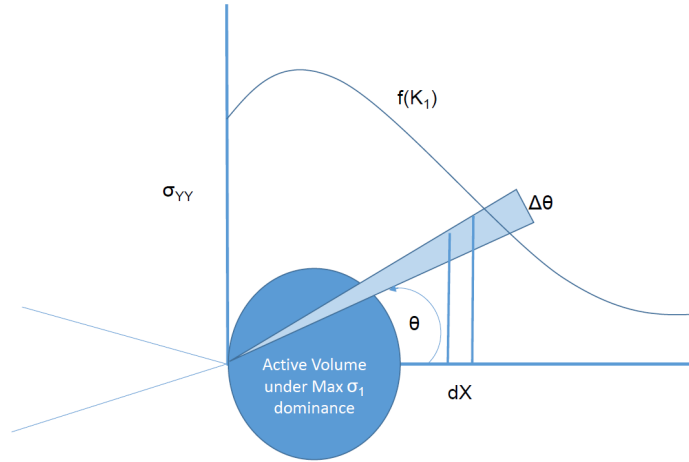


FIGURE 2.4: Crack tip defining probability of cleavage failure according to Eq.(2.24)

Using non-dimensional parameter Q as,

$$Q = \frac{X}{\left(\frac{K}{\sigma_o}\right)^2} , \quad (2.25)$$

and assuming self-similarity of stress fields or SSY condition, the integration otherwise required in thickness direction can be avoided and the probability of cleavage failure can be then written as,

$$P_f \propto 1 - \exp\left\{-NFB \sin \theta \int_{Q=0}^{Q=Q_{pl}} P(r \geq r_C) Q dQ\right\} , \quad (2.26)$$

where Q_{pl} is the value of Q at $r = r_{pl}$. By assuming the integration part to be a constant say ω (although it may not always be constant as discussed in next section) Eq.(2.27) can be re-written as,

$$P_f = 1 - \exp(-\omega BK^4), \quad (2.27)$$

, which is the basis of size adjustment equation given in ASTM E1921. The size adjustment equation used in MC method is described as,

$$K_{JC,1T} = K_{min} + (K_{JC,nT} - K_{min}) \cdot \left(\frac{B_{nT}}{B_{1T}}\right)^{1/4}, \quad (2.28)$$

where $K_{JC,nT}$ is the measured experimental fracture toughness of B_{nT} inch thick specimen and B_{1T} corresponds to 1 inch or 25 mm.

The stress dependence of reference unit volume and resulting probability of cleavage failure of active volume ahead of crack tip results in similar expression as in Eq.(2.22) and Eq.(2.26). For more details on the subject of local approaches towards cleavage fracture is reviewed in great detail by Mudry ([Mudry, 1987](#)).

2.3 Reduced activation ferritic/martensitic steels: An Overview

The steels with high Cr content are known for its application in boilers, steam pipelines and turbines of ultra-supercritical fossil power plants where the operating temperature can result the structure to go up to 650°C ([Abe et al., 2008](#)). High Cr steels are also very popular in power industry due to excellent creep properties, high thermal conductivity and low thermal expansion coefficient ([Klueh, 2005](#)). Recently, the ferritic/martensitic steels being the primary candidate material for fusion reactor first wall blanket application have attracted attention across the globe ([Möslang et al., 2005](#); [Banerjee, 2014](#); [Odette and He, 2000](#); [Yu et al., 2007](#); [Sokolov and Tanigawa, 2007](#)). Also due the application of ferritic/martensitic steels in super critical water cooled reactors in cladding and core components ([Li et al., 2010](#)), RAFM grade steels have been studied extensively in the last decade.

The operational requirement of DEMO reactor requires the material to perform in the temperature window of 350-550°C. The material is also required to have good resistance against irradiation damage. The steels developed under the category of Reduced/Low Activation Ferritic/Martensitic steels (RAFMs/LAFMs) are Eurofer97, F82H, JLF and few older versions such as MANET and OPTIFIER. These fusion reactor grade steels were developed with 9%Cr and 12% Cr steels as reference materials due to their already proven creep strength and swelling resistance. In the series of RAFM grade steels mentioned before, the basic chemical composition follows that of Mod-9Cr-1Mo steel also known as P91/T91 steels.

The RAFM differs from P91 steels in the chemistry due to the replaced high activity (half-life > 100 Years) elements from Mod-9Cr-1Mo with elements of low activity but same effect such as, W for Mo and Ta for Nb. Other transmutable elements are removed by expensive vacuum arc melting process making this grade of steel most clean and low activation.

Due to the wide spectrum of applicability of high Cr content tempered martensitic steels, several studies have been carried out in all the dimensions, including microstructural, mechanical, irradiation, welding, ductile to brittle transition, tempering, thermo-mechanical treatments, liquid metal embrittlement, electrical and magnetic aspects.

The most important property of steels having 9% Cr (unless otherwise mentioned the percentage in this work refers to weight percentage) is its creep resistance, which is attributed to its tempered martensitic lath structure. The microstructural aspects, however, remain dependent on the tempering temperature and duration. It has been found, recently, by [Mishnev et al. \(2016\)](#), that in the range of 600-650°C the tempered martensitic lath structure changes to sub-grain structure of low angle grain boundaries, which results in lower density of dislocation. On the other hand, [Sandim et al. \(2015\)](#) on his work on Eurofer97 steel, has revealed softening in hardness, drop in coercive field, Vickers micro-hardness and increase in residual electrical resistivity at tempering temperature approaching 500°C. These phenomena show the importance of precipitation sequence of carbides, carbo-nitrides, and in few cases where boron is experimented,

nitrides play important role in the resulting properties. Besides the sequence of precipitation, the size distribution, preferable sites of carbides/carbo-nitrides/nitrides (Klimenkov et al., 2015) are also important. The elements taking part in these precipitates are also given importance and have been investigated in several studies (Laha et al., 2013; Moitra et al., 2014; Mythili et al., 2013; Vanaja et al., 2012; Rosenwasser et al., 1979).

Abe et al. (2008), have investigated the coarsening of $M_{23}C_6$ carbides in 9Cr-W steels where the effect of W on the creep property was studied. It was shown in his work that W reduces the coarsening of $M_{23}C_6$ carbides at 600°C. Long term ageing of 10%Cr tempered F/M steel showed that Cr and Mo content increases in $M_{23}C_6$ carbides at the expense of Fe up to 51,072 h of creep exposure (Xu et al., 2016). Xu et al. (2016), very recently, did systematic study of 10%Cr F/M steels under long term ageing to study the kinetics of $M_{23}C_6$ carbides, and found that V starts diffusing in $M_{23}C_6$ at 650°C for 12,000 h to 25000 h. Additionally, interesting finding was also that V not only replaces Fe but also W and Mo from $M_{23}C_6$ carbides.

The involvement of Cr, Mn, Mo, Nb, Ni, V along with Fe and C in $M_{23}C_6$ for 10%Cr steel during tempering is shown in Figure 2.5. The plot shows results obtained from JMat-pro software package (Saunders et al., 2003).

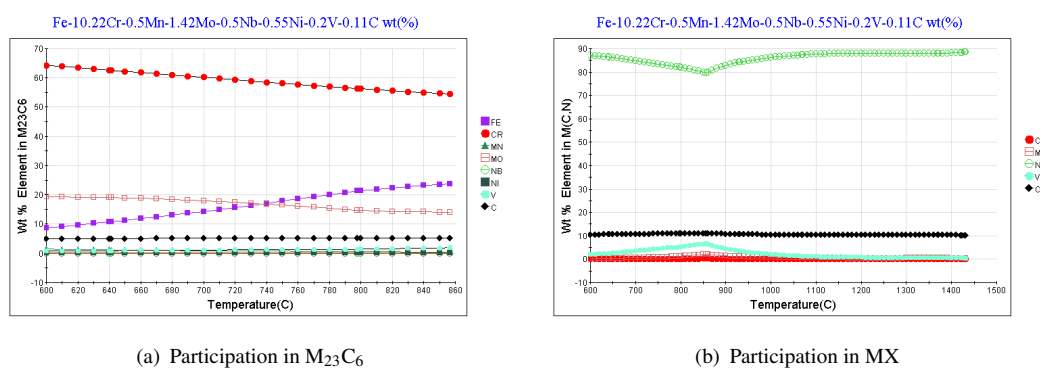


FIGURE 2.5: Participation of alloying elements in (a) $M_{23}C_6$ carbides and in (b) MX precipitates in 10%Cr steel obtained from JMat-Pro

The composition of $M_{23}C_6$ in Fig. 2.5 (a), shows clearly the continuous replacement of Cr and Mo by Fe above 600°C. In Fig. 2.5 (b) the compositional changes in MX type

precipitates are shown, where it is clear that around 870°C, Nb starts replacing V. The reason P91 steel was chosen to be the reference material for RAFM grade was not only the creep strength but also the swelling resistance (Rosenwasser et al., 1979). On the other hand, 12%Cr steels also showed similar properties under creep and irradiation. The study of Ioltukhovskiy et al. (1998) showed that 12%Cr steels were not susceptible to swelling till 100-110 dpa of irradiation. At 120-142 dpa of irradiation swelling was prominent at 400°C. The steel was also found not to be prone to irradiation embrittlement at high temperature. The work of Danon and Alamo (2002) on Eurofer97 shows prior austenitic grain boundary to be another important parameter, which affects the performance of high Cr steels. The prior austenitic grain boundary was found not to change till 1050°C and further was found to coarsen till 1200°C. The importance lies in the fact that the martensite growth depends on the pre-austenitic grain boundaries and martensite cannot continue to grow after it hits a pre-austenitic grain boundary. Therefore, a coarser pre-austenitic grain boundary will result in larger laths of martensite, which in turn will affect the creep, as well as fracture behaviour in ductile to brittle transition due to the large inhomogeneity and associated weakest links for cleavage fracture. In the recent work of Klimenkov et al. (2015), where B effect on micro-structural aspects were studied, showed that B by forming BN, decreases the spatial distribution of VN. This results in V enrichment in the matrix. The V enriched matrix makes it preferable for V to replace Ta from TaC and also finds place in $M_{23}C_6$. Ta as a replacement finds its place in VN by replacing V. The overall effect is the increment in width of laths and thus micro-structural instability.

In the study of RAFM grade steel developed in India (In-RAFMS), four different combinations of compositions by varying W and Ta content in close range with other alloying elements similar in amount to popular RAFM steels were studied by Laha et al. (2013). It was found in the study that the low cycle fatigue life increased with W and Ta content, however, tensile properties were not affected. The most sensitive property to the content of W and Ta investigated was creep rupture strength. Furthermore, it was also discovered that W and Ta affected the Ductile to Brittle Transition (DBT) behaviour.

In a different study on 9%Cr RAFM grade steels, [Tan et al. \(2013\)](#) discovered that thermo-mechanical treatment comprising hot rolling after normalizing and before tempering to the extent of 60% thickness reduction, resulted in superior tensile strength with negligible loss in ductility to oxide dispersion strengthened RAFM grade steels. The reason was attributed to the refinement of subgrains and $M_{23}C_6$ and MX type precipitates.

The effect of V and Ta on Ferritic/Martensitic steel has been extensively studied by [Xiao et al. \(2013\)](#) on 12%Cr steel recently developed for application upto 650°C with better creep properties than conventional 9%Cr RAFM grade ([Murty and Charit, 2008](#)). The effect of delta ferrite the shape of MX type precipitates was investigated and it was found that there are TaC rich MX type precipitates and V-N-rich MX type precipitates. The Ta-C rich precipitates do not dissolve in the solutionizing stage and while tempering, new precipitates of this type also add up. On the other hand, V-N-rich precipitates only show up while tempering. In the study of steels without V and Ta, with V, and with both V and Ta, micro-alloyed in Cr-W based steel, Xiao et al. confirmed that M_2X type precipitate form in first type of alloy in absence of V and Ta. In presence of V only, V-rich carbo-nitrides take over M_2X and in presence of both V and Ta, both V-N rich and Ta-C rich precipitates form. The shape of MX precipitates were observed to be planar within delta ferrite and it was concluded that V and Ta stabilize the MX precipitate in comparison to detrimental M_2X phase.

Summarizing the investigations carried out on 12%Cr-steels, 9%Cr steels, and RAFMS, it can be concluded that major properties of high chromium tempered martensitic steels are delineated by the kinetics and spatial distribution of $M_{23}C_6$ and MX precipitates, pre-austenitic grain size and lath structure of martensite. The precipitate size distribution and morphology with its influence on DBT fracture behaviour of In-RAFMS is further discussed in Chapter 4. The major features of RAFM grade, which makes it the structural material are good swelling resistance and creep strength. The crucial aspect of probability of catastrophic fracture remains open for In-RAFMS in DBT region, which is explored in depth in this work.

Chapter 3

Problem formulation

In this chapter, the methodology to meet the objectives described in Chapter 1 are discussed. The test matrix is then sketched to address the formulated problem. Subsequently the structure of the thesis is described.

For the fail-safe design approach, the characterization of fracture behaviour of In-RAFMS, requires the understanding of micro-mechanical aspects of cleavage failure probability, in DBT region. Additionally, the probabilistic distribution of cleavage fracture event and effects of parameters such as loading rate, loading type and loss of constraint (out of plane-thickness and in-plane-crack depth) on cleavage fracture, also need extensive understanding for qualification of the structural component and its safety.

As discussed in Chapter 1 and Chapter 2, the structural integrity of first wall blanket is crucial as this part faces most of the irradiation. The transmutation safety requirements control the activity issue, and the engineering of material can focus on the damage which may be induced by high energy neutron irradiation. The operational conditions demand avoiding catastrophic failure of the component, which may be caused by upward shift in ductile to brittle transition temperature due to irradiation. The fast fracture mode of cleavage makes the DBTT an important parameter to examine in comparison to creep and swelling. Owing to the component's importance in structural integrity of fusion reactor, not only the material but also the approach or methodology which described the probability of catastrophic failure event, is under scrutiny.

The most promising methodology which has come up to the standard of analysing crucial components structural integrity is the *master curve* methodology as discussed in

Chapter 2. It has also been reviewed in Chapter 2 that RAFM grade has shown deviation from the conventional approaches of this methodology with Eurofer97 and F82H as examples.

The methodology of master curve like any other standard analysis method is based on certain assumptions as discussed in Chapter 2. The cleavage event formulation under self-similar stress field at the crack tip is generally a condition which is often violated in fracture mechanics. Moreover, the future objective of fusion reactor components' structural integrity needs irradiation studies on the mechanical behaviour of component materials, which in turn imposes small specimen testing requirement. Therefore, it becomes important to understand, the extent to which the conventional approach can handle the loss of constraint associated with small specimens. Further, it is required to explore the possibilities for correcting the effects of loss of constraint.

In order to meet the objective of this work, the formulated area of studies are discussed below describing also the scope of this work.

Categorizing aforementioned requirements helps in formulating the studies of this work. The loss of constraint and corrections, which can make the conventional master curve approach usable for probabilistic analysis of cleavage fracture, includes examination of master curve approach due to loss of inplane as well as out of plane constraint. The tests on smaller specimens and shallow and deep cracks are performed and numerical approaches are used to investigate the problems of both types of constraint loss phenomena.

The pulse mode operation of ITER also imposes the condition of sudden change in loading rate, which may cause an added upward shift in DBTT in addition to that caused by irradiation. Therefore, a study of master curve approach at higher loading rate is also carried out using Indian RAFMS small specimens. Additionally, the fracture behaviour in upper DBT region is studied in greater detail with an objective to explore the domain, where no standard fracture mechanics or probabilistic approach exists at present. The upper region of of DBT is one such regime where a strong methodology, such as master curve method, does not exist. The cleavage fracture in this region of DBT is so far not

characterized by any global approach which can estimate a parameter such as reference transition temperature. It is required, therefore, to establish a method, which combines ductile tearing and cleavage fracture together to examine the probability of catastrophic fracture after ductile tearing.

The understanding of size effect on fracture behaviour requires the assessment of both out of plane and in-plane constraint loss in three dimension. Therefore, the finite element study for assessment of constraint change with the variation in size, type of loading, and ductile tearing prior to cleavage is required. The micro-mechanical aspects of cleavage fracture mechanisms are pre-requisite to the understanding of cleavage fracture probability distribution in DBT region, which is also included in the scope of this work. To meet the objectives of this work as defined in Chapter 1, the modified 9%Cr-1%Mo steel which is the reference material for RAFM grade steels is also examined and compared with responses of In-RAFMS.

3.1 Test matrix

With the above discussion on the salient desirable outcomes of this investigation, the extensive testing program for characterization of fracture behaviour of In-RAFMS in DBT region is categorized as given below.

1. Tensile testing as pre-requisite for fracture toughness measurements
2. Fracture testing for assessment of loss of constraint (both out of plane and in plane)
3. Fracture testing for assessment of loading rate effect
4. Fracture testing for assessment of loading type
5. Fracture testing for assessment of fracture behaviour on upper region of DBT

Different geometries under three point bending and tension were tested under different loading rates and test temperatures. The detailed test matrix is described in Table 3.1.

TABLE 3.1: Test matrix for fracture property assessment

Test conditions	Test Temperatures	Tensile tests	Fracture tests	Material
Quasi-static 0.5 mm.min	-110°C, -120°C, -130°C, -140°C, -150°	2 specimen per temperature	TPB , CT	In-RAFMS, P91
100 mm/min	-80°C, -100°C	2 specimen per temperature	Standard charpy TPB	In-RAFMS
1000 mm/min	-80°C, -100°C			In-RAFMS
Impact toughness		27°C, -30°C, -50°C, -85°C, -100°C, -115°C -130°C, -170°C, -196°C		In-RAFMS, P91

Chapter 4

Material

In this chapter the micro-structural aspects, phases and their transformation kinetics, heat treatment, and the properties, distributions, and types of precipitates in In-RAFMS are discussed. With the objective to characterize the fracture behaviour of In-RAFMS, more focus is given to In-RAFMS and only necessary and relevant studies are performed on mod-9Cr-1Mo steel as and when required.

4.1 Material: Ferritic/Martensitic steels

To correlate the structure and property of ferritic/martensitic steels, firstly, it is important to understand the system of ferritic/martensitic steels and changes occurring by small differences in amount of alloying elements and heat treatment dictating pre-austenitic grain boundaries, transformation temperatures and carbides structures. Secondly the importance of micro-structure and its effect on fracture is required.

In this work of investigation, to understand the fracture behaviour in DBT region two grades of ferritic/martensitic steels are studied, which are In-RAFMS and P91 or Mod-9%Cr – 1Mo steels.

The fusion reactor grade In-RAFMS, as discussed in Chapter 1, is derived from P91 grade and is made cleaner by removing the transmutable and tramp elements by vacuum remelting. The two grades therefore differ in the amount of tramp elements. The heat treatment given to these grades are close and the micro-structure for both the steels show tempered martensite with precipitates of Chromium, Tungsten/Molybdenum and

Vanadium/Tantalum located at inter lath and pre-austenitic grain boundaries as well as inside laths of martensites.

The heat treatment of both grades are designed for better creep strength and weldability. Both of the grades are air-cooled after tempering to avoid Z and Lave phases which are detrimental both for creep as well as DBTT.

4.2 Microstructural characterization of In-RAFMS

Both grades of ferritic/martensitic steels studied in this work, namely In-RAFMS and mod-9Cr-1Mo, show tempered martensitic microstructure. The carbides of Cr are found on the pre-austenitic grain boundaries and Ta/V carbides are dominantly present inside laths. The two grades show similar phases with close range of equilibrium and non-equilibrium phase transformation temperatures. The details of the equilibrium phases and microstructural features are discussed in detail below.

4.2.1 Phase transformation and heat treatment

The shape and size of precipitates, homogeneities and temperature dependencies of precipitates dictate the crack direction, cleavage failure initiation, propagation and driving force for fracture to occur and therefore, it is necessary to understand this system before characterization of fracture behaviour statistically.

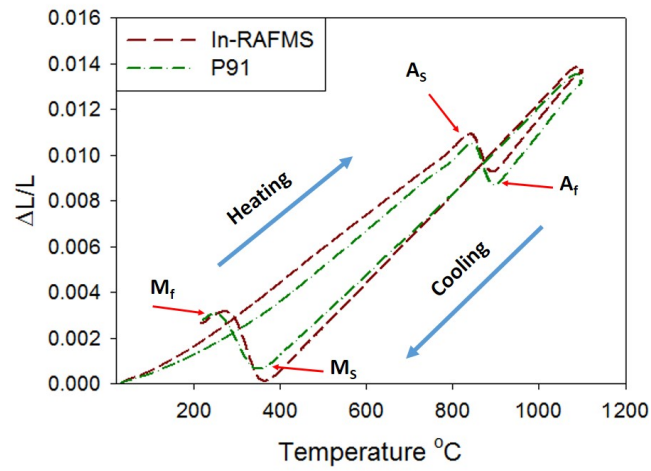
The spatial distribution of precipitates, and its effect on Ductile to Brittle Transition (DBT), as well as phase transformation are studied for two grades of ferritic/martensitic steels. More focus is given to In-RAFMS and the properties are compared with other popular RAFMS as well as high Cr tempered martensitic steels. The chemical composition and heat treatment given to In-RAFMS and P91 steels are shown in Table 4.1. The phase transformation for isothermal conditions for P91 and In-RAFMS are calculated using ThermoCalc software ([Andersson et al., 2002](#)) package as well as experimentally from dilatometry analyses. The non-isothermal martensitic transformation temperatures

TABLE 4.1: Chemical composition of ferritic/martensitic steels investigated

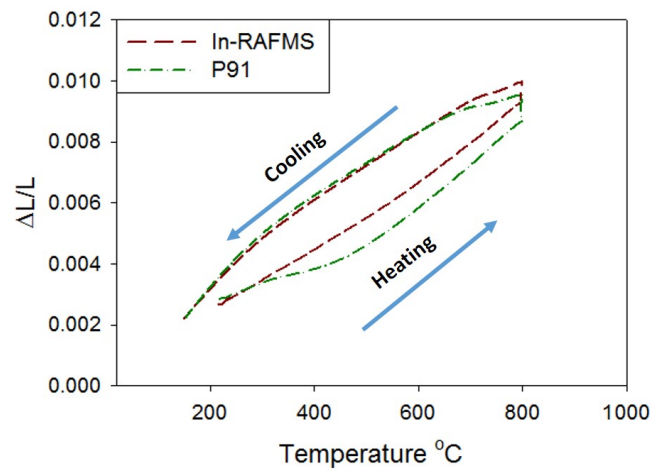
Mod-9Cr-1Mo										
Solutionized at 1050°C Tempered at 770°C, 1hr										
C	Cr	Mo	V	Nb	Si	Mn	S	N	Al	Ni
0.104	8.76	0.98	0.2	0.08	0.9	0.49	0.002	0.02	0.002	0.28
In-RAFMS										
Solutionized at 977°C Tempered at 760°C, 1hr										
C	Cr	W	V	Ta	Si	Mn	S	N	Al	Ni
0.08	9.15	1.37	0.24	0.08	0.026	0.53	0.002	0.02	0.004	0.004

are calculated using empirical correlations available in literature. The dilatometry results for mod-9Cr-1Mo as well as In-RAFMS are shown in Figure 4.1. It is evident that the phase transformation behaviour of both mod-9Cr-1Mo and In-RAFMS is similar except in the tempering region where strain gradient against temperature increases for mod-9Cr-1Mo. The austenitic start (A_s) and finish (A_f) as well as martensitic start (M_s) and (M_f) temperatures of both steels are very close. As visible in Figure 4.1, the solutionizing behaviour for In-RAFMS and mod-9Cr-1Mo is similar. Whereas, during tempering, unlike the slope of In-RAFMS which remains unchanged, mod-9Cr-1Mo steel shows a significant change in slope. This difference in tempering region may be attributed to Z and Lave phases formation which differs in two grades. In-RAFMS lacks the tramp elements which form these precipitates. The Lave and Z phases formation is avoided in manufacturing process by air-cooling the plates of steels after tempering. In dilatometer, however, the cooling rate was slow enough to cause the precipitation of undesirable Z and Lave phases. The transformation temperatures are shown in Table 4.2 along with the basic chemical compositions of different ferritic/martensitic grade steels.

The operational parameters of DEMO fusion reactor, as discussed in Chapter 1 and 3, may cause microstructural changes during service. To understand this scenario the equilibrium phase diagram was calculated for P91 as well as In-RAFMS. The two phase diagrams are shown in Figure 4.2.



(a) Solutionizing and Air cooling



(b) Tempering

FIGURE 4.1: Dilatometer response of In-RAFMS and P91 steels (a) while solutionizing and aircooling and (b) tempering

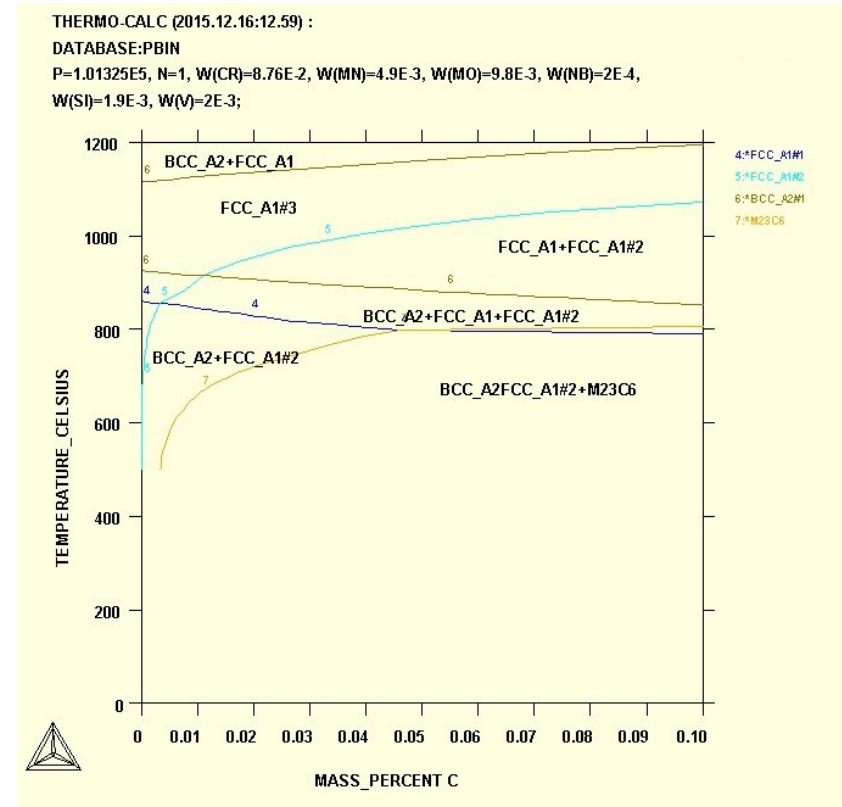
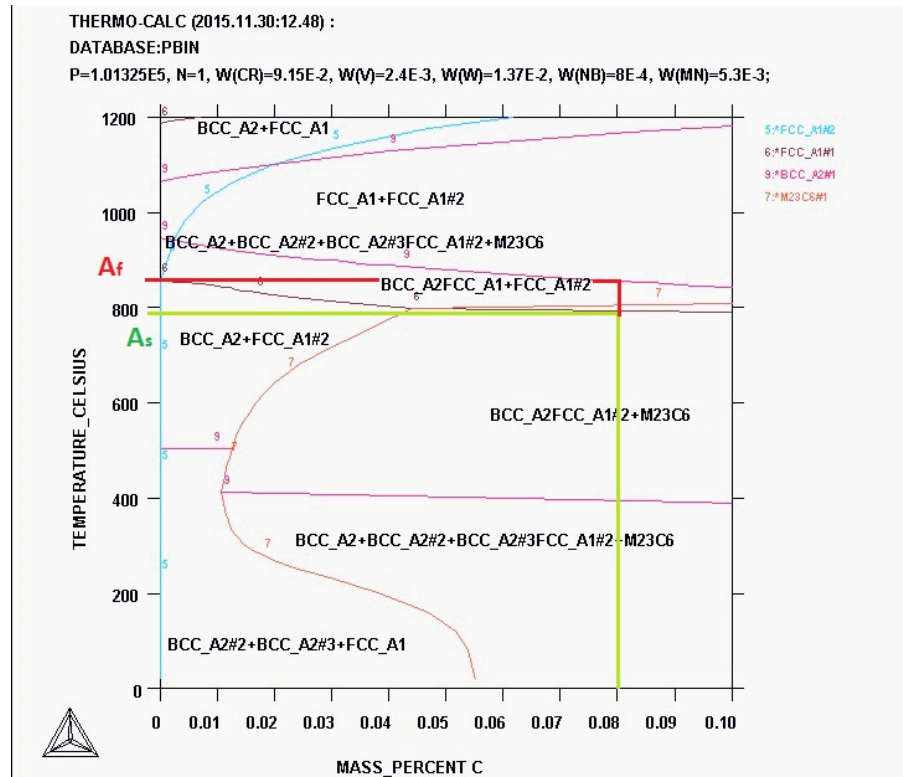


FIGURE 4.2: Phase diagram of (a) In-RAFMS and (b) P91 calculated with chemical composition estimated from Optical Emission Spectroscopy

The maximum temperature under operation is 500°C which is much lower than the A_s temperature of all popular grades of RAFMS as shown in Table 4.2. It is realized from the equilibrium phase diagram that the inter-critical region, of ferrite and Austenite phases, is $\approx 50^\circ\text{C}$.

The critical issue might be, therefore, the close values of tempering temperature which is 760-780°C and A_s temperature for RAFM grade steel falling in range of 770°C to 890°C. Any tempering process depending on its accuracy might cause some Austenite transformation. For better view and comparison of various popular grades of RAFM steels Table 4.2 is referred. The M_s temperatures, for all grade of steels in Table 4.2 are calculated using different empirical equations available in literature (Andrews, 1965; Steven and Haynes, 1956; Kunitake and Ohtani, 1969; Kunitake, 2001; Tamura, 1970; Eldis, 1977; Kung and Rayment, 1982; Andersson et al., 2002; Xu et al., 2016; Danon and Alamo, 2002; Zilnyk et al., 2015).

From above discussion, and Table 4.2, it becomes clear that for the grades of steels compared with basic composition of 9-12%Cr-W/Mo-Ta/Nb-V, the transformation temperatures are in very close range. Therefore, depending on the tempering process the pre-austenitic grain structure, and size and distribution of carbides, can be monitored. Therefore, the fracture of these steels are dictated by the structure of pre-austenitic grain boundaries and carbides type, size and its distribution.

TABLE 4.2: Comparison of various ferritic/martensitic grade steels

Material	C (Wt%)	Mn (Wt%)	Cr (Wt%)	Ni (Wt%)	Mo/W (Wt%)	Nb/Ta (Wt%)	V (Wt%)	Si (Wt%)	M _{s-1} (°C)	M _{s-2} (°C)	M _{s-3} (°C)	
10Cr steel	0.11	0.5	10.22	0.55	1.42	0.5	0.2		332.9	288.8	333.2	
F82H-Mod	0.09	0.156	7.68	0.021	1.04	0.1	0.162		395.7	364.9	396	
optifier-736	0.1	0.38	8.46			0.076	0.21		384.6	340.3	384.9	
optifier-734	0.13	0.61	9.41			0.095	0.277		351.2	301.3	351.6	
optifier-735	0.13	0.55	9.48			0.065	0.245		354.3	304.7	354.7	
In-RAFM	0.08	0.53	9.15	0.004	1.37	0.08	0.24	0.01	367.7	328.4	367.9	
P91	0.1	0.49	8.76	0.28	0.98	0.08	0.2	0.19	361.5	321.1	360.4	
Eurofer97	0.11	0.56	9.08		1.07	0.125	0.235		359.4	318.6	359.7	
ODS Eurofer	0.07	0.408	8.92		1.11	0.081	0.193	0.11	380	341.1	379.5	
JLF	0.1	0.64	8.93	0.49	1.96	0.1	0.21		345.6	308.8	345.8	
La12LC	0.09	1.13	8.92		0.73	0.1	0.3	0.03	353.3	302.8	353.4	
LA12TALC	0.1	1.13	9		0.73	0.1	0.3	0.03	347.7	297.2	347.7	
9.15Cr-0.08C	0.08		9.15						394.1	351.5	394.4	
	M _{s-4} (°C)	M _{s-5} (°C)	M _{s-6} (°C)	M _{s-7} (°C)	M _{s-8} (°C)	M _{s-9} (°C)	As(°C)	Af(°C)	Ms(°C)	Mf(°C)		Cooling rate (K/s)
10Cr steel	453	462.3	276.8	243	262.9	256.6			312	193		
F82H-Mod	492	492.1	361	323	347.3	342.9	850* ¹	910*	430*			60
optifier-736	503	503.2	339.4	328.5	324.3	325						
optifier-734	479	479	297.7	293.7	281.4	282.2						
optifier-735	483	483.4	300.6	295.7	285.3	286.1						
In-RAFM	477	476.7	319.9	282.3	302.1	295.6	778	875				
P91	469	474.7	314.4	283	301.5	297.2						
Eurofer97	470	470.1	311.5	282	295.1	290.3	820-860 † ²	880-970	360 †			0.1-1000
ODS Eurofer	490	490.4	333.2	297.1	317.8	312.6	835-875 †	915-985 †	380 †			1/∞-30
JLF	443	451.1	299.9	253	284.9	275.5	842 †	895 †	380 †	200 †		160.0
La12LC	466	466	300.9	284.7	281.3	277.5	807 †	875 †	375 †	200 †		45.0
LA12TALC	461	460.8	294.9	279.4	275.7	272	820 †	940 †	402 †	200 †		90.0
9.15Cr-0.08C	523	522.9	346.2	330.8	338.1	339						

¹*Obtained from ThermoCalc/Jmat or experimentally²† Obtained from literature

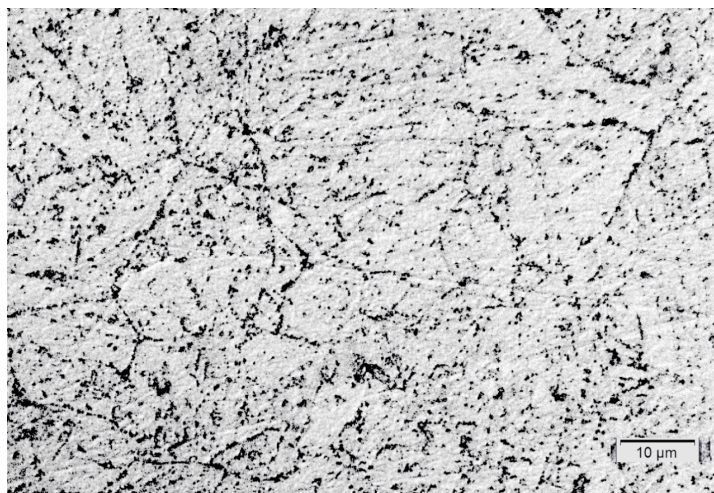
4.2.2 Microscopy: precipitates and micro-structure

The micro-structure of ferritic/martensitic grade steels is typical tempered martensite structure. The tempering, as can be seen in Table 4.1, is performed at relatively higher temperature, in order to avoid any in-service shape/ size change of precipitates, or phase transformation. The optical image of the microstructure is shown in Figure 4.3. The optical image of the microstructure shows the pre-austenitic grain boundaries decorated with carbides in dark. The lath structures are also visible in the microstructure for both the steels.

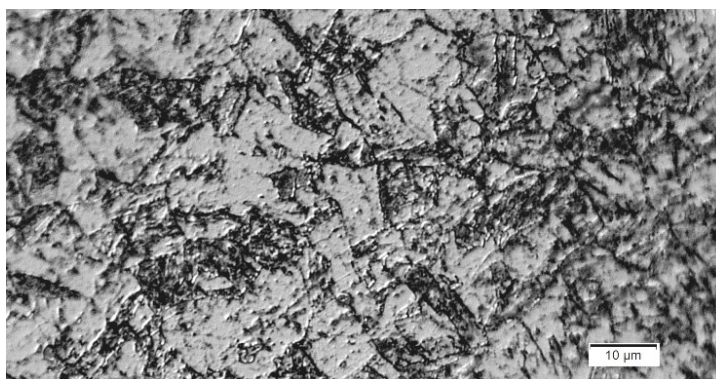
The microstructural analysis and distribution of carbides are also studied using Scanning Electron Microscopy (SEM) for ductile failure, brittle failure and for the intermediate zone of combined ductile and brittle failure. The optical microstructure shows that the pre-austenitic grain size for both the steels are close which is reportedly $15\ \mu\text{m}$ (Laha et al., 2013). A ductile to brittle transition may occur in a specimen where the initial crack starts propagating in ductile manner and due to changing crack tip stress fields the fracture mode can change to cleavage. The distribution of carbides as visible in Figure 4.3 shows that the random distribution of carbides as assumed in the formulation of master curve (Chapter 2) may not be very accurate. The carbides of larger sizes as will be discussed more based on the SEM images in this chapter, are dominantly present at the pre-austenitic grain boundaries. This local segregation of more potential cleavage initiators in comparison to the smaller carbides present elsewhere may be quantified as a function of grain size and/or lath size.

Spatial distribution of carbides; Image analyses

The fracture in complete cleavage fashion found at -120°C was used for EDXs mapping at the area near secondary crack and was analysed for Cr, V and Ta. The intensities of Cr, V and Ta as shown in Figure 4.4 (a), Figure 4.4 (c) and Figure 4.4 (e) were altered by changing the threshold limits of intensities by shrinking the band to the spectrum of pixels of the image. The image intensity shows a Gaussian distribution. To find



(a) Mod-9Cr-1Mo



(b) In-RAFMS micro-structure

FIGURE 4.3: Optical Microstructure of In-RAFMS and P91 taken after etching the polished specimens with 5% Nital for 30 seconds

the maximum frequency intensities this distribution of image intensity, for all three elements (Cr, V, Ta), were filtered with the limits (α) as $52(\leq \alpha \leq)172$ (α is the filtering parameter), so that the intensity spectrum lies in twice of standard deviation range. These images are shown in Figure 4.4 (b), Figure 4.4 (d) and Figure 4.4 (f). The image in Figure 4.4 (g) was also altered in order to visualize the white precipitates decorating lath and pre-austenitic grain boundaries clearly as shown in Figure 4.4 (h). The altered pictures were then stacked over on the mapped area image shown in Figure 4.4 (h). The stacked image containing Cr, V, Ta intensities over micro-structure is shown in Figure 4.5. The carbides as discussed earlier in Chapter 2 are generally $M_{23}C_6$ type and MX type. From the phase diagram, it is also evident that $M_{23}C_6$ is highly stable for In-RAFMS till A_s . The precipitates of M_2X are ignored due to the presence of V and Ta as

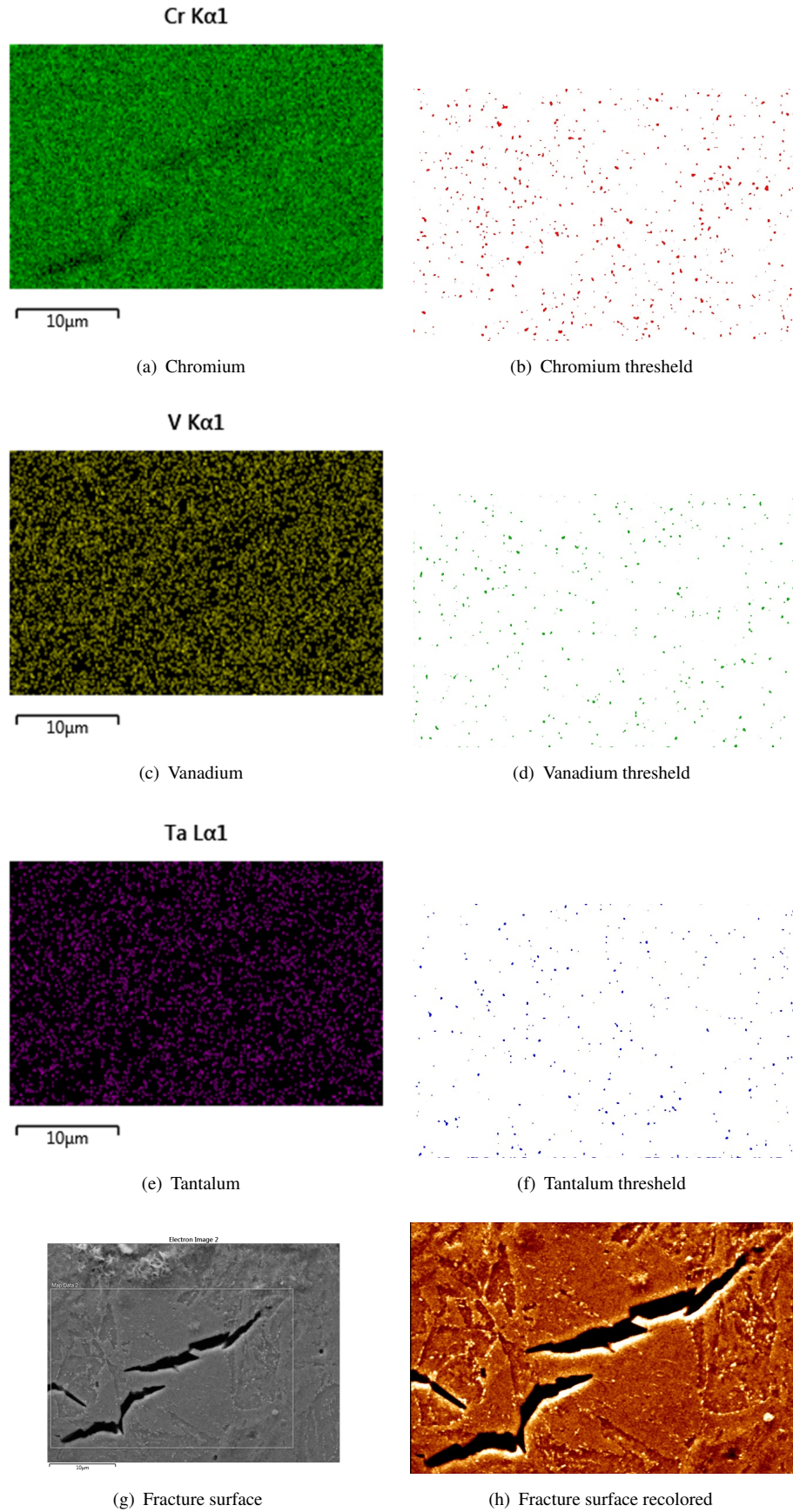


FIGURE 4.4: EDXS intensities and respective thresholds for image analysis

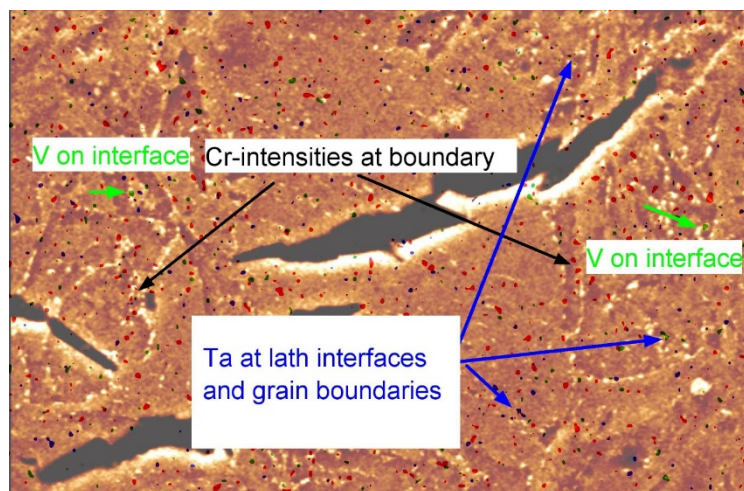


FIGURE 4.5: EDXs intensity threshold prediction of distribution of carbides

discussed earlier. The lath phases in In-RAFMS are avoided by air cooling the ferritic/martensitic steels after tempering. Therefore, the microstructure of In-RAFMS contains mainly $M_{23}C_6$ carbides which are larger in size in comparison to MX precipitates, and are located at the boundaries unlike MX precipitates of V and Ta, which are located inside the grains as visible in Figure 4.5. The $M_{23}C_6$ precipitates, as can be inferred from Figure 2.5 would contain around 58% of Cr, 17% of Fe and W/Mo and insignificant amount of V and Ta/Nb for 10% Cr ferritic/martensitic steel at 740°C. The enriched V, Ta matrix will cause MX type carbides inside grains and sub-grains for RAFMS grade owing to its less N_2 content. The size of carbides of $M_{23}C_6$ type has been reported to be 200 nm (Vanaja et al., 2013), which is also evident from Figure 4.4(g).

The SEM image of crack area after etching as shown in Figure 4.4(g) clearly reveals the carbides decorating lath interfaces and pre-austenitic grain boundaries. The carbides on pre-austenitic grain boundaries are also visible in the optical micro-graph shown in Figure 4.3. The carbide precipitates were also observed within pre-austenitic grains on the lath interfaces.

Although, in the Figure 4.5, it seems that the prediction by the image analyses matches the spatial location of precipitates; it is also observed that many of the points fall on the area (very small) where no precipitates are visible in the SEM image. The reason is that the EDXs signals of the elements are not very strong in the raw form i.e. in Figure

4.4. Therefore, the stacking procedure though is proven to be promising, depends on the initial signal of the elements scanned for.

4.3 Summary

The microstructure, equilibrium phases and transformation temperatures of phases, carbides and spatial distribution of carbides qualitatively were studied for In-RAFM and mod-9Cr-1Mo steels. The phase transformation for the two steels were studied by measuring unidirectional expansion/contraction in dilatometry test. The microstructure, phase transformation (both equilibrium and non-equilibrium) were compared with other popular grades of steels with similar composition and application. The comparison was made with the help of available literature data and empirical correlations.

The equilibrium phase calculations using numerical methods showed that the austenitic and ferritic transformation temperatures for the two steels very close. Similar is the observation for non-equilibrium phase transformation of martensite. The kinetics of phase transformation differs in the tempering region for P91, due to the precipitation of undesired Z and Lave phases.

The microstructure of two steels shows pre-austenitic grain boundaries and lath interfaces decorated with $M_{23}C_6$ carbides (M is a combination of Cr, W, Fe) and intra lath regions with MC type carbides of Ta/V. The reported size of $M_{23}C_6$ carbides are in the range of 100-300 nm with average size of 200 nm. The average size of MC carbides are 20 nm.

In case of P91 steel, the carbides were larger in size. The segregation of larger carbides on pre-austenitic grain boundaries makes the P91 steel inferior in comparison to In-RAFMS. The clean grade of In-RAFMS is expected to be free of detrimental precipitates of P, which are generally the weak links in P91 steels.

Chapter 5

Experimental and Numerical methods

In this chapter, the detailed description of the tensile and fracture tests, temperature control and test fixtures are described. In the second part of the chapter the descriptions of finite element models used for different studies such as effect of loading rate, size of specimens, type of specimens (CT and SE(B)) are detailed. The finite element analyses to model boundary layer formulation, ductile damage for simulating cleavage with prior DCG are also described.

5.1 Experimental set-up

The fracture tests as well as tensile tests were performed on servo-hydraulic universal testing machine at sub-zero temperatures. The cylindrical specimen of 4 mm diameter and 20 mm parallel length were used for measurement of tensile properties. The fracture specimen of different size and dimensions were tested using Compact Tension (CT) and Single Edge cracked Bend (SE(B)) specimens. The details of the specimen geometries used for different purpose are described in corresponding chapters. The In-RAFMS was obtained in hot rolled and tempered condition from Mishra Dhatu Nigam Ltd., Hyderabad, India in the form of 12 mm, 8 mm and 6 mm thick plates. The tensile specimens were fabricated from 6 mm thick plate. The fracture specimen of both CT and TPB geometries were fabricated from 12 mm thick plates. The engineering drawing of tensile specimen is shown in Figure 5.1.

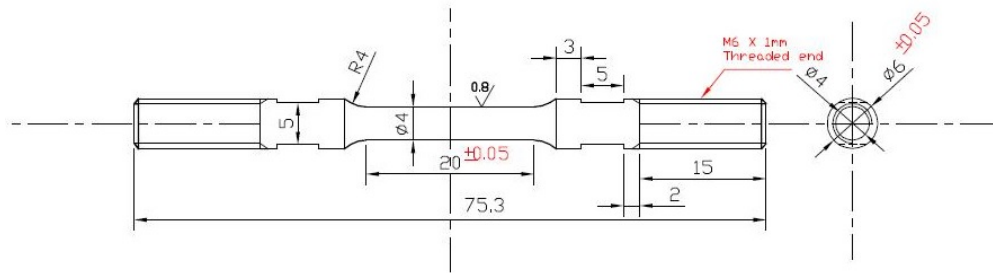


FIGURE 5.1: Engineering drawing of tensile specimens

The SE(B) specimen drawing is shown in Figure 5.2. The first lot of fracture specimens were fabricated with a thickness of 10 mm for both Three Point Bend (TPB) and CT geometries. The CT specimens were scaled for 0.5T CT according to ASTM E1921, although the thickness of the specimens were 10 mm. Therefore, the CT specimens are referred in this document as 0.4T CT and TPB as 0.4T TPB or 0.4T SE(B) specimens. The drawing of 0.4T CT specimens are shown in Figure 5.2. The TPB specimen were scaled in all directions according to ASTM E1921, as shown in Figure 5.2.

For assessment of effect of size, broken 0.4T TPB specimens were used and 0.2T specimen of $5 \times 5 \times 27 \text{ mm}^3$ were fabricated. Standard and sub-sized Charpy specimens of 10 mm and 5 mm thickness were also fabricated as discussed in corresponding chapters.



FIGURE 5.3: 0.4T CT specimen tested at sub-zero temperature in environmental chamber using UTM

The fracture tests were performed after pre-cracking the specimens to desired crack-depths using RUMUL resonant fatigue testing machine at $R = 0.1$ with decreasing load algorithm to ensure K_{min} , which is 20 MPa is never exceeded to avoid warm pre stressing at sub-zero temperatures (E1921, 2013; Wallin, 2004, 2003).

The fracture as well as tensile testing was performed for different parametric studies by placing those in an environmental chamber and the test temperature was maintained with an accuracy of $\pm 1^\circ\text{C}$ by re-circulating liquid N_2 in the chamber. The CT and TPB tests performed in environmental chamber at sub-zero temperatures. Image showing the test fixture and environmental chamber is shown in Figure 5.3 and Figure 5.4 for CT and SE(B) specimens, respectively.

The similar test specimens were tested for P91 grade steel and the details of the specimen geometries of both the grades are described in Appendix-C. The complete test

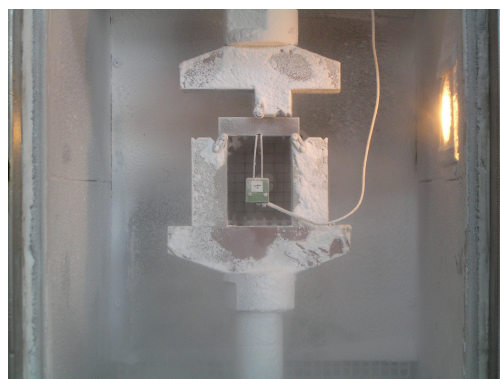


FIGURE 5.4: 0.4T TPB specimen tested at sub-zero temperature in environmental chamber using UTM

matrix of tensile tests, fracture tests, impact tests performed on In-RAFMs and P91 steels specimens is provided in Table [5.2](#).

TABLE 5.1: Datasets generated for different parametric studies

Objective	Test Temperature	loading rate	No. of Tests	Specimen geometry	Specimen size	a/W
Assessment of constraint loss (out of plane)	-110°C, -120°C, -130°C, -140°C -150°	0.5 mm/min	29	TPB	0.2T (5 × 5 × 27)	0.5
					0.2T (5 × 10 × 55)	0.5
Assessment of constraint loss (in plane)	-110°C, -120°C, -130°C, -140°C -150°	0.5 mm/min	29	TPB	0.2T (5 × 5 × 27) 0.2T (5 × 10 × 55)	0.3-0.7
Assessment of loading rate	-80°C, -100°C	0.5 mm/min 100 mm/min 1000 mm/min	29	TPB	0.4T ($W = 25, B = 10mm$)	0.5
Assessment of loading type	-110°C, -120°C, -130°C, -140°C -150°	0.5 mm/min	29	TPB	0.2T (5 × 10 × 55)	0.5
				CT	0.4T (10 × 10 × 55)	0.5
Assessment of prior ductile tearing on cleavage ¹						

¹Dataset of 0.2T TPB for MC analysis was used for upper DBT region

TABLE 5.2: All type of tests with experimental conditions performed in this work

Type of Test	No of tests	Material	Test temp (°C)	Loading rate	Specimen Type
Tensile	2 per temp	In-RAFMs	300, 200, 100, RT,-50, -70, -110, -120, -130, -140 , -150, -196	0.5mmpm	M6 Tensile
			-80,-100	100 mmpm	
			-80,-100	1000 mmpm	
		P91	-60,-70, -100,-110	0.5mmpm	
Impact	5 per temp	In-RAFMs	RT ,-30,-50, -85,-100,115, -133,-177,-189		Standard Charpy
	5 per temp	P91	RT, 0, -30, -50, -77, -89, 95, -190		
Fracture tests	26	In-RAFMs	-50, -70, -110, -120, -130 , -140 , -150	0.5mmpm	CT
	33				TPB (0.4T TPB)
	39				TPB (0.2T TPB)
	10		-80,-100	100 mmpm	TPB (0.4T TPB)
	18		-80,-100		TPB (0.4T TPB)
	12		-60,-70		CT (1T)
	15	P91	-100,-110	0.5mmpm	TPB
	20		-110		CT (0.16 T)

5.1.1 Metallographic studies

The In-RAFMS and P91 steel specimens were used for the study of phases, grain size and carbides' spatial distribution. For these studies and also for the damage study by observation of voids steel specimens of both grades, metallographic specimens were obtained from broken fracture test specimens. The specimens were polished on SiC papers followed by suspension polishing. The polished specimens were etched by dipping the specimens in 5% and 10% Nital (mixture of HNO₃ and H₂O). The metallographic studies were performed under both optical as well as scanning electron microscopy. The

broken specimen used for study of ductile damage were cut normal to the crack plane and polished.

5.1.2 Tensile and Charpy testing

The tensile tests were performed on the specimens described in section 5.1. The specimens were tested in the environmental chamber as discussed in section 5.1. The tensile tests were performed in the range of -50°C to -150°C . The load displacement record obtained from the UTM were used for calculation of engineering stress and strain. The elastic modulus was calculated at room temperature by testing the tensile specimen with extensometer. The Elastic modulus measured at room temperature was 207 GPa. The elastic modulus variation with temperature used for fracture toughness measurement followed the correlation given by [Moattari et al. \(2016\)](#).

The charpy tests were performed in a CEAST impact testing machine of 300 Joules capacity. The standard charpy specimens were soaked in cooling bath for 30 minutes. At each temperature five specimens were tested and average was used for the sigmoidal fitting as described in Chapter 6. The cooling bath were made by cooling ethyl alcohol with the help of liquid nitrogen and dry ice. The temperatures below -60°C were achieved by cooling the alcohol with liquid nitrogen only. Temperature below -100°C were achieved by cooling a bath of isopentane. The results of charpy tests are provided in Chapter 6.

5.1.3 Fracture toughness testing and measurement in DBT region

Before performing the fracture tests the specimens of different geometries were pre-cracked under cyclic loading. The fatigue precracking was performed on RUMUL resonant fatigue testing machine. The precracking followed a decreasing load algorithm with the intention to have maximum K less than $20 \text{ MPa m}^{1/2}$ in all cases.

The fracture tests were performed on the UTM in environmental chamber as described in section 5.1. The load load line displacement record was used for fracture toughness

measurement. The broken specimens were observed under low magnification stereo microscope for initial crack length measurement. The initial precrack was measured by measuring the ligament length at 9 equidistant points along the crack front. The measurements were avoided in the 0.01 times thickness at the sides of the specimen. The initial crack length were calculated from the 9 point measurements as described in ASTM E1921 and ASTM E1820. The average value of measurements at the ends are summed with the 7 measurements made in the two extreme points. The 1/8th fraction of this sum, which is average of 8 divisions is considered as initial crack length.

The K_{JC} is obtained by measuring the value of J integral without crack growth correction. The J integral is measured as,

$$J = J_e + J_p, \quad (5.1)$$

where J_e is the elastic part of J integral and J_p is the plastic part of J integral. The elastic part is calculated as,

$$J_e = \frac{(1 - \nu^2)K_e^2}{E}, \quad (5.2)$$

where ν is the Poisson's ratio, E is the plane strain Elastic modulus, and elastic stress intensity factor K_e is given for CT specimen as,

$$K_e = \left[\frac{P}{(BB_N)^{1/2}} \right] f\left(\frac{a}{W}\right), \quad (5.3)$$

where B is the thickness of the specimen, W is the specimen width and B_N is the effective thickness obtained by subtracting the side groove depth from B . $f\left(\frac{a}{W}\right)$ is a function of crack depth and specimen width ratio and it differs for CT and SE(B) geometries as described in ASTM E1921 and ASTM E1820. For specimens loaded under three point bending, K_e is given as,

$$K_e = \left[\frac{PS}{(BB_N)^{1/2}W^{3/2}} \right] f\left(\frac{a}{W}\right). \quad (5.4)$$

The J_p is calculated as,

$$J_p = \frac{\eta A_p}{B_N b_o}, \quad (5.5)$$

where b_o is the initial ligament length. The plastic part of area under load displacement curve is obtained as,

$$A_p = A - \frac{1}{2}C_oP^2, \quad (5.6)$$

where A is the area under the load displacement curve, which is calculated in this work by applying Simpson's trapezoidal rule to the load displacement data points. C_o is the reciprocal of the initial elastic slope. P is the force at the end. For more detailed description of the area under load displacement curve and calculations pertaining to load displacement with multiple pop-ins, ASTM E1921 is referred. The η factor for J_p calculation using Clip on Gauge (COD) response, is given as,

$$\eta = 2 + 0.522\left(\frac{b_o}{W}\right), \quad (5.7)$$

for CT specimens. For specimens tested in three point bending scheme, the η is described as,

$$\eta = 3.667 - 2.199\frac{a_o}{W} + 0.4376\left(\frac{a_o}{W}\right)^2. \quad (5.8)$$

For three point bend tests in this work load line displacement is used for J_p calculation with a value of $\eta = 1.9$. For CT specimens, however, COD response is used for J_p calculation and η from Eq.(5.7) is used.

The J_C is then obtained by adding the J_e and J_p and K_{JC} is calculated as,

$$K_{JC} = \sqrt{J_C \frac{E}{(1 - \nu^2)}}. \quad (5.9)$$

5.2 Finite element analysis

The Finite Element Analysis (FEA) method is used in this work throughout for assessment of loss of constraint, effect of loading rate, ductile crack growth prior to cleavage, and for calculation of micro-mechanical Weibull stress. The FEA is implemented in all these applications using ABAQUS commercial package (Hibbitt et al., 1998). There are two types of simulations performed in this work. First being the continuum FEA where

damage in material is not incorporated and second where damage is considered. The micro-crack nucleation and effect of micro-cracks on cleavage failure mechanism is not implemented using any damage parameter in conventional or modern FEA methods anywhere. The cleavage fracture is assessed using micro-mechanical parameter known as Weibull stress, which is defined later in Chapter 9 and 10. The micro-mechanical condition to define cleavage follows generally the stress based criteria (Ritchie et al., 1973) and modern approaches including Weibull stress and WST approach is based on this idea. The ductile damage on the other hand is a strain based phenomena, and is taken care of by means of continuum damage mechanics. The two types of FEA implemented in this work is explained in a generic way for all the numerical analyses performed in this work. Case specific details are described in corresponding chapters.

5.2.1 Continuum FEM

The continuum finite element analyses without damage was performed using incremental plasticity for assessment of micro-mechanical parameters for cleavage failure probability measurement. The material behaviour in terms of mechanical response obtained experimentally was used as input. The material behaviour followed J_2 flow theory with incremental plasticity and complete linear pre-plastic behaviour. The true stress (σ) logarithmic strain (ϵ) curve follows a power law hardening plastic behaviour as,

$$\frac{\epsilon}{\epsilon_o} = \frac{\sigma}{\sigma_o} \quad \text{for} \quad \epsilon < \epsilon_o \quad (5.10)$$

$$\frac{\epsilon}{\epsilon_o} = \left(\frac{\sigma}{\sigma_o}\right)^n \quad \text{for} \quad \epsilon \geq \epsilon_o \quad (5.11)$$

where σ_o and ϵ_o are the yield strength and corresponding strain. The non-linear behaviour starts after the plastic strain reaches ϵ_o . The hardening non-linearity is described by the hardening coefficient n .

The crack tip modelled for different geometries were generally used for J -Integral calculation by means of domain integral (Parks, 1992; Anderson, 2005) and the element type in all the three dimensional models was 20 noded brick elements.

A very specific two dimensional modelling approach is applied for measurement of crucial parameters and highly accurate crack tip stress-strain analyses, known as boundary layer model. In this scheme, the crack tip region encircled at a radius where the material remains elastic is scooped out and loading is applied at this circular boundary following set of equations given as,

$$u_x = \frac{K(1+\nu)}{E} \cdot \sqrt{\frac{r}{2\pi}} \cdot \cos\left(\frac{\phi}{2}\right) \cdot (3-4\nu - \cos(\phi)) + T_{stress} \cdot \frac{1-\nu^2}{E} \cdot r \cdot \cos(\phi), \quad (5.12)$$

$$u_y = \frac{K(1+\nu)}{E} \cdot \sqrt{\frac{r}{2\pi}} \cdot \sin\left(\frac{\phi}{2}\right) \cdot (3-4\nu - \cos(\phi)) - T_{stress} \cdot \frac{\nu(1+\nu)}{E} \cdot r \cdot \sin(\phi). \quad (5.13)$$

The scooped out region given displacements according to Eq.(5.12) and Eq.(5.13) with second order stress function of William's expansion (Williams, 1961) is referred as Modified Boundary Layer (MBL) model.

In Eq.(5.12) and Eq.(5.13), u_x and u_y are the displacements in Cartesian coordinates x and y as shown in the schematic Fig. 2. r , is the radius of the scooped out region, E is Young's modulus, T_{stress} is the elastic stress of the second term of William's crack tip stress expansion series, ν is Poisson's ratio, K is the stress intensity factor in opening mode and ϕ is the angle from crack surface.

The meshing of MBL has also been studied extensively with 20 noded serendipity elements. The mesh size is refined from the outer to inner layers. As the mesh refinement, in three dimensional problems, causes longer durations for analysis; many time saving practices has been used. In WARP 3D FEA open source package, the plane strain elements formulation is absent, which demands a 3D model to have imposed a boundary condition of zero displacement in thickness direction. Nevalainen and Dodds (Nevalainen and Dodds Jr, 1996) have used linear pre-conditioned conjugate gradient (LPCG) method that avoids assembling large stiffness matrices, thereby decreasing both the solution runtime as well as the physical memory in comparison to direct solvers. On the other hand computations by Delorenzi and Shih (1983); Koers et al. (2013) with

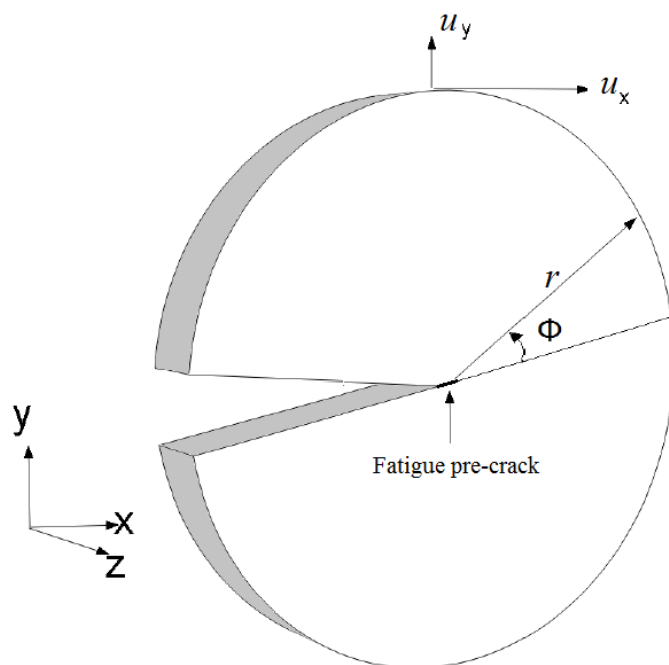


FIGURE 5.5: Schematic of Modified Boundary Layer model showing boundary conditions

moderate meshing has shown satisfying results of J variation along three dimensional crack fronts. The MBL model has been used by Nevalinen and Dodds for the assessment of CT and SE(B) geometries with shallow and deep notch for strong, moderate and low hardening materials in comparison with small scale semi-infinite solutions. The model by Nevalinen has also used hexahedral elements with 14 layers along the thickness direction.

In another study by [Dodds Jr et al. \(1991\)](#) investigating effect of crack depth on crack tip stress field it was emphasized that reduced integration 2×2 Gauss quadrature eliminates locking of arbitrarily shaped elements once the incompressible conditions of fully plastic deformation constrain volumetric changes in the displacement gradients. The importance of crack tip blunting has also been recommended in the study of [Petti and Dodds Jr \(2005\)](#), where it was found that the smaller root radius helps in convergence of the finite element analysis for boundary layer model. The root radius of MBL analysed by Petti and Dodds was $2.5 \mu\text{m}$.

Based on above works, the MBL modelled in this work has 40 layers of concentric circles of elements surrounding the region near the crack tip, which was meshed with

constant mesh size of $3\mu\text{m}$.

5.2.2 Ductile damage implementation

The numerical analysis to simulate prior ductile crack growth to cleavage, was carried out with ductile damage. The failure criteria of elements were ductile damage dependent. The load displacement response of the model was used to calculate K_{JC} by assuming cleavage to occur at each increment of crack. The finite element analyses of both CT and TPB geometries were performed for measurement of change in constraint with ductile tearing. The ductile damage was introduced in the finite element analyses using Gurson, Trevergaard and Needleman (GTN) (Gurson, 1977; Tvergaard, 1981; Tvergaard and Needleman, 1984) model. The GTN model describes the yield function Ψ as,

$$\Psi = \left(\frac{\sigma_{eq}}{\sigma_o}\right)^2 + 2q_1 f^* \cosh\left(q_2 \frac{3\sigma_h}{2\sigma_o}\right) - (1 + q_1^2 f^{*2}), \quad (5.14)$$

where σ_{eq} , is the equivalent stress, σ_o is the yield strength of the material, σ_h is the hydrostatic stress, q_1 , q_2 are the GTN models fitting parameters and f^* is the void volume fraction in the material.

The plastic behaviour of the model according to GTN theory is described by the void volume fraction in the material. The ductile damage occurs due to nucleation, growth and coalescence of voids in the material. The nucleation and growth according to GTN theory is dependent on the equivalent and hydrostatic components of the stresses. The coalescence is taken care of by giving a steep increment to f^* after a threshold value of f_C . The nucleation rate, \dot{f}_N for a GTN type damage is described as,

$$\dot{f}_N = Z \cdot \dot{\epsilon}_{eq}^p, \quad (5.15)$$

and the void growth rate is described as,

$$\dot{f}_G = (1 - f) \cdot \dot{\epsilon}_{kk}^p, \quad (5.16)$$

where ϵ_{eq}^p , is the equivalent plastic strain rate, $\dot{\epsilon}_{kk}^p$ is the volumetric strain rate, f is the instantaneous void volume fraction at the step increment in finite element calculation and Z is a parameter, which describes the probability density of nucleation of voids as,

$$Z = \frac{f_M}{\sigma_{std}\sqrt{2\pi}} \left[-\frac{1}{2} \left(\frac{\epsilon_{eq}^p - \mu}{\sigma_{std}} \right)^2 \right], \quad (5.17)$$

where, f_M is a constant, σ_{std} is the standard deviation of distribution of nucleation sites, ϵ_{eq}^p is the equivalent plastic strain and μ is the mean of the distribution. The rate of increment of the void volume fraction at any stage of the loading (time increment of simulation) is sum of nucleation and growth rate. The ductile damage is implemented in the finite element analyses by deleting the elements following fracture criteria defined as,

$$f^* = f \quad \text{when} \quad f < f_C \quad (5.18)$$

$$f^* = f_C + \frac{f_U^* - f_C}{f_F - f_C} \cdot (f - f_C) \quad \text{when} \quad f > f_C \quad (5.19)$$

In this work, to introduce the ductile crack growth prior to cleavage, a user material program VUMAT, which can be coupled with ABAQUS FEA software was written (Hibbitt et al., 1998). The VUMAT subroutine used here, calculated the yield function and void volume fraction in each elements locally. The element deletion option was used with VUMAT to induce ductile crack growth.

5.3 Solver, mesh and sensitivity analyses

The finite element analyses used incremental plasticity with full Newtonian solution method, in which each increment is approximated by remaking the Jacobian matrix to capture the non-linear load displacement response. This method is better for accurate solutions and also economical for not very large number of elements (Hibbitt et al., 1998). For ductile damage simulations, deletion of elements based on failure criteria was applied following explicit solution technique. The rest were solved using implicit displacement increment. The details of implicit and explicit algorithms of boundary

condition application can be found in user manual of Abaqus package ([Hibbitt et al., 1998](#)).

For In-RAFMS CT as well as bend geometries the models were tested for sensitivity analyses of mesh size. The mesh independent values of crack tip features were found for an element size of 0.2 mm^3 . Therefore, all the FEA analyses has been performed with elements of size 0.2 mm^3 or less.

Chapter 6

In-RAFMS: Mechanical behaviour in DBT & conventional master curve

In this chapter, the first part details the tensile and impact properties of Indian Reduced Activation Ferritic/Martensitic Steels (In-RAFMS) in DBT region. The DBT behaviour of In-RAFMS is discussed with the fractographic observations. The second part of this chapter presents the conventional master curve results of In-RAFMS. The conventional master curve approach using single and multi-temperature methods are compared and it's advantages and disadvantages are discussed.

6.1 Impact toughness, damage in DBTT and Tensile properties

The operational condition of fusion reactor demands the first wall blanket to perform in the temperature range of 350-500°C. As described earlier, high chromium steels due to its better creep properties are best suitable for this application. However, it has shown by [Kytka et al. \(2011\)](#) that the shift in quasi-static DBT temperature after 2.43 dpa of irradiation damage shifts upward by 110°C. Therefore, the fracture behaviour in DBT region becomes a huge liability on the RAFM steels for these to perform in fusion reactors with irradiation damage induced by high energy (≈ 14.1 MeV) neutrons.

The Charpy impact test energy can be used to estimate the reference transition temperature as described by Wallin ([Donald E. McCabe, 2005](#)). The impact energy behaviour of In-RAFMS and P91 steels, investigated in this work, are shown in [Figure 6.1](#) with a sigmoidal fit showing differences in transition behaviour of the two grades.

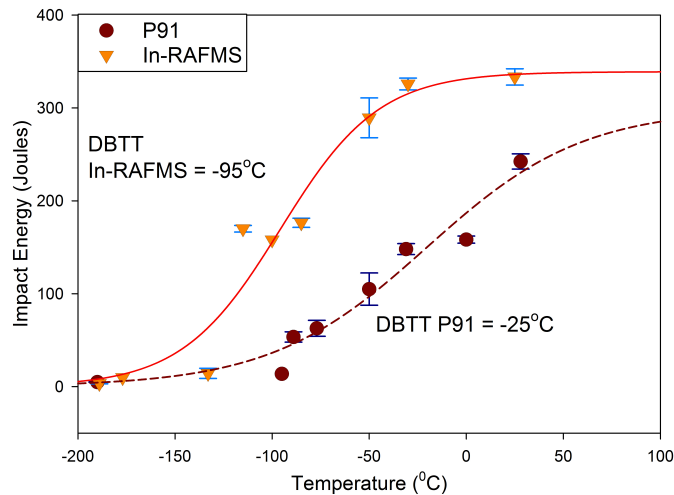


FIGURE 6.1: Impact energy variation in DBT region for In-RAFMS and P91 steels

The damage mechanisms in SEM fractographs for In-RAFMS is shown in Figure 6.1. The Charpy test result behaviour makes it evident that the P91 steel is inferior in impact toughness to In-RAFMS. The transition temperature DBTT obtained by averaging the upper and lower shelf of the sigmoidal fit in Figure 6.2, shows that P91 has a DBTT 70°C higher than that for In-RAFMS. Figure 6.2 shows the signatures of dimples at higher temperatures and cleavage facets at lower temperatures showing a typical ductile to brittle transition. In the SEM image of fracture specimen broken under quasi-static loading at -70°C shown in Figure 6.3, the fracture is clearly followed by void coalescence as can be seen in Figure 6.3(c).

6.1.1 Brittle fracture in DBT region

The brittle fracture was examined using fracture specimen broken at -120°C which was used for image analyses in Chapter 4 (Section 4.2.2). It is found in this work, by testing in lower shelf, that secondary crack formation is almost 100% for specimens tested in lower shelf. The SEM image was also taken at the secondary crack, however, the specimen analysed did not belong to lower shelf.

In the region of DBT or in lower shelf the fracture is well known to be by microcrack formation in the volume encompassed by a critical value of maximum principal stress [Nevalainen and Dodds Jr \(1996\)](#); [Ritchie et al. \(1973\)](#). This volume is also known as

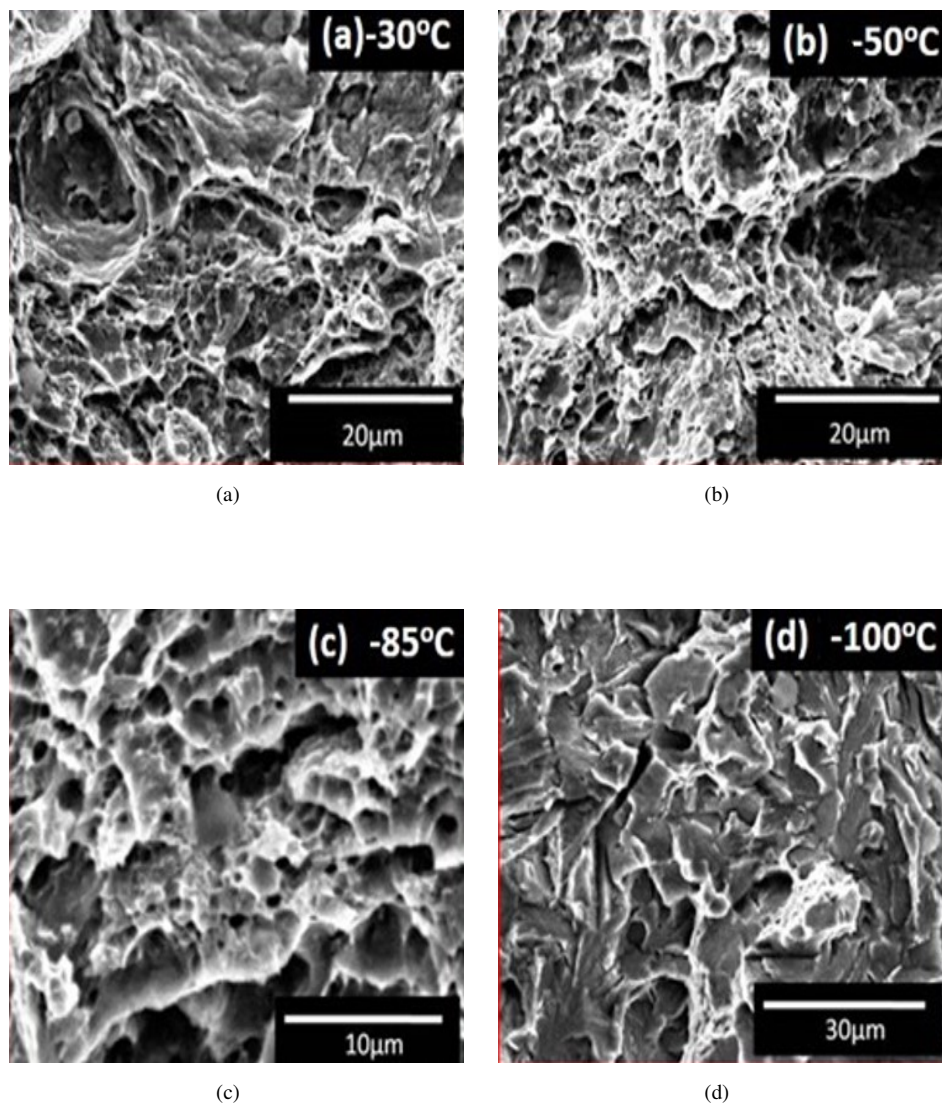


FIGURE 6.2: Fracture surface of broken Charpy specimens of In-RAFMS in DBT region with ductile fracture at (a) -30°C (b) -50°C, (c) intermediate fracture at -85°C and (d) complete cleavage at -100°C

active sampled volume and is the same volume which is used by master curve methodology for modelling cleavage failure as discussed in Chapter 2. The micro-cracks form due to failure of carbides or inhomogeneities. Inclusions in steels not fail but debond. RAFMS is a cleaner grade of steels, free of inclusion and hence does not show any debonding. This failed carbide acts as a micro penny shaped crack, which requires energy to propagate to the matrix grain and then to cross the grain boundary. This requires dynamic propagation of microcrack as steady growth is not energetically sufficient for the microcrack to cross the boundary. This results in a competition of two mechanisms; one which defines the propagation of microcrack resulting in catastrophic failure by

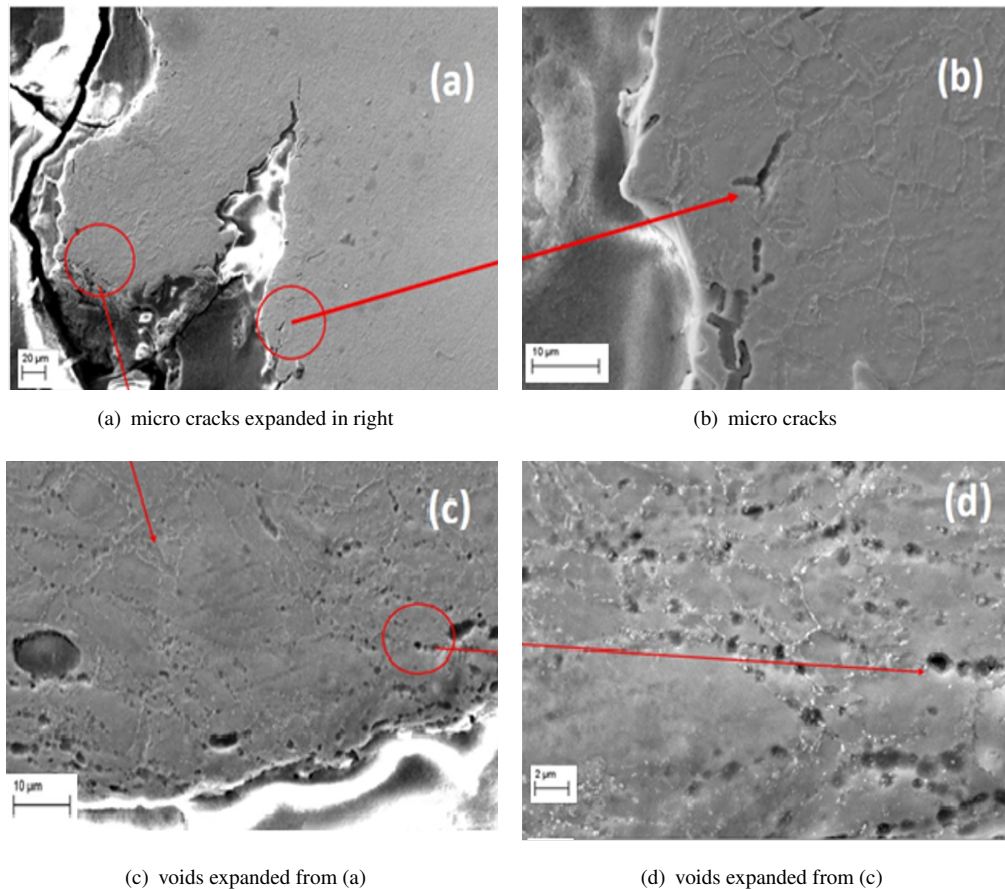


FIGURE 6.3: SEM image of near crack tip region of In-RAFMS broken specimen at -70°C showing ductile damage signatures along with microcracks

cleavage, and another which is caused by plastic strain if the tensile stress does not provide sufficient energy for dynamic propagation of the crack. These behaviours are visible in Figures 6.3 and 6.4.

6.1.2 Intermediate fracture in DBT region

The intermediate region is described where fracture is found to be a mixture of transgranular and intergranular fracture. The plastic strain criteria is met and the micro-void coalescence as shown in Figures 6.3 and 6.4 for both In-RAFMS and P91, causes steady ductile tearing. The crack starts with blunting the crack tip followed by ductile tearing. This process as the ligament length decreases results in increase in constraint which then makes cleavage to occur. The combination of ductile and brittle fracture is observed as intergranular fracture followed by transgranular fracture.

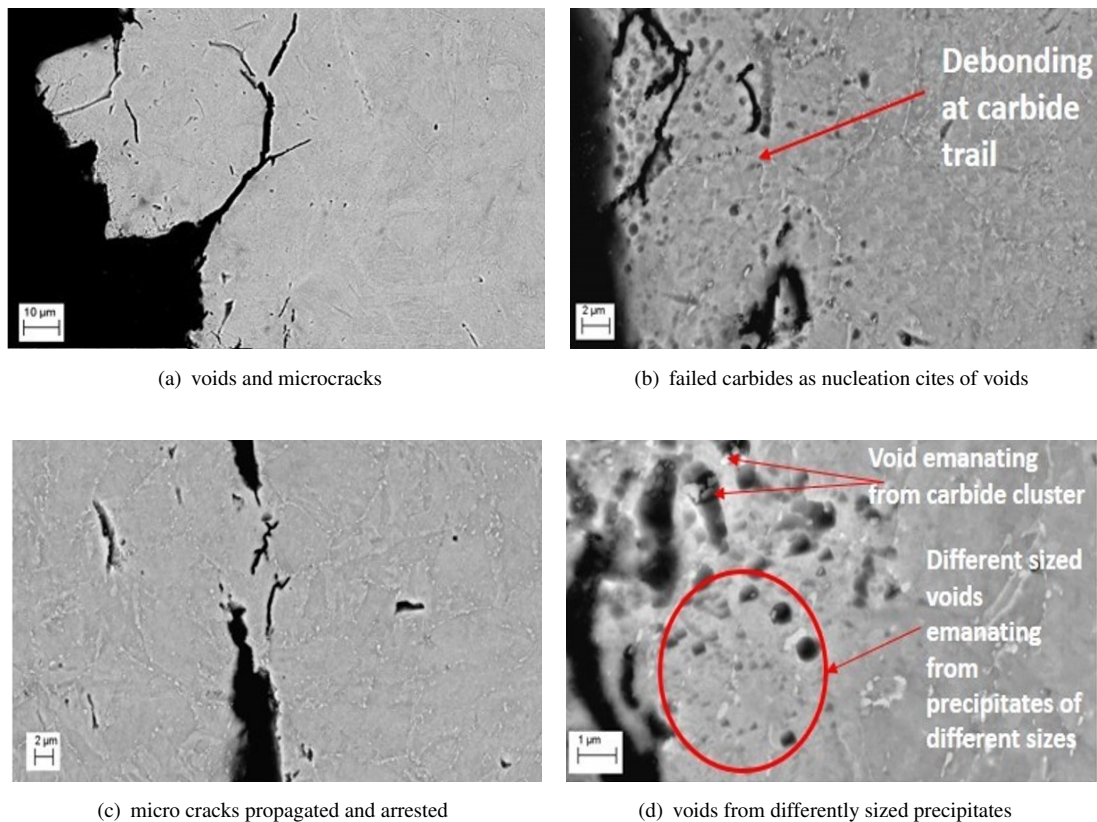


FIGURE 6.4: SEM image of near crack tip region of P91 broken specimen at -70°C showing ductile damage signatures along with micro-cracks

On the right side in Figure 6.3(d) the magnified view of the ductile damage area encircled in Figure 6.3(c) shows the trail of larger voids at the pre-austenitic grain boundaries which is accompanied by smaller size voids following the smaller carbides inside the grains. This is due to the higher stress concentration and higher strain incompatibility associated with larger carbides at the pre-austenitic grain boundaries. Moreover, as the carbides at the boundaries are generally larger in size, the coalescence of the voids are also easier. This is also revealed in the Figure 6.3(c). The void coalescence is also largely visible at the pre-austenitic grain structure. Similar is the finding for P91 grade as shown in Figure 6.4.

Tan et al. (2013) has shown that the triggering particles in Ta alloyed ferritic/martensitic steels of similar composition, as discussed in this work, are oxides of Mn-rich particles in ductile tearing and smaller dimples were formed at Ta-rich oxides.

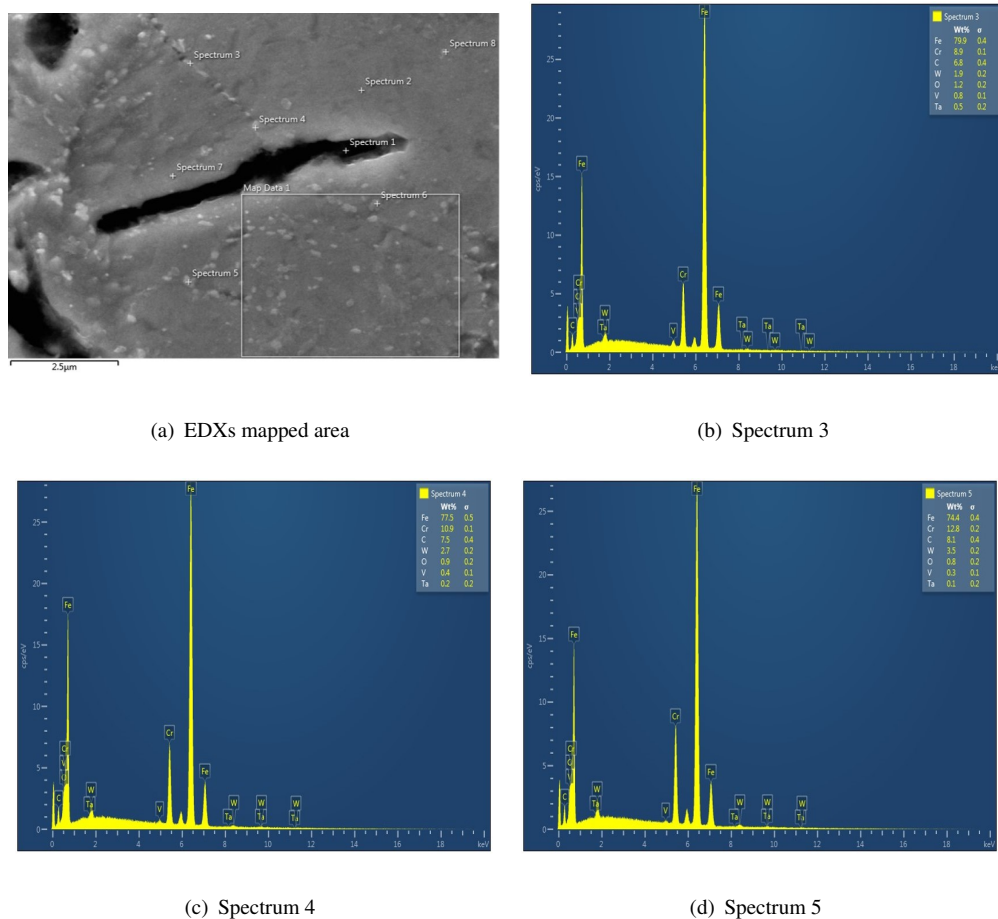


FIGURE 6.5: EDXs mapping of surface near micro-crack of In-RAFMS showing chemical composition

The EDXs analysis a part of which was shown in Figure 4.4 also showed higher concentration of oxygen as well as carbon at the Ta and W rich sites, however, the accurate distinction of the particles being carbides or oxides was not possible in this study. The EDXs compositional analysis of the precipitate sites are shown in Figure 6.5.

6.1.3 Tensile properties

The tensile properties obtained by testing 4 mm diameter cylindrical specimens are shown in Figure 6.6. In Figure 6.6, the strain on the horizontal axis is calculated by

subtracting the elastic strain based on the initial Elastic modulus. The values are qualitative only after necking and are shown for the differentiation in failure points of the specimens at different temperatures.

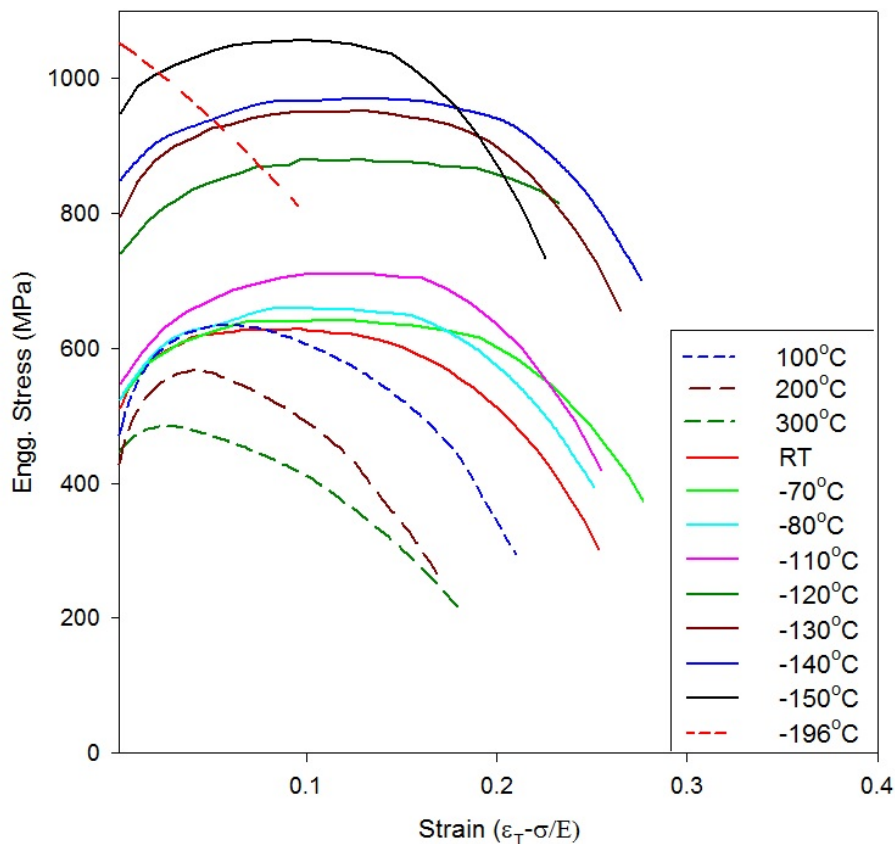


FIGURE 6.6: Engineering stress-plastic strain ($\epsilon_T - \sigma/E_0$) response of In-RAFMS in DBT region

The trend of yield strength and Ultimate Tensile Strength (UTS) as appearing in Figure 6.6 shows conventional behaviour except at -50°C . Due to this discrepancy and also due to the expected transition temperature (with the help of Charpy Impact toughness) to be lower than -50°C , fracture tests were avoided in the temperature range more than -50°C . Only exception was 0.4T CT specimen, some of which were tested at -50°C to examine the effect of prior ductile tearing on cleavage fracture.

The tensile behaviour in Figure 6.6 also shows an upward jump for temperatures more than -110°C . The post necking strain decreases significantly after -140°C . The behaviour of YS and UTS is also shown in Figure 6.7, where it is clear that with decreasing

temperature the YS and UTS tend to converge, showing difficulty in dislocation movement due to less slip systems and converges at -196°C, where apparently the lower shelf fracture without any work hardening occurs.

The tensile behaviour of ferritic/martensitic grade steel (Eurofer97) has been studied in great detail by Bonad et al. (2008); Bonadé (2006). For the constitutive relationship of true stress and logarithmic strain, to be used for finite element analyses it has been a trend to linearly extrapolate the behaviour till UTS beyond necking. The post necking extrapolation of logarithm of true stress and strain has been discussed in detail by Hasegawa et al. (2009). It should however not be ignored that the post necking behaviour might be completely different from the pre-necking tensile behaviour due to the damage kinetics. Still, in this work the linear extrapolation of logarithm of true stress strain has been followed. The reason for the extrapolated tensile behaviour is to simulate the crack front which generally strains beyond uniform strain. In the work of Bonad et al. (2008), where fracture behaviour of Eurofer97 is studied, similar approach is applied.

The tensile properties in form of true stress and logarithmic plastic strain were obtained till Ultimate Tensile Strength (UTS) from the raw data in form of load and load-line displacement. The natural logarithm of true stress-logarithmic strain behaviour obtained for In-RAFMS as well as P91 when plotted till UTS showed a linear behaviour. The finite element analyses of crack tip elements requires the material's tensile response beyond UTS and therefore, this linear logarithmic response was extrapolated by fitting the behaviour as,

$$\ln(\sigma_{true}) = a_1 \ln(\epsilon_p) + a_o , \quad (6.1)$$

where a_o and a_1 are fitting parameter. The tensile properties extrapolated to a plastic strain of 2 were used in numerical calculation. The details of extrapolated tensile responses are detained in corresponding chapters. Similarly the tensile response of P91 were also extrapolated.

The yield strength (σ_o) and UTS is shown in Figure 6.7 for In-RAFMS tested at quasi-static loading rate of 0.5 mm/min. The ratio $\frac{\sigma_{UTS}}{\sigma_o}$ is shown in Figure 6.7 for quasi-static

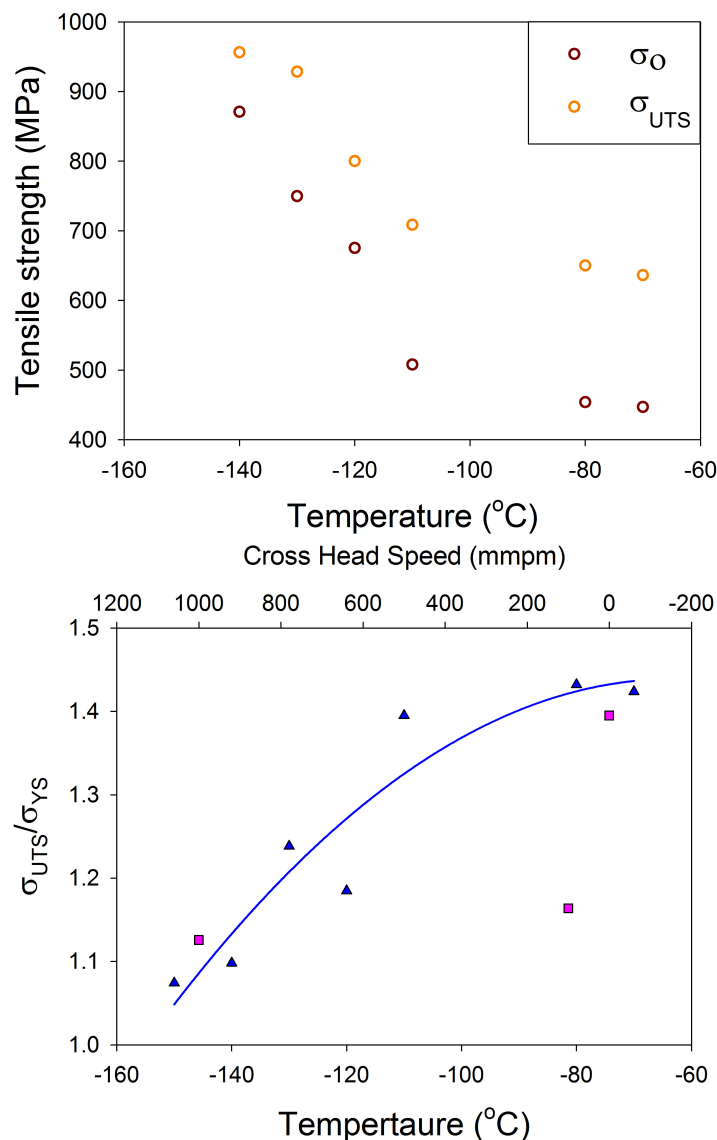


FIGURE 6.7: Yield strength, UTS responses at (a) different temperatures and hardening behaviour in form of σ_0/σ_{UTS} at (b) different strain rates

(0.5 mm.min) as well as for higher actuator (Cross Head Speeds) speeds, such as 100 mm/min and 1000 mm/min corresponding to strain rates of 0.083 s^{-1} and 0.83 s^{-1} , respectively.

After studying the micro-structure, phase transformation, precipitate size and distributions, and tensile behaviour of In-RAFMS, a detailed property chart of In-RAFMS is enlisted in Table 6.1.

TABLE 6.1: Summary of microstructural and mechanical properties of In-RAFMS

Chemical composition (Wt %)								
C	Cr	W	V	Ta	Si	Mn	S, N	Al, Ni
0.08	9.15	1.37	0.24	0.08	0.026	0.53	< 0.002	< 0.004
Hardness	220 HVC at RT (Microhardness 253 tempered martensite/207 ferrite and carbide (Raju et al., 2009))							
Heat Treatment	Solutionizing 977°C for 0.5 hr normalizing & Tempering 760°C for 1hr air cooled							
Microstructure	Tempered martensite Cr ₂₃ C ₆ (100-300 nm) at pre-austenitic & interlath boundaries (Ta/V)C carbides inside laths of 20 nm size.							
Phase and transformation temperatures				DSC	ThermoCalc			
Curie Temperature				745°C		M23C6 dissolution	1277°C	
Ac1				832°C	778°C	Delta ferrite start	1302°C	
Ac3				867°C	875°C	MX compete dissolution	1408°C	
Martensite to ferrite + M23C6				664°C		Liquid start	1457°C	
Ms				441°C	302-477 °C (Table 4.2)	Complete melting	1532	
Mf				345°C		H alpha-gamma	13-14 J/g	
						Enthalpy of Melting	364 J/g	
Heat capacity Cp	$C_p = AT + BT^2 + CT^3 + D/T + E \ln(\frac{T-T_c}{T_c})$							
	10.64	-0.018	8.57×10^{-6}	-760670.77		-30653.01		
Tenile behaviour								
Temperature (°C)	YS (MPa)	UTS (MPa)	DBTT					
300	418	485	68J criteria			-85°C		
200	436	570	DBTT			-95°C		
100	430	609	(Average of upper					
RT	410	637	& lower shelf)					
-70	560	636.4						
-80	564	650.2						
-110	587	708.7						
-120	765	800.2						
-130	845	928.5						
-140	878	956.4						
-150	957.51	978						
-196	1086	1096						

6.2 Conventional master curve analysis of In-RAFMS

The conventional master curve analysis was performed on the fracture dataset of standard Single Edge Notched Bend specimens (SENB) with specimen width W being twice of thickness. The specimen dimension is shown in Appendix-C with the geometry of knife edges and notch root radius. The conventional master curve as discussed in Chapter 2 can be performed on the fracture dataset generated at different temperatures which is known as multi-temperature master curve method . A special and simpler case when the dataset generated at single temperature is analysed is referred as single-temperature master curve . The conventional master curve takes the athermal part of fracture toughness as $30 \text{ MPa m}^{1/2}$ and thermal part takes the value of $70 \text{ MPa m}^{1/2}$ in Eq.(2.6).

The conventional master curve involves certain validity criteria as discussed in section 2.2.2. As the assumption of master curve methodology demands single parameter characterization of crack tip stress field either by J or K_J , the self-similarity of the stress field becomes an implicit requirement. For smaller specimens this is almost impossible which results in non-uniformity of the T_0 assessment by single and multi-temperature master curve methods.

The extensive study to assess the uncertainty involved in examined on the 0.4T SEB dataset as well as 0.2T TPB dataset as shown in Table 6.2.

It has also been discussed earlier that various studies such as [Joyce and Tregoning \(2005a\)](#); [Nevalainen and Dodds Jr \(1996\)](#) has shown both experimentally and by finite element analyses results that for SEB type specimens loaded under three point bending the constraint parameter for censoring should be made more strict. The study by [Faleskog et al. \(1998\)](#) suggests the M parameter in Eq.(2.13) should be as high as 70, however on the other hand earlier study by [Joyce and Tregoning \(2005a\)](#) recommends it to be as high as 200 for smaller SEB specimens to achieve SSY conditions. To study the effect of strict censoring 0.4T SEB dataset was used as 0.2T dataset had less valid data for maximum likelihood analysis. The conventional multi-temperature master curve

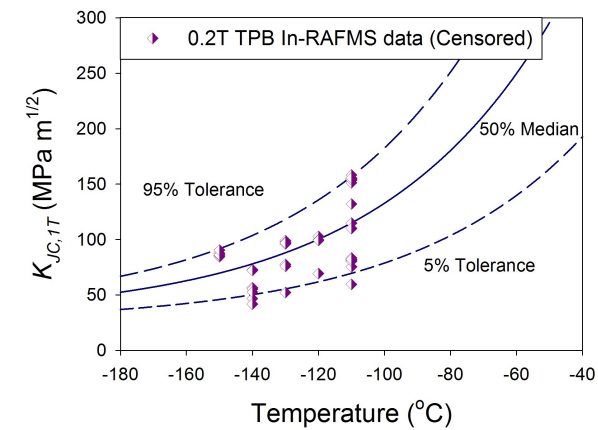
analysis of 0.4T SEB, 0.2T TPB and 0.4T CT specimens of In-RAFMS are shown in Figure 6.8.

6.2.1 Single and multi-temperature master curves

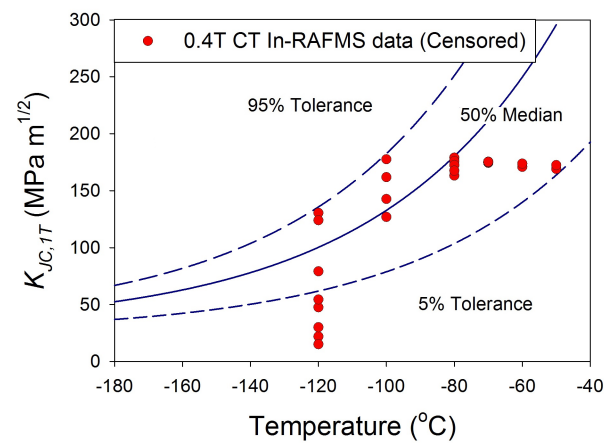
The single temperature master curve analysis estimates the behaviour of fracture toughness dependence with temperature using dataset only at one test temperature. This inherently restricts involvement of fracture toughness thermal dependence and forces maximum likelihood to result to follow the empirical thermal dependence of master curve. The trend of fracture toughness w.r.t. temperature, therefore, is decided by the median found at single temperature as shown in Figure 6.9. The effect however is mitigated as the master curve assumes a standard shape and the dependence is not generally altered for ferritic and ferritic martensitic steel. A case study on Eurofer97 is discussed in Chapter 2, where this conventional dependence was challenged and thermal athermal part of master curve were re-analysed. Statistical analysis of same dataset may show variation in result to different degrees due to many reasons. Every specimen has its own reference transition temperature, which is decided by its unique geometry and the alignment while testing, considering all other affecting parameters such as constraint, loading rate e.t.c. The actual temperature felt by the specimen at the crack tip while testing is decided by the micro-mechanism which may change the temperature felt by specimen such as adiabatic heating at elevated loading rates, distribution of cleavage initiators and the degree of triaxiality at the crack tip.

The general effect of single and multi-temperature analyses does not show a correlation as shown in Figure 6.9 as well as in Figure 6.10. The 0.2T, 0.4T TPB and 0.4T CT dataset multi-temperature analyses results in a T_0 of -120°C . The effect of strict censoring and single temperature master curve analysis are discussed in the following section.

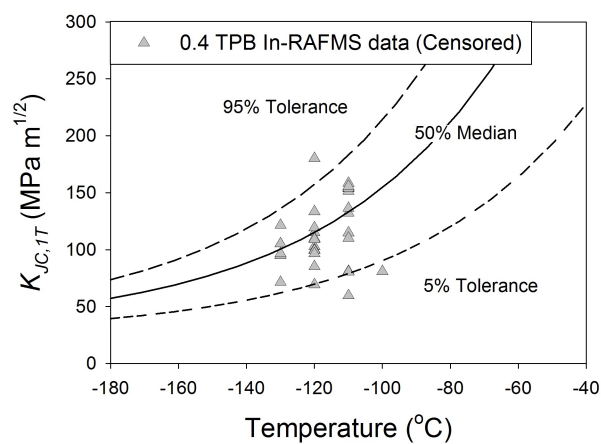
The differences in reference transition temperature T_0 obtained by performing single temperature maximum likelihood analyses are shown in Table 6.2.



(a) 0.2T TPB dataset ($T_0 = -123^\circ\text{C}$)



(b) 0.4T TPB dataset ($T_0 = -120^\circ\text{C}$)



(c) 0.4T CT dataset ($T_0 = -129^\circ\text{C}$)

FIGURE 6.8: Conventional master curve of In-RAFMS

TABLE 6.2: Single and Multi-temperature analysis of 0.4T and 0.2T SEB datasets of In-RAFMS

Specimen Geometry	Total Tests	Valid Tests	Test Temp.	MLE Method	Validity Parameter 'M'	T_0 (°C)
0.2T TPB (5×5×27)	7	7	-140	ST	30	-91
0.2T TPB (5×10×55)	7	6	-120	ST	30	-104.5
	14	10	-130	ST	30	-120
	39	26	-110,-120,-130,-140,-150	MT	30	-123.5
	14	9	-110	ST	30	-132.7
	12	12	-120	ST	30	-129.2
	7	7	-130	ST	30	-126
0.2T TPB (10×20×90)	33	26	-110,-120,-130	MT	30	-129.8
	33	26	-110,-120,-130	MT	40	-127.7
	33	21	-110,-120,-130	MT	50	-125.3
	33	19	-110,-120,-130	MT	60	-123.3
	33	17	-110,-120,-130	MT	80	-126.73
	33	16	-110,-120,-130	MT	100	-122.3

The estimated T_0 can be much away from the more reliable T_0 estimated by multi-temperature master curve on a bigger dataset. It can be higher or lower than the T_0 estimated by multi-temperature master curve and can show variation for dataset belonging to test temperature falling below actual T_0 or above it. The ASTM standard E1921 dictates the reproducibility limit to show a half standard deviation of 20° which is huge for design aspects. However, in general the difference found is not that great if the analysis contains more valid data and a large dataset of 20 or more valid data.

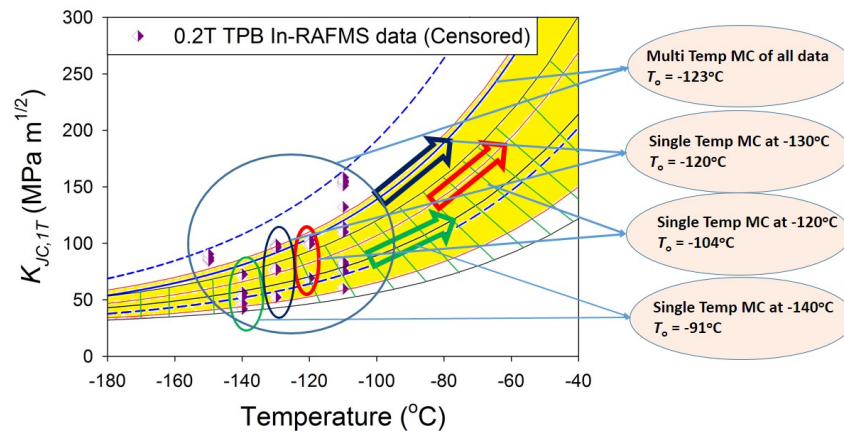


FIGURE 6.9: Effect of single and multi-temperature analyses on conventional master curve of 0.2T TPB dataset of In-RAFMS

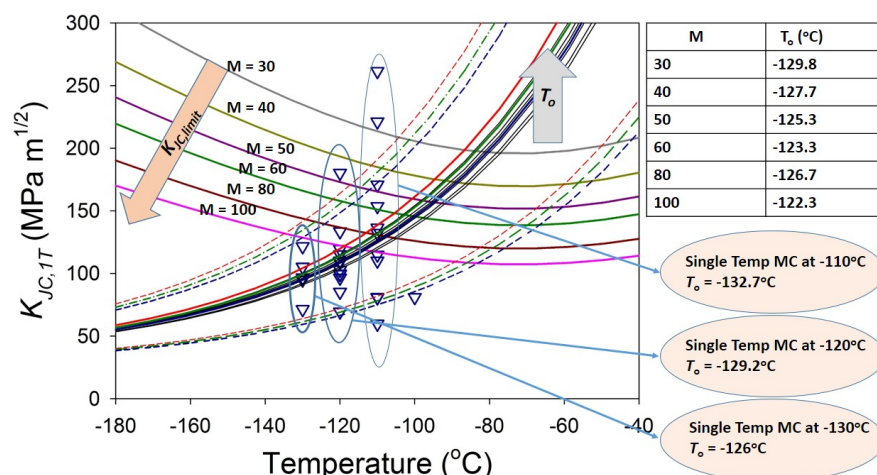


FIGURE 6.10: Effect of strict censoring on master curve of 0.4T TPB dataset of In-RAFMS

6.2.2 Strict censoring

The increment in constraint parameter which becomes a function of temperature following the dependence of Yield strength as evident from Eq.(2.13) invalidates many data points and makes the certainty of T_0 compromise on the conservative approach towards T_0 estimation.

In Figure 6.10 the dataset of 0.4T SEB specimens have been analysed with increasing M parameter starting from conventional value of 30 to a very strict value of 100. As the validity criteria gets tough the number of valid data decreases and censored values start taking over the results. However the result does not change much in the case of In-RAFMS as the number of valid data even at $M = 100$ are 16 out of 33, which is more than 50% of the data. However the drastic effect of data points getting invalidated as M increase is clear from Figure 6.10.

The method of making validity tough by increasing M parameter is one way to address the problem of non self similar stress field in small specimens. There can be various other ways to solve the problem without making experimental data invalid. Some of the methods such as side grooving the specimen, numerical correction and thickness scaling, triaxiality measurements are examined in this work which will be discussed in forthcoming chapters.

6.3 Conclusions

The tensile, impact, and fracture properties of In-RAFMS were studied in DBT region. The competing ductile and microcrack based damage is measured and fractographic examination is used for understanding the DBT region. At higher temperature the larger dimple size showed the dominance of ductile behaviour in Charpy specimens. It is noteworthy that higher temperature do promote ductile tearing however this does not mean that the cleavage failure probability decreases. The reality is actually quite contrary and results in increased probability of cleavage failure with ductile tearing. This is discussed in Chapter 11. The distribution of carbides and absence of inclusions imposes the understanding that the cracking of carbides is one of major parameters which describes the cleavage event, apart from the availability of energy/stresses for dynamic propagation/arrest of microcracks and number of carbides taking part in microcrack nucleation. The distribution of carbide is found to be homogeneous for both the steels with bigger size of carbides in P91 in comparison to In-RAFMS which results in higher DBTT for P91 as reflected in the impact toughness response depicted in Figure 6.1.

The master curve assumes homogeneous distribution of second phase particles in the matrix for assessment of fracture behaviour. An advance approach may incorporate the certainty of finding bigger inhomogeneities at the pre-austenitic grain boundaries, which can be quantified as a function of pre-austenitic grain size. However, this would complicate the simple engineering approach of master curve and maximum likelihood analysis to a great extent. Therefore, unnecessary complications are avoided by ruling out the approach to quantify distribution of carbides and a simple and effective Gaussian distribution of carbides embedded into master curve methodology is followed. Nevertheless, for a crystal plasticity based understanding of local cleavage failure probability, quantifying secondary phase distribution may be helpful.

The conventional master curve analysis resulted in a T_0 of -120°C . The T_0 obtained from differently sized and shaped specimens differed at most by 9°C , with 0.4T SE(B)

specimen to have a T_0 of -129°C . The conventional master curve analyses appear to converge for different dataset and with different levels of constrained maximum likelihood analysis for In-RAFMS.

Chapter 7

Master curve: effect of out of plane constraint loss

This chapter deals with the out of plane constraint loss assessment in small three point bend specimens. Fracture behaviour of In-RAFMS is investigated using small specimens in three point bend loading in subzero temperature range of -110°C to -150°C . The transition reference temperature, T_0 , is calculated using Master Curve approach. The small specimens resulted in a non-conservative T_0 , due to Large Scale Yielding (LSY) condition near crack tip. A numerical correction method is described in this chapter, which is used to transform LSY fracture toughness to equivalent Small Scale Yielding (SSY) value. The numerical correction method simulated using commercial FEM package is validated on two datasets, 1) given by Sokolov et.al and 2) by Euro Fracture Data. The methodology is then applied on the In-RAFMS data and used for estimation of conservative T_0 value corresponding to specimen's crack tip under SSY condition.

The results and findings presented in this chapter are published in:

Tiwari A., Avinash G., Sunil S., Singh R., Stahle P., Chattopadhyay J., Chakravartty J. (2015) Determination of reference transition temperature of in-rafms in ductile brittle transition regime using numerically corrected master curve approach. *Engineering Fracture Mechanics* 142:79-92

7.1 Introduction

The fracture behaviour of steels in transition regime shows huge scatter and master curve approach deals with this phenomenon by identifying the scatter as stochastic effect and solves it using Weakest Link Theory (Weibull, 1951). The foundation of MC methodology, which is developed largely by Wallin (Wallin, 1993, 1989a, 1999), requires small scale yielding (SSY) condition to be met by the specimen. In reality however, this condition of SSY is hardly reached for small and miniature specimens (Landes and Shaffer, 1980). Moreover, the thickness scaling method of master curve approach (also referred as size adjustment), which scales the K_{JC} to an equivalent 1T SSY condition, described in ASTM E1921 (E1921, 2013) does not completely transform the original experimental value to the equivalent SSY value of K_{JC} at 1T, This is due to the fact that the existing thickness correction of ASTM E1921 does not take care of non-SSY condition of stresses in small specimens.

Many researchers, including Wallin, such as Wallin et al. (2001); Wallin (2001); Gao and Dodds Jr (2000); Dodds Jr et al. (1991) have discovered various correction methods to resolve the problem due to out of plane constraint loss. In order to understand the cleavage phenomenon using a statistical approach, many analytical models have been proposed, such as the classic work of Landes and Shaffer (1980). Another approach to model cleavage phenomenon is established by Wallin, Saario, Törrönen, which is known as WST (Wallin et al., 1986; Wallin and Laukkanen, 2008) model. In WST approach, Griffith instability criteria is used to identify the critical cleavage initiator size as described earlier in Chapter 2 by Eq.(2.23). The implicit assumption in Eq.(2.23) is the spherical shape of crack initiator. The idea of size adjustment equation in MC methodology originates from Eq.(2.18), described in Chapter 2, where assumption of SSY condition helps to use a non-dimensional scale Q as in Eq.(2.16), and simplifies the probability of failure expression to be written in integration form as in Eq.(2.19). The use of non-dimensional parameter Q assumes the self-similarity of stress fields.

The problem in the size adjustment equation lies in the concept of volume responsible for cleavage trigger. The methodology assumes that the volume responsible for cleavage

in 3 dimension (3D) can be obtained by extruding the 2 dimensional (2D) area along the thickness, which is only realistic when the stress distribution is self-similar along the crack front. This assumption is valid for SSY condition but questionable in the case of small or miniature specimens especially for specimens to be tested in bending (Joyce and Tregoning, 2005a). The problem of transformation of a non-SSY value of K_{JC} to an equivalent SSY value is addressed in this study numerically using finite element analysis. The numerical correction is validated with the experimental data of Sokolov and Tanigawa (2007) work and a part of dataset provided in the report of Belgian Nuclear Research Centre, which is also known as Euro fracture data (Heerens and Hellmann, 2002; Lucon and Scibetta, 2011; Heerens and Hellmann, 1999). The same correction has been used in this work to find reference transition temperature for In-RAFMS.

7.2 Fracture dataset

The test and experimental details are described in Chapter 5. The dataset used for the analysis of out of plane constraint loss belongs to quasi-static 0.2T TPB dataset as described in Chapter 2. The yield strength at test temperature of -70, -80 and -110°C were linearly extrapolated. The complete tensile dataset was not generated during the assessment of constraint loss, therefore, the tensile behaviour was assumed linear and extrapolated. Though, as shown in Chapter 5 that this extrapolation does not follow the true behaviour of yield strength for In-RAFMS, the linear extrapolation remains conservative to -150°C. The temperature dependence of yield strength behaviour is shown in Figure 7.1. The tensile properties at -110°C was used as input data in finite element simulation.

Fracture toughness testing of In-RAFMS

From the Charpy impact toughness work on In-RAFMS by Laha et al. (2013), the estimated transition temperature $T_{0,est}$ was found to be -108°C obtained using 41 Joule

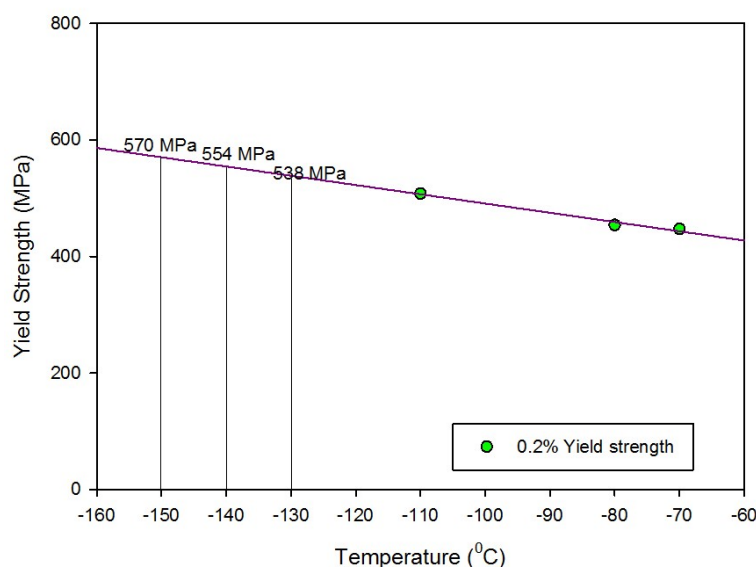


FIGURE 7.1: Extrapolated yield strengths for fracture toughness measurements in the range of test temperatures

criteria following Wallin's method (Donald E. McCabe, 2005). The fracture toughness tests, in this work, were carried out using 0.2T single edge notched bend or SE (B) type samples at temperatures of -110°C , -130°C , -140°C and -150°C at a loading rate of 0.5 mm/min on the same servo-hydraulic machine used for tensile testing, which is described in Chapter 5.

After test completion, the broken samples were examined under low magnification stereo microscope for measurement of initial crack length. The method of crack length measurement and testing scheme is described in Chapter 5. The fractographic measurement confirmed that none of the specimens had stable crack growth more than 0.05 times of the ligament. None of the tests completed failure without cleavage.

7.3 Numerical assessment of constraint loss

In Finite Element Analysis (FEA) the major aim was to find a method, which can correctly transform the experimental K_{JC} value to an equivalent SSY value. The classical model of Ritchie, Knott and Rice (RKR) (Ritchie et al., 1973) defines cleavage to occur at a characteristic length ahead of crack tip where maximum principal stress surpasses

a critical amount. This characteristic length in annular stress field is an area and in 3 dimension becomes a volume. Therefore, cleavage is said to occur if the maximum principle stress σ_1 goes beyond a critical value σ^* in a critical volume V^* . This approach of defining cleavage fracture is referred as $\sigma^* - V^*$ model. The same approach was used by [Mueller et al. \(2009\)](#) to investigate the non-SSY condition effect on sampled volume ahead of crack tip. Although V^* variation is explored by [Odette and He \(Odette and He, 2000\)](#), in this work it is assumed that V^* is independent of temperature.

The WST model is also based on extrusion of 2 dimensional area along the thickness, which is erroneous to various degrees depending on the size of the sample as the fraction of the sample thickness exhibiting SSY condition depends on its size. Therefore, to address the aforementioned issue, numerical analysis using finite element method was performed and the results were validated with the work of [Sokolov and Tanigawa \(2007\)](#) on F82H steel. Same numerical correction was also applied on a part of Euro fracture toughness dataset and the reference transition temperature, T_o , was validated against that obtained from the complete dataset.

7.3.1 Numerical correction of Sokolov's Work

[Sokolov and Tanigawa \(2007\)](#) performed tests using 1T, 0.4T and 0.16T CT samples machined from F82H steel plates. The steel plates were Electron Beam and Tungsten Inert Gas welded and further post weld heat treated. The T_o found by conventional multi-temperature MC was -105°C ([Sokolov and Tanigawa, 2007](#)). In the present work, only 0.4T CT sample data has been used for application of numerical correction, as most of the data at single temperature were available only for this geometry. Finite element analysis was performed on 0.4T CT geometry using FEM package. The specimen geometry is shown in [Figure 7.2](#).

The Sokolov's dataset for 0.4T CT geometry is reproduced in [Table 7.1](#). Experimental K_{JC} corresponding to serial no. 6 in [Table 7.1](#) was invalid due to excessive stable crack growth ($K_{JC,\Delta a}$ criteria of ASTM E1921-13a). Therefore, to find reference temperature by single temperature MC approach 1 data of size 1T (Serial No.7) was included. Data

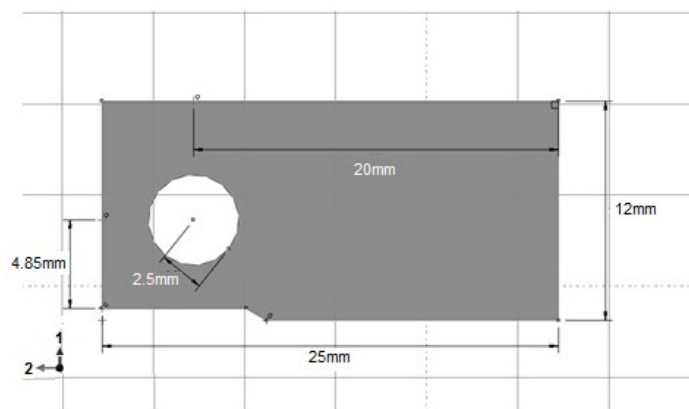


FIGURE 7.2: Dimensions of CT specimen geometry

corresponding to serial no. 6 was replaced by maximum valid fracture toughness of $173.4 \text{ MPam}^{1/2}$ from dataset of Sokolov following ASTM E1921-13a. The 1T data was assumed to be in SSY condition and was not therefore corrected numerically in this study. The transition temperature obtained by using the dataset shown in Table 7.1, by single temperature approach comes out to be -115°C .

7.3.2 Pre processing

In order to apply numerical correction, 0.4 CT geometry was modelled with isotropic incremental plasticity. Modelling of 0.4CT geometry was carried out in both 2 and 3 dimension. Only quarter of the specimen volume was modelled due to symmetry and the load was applied on the reference point RP-1 as shown in Figure 7.3.

In case of 3D modelling, due to the two-fold symmetry of the problem only a quarter ($x_1 \geq 0$, $x_2 \geq 0$) of the body was modelled with boundary condition as follows: 1. X-axis symmetry along the ligament ($u_1 = ur_2 = ur_3 = 0$) 2. Z-axis symmetry along thickness ($u_3 = ur_1 = ur_2 = 0$) where u denotes displacement and ur rotation with 1(x), 2(y) and 3(z) as Cartesian coordinate axes. The reference point as shown in Figure 7.3(a) was kinematically coupled with the pinhole surface of CT specimen. The load and displacement in mode 1 direction was extracted as reaction force and displacement at reference point RP-1. The load was multiplied by 2 in case of 3D model and displacement was multiplied by 2 to get the load displacement response of a full sample.

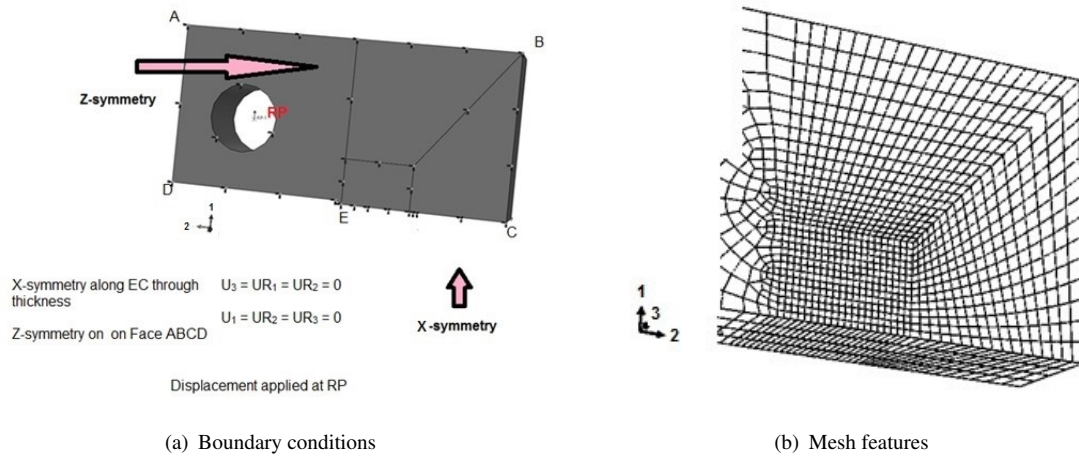


FIGURE 7.3: Boundary condition and mesh of 0.4T CT geometry of Sokolov’s work (Sokolov and Tanigawa, 2007)

In case of 2D model, the load per unit thickness was multiplied by twice of thickness of the sample and displacement was multiplied by 2. Three dimensional model was meshed with 20 noded brick elements whereas 2D was meshed with 8 noded quadrilateral plane strain elements. The computation was carried out using reduced integration full Newtonian non-linear analysis. Meshed geometry is shown in Figure 7.3(b). The element size was kept constant near crack tip to facilitate ease of V^* calculation.

7.3.3 Post processing

In order to find the volume surrounded by critical maximum principal stress, guidelines of IAEA project CRP-8 (IAEA, 2009) used for finite element round robin analyses was followed. The volume ahead of crack tip containing the region surrounded by maximum principal stress, was calculated by extracting all the nodes enduring $\sigma_1 \geq 1.7\sigma_o$ and $\epsilon_p \geq 0.001$. In case of 3D analysis the volume V^* was calculated as,

$$V_* = \frac{\text{Nodes enduring } \sigma_1 \geq 1.7\sigma_o}{\text{Nodes per unit element}} \cdot \text{Volume of an element} . \quad (7.1)$$

The critical volume calculated by Eq.(7.1) was also re-calculated by counting elements for, which the maximum principal stress at the centroid of the element endured 1.7 times of yield strength (σ_o). The numbers of elements found in this way multiplied

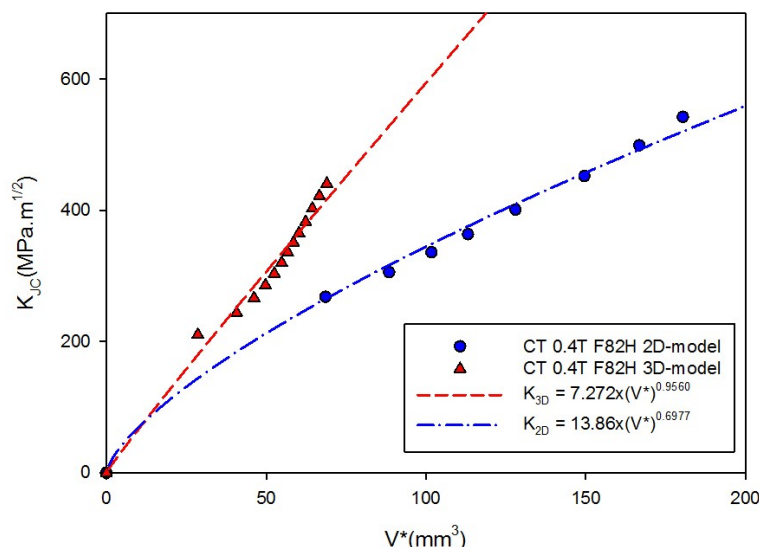


FIGURE 7.4: $K_{2D \approx SSY}$ and $K_{3D \approx non-SSY}$ obtained from FEA of Sokolov's geometry

with elemental volume resulted in values close to the result found by using Eq. (7.1). Therefore, for all further analyses Eq. (7.1) was used for V^* calculation. In case of 2D analyses, areas under critical maximum principal stress were calculated by Eq. (7.1), after replacing the elemental volume term with elemental area. After the calculation of critical area, the value was multiplied by thickness. Therefore, the volume in case of 2D was an extrusion of area along the thickness. The total volume obtained from quarter symmetric 3D model was multiplied with 4. In 2 dimensional analysis, the total volume was found by multiplying the area enduring $\sigma_1 \geq 1.7\sigma_o$ with twice the thickness. From the load displacement values extracted from 2D and 3D FEM model, K_{JC} was calculated following ASTM E1921-13a method from load and load line displacement. The K_{JC} versus Critical volume plots for 2D model and 3D model calculations is shown in Figure 7.4.

In the local approach to analyse cleavage phenomena numerically, $\sigma^* - V^*$ approach defines cleavage with bi-parametric criterion. For the same material at same temperature, attainment of equivalent amount of critical volume V^* in samples implies same probability of cleavage failure (Nevalainen and Dodds Jr, 1996). Therefore, the experimental K_{JC} obtained from the experimental load displacement response should correspond to a

3D model and whereas the 2D model K_{JC} corresponding to equally stressed volume in 3D will represent SSY equivalent value of K_{JC} .

In order to simulate the SSY condition, a boundary layer model can be solved, however the boundary layer model results are independent of loading conditions i.e. tension or bending. In specimens of any size/thickness the constraint is always highest at the centre and the specimen remains in plane stress at the surface.

The SSY condition is achieved when $T_{stress} = 0$, however, at the mid plane the T_{stress} is generally > 0 , resulting in high constraint by compressive hydrostatic stress field. Wallin (Wallin et al., 2001) has shown that, this compressive T_{stress} has insignificant effect on fracture parameters such as K_{JC} in comparison to SSY ($T_{stress} = 0$) condition. Therefore, in order to capture the effect of loading type the 2D geometry was modelled. The area confined by maximum principal stress in a 2D model when extrapolated for a thickness gives the volume under high constraint. Taking into consideration, the insignificant effect of compressive T_{stress} in comparison to SSY condition, this volume represents the equivalent SSY sampled volume.

The $\sigma^* - V^*$ plots for 2D and 3D models were fitted in two parameter power law as it is well known that the stressed volume scales with K_{JC} following power law. From these power law fitted plots the equivalent SSY K_{JC} was obtained for each experimental value. The power law fitting was chosen by taking the inspiration from the fact that the volume scales with a power of 4, which comes from the area integration along crack front. The area of stressed volume is proportional to the stressed zone radius, which scales with K^2 , K being mode 1 stress intensity factor. Therefore, area will be proportional to K^4 . The lacking information here is that K varies along the thickness on non-SSY condition due to constraint loss and therefore, K^4 relation with stressed volume in LSY condition remains questionable. After fitting the $\sigma^* - V^*$ plots the relation of equivalent SSY K_{JC} was found as,

$$K_{2d,SSY} = 13.86 \left(\frac{K_{exp}}{7.272} \right)^{0.7298} . \quad (7.2)$$

TABLE 7.1: Fracture toughness dataset obtained using 0.4T CT specimen at -100°C in Sokolov's work used for validation of numerical modelling performed in this work (σ_o at -100°C = 575 MPa)

Serial No.	K_{JC}	$K_{JC,1T}$	$K_{JC,limit}$	Sample size	Validity
1	81	68.6	214	0.4T	Valid
2	161.3	132.5	211	0.4T	Valid
3	92.9	78	218	0.4T	Valid
4	135.1	111.5	211	0.4T	Valid
5	116.8	96.9	217	0.4T	Valid
6	225.5	183.4	217	0.4T	Invalid
7	111.7	111.7	326	1T	Valid

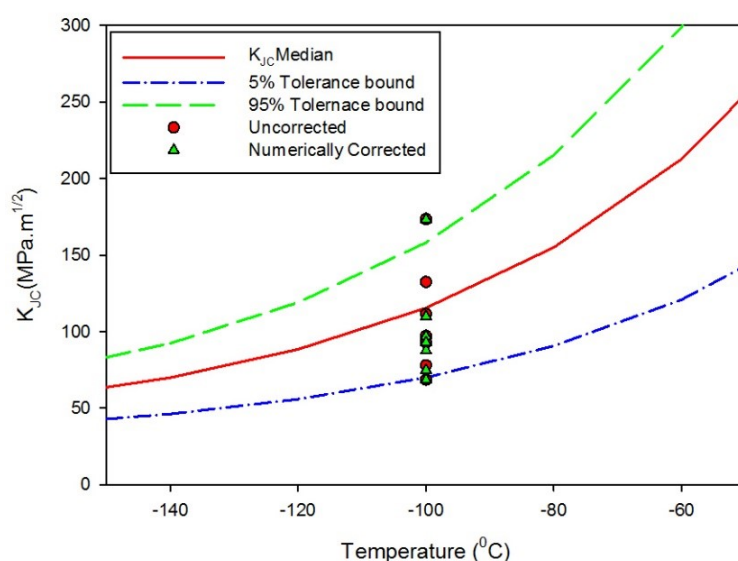


FIGURE 7.5: Comparative master curve of Sokolov's dataset

It is important to note here that the coefficient in the power law fitting of the form expressed by

$$K_{JC} = A \cdot (V^*)^C . \quad (7.3)$$

All the six data in Table 7.1 were transformed to an equivalent 2D or SSY data and used for master curve analysis by single temperature method. MC obtained by these data as received from Sokolov's work and with transformed dataset are shown in Figure 7.5.

The reference transition temperature determined in the present work by single temperature MC approach using uncorrected K_{JC} values of Sokolov's work is -115°C, whereas the same determined in the present work by single temperature MC approach using numerically corrected data yielded a T_o of -106°C, which is close to T_o of -105°C obtained

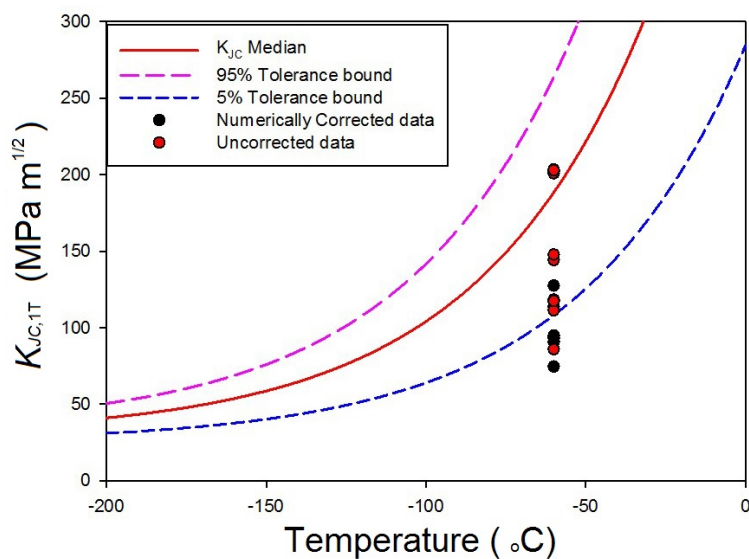
by Sokolov using multi-temperature MC approach. Noticeable observation is that major part of data is on lower side of the median curve, which is similar to the findings of Kim et al. (Kim et al., 2013) indicating inhomogeneity.

7.3.4 Numerical correction on Euro dataset

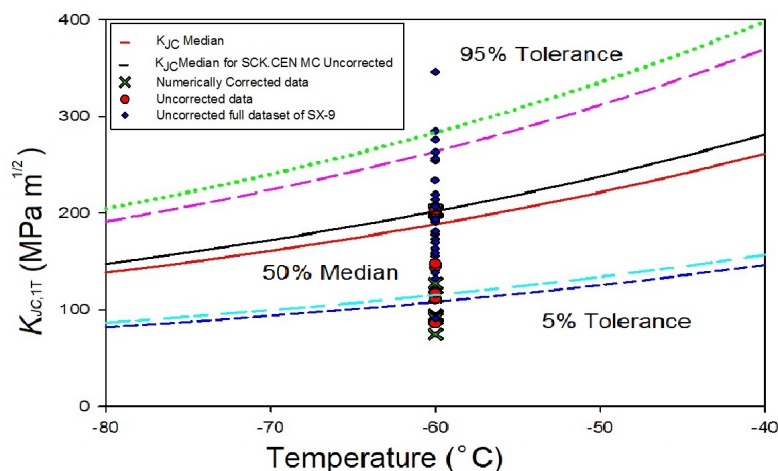
The Euro fracture toughness dataset is one of the biggest dataset ever created for fracture toughness investigation of reactor pressure vessel steel in ductile brittle transition regime. In the present work only one part of the dataset i.e. the dataset of block SX9 was used. In the documented work, the fracture toughness tests were carried out on 2T and 0.5T CT specimens at -60°C . Total number of tests were 36 out of, which 30 tests were valid according to ASTM E1921-05. The Euro dataset reports the reference temperature obtained by MC, multi-modal master curve, bi-modal master curve, Single point estimate and SINTAP lower tail method.

In order to apply numerical correction, 0.5T CT geometry was modelled in the present work in a similar way as for Sokolov's work using material properties of 22NiMoCr37 Reactor Pressure Vessel steel. The reason to model 0.5T CT geometry was that this geometry was the smallest size tested in the Euro fracture dataset. Specimen of thickness 1T or higher would probably not suffer from constraint loss in lower DBT region. The $K_{JC} - V^*$ plot obtained from the FE analysis is shown in Figure 7.6. The reference temperature obtained using 30 valid data out of 36 tests performed at -60°C reported by Belgian Nuclear Research Centre is -107°C by conventional single temperature MC, -104°C by Multi-modal MC. The Bi-modal MC approach yielded $T_{o,1}$ and $T_{o,2}$ values of -93°C and -115°C , respectively.

The master curve obtained in the present work after applying numerical correction on 12 data of 0.5T-CT samples K_{JC} values, is shown in Figure 7.6(a). The master curve obtained by SCK.CEN for SX-9 block with all 30 valid data is also shown along with numerically corrected MC in Figure 7.6 (b) for comparison.



(a) Transformed and untransformed dataset $T_0 = -104^\circ\text{C}$



(b) Transformed dataset with rest of SX9 and Euro data at single temperature

FIGURE 7.6: Comparison of master curves obtained from Euro data transformed to SSY and untransformed conditions

From Figure 7.6 (a) it seems that the numerically corrected MC does not follow the median and many data falls in 50% to 2% probability range, however in Figure 7.6 (b) it can be seen that numerically corrected MC does pass through the median. Noticeable observation is that few tests values used after numerical correction could predict a reference temperature value close to that obtained using larger dataset.

7.3.5 Numerical Correction on In-RAFMS

In order to apply the same numerical correction on experimental data obtained using 0.2T SE(B) sample geometry were modelled in both 2D and 3D with plastic behaviour of material given in form of stresses and plastic strains obtained from tensile behaviour of In-RAFMS.

Elastic modulus of In-RAFMS was obtained from tensile test at room temperature using extensometer.

7.3.6 Pre-processing

The 0.2T SE(B) geometry was modelled in ABAQUS FEM package (Hibbitt et al., 1998) similar to CT geometry models. The solutions for FE analysis was obtained by $2 \times 2 \times 2$ reduced integration. The area ahead of crack tip was refined with element volume of $0.1 \times 0.1 \times 0.2 \text{ mm}^3$ and $\frac{1}{r}$ singularity at the crack tip was imposed. In case of 2D model except the elements (8 noded quadrilateral plane strain elements) and elemental area ($0.1 \times 0.1 \text{ mm}^2$) all other parameters were kept same.

The boundary condition of application of load and extraction of load and displacement was done by following guidelines of IAEA CRP-8 (TECDOC 1631) project finite element round robin program. The boundary conditions and the mesh is shown in Figure 7.7.

7.3.7 Post Processing

In a 3D quarter symmetric model of a CT geometry, the reaction force is calculated at the reference point which is kinematically coupled with the pinhole surface. The surface is half of the full thickness and reaction force includes the effect of symmetry on the crack plane. Thus a multiplication factor of 2 to reaction force is required for load calculation. The displacement in a CT specimen model only counts for half symmetry and therefore, displacement also requires a multiplication factor of 2.

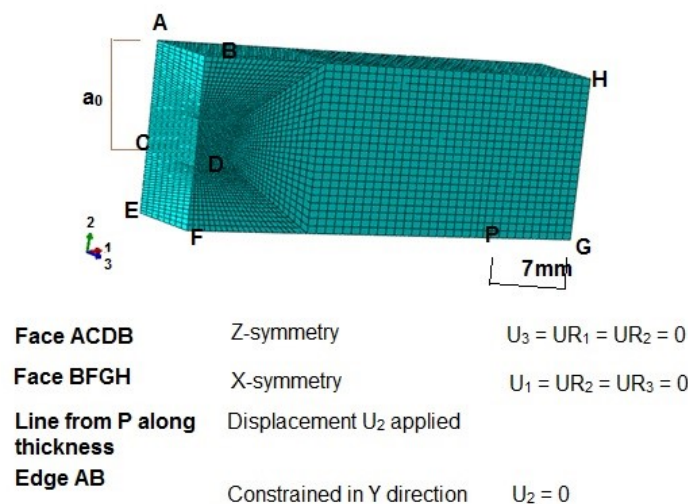


FIGURE 7.7: Boundary conditions imposed and mesh of 0.2T TPB specimen of In-RAFMS

For a TPB model, when the reaction forces are extracted at pin loading point, the quarter symmetry effect comes in. This requires a multiplication factor of 4. On the other hand, the TPB model displacement does not require any multiplication factor. This is evident as the quarter symmetric TPB model does not have any symmetric boundary condition on the constrained points (roller pin locations) in the direction of displacement.

In 3D analysis, the load was extracted on the part shown in Figure 7.7 as reaction force in Y-direction and was multiplied by 4 to get response of full geometry. In case of 2D model, the load per unit thickness was extracted and was multiplied by 2 times of thickness. This was required as the load values without assigning any plane strain thickness in ABAQUS corresponds to a unit dimension thick strip. The load for full specimen geometry thus requires a multiplication factor of $2 \times$ thickness of the specimen. The displacement would represent value for full geometry unlike CT quarter symmetric model and thus was used as extracted.

Load line displacement was obtained by subtracting the displacement data in Y direction, extracted at edge AB and line from point P in 3D model as shown in Figure 7.7(b). In 2D model the same procedure was applied at points instead of lines.

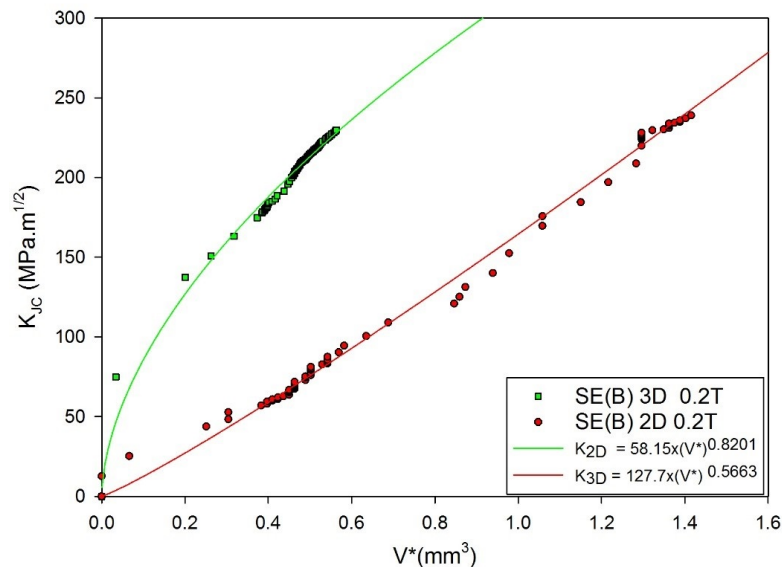


FIGURE 7.9: Active volume V^* versus K_{JC} under non-SSY condition with loss of constraint

being thickness and other in plane constraint. The V^* behaviour with K_{JC} for 0.2T SE(B) geometry shows that the difference of volume obtained from 3D and 2D model is higher than that obtained in case of CT geometry of 0.4T and 0.5T analysis. The difference is an evidence of high constraint in case of higher thickness specimens in comparison to 0.2T SE(B) samples.

Similar to the analysis performed on Sokolov's data, $K_{JC} - V^*$ plots were fitted in power law

$$K_{2d,SSY} = 58.15 \cdot \left(\frac{K_{exp}}{127.7} \right)^{1.4483}, \quad (7.4)$$

which was used to transform K_{JC} experimental to equivalent SSY values.

The reference transition temperature obtained from numerically corrected MC for In-RAFMS is -109°C . The Master Curve plot of numerically corrected data can be seen in Figure 7.10. The reference transition temperatures of Eurofer 97, F82H and Modified 9Cr-1Mo steels, which are similar to In-RAFMS in composition and heat treatment are shown in Table 7.2 for comparison. It can be realized from Table 7.2 that the numerically corrected T_o estimate of -109°C for In-RAFMS is close to the other RAFMs reference temperatures obtained by various methods of constraint correction [18, 28-30]. The uncorrected data are labelled LSY. It can be seen in Figure 7.10 that many

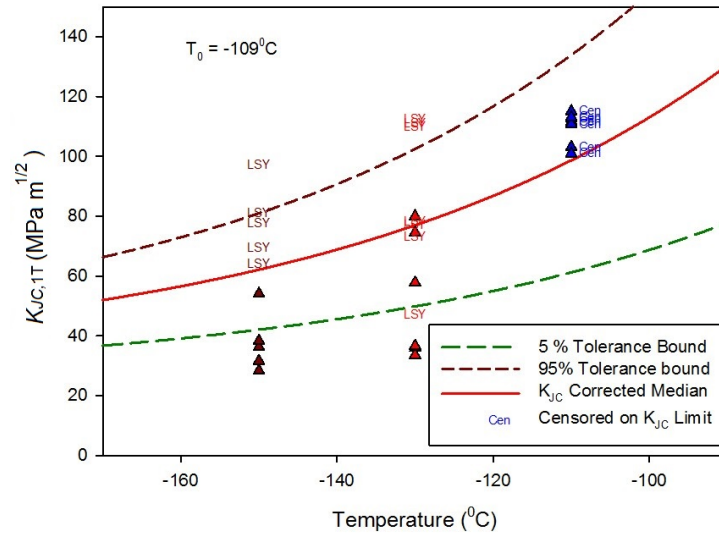


FIGURE 7.10: Master curve of In-RAFMS with untransformed and transformed datasets

of corrected data are outside the 5% tolerance bound, which was also the case with uncorrected MC shown in Figure 7.5.

TABLE 7.2: Comparison of reference transition temperatures of popular RAFM steels

Chemical composition (Wt %)									
	C	Cr	W/Mo	V	Nb/Ta	Si	Ni	Mn	
Eurofer97	0.14	8.94		1.07	0.2	0.15			
F82H Mod	0.09	8		1.88	0.19	0.02	0.11		0.16
Modified 9Cr 1Mo	0.085	9.37		0.911	0.189	0.08	0.336	0.097	
In-RAFMS	0.08	9.15		1.37	0.24	0.08	0.026	0.004	0.53
Heat Treatment									
	Austenitizing				Tempering after normalizing				
Eurofer97	980 °C for 0.5 hrs				760 °C 1.5 hrs				
F82H Mod	1040 °C for 0.67 hrs				960 °C for 0.5 hrs				
Modified 9Cr 1Mo	1050 °C for 1 hr				770 °C for 0.5 hr				
In-RAFMS	977 °C for 0.5 hr				760 °C for 1 hr				
Reference transition temperature, T _o (°C)									
	Uncorrected			SSY corrected					
Eurofer97				-77					
F82H Mod	-133 to -137			-103 to -105					
Modified 9Cr 1Mo	-67.7 to -72.4								
In-RAFMS	-123			-109					

This particular outlier behaviour has been also found with Sokolov's data analysis. The inference from this behaviour suggests that much of effect on mean value estimation comes from the censored data. Sokolov and Tanigawa (2007) solved this problem by random inhomogeneity analysis of the data. It might also occur, if a significant amount of ductile crack growth occurs during the test. Ductile crack growth (DCG) may cause the fracture toughness to increase and get censored, due to K_{Jc} limit criteria. Moreover, the numerical correction method will not be valid for DCG effect in fracture tests.

It can be concluded that uncorrected reference transition temperature of -123.5°C for In-RAFMS is applicable to miniature specimens with very small thickness whereas, reference temperature of -109°C obtained by analysing numerically corrected data resemble the behaviour of structure loaded in SSY condition.

7.5 Conclusions

The fracture behaviour of In-RAFM steel is investigated in ductile brittle transition regime using 0.2T three point bend samples. The transition temperature estimated to be -123.5°C from conventional multi-temperature master curve methodology is non-conservative.

The constraint loss at smaller dimensions invalidates the SSY assumption of MC methodology. Numerical analyses was used to obtain an equivalent SSY value. The numerical approach was validated on test data of Sokolov and Euro fracture datasets. Predicted reference temperature from multi temperature MC approach on In-RAFMS using numerically corrected MC yields a reference temperature of -109°C , which is more conservative and close to the transition temperatures obtained by applying different constraint correction methods to steels belonging to RAFMS family.

Chapter 8

Master curve: effect of in plane constraint loss

In this chapter, the fracture behaviour of In-RAFM steels is investigated with systematically varying a/W using Master Curve approach. This a/W effect is investigated using $\sigma^* - V^*$ approach by calculating the active volume at simulated crack front. The fitting parameter of $\sigma^* - V^*$ approach is compared with changing constraint parameter ΔT_{stress} .

The results and findings presented in this chapter are published in:

Tiwari, Abhishek, R. N. Singh, Per Ståhle, and J. K. Chakravarty. "A loss of constraint assessment using $\sigma^* - V^*$ approach to describe the effect of crack depth on reference transition temperature T_0 ". *Procedia Structural Integrity* 2 (2016): 690-696

8.1 Introduction

The conventional Master Curve approach, which is used to characterize the fracture behaviour of ferritic and ferritic/martensitic steels, restricts the crack depth to be in the range of $0.45 \leq a/W \leq 0.55$. The reference transition temperature is known to increase with increasing crack depth owing to increase in constraint. Despite the fact that the fracture parameters corresponding to shallower crack depth are unconventional due to its non-conservative values, in transition region a correlation to assess the shift in reference transition temperature with different crack depth is of great importance.

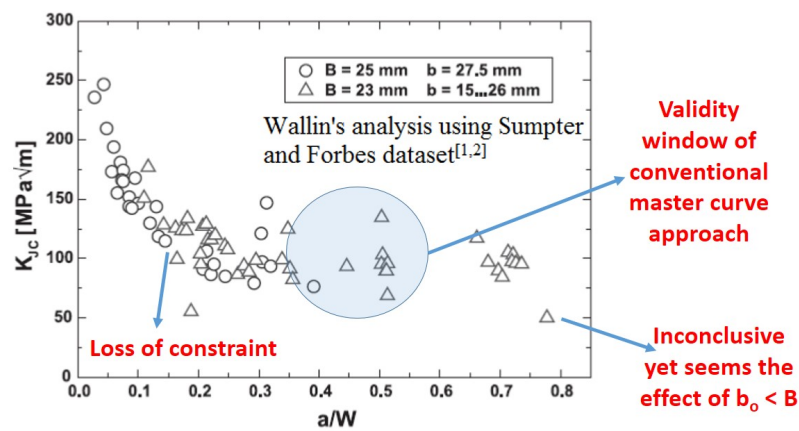


FIGURE 8.1: Experimental analyses of Sumpter showing effect of crack depth on fracture toughness

Additionally the experimental work of [Sumpter and Forbes \(1993\)](#) shows that the validity window of master curve can easily be extended to at least from $0.3 \leq a/W \leq 0.6$ as shown from Figure 8.1. It is clear from Sumpter's work that the loss of constraint dominates for $a/W \leq 0.3$ where SSY assumption is completely unreliable due to plastic hinge formation and single parameter description of crack tip stress field is impossible. However for deeper cracks there is no violation of SSY condition as long as $b_o > B$.

Therefore, to figure out whether master curve approach can be extended in the range of crack depth, the experimental as well as numerical analyses are performed on the dataset of In-RAFMS.

The fracture toughness of ferritic and ferritic/martensitic steels having BCC structure, generally shows a transition not only with temperature, but also with crack depth being tougher for shallower crack and brittle for deeper crack in DBT region. This is attributed to constraint loss for shallow cracks. In this work, the MC methodology is used to estimate reference transition temperature for different crack depths and the loss of constraint is examined numerically.

8.2 Experimental dataset

The fracture specimens pre-cracked to obtain width normalized crack length in the range of 0.2 to 0.6 were used for this analyses. The specimens after measurement of pre-crack length, were categorized according to their a/W values in ranges of $0.2-0.3\pm 0.04$, 0.4 ± 0.04 , 0.5 ± 0.04 , 0.6 ± 0.09 , as shown below. The details of the experimental methods and set-ups are described in Chapter 3.

- Group 1 (Gr-1) = 0.29-0.34
- Group 2 (Gr-2) = 0.35-0.44
- Group 3 (Gr-3) = 0.45-0.54
- Group 4 (Gr-4) = 0.55-0.69

8.3 Numerical Analysis

To understand the effect of crack depth on the volume sampled ahead of the crack tip under the maximum principal stress dominance, numerical analyses were performed on a/W of 0.3, 0.4, 0.5, 0.6 and 0.7. The geometry used for modelling was $5 \times 10 \times 55 \text{ mm}^3$ sub-size charpy specimen with $2 \times 2 \times 2$ reduced integration and incremental loading algorithm. The tensile properties were used for -110°C obtained from 4 mm diameter and 20 mm gauge length round bar tensile specimen. The quarter symmetric geometry modelled is shown in Figure 8.2.

The numerical analysis was post processed for the $\sigma^* - V^*$ approach as described in previous chapter (Chapter 4) behavior investigation. The cleavage failure is described in this approach by the volume ahead of the crack tip encompassed under maximum principal stress σ_1 higher than a threshold. The threshold value is generally taken to be twice of yield strength σ_o . The details of calculation involved in $\sigma^* - V^*$ approach can be found in earlier work by Tiwari et al. (Tiwari et al., 2015) as well as in Chapter 4.

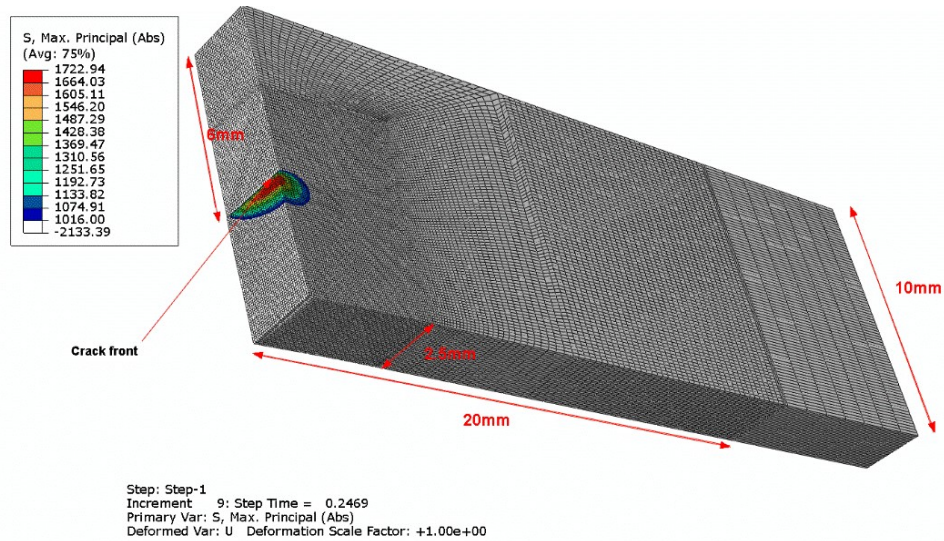
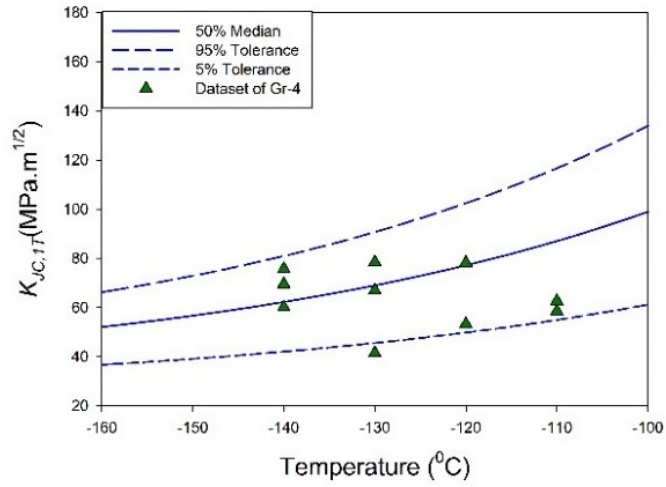


FIGURE 8.2: Quarter symmetric charpy geometry with active volume at crack front

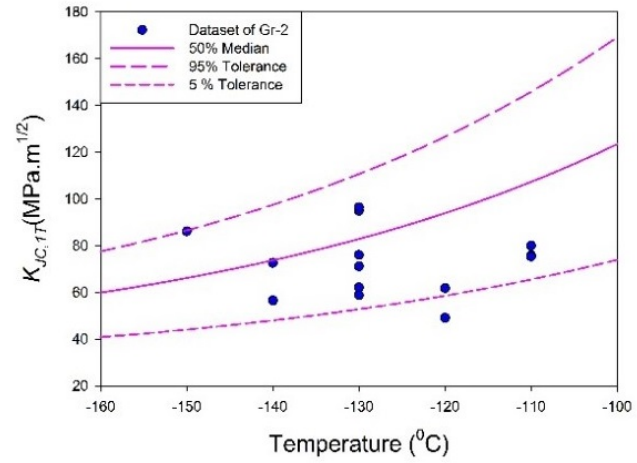
8.4 Results

The Master Curves for test data categorized in four groups are shown in Figure 8.3. The cumulative plot of median curves for all categories is shown in Figure 8.4, with respective reference transition temperatures T_0 obtained according to conventional master curve approach described by E1921 (2013). The effect of crack depth is evident from Figure 8.4 showing an increasing T_0 with increasing crack depth.

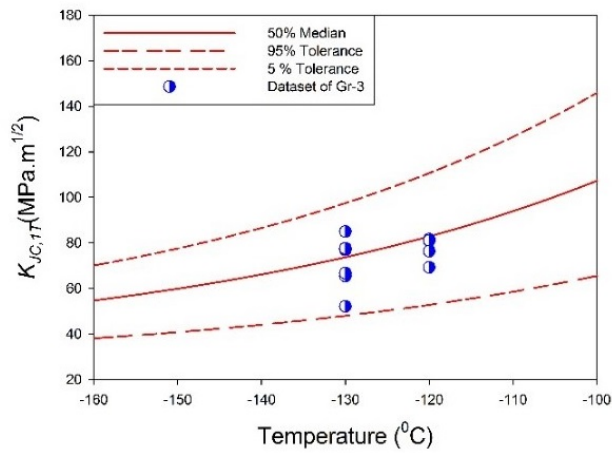
The master curve analyses of the four grouped dataset shows a systematically increasing T_0 with increasing crack depth. The increasing constraint, which causes otherwise non-critical cleavage initiators such as carbides to trigger cleavage by developing high stress field explains the result. Also the matrix helps under higher constraint by allowing micro-crack formation in the active volume ahead of crack tip.



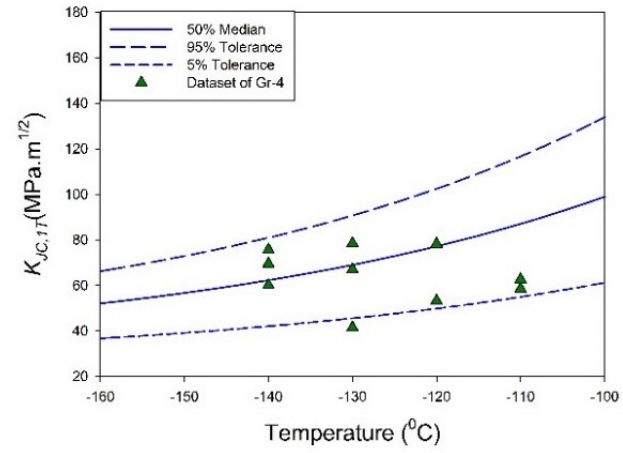
(a) Gr-1 master curve $T_0 = -125^\circ\text{C}$



(b) Gr-2 master curve $T_0 = -115^\circ\text{C}$



(c) Gr-3 master curve $T_0 = -105^\circ\text{C}$



(d) Gr-4 master curve $T_0 = -99^\circ\text{C}$

FIGURE 8.3: Master curves showing data outside tolerance bounds for shallower crack datasets and workable scatter for deeper crack datasets

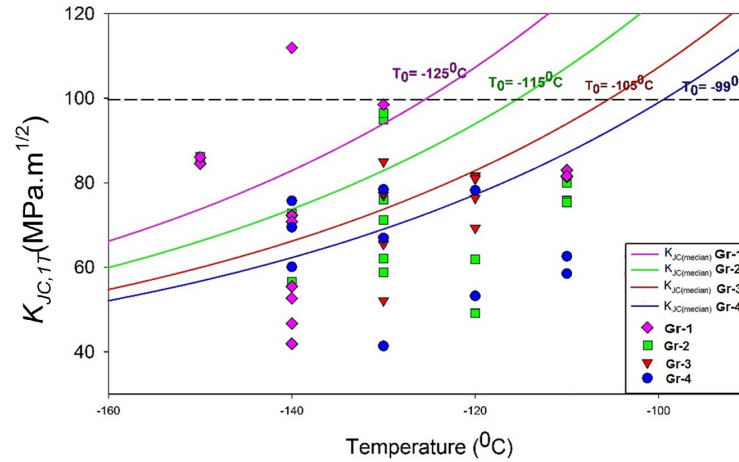


FIGURE 8.4: Shift in transition temperatures with increasing crack depth

The constraint due to changing crack depth is measured by calculating Weibull triaxiality as explained earlier. The active sampled volume is calculated for a/W ratio of 0.3, 0.4, 0.5, 0.6 and 0.7. The behaviour of active volume is plotted against K_{JC} calculated from load-load line displacement response of simulated model. The K_{JC} vs. V^* is fitted using power relation as,

$$K_{JC} = Z(V - V_o)^\beta . \quad (8.1)$$

It can be seen in Figure 8.5 that the fitting parameters of Eq.(8.1) show a systematic trend with crack depth.

8.5 Discussion

The active volume under SSY condition of stresses at crack front can be estimated as BK^4 , as discussed in Chapter 1. The active volume correlates plastic zone radius to the radius of area under maximum principal stress dominance. Under non-SSY condition where the stress field is not self-similar along the crack front the volume will not scale with BK^4 . Under the circumstances where loss of constraint occurs there can be three approaches, which can be applied to understand the generic cleavage failure probability

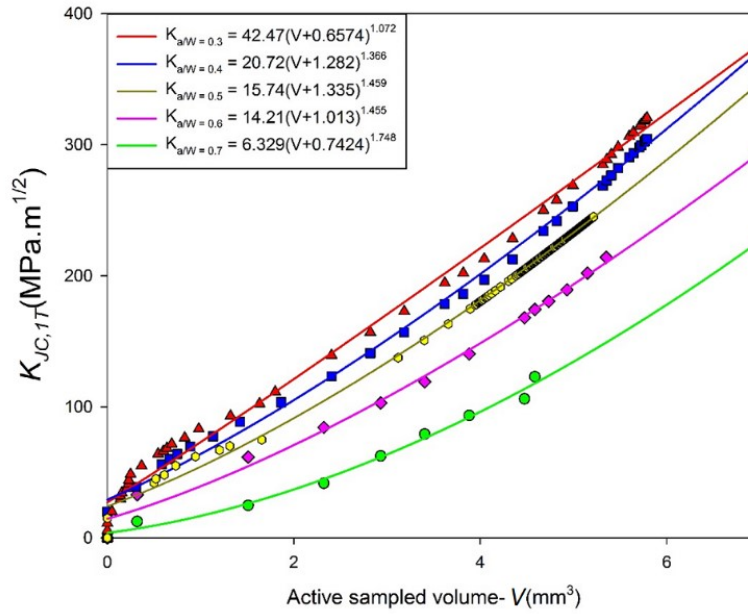


FIGURE 8.5: Curve fitting of active volume calculated according to Eq.(8.1)

as described earlier in Eq.(2.18) in Chapter 2. The three possibility which emerge for non-SSY conditions are as follows.

1. In this approach, described by [Anderson \(2005\)](#) the active volume is equated with a volume where SSY condition would exist and cleavage failure probability will scale with BK^4 . The cleavage failure probability in this case is described as,

$$P_f = 1 - \exp(-\omega \cdot B_{eff}K^4) . \quad (8.2)$$

2. In second approach which was first given by [Wang and Parks \(1992\)](#) in his doctoral thesis and was later developed by [Gao and Dodds Jr \(2000\)](#) describes the cleavage failure probability with a constraint parameter known as g -function. The cleavage failure probability in this case is described as,

$$P_f = 1 - \exp(-\omega \cdot gBK^4) . \quad (8.3)$$

3. The third approach assumes that the effect of loss of constraint results in a scaling

with volume which does not obey power 4 scaling with cleavage failure probability. The cleavage failure probability in this case is described as,

$$P_f = 1 - \exp(-\omega \cdot BK^\lambda) . \quad (8.4)$$

The third approach can be used for scaling the non-SSY conditions to SSY condition. The approach of $\sigma^* - V^*$ is basically equating the third approach with Eq.(2.27). The second approach is cumbersome due to the pre-requisite finite element analysis of modified boundary layer formulation. The detailed calculation of second approach is used in calibration of Weibull slope in Chapter 10. The first approach is also comparatively easier in comparison to second approach in calculation. However, in this work, third approach is used due to its applicability in transformation of non-SSY fracture toughness to SSY condition in both out of plane and in plane cases of constraint loss.

It is also assumed that the same deformed volume for any two condition would result in same probability of cleavage failure. This assumption gives a benefit of transforming the non-SSY condition to SSY condition as described in Chapter 7.

By equalizing the sampled active volume for two different crack depth specimens, namely A and B , the transformation of $K_{JC,B}$ to $K_{JC,A}$ can be expressed as,

$$K_{JC,A} = Z[(V_{o,B} - V_{o,A}) + (\frac{K_{JC,B}}{Z_B})^{1/\beta_B}]^{\beta_A} . \quad (8.5)$$

Using Eq. (8.5), the transformed data at $0.5 a/W$ were analyzed using MC method which is shown in Figure 8.6.

The Master curve plot with different a/W shows the expected effect on reference transition temperature. The shift in temperature with a/W increment is shown in Figure 8.4. The $K_{JC,median}$ calculated at -110°C and the standard deviation of the Weibull fit calculated using ASTM E1921-14a is shown in Table 8.1.

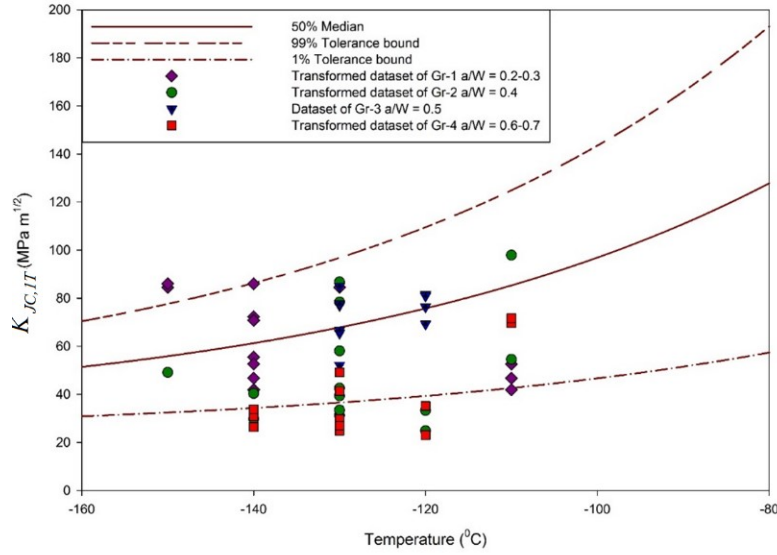


FIGURE 8.6: Master curve plot of all K_{JC} transformed to $a/W = 0.5$

The standard deviation of fitted Weibull distribution in master curve approach is described in ASTM E1921 as,

$$\sigma_{d,1} = 0.28K_{JC,med} \left(1 - \frac{20}{K_{JC,med}}\right). \quad (8.6)$$

The standard deviation of estimation of T_0 , is described in ASTM E1921 as,

$$\sigma_{d,2} = \sqrt{\frac{\beta^2}{r} + \sigma_{exp}^2}, \quad (8.7)$$

where β is the sample size uncertainty factor which is obtained from ASTM E1921-13a section (10). r is the number of valid tests, and σ_{exp} is taken as 4°C as recommended in ASTM E1921-13a. For β factor to be obtained, an equivalent fracture toughness $K_{JC,med}^{Eq}$ is calculated as,

$$K_{JC,med}^{Eq} = \frac{1}{r} \sum_{i=1}^r 30 + 70 \exp\{0.019(T_i - T_0)\}, \quad (8.8)$$

where T_0 is the test temperature of individual tests.

The shift in transition temperature T_0 was found to be increasing by 10°C with increment in a/W . This however may change as the increment value depends on number of

TABLE 8.1: Statistical details of MC analysis of grouped datasets

	Total no. of tests	r Valid tests	K_{JC}^{Eq} (MPa m ^{1/2}) (Eq.(8.8))	T_o (°C)	$\sigma_{d,1}$ (Eq.(8.6))	$\sigma_{d,2}$ (Eq.(8.7))
Gr-1	15	9	80.62	-125	28.86	43.27
Gr-2	15	9	81.22	-115	24.35	43.27
Gr-3	12	8	75.8	-105	20.62	48.18
Gr-4	12	8	67.33	-99	18.7	48.18

data used for analysis and also on the number of censored data.

The numerical analysis of 0.2T geometry for different crack depths were fitted according to Eq.(8.1) and shown in Figure 8.5. The coefficient Z and the degree β of Eq.(8.1) shows a trend with changing crack depth. As discussed earlier the power 4 scaling of K_{JC} with active volume V , is not followed under LSY conditions. The fitting parameters Z and β are plotted with increasing a/W in Figure 8.7. Unlike the constant increment in T_o found experimentally these parameters show a transition from shallow to deep crack with a minimum slope in the a/W range of 0.4 to 0.6.

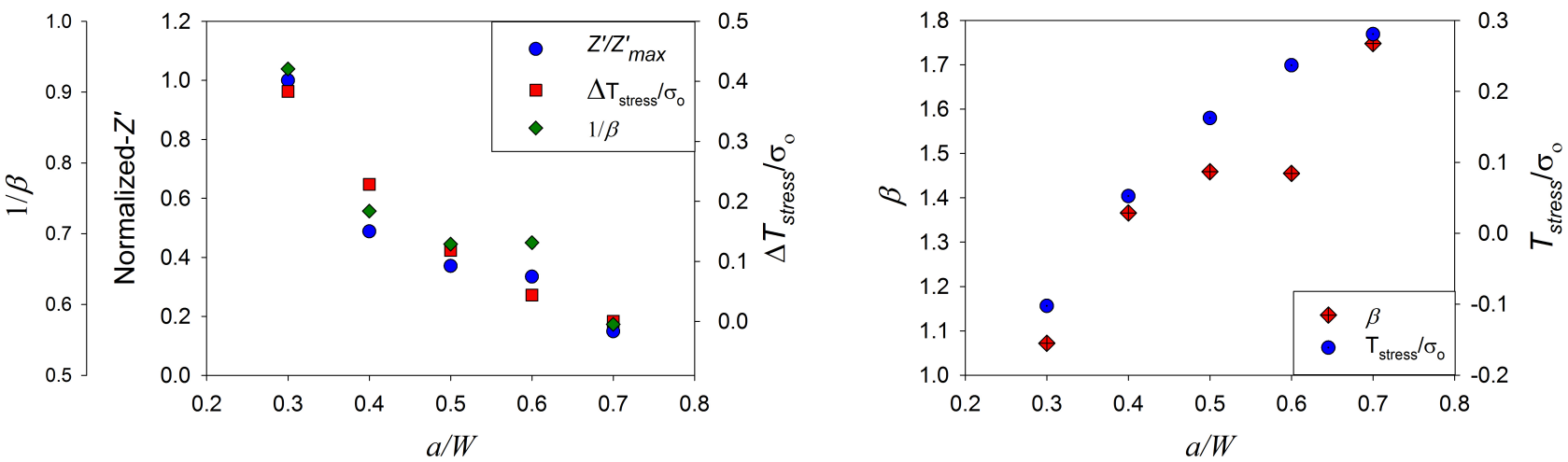


FIGURE 8.7: Correlation of fitting parameters of Eq.(8.1) with (a) change in constraint parameter ΔT_{stress} and (b) T_{stress} with a/W

To understand whether these parameters have ability to quantify constraint, standard constraint parameter T_{stress} was calculated using the fifth degree polynomial used by Wallin (Wallin et al., 2001) for bend geometry as

$$\frac{T_{stress,TPB}}{\sigma_o} = -1.13 + 5.96\left(\frac{a}{W}\right) + 12.68\left(\frac{a}{W}\right)^2 + 18.31\left(\frac{a}{W}\right)^3 + 15.7\left(\frac{a}{W}\right)^4 + 5.6\left(\frac{a}{W}\right)^5 . \quad (8.9)$$

The difference in normalized T_{stress} with a/W is also calculated as

$$\frac{\Delta T_{stress,TPB}}{\sigma_o} = 5.96\left(\frac{\Delta a}{W}\right) + 12.68\left(\frac{\Delta a^2 + 2a_o\Delta a}{W^2}\right) + 18.31\left(\frac{\Delta a^3 + 3a_o^2\Delta a + 3a_o\Delta a^2}{W^3}\right) . \quad (8.10)$$

where a_o is the crack length for 0.5 a/W if the normalized ΔT_{stress} is being calculated for a/W of 0.6 a/W . The difference $\Delta \frac{a}{W}$ is 0.1 for the calculation in this case.

The plot of normalized T_{stress} and ΔT_{stress} is shown in Figure 8.7 in comparison with fitting parameters. It is evident from the figure that the fitting parameter Z shows a one to one correlation with normalized ΔT_{stress} . However, fitting parameter β shows although an increasing trend as shown by normalized T_{stress} but the differs in slope with normalized T_{stress} as shown in Figure 8.7 (b). Reciprocal of β shows a unique correlation with normalized ΔT_{stress} as shown in Figure 8.7 (a). On the other hand, β shows a cubic polynomial behaviour, whereas, normalized T_{stress} shows a parabolic trend in Figure 8.7 (b). The behaviour of $1/\beta$ as well as Z varies in correspondence to normalized ΔT_{stress} , uniquely. From this it becomes evident that the fitting parameters of $\sigma^* - V^*$ have the potential to be used as a constraint measurement parameter.

By equalizing the sampled active volume for two different crack depth specimens, namely A and B , the transformation of $K_{JC,B}$ to $K_{JC,A}$ can be expressed as,

$$K_{JC,A} = Z'[(V_{o,B} - V_{o,A}) + \left(\frac{K_{JC,B}}{Z'_B}\right)^{1/\beta_B}]^{\beta_A} . \quad (8.11)$$

8.6 Conclusions

Master curve fracture toughness analysis was carried out on 0.2T specimen in the range of 0.2 to 0.7 a/W . The dataset were categorized based on a/W and analysed for reference transition temperature determination. The T_0 was found to be increasing for higher a/W . The numerical analysis showed that under non-SSY stress field condition for both constraint loss and high constraint specimens the active volume scaling with K_{JC} changes drastically and cannot be analysed using conventional master curve method. On the other hand in the range of $0.37 \leq a/W \leq 0.7$, the data can be analysed using master curve by transforming the dataset to a single a/W scale. The numerical analysis of active volume ahead of crack front showed a good correlation with change in T_{stress} . The fitting parameters Z' was found to follow one on one correlation with ΔT_{stress} and therefore this parameter can be used as a measure of constraint for cleavage fracture.

Chapter 9

Master curve: effect of specimen geometry (CT and SE(B))

The fracture behaviour of steels are generally studied by testing Compact Tension (CT) and Single Edge cracked Bend (SE(B)) specimens. The CT specimen data results in a conservative reference transition temperature. On the other hand, small SE(B) specimens are of great importance for irradiation studies. However, these small SE(B) specimens suffer from greater loss of constraint in comparison to CT geometry. In this chapter, CT and SE(B) specimens response in DBT region are studied using Master Curve method and loss of constraint between CT and SE(B) specimens is examined by a novel constraint parameter, Weibull Triaxiality (q_W). q_W is developed as a micro-mechanical tool to understand the distribution of the ratio of hydrostatic stress (σ_h) and equivalent stress (σ_{eq}) components, in the volume directly influencing the cleavage phenomena. The q_W parameter is used to modify Beremin's model. The cleavage failure probability predicted using modified Beremin's model shows better accuracy when compared to experimental results. Also master curve results are examined for two grades of ferritic/martensitic steels namely, Mod-9Cr-1Mo and Indian Reduced Activation Ferritic/Martensitic Steel (In-RAFMS).

9.1 Introduction

In DBT region, a single specimen can show all the features of ductile to brittle transition, starting with blunting of the tip to ductile tearing which accelerates the crack propagation and increases the triaxiality, which later causes the specimen to fail in cleavage fashion (Knott, 1995). The scatter in the fracture toughness behaviour in the region of DBT for general purpose conventional BCC steels can be attributed to following parameters.

1. Experimental errors
2. Constraint loss and distribution of cleavage initiators
3. Ductile tearing
4. Thickness/size of the sample

The constraint level describing the intensity of stress field at the crack tip differs for different geometries used for fracture toughness measurement. There have been studies on fracture toughness with many geometries of specimens, such as Single Edge Notched in Tension (SENT) and in Bending (SENB or SE(B)), Double Edge Notched Tension (DENT), Centre Cracked specimen (MT) and Compact Tension (CT) specimens. The most commonly used specimens out of the aforementioned are SE(B) and CT. The fracture toughness measurement standards for general testing (E1820) and testing in DBT regions using master curve approach (E1921, 2013) focus on SENB and CT specimens with or without side grooving. CT specimens in a context of fracture testing at sub-zero temperatures for fracture assessment shows less scatter of fracture data in comparison to the specimens tested in bending. The specimens in bending are rectangular bar geometries with fracture specimen's width to thickness ratio (W/B) = 1 or 2. These specimens can have misalignment issues while testing in the plane normal to the crack path as well as along the load axis, whereas in CT specimens the alignment is assured by the test fixtures. The alignment issues can be resolved by fixture modifications, but even so, it remains difficult to use miniature specimens and therefore the usage imposes challenges towards the reproducibility of the fracture parameters. The fatigue pre-cracking prior to fracture testing also plays an important role in deciding the stress profile near the crack

tip. Any misalignment of the pre-crack not visible from surface will also contribute to the scatter.

Apart from the type of loading and geometry, the assessment of fracture toughness based on load Crack Mouth Opening Displacement (CMOD) or on load-Load Line Displacement (LLD) also causes scatter (Nevalainen and Dodds Jr, 1996) to the order of 20-25% for fracture toughness measured using LLD. The most important parameter to model scatter in cleavage fracture in DBT regime is the distribution of cleavage initiators. The spatial distribution of the cleavage initiators vary depending on the size of precipitates, phase distribution, number of phases present in the microstructure and grain size. In general purpose conventional ferritic steels, the cleavage initiates from secondary phase particles due to their bigger size and stress raising shapes unless the shapes are modified by metal working. In steels, the cleavage is caused by microcracks originating from carbides. In general, any second phase having different plasticity may lead to micro-crack generation and further to cleavage if the micro-crack is generated before the peak stress is reached making the dynamic propagation possible for the micro-crack from the secondary phase to the grain and beyond (Neville, 1988; Nevalainen and Dodds Jr, 1996).

In cleavage fracture the effect of size is prominent as assessed in the pioneer work of Landes and Shaffer (Landes and Shaffer, 1980). The thickness of test specimens affect the fracture toughness first by increasing the constraint and secondly by increasing the probability of initiation of catastrophic failure. The reason for the latter is the increased number of cleavage initiators that fall in the active volume of maximum principal stress exceeding the threshold for cleavage fracture (Ritchie et al., 1973). The active volume in case of cleavage fracture phenomena is referred to the volume ahead of crack tip under the maximum principal stress (σ_1) larger than a threshold value of (σ_1) which is defined in proportion to yield strength (σ_o) (Bonadé et al., 2008).

The objective of this part of the work is to experimentally investigate the DBT region fracture behaviour of In-RAFMS and P91 steels using CT and TPB specimens. The difference of constraint is studied using Beremin's model and a novel method or

Weibull Triaxiality, q_w , is developed to correct the numerical predictions obtained using Beremin's model.

9.2 Material and Experimental Details

The fracture behaviour of ferritic/martensitic steels of two different grades namely, Mod-9Cr-1Mo and Indian Reduced Activation Ferritic/Martensitic Steels (In-RAFMS) are investigated in DBT region using both CT and SENB geometries.

The details of the material differences and similarities of the two grades are described in Chapter 4. As the master curve approach sets its reference thickness at 1 inch i.e. 1T, the testing on P91 steel was carried out on 1T CT specimens with 10% side grooves. For TPB, the tests were performed on widely used specimen geometry of full sized standard charpy. Due to the scarcity of the RAFM grade steel, the fracture testing on In-RAFMS was carried out on $55 \times 10 \times 5$ mm³ sub-size charpy geometry and 0.4T-CT specimens with $W/B = 2.5$. The CT specimens were side-grooved unlike Pre-cracked V notch sub-size Charpy (PCVN) specimens. The tests were conducted in accordance with ASTM E1921-13a, in DBT region for both the steels. The details of the experiments are discussed in Chapter 4 and the specimen geometries used for experimental and numerical analyses are detailed in Appendix-C.

9.3 Cleavage failure probability, Weibull Triaxiality

The approach used generally for understanding the cleavage failure mechanism numerically in DBT region started with the pioneer study of Beremin's group ([Beremin et al., 1983b](#)). The detailed method of cleavage fracture prediction based on Beremin's model is described in Chapter 10. The cleavage failure probability based on Weibull stress is described as

$$P_f = 1 - \exp\left[-\left(\frac{\sigma_w}{\sigma_u}\right)^m\right], \quad (9.1)$$

where P_f is the numerical probability of cleavage failure, σ_u is the scaling parameter and m is the Weibull slope. For a Griffith crack, in a crack tip volume actively taking part in cleavage phenomena (Active Volume), the probability, P to find a micro-crack of size in the range of l_o to $l_o + dl_o$ in a small fraction of active volume, V_S can be described as,

$$P = \int_{l_o}^{\infty} P(l_o) dl_o = \left(\frac{\sigma_1}{\sigma_U} \right)^m, \quad (9.2)$$

where σ_U is a constant and σ_1 is maximum principal stress. Using Eq. (9.2), the cumulative probability of cleavage fracture of active volume can be described by integrating P for all V_S in active volume V as,

$$P_f = 1 - \exp\left[-\frac{1}{V_o} \int_V \left(\frac{\sigma_1}{\sigma_U} \right)^m\right], \quad (9.3)$$

where the integration is defined in a volume which is dominated by maximum principal stress surpassing a threshold value. The general trend is to define the boundary of the active volume where σ_1 is twice of σ_o . Defining Weibull stress, σ_W , as

$$\sigma_W = \left[\frac{1}{V_o} \int_{V^*} \sigma_1^m dV \right]^{1/m}, \quad (9.4)$$

where V_o is the reference volume not too big to have significant stress gradient nor too small to violate the characteristic length of RKR model (Ritchie et al., 1973) which is a few grains. Maximum principal stress, σ_1 , is integrated in the volume V^* . The volume V^* is described to be the volume for which $\sigma_1 > \lambda \sigma_o$, where σ_o is the yield strength of the material. Generally the value of λ is taken as 2 (Petti and Dodds Jr, 2005; Gao and Dodds Jr, 2005a; Wasiluk et al., 2006).

For the importance of reference volume, V_o , it is reviewed by Dowling and Lidbury (2000) that relatively larger elements in finite element analyses gives accurate results for Weibull stress calculations and it is not obligatory to refine mesh in order to have single element size equal to be in exact correspondance to V_o . Dowling and Lidbury (2000) showed, by studying the element size equal to V_o (which was of dimension 50

μm) and greater, that the important aspect was to capture the stress strain field at the crack tip accurately.

The relation of σ_W with fracture parameter J or K for self similar stress field at the crack tip is described by [Beremin et al. \(1983b\)](#); [Wasiluk et al. \(2006\)](#) as,

$$\sigma_W^m = \zeta B J^2 = \bar{\zeta} B K^4, \quad (9.5)$$

where $\bar{\zeta} = \zeta \left[\frac{(1-\nu^2)}{E} \right]^2$, varies with change in temperature and flow properties. Using Eq.(9.5), the cleavage failure probability in three parameter Weibull distribution is described as,

$$P_f = 1 - \exp\left[-\left(\frac{\sigma_W^{m/4} - \sigma_{W-min}^{m/4}}{\sigma_U^{m/4} - \sigma_{W-min}^{m/4}}\right)^4\right], \quad (9.6)$$

which is obtained by finding a corresponding Weibull stress to the fracture parameter K_{JC} used in the description of master curve approach according to Eq.(2.7). The threshold of cleavage initiation, σ_{W-min} corresponds to K_{min} and σ_U corresponds to K_0 .

For the numerical prediction of cleavage failure probability, it is a pre-requisite to calibrate the Weibull slope m . The scaling parameter σ_U is then the σ_W corresponding to K_0 . The history of Weibull stress based cleavage failure probability starts as discussed earlier with the work of Beremin's group ([Beremin et al., 1983b](#)), which was then a two parameter Weibull analysis. The calibration procedure for two parameter as well as three parameter Weibull cleavage failure probability was developed mostly by [Gao and Dodds Jr \(2005a\)](#), [Petti and Dodds Jr \(2005\)](#), [Wasiluk et al. \(2006\)](#) and [Ruggieri et al. \(1998\)](#). The approach in these works brought cleavage failure probability very close to the master curve methodology. In other words, the stress based cleavage failure probability was coupled with master curve methodology, especially with three parameter Weibull probability distribution function as described in Eq. (9.6). Simultaneous efforts were also made to introduce plastic strain factor in the cleavage failure probability. The plastic strain correction and evolution of Weibull stress based cleavage failure probability is recently reviewed in the work of [Ruggieri and Dodds Jr \(2015\)](#).

The calibration procedure following the procedure suggested by Wasiluk et al. (2006) which is similar to one used by Gao et al. (2006) is detailed in Chapter 10.

9.3.1 Weibull Triaxiality

For the described method of cleavage probability distribution estimation above, the Beremin's model has an implicit assumption to arrive at Eq.(9.2) to Eq.(9.3). The assumption which is crucial for Beremin's model formulation is that all the Reference Volume Elements (RVEs) for which the probability of failure is described by Eq.(9.2), should have the same stress levels. The Beremin's model therefore, is correct for a self-similar stress field. However, the case deviating from SSY condition needs a correction in the Beremin's formulation. This issue is addressed by assigning the ratio of triaxiality at the RVE, q_{RVE} , under consideration to the triaxiality level which is achieved at the centre or mid plane of the specimen geometry, q_{mid} as a weight factor to the probabilities of RVEs i.e. P of Eq.(9.2).

With above description where q is the triaxiality factor defined as the ratio of hydrostatic, σ_H , and equivalent σ_{eq} , stress components, Eq.(9.5) is re-written for modified Weibull stress σ_{Wm} as,

$$\sigma_{Wm}^m = \frac{1}{NV_o} \sum_{i=1}^N \sigma_{1,i}^m V_i \frac{q_{RVE}}{q_{mid}}, \quad (9.7)$$

where, there are N RVEs in the active volume V^* , each corresponding to a volume of V_i . The division by N is to make the quantity independent of finite number of RVEs involved in a Finite Element (FE) post processing calculation. Using Eq.(9.4) the σ_{Wm} can be expressed as,

$$\sigma_{Wm} = \sigma_W \left\{ \frac{1}{N} \sum_{i=1}^N \frac{q_{RVE}}{q_{mid}} \right\}^{1/m}. \quad (9.8)$$

The extra terms in Eq.(9.8) is defined as Weibull Triaxiality and denoted as q_W as,

$$q_W = \left\{ \frac{1}{N} \sum_{i=1}^N \frac{q_{RVE}}{q_{mid}} \right\}^{1/m}. \quad (9.9)$$

This new parameter is a measurement of deviation of self-similarity in a specimen geometry and therefore, it also measures the constraint in a geometry with a reference

frame set at SSY condition. The reference point is SSY condition as for a self-similar stress field the q_W is always 1. Therefore, q_W calculation avoids the modified boundary layer modelling for assessments of constraint deviation.

Due to the modifications described here, the probability of cleavage failure can be re-defined as,

$$P_f = 1 - \exp\left[-\left(\frac{\sigma_{Wm}^{m/4} - \sigma_{Wm-min}^{m/4}}{\sigma_{Um}^{m/4} - \sigma_{Wm-min}^{m/4}}\right)^4\right], \quad (9.10)$$

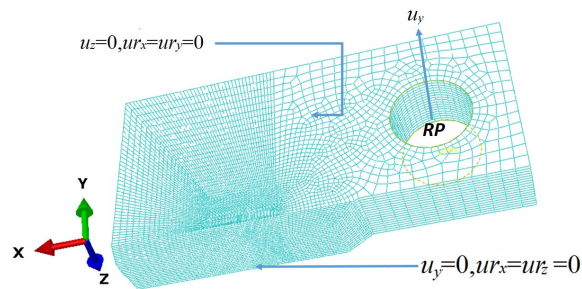
where σ_{Wm-min} and σ_{Um} are the minimum modified Weibull stress and modified scaling parameter. The values of σ_{Wm-min} and σ_{Um} are obtained from the history of $\sigma_{Wm} - K_{JC}$.

9.4 Finite element analysis

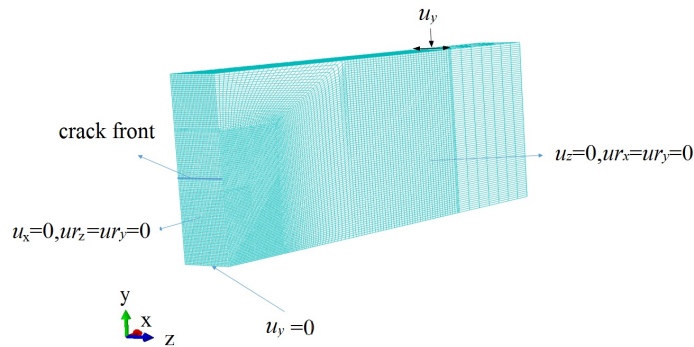
The test geometries of $5 \times 10 \times 55 \text{ mm}^3$ SE(B) specimen was modelled in three dimension with 31 layers of elements of uniform meshing along thickness. The CT geometry of $W = 25$ and $B = 10$ mm was modelled with 10% side grooved quarter symmetric geometry. The mesh of both CT side grooved and SE(B) geometries are shown in Figure 9.1(a) and 9.1(b), respectively. The mesh in these geometries at the crack tip were kept constant in size for the volume calculation in post processing.

In Figure 9.1 ur_i refers to the rotation along the axis defined by i direction. The method of Weibull Triaxiality is applied in this work to the tested geometries. The Weibull slope calibration mentioned in detail in section 10.1.3 used the high constraint and low constraint datasets for minimizing the differences between SSY, high constraint and low constraint datasets (Wasiluk et al., 2006). The Weibull slope obtained using the method of Wasiluk et al. (2006) for In-RAFMS and P91 were found to be 9 and 15, respectively.

The Weibull Triaxiality was checked for its dependency on number of elements involved in the calculation. The sensitivity analysis showed accurate results for more than 800 elements in the active volume.



(a) 0.4 T CT side grooved geometry mesh



(b) 0.2T TPB geometry mesh

FIGURE 9.1: Mesh of (a) side grooved 0.4T-CT specimen (RP represents a Reference Point which is kinematically coupled with the pin hole surface) and (b) 0.2T SE(B) specimen

9.5 Results

The charpy results, as shown in Figure 6.6 in Chapter 6, were used to estimate the T_0 according to the criteria suggested by [Donald E. McCabe \(2005\)](#). The estimated T_0 was found to be -130°C for In-RAFMS and -110°C for P91. The fracture tests for In-RAFMS were performed at -110°C , -120°C , -130°C , -140°C and -150°C , whereas P91 was tested at -60°C , -70°C , -100°C and -110°C . The 1T-CT specimens of P91 steel were tested at higher (-60°C and -70°C) temperatures due to the expected high constraint, whereas the SE(B) specimens of P91 were tested at relatively lower (-100°C and -110°C) temperatures.

The Master Curves of 0.4T-CT side grooved specimens and 0.2T SE(B) specimens of In-RAFMS are shown in Figures 9.2(a) and 9.2(b) with the scatter shown for both datasets for comparison. The T_0 for 0.4T-CT dataset and 0.2T TPB dataset were found

to be -120°C and -123°C . Similarly the Master Curves for P91 steel 1T-CT side grooved specimens giving a T_0 of -103°C and 0.4T-standard charpy specimen resulting in T_0 of -132°C , are shown in Figures 9.2(c) and 9.2(d). In Figures 9.2(c) and 9.2(d), for the comparison, alternate geometry dataset is also shown.

Apart from aforementioned test conditions a dataset of fracture tests following ASTM E1921 which was used as low constraint condition for Weibull slope calibration is also included in this work for the assessment of constraint loss and for comparison with experimental behaviour at test temperature of -110°C . As the 1T CT dataset of P91 is tested at -60°C and -70°C , it cannot be compared with 10×10 SE(B) dataset which is obtained at -110°C . This dataset which was created on specimens of 4 mm thickness and other dimensions of 1T CT could not be used for T_0 estimation due to less numbers of valid data, nevertheless, it is used for the rank probability calculation and comparison with the numerical predictions based on Beremin's model.

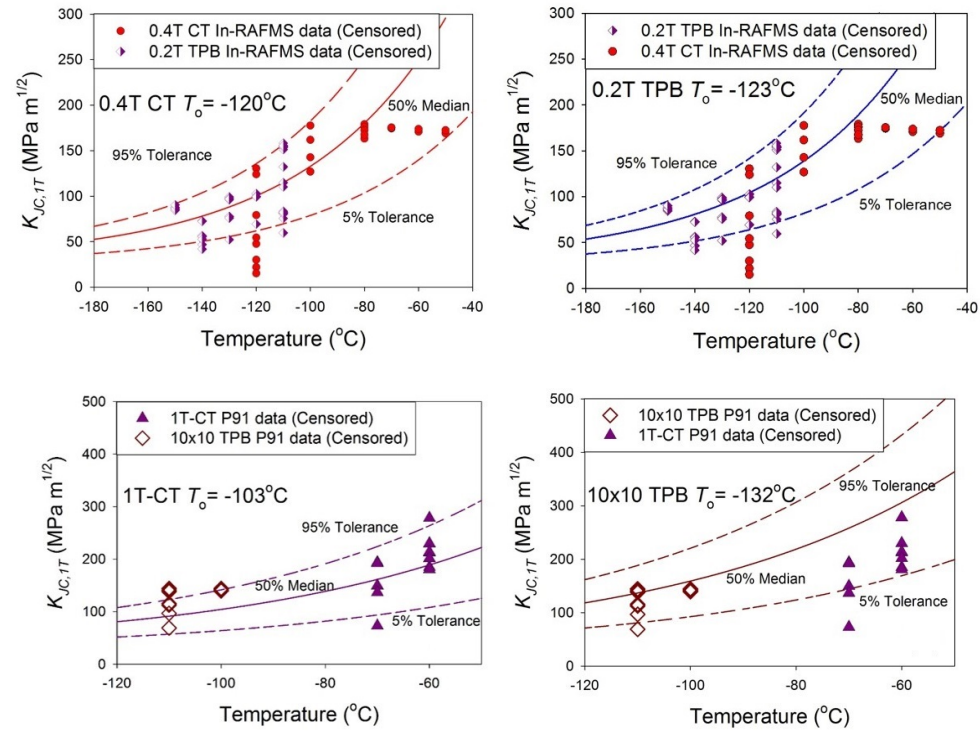


FIGURE 9.2: Comparison of master curves for (a) In-RAFMS 0.4T-CT specimens with the TPB dataset (b) In-RAFMS 0.2T TPB specimens with 0.4T-CT datasets (c) P91 1T-CT specimens with 0.4T standard charpy dataset and (d) P91 0.4T standard charpy specimens with 1T-CT dataset for comparison

The results for In-RAFMS show very close values of reference transition temperature, T_0 for both CT and TPB specimens. The deviation of T_0 is larger for P91 specimens. The statistical parameters of Master Curve Weibull fit is compared in Table 9.1 for two steels.

TABLE 9.1: Statistical parameters of In-RAFMS and P91 Master Curve analysis ¹ n_i is the weight factor used according to ASTM E1921-13a for validity criteria

	Total No. of fracture tests	Valid tests(r_i)	$\Sigma r_i n_i$ ¹	$K_{JC,med}$ at -110°C	T_0	$\sigma_{d,1}$ ¹
In-RAFMS 0.4T-CT	26	14	2.33	114.64	-120	32.9
In-RAFMS 0.2T-TPB	39	26	4.07	119.61	-123	34.3
P91 1T-CT	12	12	2.00	91.28	-103	26.3
P91 0.4T-TPB	15	7	1.16	136.32	-132	39

9.6 Discussions

9.6.1 Effect of CT and SE(B) geometries on T_0

The master curve methodology is used for determination of T_0 for In-RAFMS and P91 steels. In the investigation of the differences of fracture specimen geometries in DBT region, Wallin (Wallin, 2001) has expressed that the results obtained by testing CT specimens are more conservative with the difference in T_0 to be only 8°C. In case of In-RAFMS there was a difference of 3°C found in this work. On the other hand, the difference of T_0 in case of P91 was 29°C.

Despite the fact that the difference of 29°C, which in T_0 is still in the expected standard uncertainty (ASTM E1921-13a), an explanation is required as it is known that standard charpy geometry with 10×10 mm cross-section i.e. specimens in TPB with $W = B$ shows highest constraint (Nevalainen and Dodds Jr, 1996) and 1T-CT specimens are also expected to show high constraint that too with CT geometry. Therefore, the loss of constraint as an explanation for this behaviour can only be true if the test temperatures were relatively higher or the censoring was loose. The effect of constraint on T_0 cannot

be verified by making more strict censoring as increasing censoring parameter M from conventional value of 30, results in less number of available valid tests than required for determination of T_0 .

The reference transition temperature estimate depends on statistical dataset available and also on the amount of censoring. Apart from these, the T_0 estimation is also known to be affected by the test temperature (Bhowmik et al., 2015, 2012; Lucon and Scibetta, 2011). The T_0 estimation is generally lower if obtained by analysing fracture toughness data generated at higher temperatures. The reason is that as the test temperature increases, the material's flow becomes easier making the material more ductile in comparison to one at lower temperature. This results in greater non-linearity in the load displacement behaviour due to loss of constraint. On the other hand choosing comparatively lower test temperatures with a controlled estimation of not falling into lower shelf, may also result in lower T_0 estimation as the yield strength of the material increases with lowering of the temperature. This increase in yield strength results in loose censoring limit by increasing $K_{JC,limit}$, resulting further in lower T_0 estimation due to involvement of loss of constraints validated by censoring method. An approach to vary censoring parameter M instead of keeping it independent of test temperature may be explored especially for specimens loading in three point bending as for this type of loading, it is suggested by many researchers (Joyce and Tregoning, 2005b; Rathbun et al., 2006; Nevalainen and Dodds Jr, 1996) to increase censoring limits. Rathbun et al. (2006) states in his extensive work by studying the effect of constraint loss for both change in crack depth and thickness that the loss of constraint for TPB starts very early at $M \approx 200$ and that the BK^4 scaling is also not very accurate for both very high thickness and very small thickness specimens. However, the approximation of power 4 scaling of master curve method remains close to the experimental results and gives a good estimation of T_0 . The master curve analysis of a combined dataset of CT and SE(B) specimens of P91 steel results in a T_0 of -108°C which is close to one obtained by analysing 1T CT dataset alone (-103°C). The master curve for combined dataset is shown in Figure 9.3.

Figure 9.3 in comparison to Figure 9.2(c) and (d) shows that the the estimated T_0 by 1T CT and combined dataset captures the experimental behaviour in the 5% and 95%

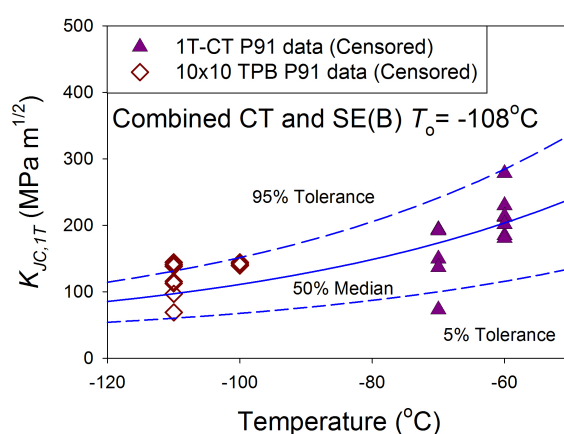


FIGURE 9.3: Master Curves of the combined dataset of P91 standard charpy specimens and 1T-CT specimens

tolerance bounds. This estimate is more reliable statistically as the combined dataset has more valid tests than SE(B) dataset alone. The P91 steel is known to show inferior fracture resistance owing to the phosphorus content and tramp elements (Bhowmik et al., 2012). The carbides' clusters are also found to add to its inferiority in comparison to In-RAFMS. The voids and microcrack formations in In-RAFMS and P91 steels were shown in Chapter 6 in Figures 6.3 and 6.4, respectively.

It is evident from Figure 6.3 (c) and (d) and from Figure 6.4(a),(b) and (d) that the number density of damage emanating sites are more in P91. Moreover, in case of In-RAFMS microcracks are less in number at -70°C in comparison to P91, which shows that P91 steel's tendency to show catastrophic failure at comparatively higher temperature is more. The same behaviour was expected from the Impact energy transition shown in Figure 6.6.

It was found by FE analysis that CT specimens show higher constraint and with side grooving the self-similarity of stresses are achieved to considerable amount in smaller specimens. The 0.4T CT side grooved specimen crack tip stress field is shown in Figure 9.4. Therefore, the close value of T_0 obtained from 0.2T TPB to that obtained from 0.4T CT specimen dataset, leads to the understanding that the loss of constraint effect coming in 0.2T TPB dataset of In-RAFMS were taken care off by the censoring and large

number of valid data as shown in Table 9.1. This is proven by the standard deviation shown in Table 9.1 and also by the validity index r_i/n_i .

The In-RAFMS data of both geometries were statistically large and thus the close values of T_0 is expected. The difference in T_0 for P91 CT and TPB datasets is due to less (though sufficient for T_0 estimation (E1921, 2013)) number of valid data, which is again reflected in standard deviation in Table 9.1. The 1T CT dataset of is more reliable as it has the highest amount of constraint at the test temperatures and more number of valid test data in comparison to SE(B) dataset which may also have maintained higher constraint but for which the number of valid test data is less.

9.6.2 Constraint differences in CT and SE(B) and numerical prediction of cleavage failure probability

The q_W values for CT and SE(B) geometries of P91 at -110°C and -60°C, as shown in Figure 9.5 indicates that the level of constraint remains unchanged at these test temperatures. Therefore, the T_0 difference cannot be explained by differences in constraint with the fact in consideration that for $W = B$ the constraint is generally higher. The constraint measured in form of q_W shows expected behaviour for In-RAFMS as well. The q_W for CT and SE(B) test geometries of In-RAFMS are compared at -120°C in Figure 9.6. The q_W behaviour should not be compared for In-RAFMS and P91 as the tensile properties for both the steels as well as the test temperatures are different. However, it is evident by comparing Figure 9.5 and 9.6, that the level of self-similarity or constraint differs for 0.2T SE(B) and other geometries by a significant amount. The q_W values for 0.4T CT specimens as well as for 1T CT specimen were much closer to SSY value of 1. This behaviour was also reflected in numerical probability prediction as the modified Weibull stresses were decreased by 15% approximately for these geometries in comparison to conventional Weibull stresses due to q_W . The close to SSY stress fields observed in FE analysis for 0.4T CT specimen is shown in Figure 9.4.

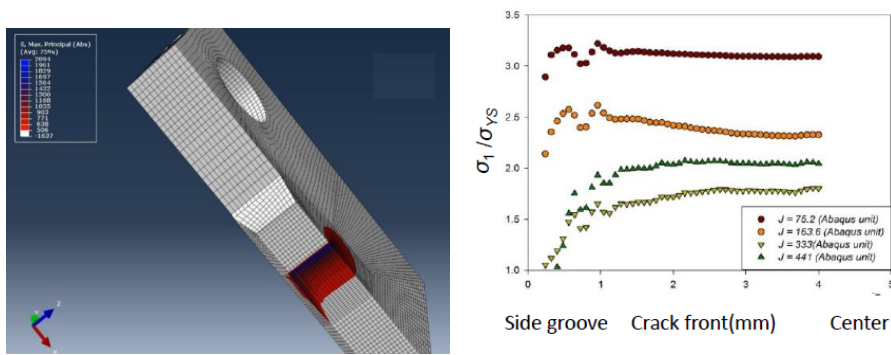


FIGURE 9.4: (a) The stress field near crack tip in visualization mode of ABAQUS and the (b) normalized stress profile along crack front in 0.4T-CT geometry model

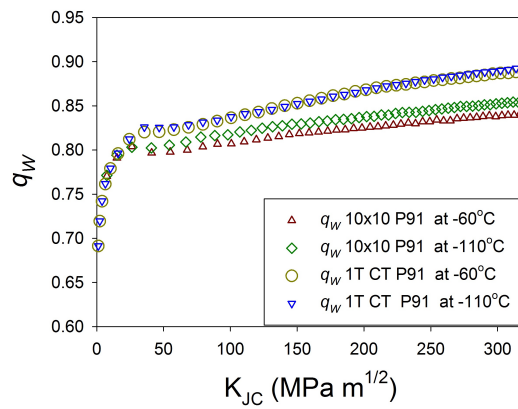


FIGURE 9.5: Weibull triaxiality q_W for P91 steel calculated at -60°C and -110°C for CT and SE(B) geometries

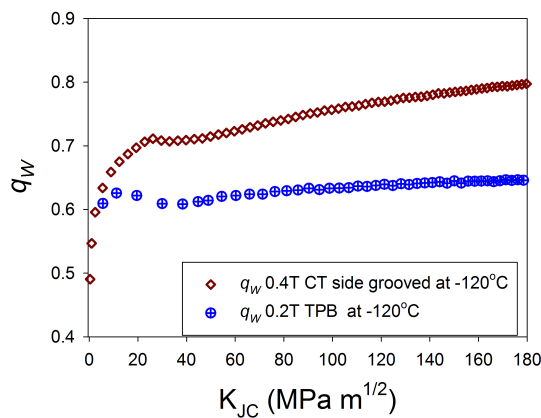


FIGURE 9.6: Weibull triaxiality q_W for In-RAFMS steel calculated at -120°C for CT and SE(B) geometries

The predictions based on modification brought to cleavage failure probability by q_W appears to be not very different from conventional Beremin's model predictions. However, the modified predictions are better as compared with experimental behaviour. For the comparison of q_W effect on P91, the test data of 0.16 T CT specimens, which were used for calibration of P91 Weibull slope, were used. The cleavage failure probability studied at -110°C for standard Charpy dataset and 0.16 T CT dataset are shown in Figure 9.7(a) and 9.7(b).

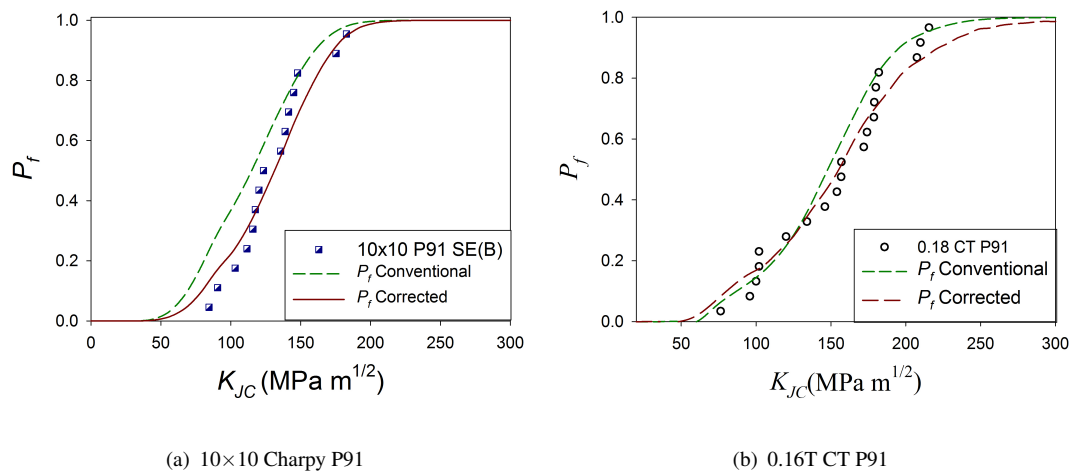


FIGURE 9.7: Numerical and experimental cleavage failure probabilities comparison at -110°C for P91

It is evident from Figure 9.7 that the q_W corrected cleavage fracture probability follows the experimental behaviour closely in comparison to uncorrected prediction. Although, it was found that q_W does not change by any significant amount for both Charpy and 1T CT specimens at -110°C and -60°C , yet the probability distribution would differ for assessment using rank probability method which was used for cleavage failure probability estimation for experimental data. The cleavage failure probability for 1T CT dataset of P91 steel at -60°C and for 0.4T CT and 0.2T SE(B) datasets of In-RAFMS at -120°C are shown in Figures 9.8, 9.9(a) and 9.9(b), respectively.

In all the cases, the modification due to q_W results in better approximation of experimental behaviour. It is also anticipated that for a non-self similar stress condition the

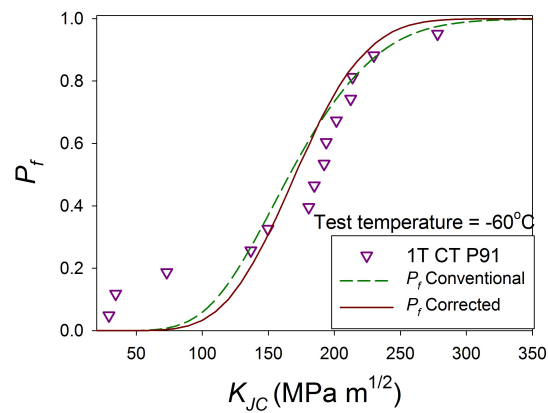


FIGURE 9.8: Numerical and experimental cleavage failure probabilities comparison at -60°C for 1T CT dataset of P91 steel

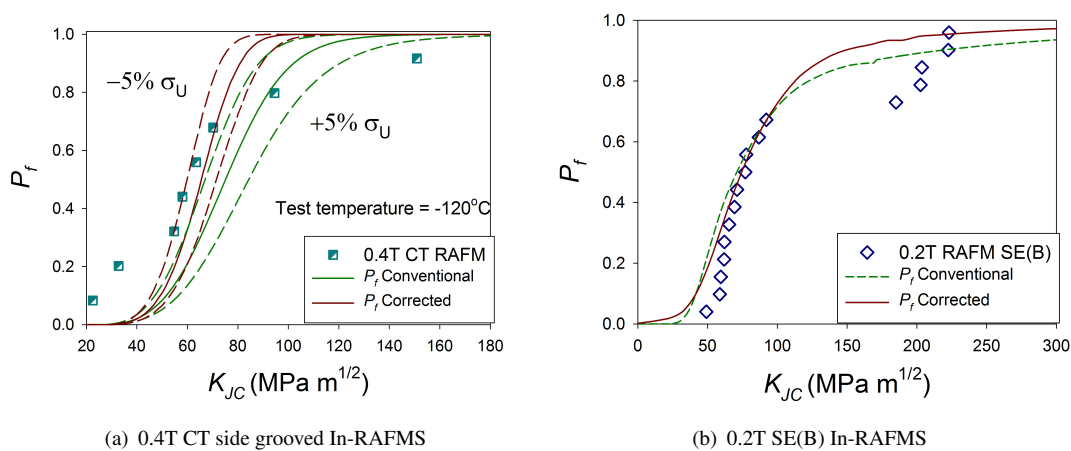


FIGURE 9.9: Numerical and experimental cleavage failure probabilities comparison at -120°C for In-RAFMS

scaling should be at lower levels. This is seen by modification due to q_W as the σ_{Um} is decreased in comparison to conventional scaling parameter σ_U . The σ_{W-min} does not change the probability estimation significantly and can be kept as obtained from conventional Beremin's model. The close behaviour of corrected cleavage fracture probability and conventional cleavage fracture probability for specimen geometries showing higher constraint, is due to the higher constraint coming from their virtue of geometry, such as CT, and TPB specimens with $W = B$. As explained in the section 9.3, the Beremin's model assumes all the RVEs to be under same stress conditions which is accurate for SSY condition. For any deviation from SSY condition especially for loss of constraint, this assumption is inaccurate and the correction is provided by q_W . For over constrained

conditions stresses remain close to SSY conditions (Parks, 1992), and correction may not be required. It is evident from the experimental behaviour and numerical predictions shown in these figures that the Beremin's model in its conventional form results in a conservative predictions. The modified probability predictions using q_W shows accurate estimates for all the experimental datasets, leading to the understanding that q_W correction has the potential to solve for the violation of the assumptions that all RVEs in the active volume remain at self-similar stress conditions.

9.7 Conclusions

Two different grades of ferritic/martensitic steels with similar composition, heat treatment and microstructure were tested in DBT regime and the fracture behaviour is analysed using master curve approach. The experimental investigation included two popular fracture test geometries, namely CT and SE(B)/TPB. The reference transition temperature, T_0 of In-RAFMS obtained for both type of tested specimen geometries, was found to be almost equal, whereas, for Mod-9Cr-1Mo, the SE(B) specimens in three point bending showed a T_0 , 29°C lower than that for CT geometry. The differences in T_0 obtained on CT and TPB specimens showed, a conservative value for CT geometry, for both steels supporting the earlier studies. The large difference in T_0 obtained using CT and TPB specimens of Mod-9Cr-1Mo steel is attributed to the small dataset of TPB specimens tested at lower temperatures. The results, however, are under the expected reproducibility limit. The inferior DBT transition behaviour in terms of DBTT or T_0 is due to the larger carbides and more impurities in comparison to In-RAFMS which is a cleaner steel grade, with detrimental elements P, As, Sb etc. reduced to ppm levels.

The novel method of Weibull Triaxiality, q_W is developed and applied using Beremin's model for numerical prediction of cleavage failure probability. The q_W showed the potential to correct the predictions without performing SSY calculation. The numerical probability prediction were found more accurate with q_W formulation. The effect of q_W was found more prominent on scaling parameter σ_U .

The constraint differences between CT and TPB geometries were examined using q_W . The parameter q_W , shows the level of non-self similarity with a reference frame set at SSY condition. It was also brought out, as expected, using q_W that the level of constraint is always higher in CT geometry and for SE(B) type specimens the constraint is higher when $W = B$.

Chapter 10

Master curve: effect of loading rate

In this chapter, effect of loading rate on cleavage failure probability for ferritic/martensitic steels using Weibull stress analysis is studied. Calibration of Weibull slope for two grades of fusion reactor blanket steels namely, Indian Reduced Activation Ferritic/Martensitic Steel referred as In-RAFMS, F82H and a non fusion grade modified 9Cr-1Mo steel (P91) are performed for the first time. The calibrated values of Weibull slope is used to predict the fracture behaviour of In-RAFMS at three different loading rates. The effect of loading rate is also examined on reference transition temperature using Wallin's correlation based on Zener-Hollomon strain rate parameter.

The results and findings presented in this chapter are published in:

Tiwari A, Gopalan A., Shokry A., Singh R. N., Stahle P. (2017) "Fracture study of ferritic/ martensitic steels using weibull stress analysis at quasi-static and higher loading rates. International Journal of Fracture pp. 17, DOI 10.1007/s10704-017- 0184-4

10.1 Introduction

The fracture behaviour of ferritic steels in DBT region have been extensively investigated using probabilistic master curve approach in last two decades. The extensive experimental work of [Heerens and Hellmann \(2002\)](#); [Lucon and Scibetta \(2011\)](#); [Heerens and Hellmann \(1999\)](#), which resulted in the largest dataset (Euro Fracture data) along with statistical analysis of Wallin ([Wallin, 2013, 2002, 2010a, 2004, 2003](#); [Wallin et al., 2001](#); [Wallin, 2001, 1989a,b](#); [Wallin et al., 2015, 2004](#)) have contributed significantly

in standardization of master curve methodology (ASTM E1921). A similar approach in understanding the cleavage failure mechanism numerically in DBT region started with the pioneer study of Beremin's group (Beremin et al., 1983b) on cleavage failure probability based on Weibull stress, which is described in Chapter 9. The two parameter Weibull distribution of cleavage fracture probability is described in Eq.(9.2). The Weibull stress approach later developed into a numerical methodology, which reciprocates the master curve methodology in numerical or Weibull stress form. The master curve methodology and cleavage failure probability assessment using Weibull stress approach to investigate effects of change in loading rates, are explained briefly in following sections.

10.1.1 Master Curve Methodology and effect of loading rate

The general variation of fracture toughness measured according to ASTM E1921 with temperature in transition region is explained in detail in Chapter 2. The loading rate effect on reference transition temperature T_0 was studied by Wallin (1997) and a correlation of shift in reference transition , T_0 was suggested by Wallin, which is described as,

$$\Delta T_0 = \frac{(T_{0,1} - 273) \ln\left(\frac{dK}{dt}\right)}{\Gamma - \ln\left(\frac{dK}{dt}\right)}, \quad (10.1)$$

where dK/dt is the rate of change of opening mode stress intensity factor in terms of MPa m^{1/2} s⁻¹, Γ is the Zener-Hollomon strain rate sensitivity parameter (Zener and Hollomon, 1944), $T_{0,1}$ is the quasi-static reference transition temperature in °C and ΔT_0 is the shift in reference transition temperature from the value obtained at quasi-static loading. The Zener-Hollomon strain rate parameter is described as,

$$\Gamma = 100.9 \exp\left[\left(\frac{T_{0,1} - 273}{190}\right)^{1.66} + \left(\frac{\sigma_{0,1}}{722}\right)^{1.09}\right], \quad (10.2)$$

where $\sigma_{0,1}$ is the yield strength of the material in MPa at quasi-static reference transition temperature, $T_{0,1}$. The loading rate correlation is derived from the fact that the the

effect of loading rate resulting in inertia of the material is annulled by diffusion causing relaxation of material as described in the pioneer work of [Zener and Hollomon \(1944\)](#).

10.1.2 Cleavage failure probability, Weibull stress and loading rate

The Weibull stress analysis as a tool to predict cleavage failure probability started with the pioneer work of [Beremin et al. \(1983b\)](#). For a Griffith crack, in a crack tip volume actively taking part in cleavage phenomena (Active Volume), the probability, P to find a micro-crack of size in the range of l_0 to $l_0 + dl_0$ in a small fraction of active volume, V_S was described in Chapter 9, in Eq.(9.2). Using Eq. (9.2), the cumulative probability of cleavage fracture of active volume can be described by integrating P for all V_S , as shown in Eq.(9.3). The Weibull stress then takes the form shown in Eq.(9.4). The three parameter cleavage failure probability involves an extra term, σ_{W-min} , which is similar to K_{min} in master curve methodology, as described in Eq.(9.6).

10.1.3 Calibration of Weibull parameters

For the numerical prediction of cleavage failure probability, it is a pre-requisite to calibrate the Weibull slope m . The scaling parameter σ_U is then the σ_W corresponding to K_0 . The history of Weibull stress based cleavage failure probability starts as discussed earlier with the work of Beremin's group ([Beremin et al., 1983b](#)), which was then a two parameter Weibull analysis. The calibration procedure for two parameter as well as three parameter Weibull cleavage failure probability was developed mostly by [Gao and Dodds Jr \(2005a\)](#), [Petti and Dodds Jr \(2005\)](#), [Wasiluk et al. \(2006\)](#) and [Ruggieri et al. \(1998\)](#). The approach in these works brought cleavage failure probability very close to the master curve methodology. In other words, the stress based cleavage failure probability was coupled with master curve methodology, especially with three parameter Weibull probability distribution function as described in Eq. (9.6). Simultaneous efforts were also made to introduce plastic strain factor in the cleavage failure probability. The plastic strain correction and evolution of Weibull stress based cleavage failure probability is recently reviewed in the work of [Ruggieri and Dodds Jr \(2015\)](#).

The calibration of Weibull slope is described and used by many researchers such as [Gao et al. \(2006\)](#); [Wasiluk et al. \(2006\)](#); [Qian et al. \(2011, 2015\)](#); [Petti and Dodds Jr \(2005\)](#); [Dowling and Lidbury \(2000\)](#). The calibration procedure used in this work follows the procedure suggested by [Wasiluk et al. \(2006\)](#), which is similar to one used by [Gao et al. \(2006\)](#). The g -function used as calibration procedure in the work of [Gao et al. \(2006\)](#) and [Petti and Dodds Jr \(2005\)](#) is a measure of differences in stress fields under Small Scale Yielding (SSY) and real crack tip conditions. For detailed description of the g -function, readers are referred to the work of [Gao et al. \(2006\)](#), [Petti and Dodds Jr \(2005\)](#) and [Wasiluk et al. \(2006\)](#). The relation of σ_W with fracture parameter J or K for self similar stress field at the crack tip was described in Eq.(9.5), in Chapter 9. For real crack tip conditions, which are non-SSY conditions, Eq. (9.5) is modified ([Gao and Dodds Jr, 2000](#)) with a dimensionless parameter known as g -function. The modified form of Eq.(9.5) with K as fracture parameter is

$$\sigma_W^m = \bar{\zeta} g(M) B K^4 . \quad (10.3)$$

The calibration of Weibull modulus procedure has been described by many researchers in different ways ([Dowling and Lidbury, 2000](#); [Beremin et al., 1983b](#); [Wasiluk et al., 2006](#); [Petti and Dodds Jr, 2005](#)). In the work of [Dowling and Lidbury \(2000\)](#), the calibration process is described in, which the data is generated in psuedo-random fashion and the ML analysis is carried out on these data. The procedures described by [Wasiluk et al. \(2006\)](#) and [Gao et al. \(2006\)](#) differs from the earlier procedures with an addition of SSY correction and calibration with real test data. The SSY correction's importance is based on the fact that the Weibull stress analysis model stands on the assumption of Griffith type micro-cracks in a unit cell volume of V_0 . It thus becomes a pre-requisite to transform the $\sigma_W - K$ history to SSY condition before attempting calibration of Weibull slope.

The calibration procedure requires two datasets of fracture specimens, one of which shows significant loss of constraint without significant ductile crack growth, and other

shows high constraint. In the work of [Gao et al. \(2006\)](#) the high constraint (HC) is obtained on Compact Tension (CT) specimens with crack length to specimen width ratio $(a/W) = 0.6$ and the low constraint (LC) is obtained by Three Point Bend (TPB) specimens with $(a/W) = 0.2$. The choice of LC and HC may differ and can be achieved by changing the thickness of specimen as well. However, for calibration of Weibull slope the dataset should be obtained at single temperature. Further the process of calibration described by [Wasiluk et al. \(2006\)](#) follows stepwise.

1. The HC experimental dataset is assured to have high constraint i.e. $M \geq 100$, and LC dataset is assured to have no significant ductile crack growth. Here $M = bJ/\sigma_0$ is a dimensionless parameter with b as ligament length.
2. The two dataset are created at single temperature suggested ([Wasiluk et al., 2006](#)) to be above reference transition temperature T_0 .
3. The tensile response at this test temperature say T_{test} is extrapolated to a plastic strain of 2.0 and is used for Finite Element (FE) modelling of HC and LC test geometries.
4. A Modified Boundary Layer (MBL) Small Scale Yielding (SSY) condition representing plane strain 1T SSY crack tip stress field, which is obtained by applying boundary conditions with zero T_{stress} is modelled with tensile behaviour, i.e. true stress and plastic strain at T_{test} extrapolated to plastic strain of 2.0. The details of boundary layer modelling is given in Chapter 6. The finite element analyses in this work follow incremental plasticity with quadratic elements and reduced integration for MBL model.
5. In FE analyses of HC, LC and SSY MBL conditions, Weibull stress can be computed using WSTRESS algorithm from WARP 3D software ([Koppenhoefer et al., 1994](#)). In this work a different post processing method is used for Weibull stress calculation based on the active volume calculation method described by [Tiwari et al. \(2015\)](#) using ABAQUS FE software package ([Hibbitt et al., 1998](#)). The history of σ_W and J is recorded for three models with trial values of m and K_{min} . From the assumed value of K_{min} , value of σ_{W-min} is set.
6. The HC and LC experimental fracture toughness values, i.e. $K_{JC}^{(HC/LC)}$ are corrected

to 1T SSY condition i.e. $K_{JC}^{SSY(1T)}$ following the correction as,

$$K_{JC}^{SSY(1T)} = K_{min} + [g(M^{(HC/LC)})^{1/4} K_{JC}^{(HC/LC)} - g(M_{min}^{(HC/LC)})^{1/4} K_{min}] \left(\frac{B^{(HC/LC)}}{B_{1T}} \right)^{1/4}, \quad (10.4)$$

where $g(M^{(HC/LC)})$ is a function describing the difference in level of constraint (Gao et al., 2006) for HC and LC geometries and $B_{(HC/LC)}$ and B_{1T} are the thickness of the modelled HC or LC and 1T SSY conditions respectively. The 1T SSY corrected datasets are referred here as $K_{JC}^{HC/LC-1T,SSY}$.

7. Using single temperature master curve methodology, parameter $K_o^{HC-1T,SSY}$ is calculated from the corrected HC dataset. The $K_o^{HC-1T,SSY}$ and trial K_{min} values are used to define a continuous, cumulative probability distribution function referred here as $P_{f,1T-SSY}$ vs K_{JC}^{1T-SSY} .

8. The error is calculated in two parts. First part of the error comprises the summed differences of $K_{JC}^{HC/LC-1T,SSY}$ and K_{JC}^{1T-SSY} and the second part comprises of the difference of $K_{JC}^{HC/LC-1T,SSY}$ i.e. the differences in corrected K_{JC} values of HC and LC datasets, which is referred here as $\Delta K_{JC}^{HC/LC-1T,SSY}$. The error for trial values of m and K_{min} is described as

$$Error = \sum_{i=1}^{(nLC+nHC)} |K_{JC(i)}^{HC/LC-1T,SSY} - K_{JC(i)}^{SSY(1T)}| WF_{(i)} + \sum_{i=1}^{min(nLC+nHC)} |\Delta K_{JC}^{HC/LC-1T,SSY}| WF_{(i)}, \quad (10.5)$$

where WF denotes the Weight Factor, which is explained in detail in the work of Wasiluk et al. (2006).

The procedure described above is repeated for a range of trial values of m and K_{min} and the calibrated pair of values of m and K_{min} are obtained for which the Error defined in Eq.(10.5) is minimum. The scaling parameter σ_U for different conditions are obtained

from $\sigma_U^{1T,SSY}$, which corresponds to σ_W at $K_{JC} = K_0^{1T,SSY}$ as

$$\sigma_U^{(HC/LC)} = [(\sigma_W^{1T,SSY})^{\frac{m}{4}} - (\sigma_{W-min}^{1T,SSY})^{\frac{m}{4}} + (\sigma_{W-min}^{HC/LC})^{\frac{m}{4}}], \quad (10.6)$$

where σ_{W-min} for 1T,SSY and HC/LC conditions corresponds to σ_W at $K_{JC} = K_{min}$. Eq.(10.6) is based on the fact that the denominator in Eq.(9.6) does not change for different conditions (Wasiluk et al., 2006). In the pioneer work of (Beremin et al., 1983b), as described in Eq.(9.1), the scaling parameter σ_U is described as a material property independent of temperature, and level of constraint. In Beremin's work the model was 2 parameter as shown in Eq.(9.1). In three parameter description of cleavage failure probability which follows Eq.(9.6), the value of σ_U cannot remain constant as it has to compensate for the changes brought in due to change in σ_{W-min} .

Koppenhoefer and Dodds Jr (1997) studied numerically the effect of loading rate on Weibull stress based cleavage failure probability using pre-cracked charpy V notch fracture specimen geometry. In their study the parameter m was assumed to be invariant and it was suggested to generate experimental data to investigate further. The loading rate effect on Weibull stress based cleavage failure probability is assessed extensively in the work of Gao and Dodds Jr (2005a,b); Gao et al. (2008, 2001). Initially, in the work of Gao et al. (2001), the Weibull parameter was investigated on A-515-70 strongly rate sensitive steel where the range of loading rate investigated was in the range of $0.8 \text{ MPa m}^{1/2}\text{s}^{-1}$ to $3200 \text{ MPa m}^{1/2}\text{s}^{-1}$. In their work, the calibrated value of m was 11.2 and it was found that the m value remained fixed for quasi-static to elevated loading rates. On the same material in other work, where the range of loading rate was $\leq 2200 \text{ MPa m}^{1/2}\text{s}^{-1}$, it was re-confirmed that the m is invariant with loading rate. σ_U was found to be decreasing with increasing loading rate and σ_{W-min} was found to be increasing with increasing loading rate.

In the work of Gao et al. (2008) on 22NiMoCr37 pressure vessel grade steel, the variation of m parameter was studied in the range of loading rate from quasi-static to $3000 \text{ MPa m}^{1/2}\text{s}^{-1}$. In this work also it was proven that the value of m remains invariant with

change in loading rate in the investigated range and σ_U decreases and σ_{W-min} increases with increase in loading rate.

The objective of present work is to investigate the effect of loading rate experimentally on Indian Reduced Activation Ferritic/Martensitic Steels (In-RAFMS) and to analyse the fracture behaviour using master curve method with numerical prediction of cleavage failure probability. As the Weibull stress analysis is not carried out on fusion reactor grade material till date, the second objective of this work was to calibrate the Weibull slope for In-RAFMS, which also is a pre-requisite for the first objective. Further the calibrated Weibull slope is used here to understand whether the cleavage failure probability reciprocates the experimental behaviour.

With the support of the extensive work by [Gao and Dodds Jr \(2005b\)](#); [Gao et al. \(2008, 2001\)](#), it will be reasonable to assume calibrated value of m to be invariant in the range of loading rate examined in this work. Some of the concerns related to plastic strain in Weibull stress analysis are also discussed in this work. Although, the effect of plastic strain on cleavage failure probability is not studied in this work.

10.2 Experimental dataset

For the assurance that the calibrated value of m obtained in this work for In-RAFMS is justifiable, another fusion reactor grade steel known as F82H is also investigated using the fracture data from the work of [Sokolov and Tanigawa \(2007\)](#). The material tested by [Sokolov and Tanigawa \(2007\)](#) was produced for International Energy Agency (IEA) round robin tests and is also referred as F82H-IEA. In the work of [Sokolov and Tanigawa \(2007\)](#), fracture tests were conducted on 1T, 0.4T and 0.16T CT specimens in DBT region. The dataset was reported to be inhomogeneous, however, due to the lack of available dataset on RAFM grade steel, this dataset was chosen. Apart from F82H, Mod-9Cr-1Mo or P91 steel is also calibrated for, which the data is generated and analysed in this work only for quasi-static loading condition. The details about differences and similarities of these steels are already discussed in Chapter 4.

It is important to bring forward the fact that the F82H dataset is only used to find whether the calibrated m value falls close to one calibrated for In-RAFMS. The details of materials and experiments are provided in Chapter 4.

The fracture toughness tests were carried out at test temperatures of -110°C , -120°C , -130°C , -140°C and -150°C for quasi-static condition. The tests were performed on standard charpy specimens at -80°C and -100°C for higher displacement rates of 100 and 1000 mm/min. These actuator speeds corresponded to dK/dt in range of $250\text{ MPa m}^{1/2}\text{s}^{-1}$ to $370\text{ MPa m}^{1/2}\text{s}^{-1}$ for 100 mm/min and 650 to $1450\text{ MPa m}^{1/2}\text{s}^{-1}$ for 1000 mm/min. The dK/dt was calculated as the ratio of K_{JC} and the time of fracture t_f for each test.

For calibration purpose, the P91 standard charpy specimens were tested at -100°C and -110°C . This dataset was used as HC dataset as from the work of [Nevalainen and Dodds Jr \(1996\)](#) it is clear that the standard Charpy geometry shows highest constraint with respect to other geometries tested in TPB. For the LC dataset 4 mm thick specimens with specimen width $W = 50$ were tested. This dataset is a part of undergoing study where the effect of thickness without changing the ligament length is being investigated on Mod-9Cr-1Mo steels.

10.3 Finite element analysis

The finite element analysis for In-RAFMS, P91 and F82H steels were carried out using ABAQUS FE software package with incremental plasticity and 20 noded serendipity elements. For HC, LC and SSY conditions the J was stored as history output by defining contour integral at the crack front. Except the SSY condition for both the steels, the FE modelling was carried out in three dimension. The SSY models were meshed with 8 noded reduced integration quadrilateral elements. The detailed FE analysis is explained for both the dataset is discussed below.

10.3.1 Finite element analysis of In-RAFMS

Finite element analysis was carried out on In-RAFMS dataset for quasi-static condition for calibration of Weibull slope. The dataset chosen for calibration was 0.4T CT side grooved specimen geometry for HC and TPB 0.2T geometry for LC model. The fracture tests corresponding to -120°C was selected at, which the number of HC data were 8 and LC were 18. The true stress plastic strain response recorded at -120°C was used for FE modelling of HC, LC and SSY conditions for In-RAFMS. The mesh for 0.4T CT side groove geometry and 0.2T TPB geometry modelled as HC and LC conditions respectively are discussed in Figure 9.1 in Chapter 9.

The specimens tested at higher loading rates i.e. at 100 mm/min and 1000 mm/min were standard full size charpy specimens in TPB, therefore, for Weibull calculation at elevated loading rates quarter symmetric standard charpy geometry was modelled with tensile response obtained at test temperature of -100°C . As it is assumed based on the work of [Gao and Dodds Jr \(2005b\)](#); [Gao et al. \(2001\)](#) that the Weibull slope m remains invariant with loading rate, the Weibull stress for elevated rate assessments were calculated for tensile input corresponding to the tensile test response at -100°C .

The meshing of MBL has also been studied extensively using 20 noded serendipity elements with layered meshing of 20 or more layers. The mesh is refined from the outer to inner layers. As the mesh refinement in three dimensional problems causes longer durations in CPU time for analysis, many time saving practices have been used. [Nevalainen and Dodds Jr \(1996\)](#) have used linear pre-conditioned conjugate gradient (LPCG) method that avoids assembling large stiffness matrices, thereby decreasing both the solution runtime as well as the physical memory in comparison to direct solvers. On the other hand quantitative assessments of ([Delorenzi and Shih, 1983](#); [Koers et al., 2013](#)) with moderate meshing has shown satisfying results of J variation along three dimensional crack fronts.

The meshing scheme of MBL model is described in detail in Chapter 5, section 5.2.1. The MBL is solved in two dimension with reduced integration full Newtonian solution

procedure following incremental plasticity. The mesh of the MBL model is shown in Figure 10.1.

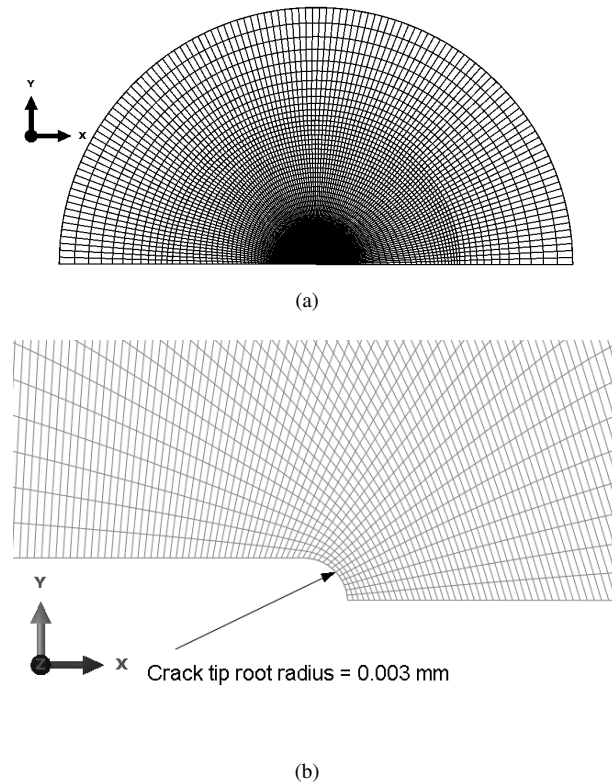


FIGURE 10.1: (a) Two dimensional MBL model quarter symmetric geometry mesh, (b) magnified crack tip root radius

In the similar study on cleavage failure probability by [Gao and Dodds Jr \(2000\)](#), the MBL was modelled by a crack tip root radius of $2.5 \mu\text{m}$ and $0.25 \mu\text{m}$. It was found that the model with $0.25 \mu\text{m}$ root radius resulted in unacceptable crack tip element distortion at higher J values. On the other hand the model with larger crack tip root radius of $2.5 \mu\text{m}$ permitted deformation at higher J values. The crack tip root radius in the work of [Petti and Dodds Jr \(2005\)](#); [Gao and Dodds Jr \(2000\)](#) was also modelled for easy convergence.

The post processing method used for Weibull calculation in this work is carried out extracting maximum principal stress σ_1 and maximum principal strain $\epsilon_{p,1}$. The process is described below.

Step 1. Extraction of σ_1 and Maximum Principal Strain $\epsilon_{p,1}$ at nodes where $\sigma_1 \geq 2\sigma_0$ in the model.

Step 2. Counting the number of nodes in each increment for stresses starting from $2\sigma_0$ to maximum value of σ_1 , i.e. $\sigma_{1,max}$ in the model.

Step 3. For each increment and each value of σ_1 in range of ($2\sigma_0$ to $\sigma_{1,max}$) calculating the volume using method described in Chapter 7 (Tiwari et al., 2015).

Step 4. Multiplying the volume with σ_1 corresponding to each stress level and adding the products at the end.

For example, starting from $\sigma_1 = \sigma_{1,ini}$ to $\sigma_1 = \sigma_{1,max}$, where $\sigma_{1,ini}$ is the starting value for each step of calculation.

Start a for loop as For $j = \sigma_{1,ini}$ to $\sigma_{1,max}$ with an interval of $\delta\sigma_1$

$V_j =$ Volume of nodes having $\sigma_{1,ini} \leq \sigma_1 \leq \sigma_1 + \delta\sigma_1$ with assumed value of m .

End the for loop

This results in $\sigma_W^m V_0 = \sum_{j=\sigma_{1,ini}}^{j=\sigma_{1,max}} V_j \cdot (\sigma_1 + \delta\sigma_1)^m$

It was studied earlier by Rice et al. (1970) and explained by McMeeking (1977) that an initial root radius in a plane strain MBL analysis is expected to attain a steady state solution for contained yielding, which is independent of initial notch geometry. The steady state in terms of stress field at crack tip is attained when the deformed root radius is much larger than the initial root radius. To reduce the effect of initial crack tip root radius the MBL results were extracted after the deformed crack tip root radius exceeded thrice of initial crack tip root radius. Further the results were limited till the plastic zone size was significantly smaller in comparison to the remote boundary. The results were extracted till the plastic zone radius r_p was less than $r/20$ where r is the radius of the remote boundary. Similar approach was applied in the work of Gao and Dodds Jr (2000) for MBL modelling.

10.3.2 Finite element analysis of F82H

The F82H dataset from the work of Sokolov and Tanigawa (2007) comprises fracture data of 1T, 0.4T and 0.16 CT specimens. Out of these, 1T dataset was chosen to simulate HC and 0.4T CT dataset was chosen to simulate LC condition as 0.16 CT dataset was very small. The maximum number of fracture data were available for -100°C , which

therefore was chosen to model the HC, LC and SSY conditions. The yield strength at this temperature for F82H is reported to be 575 MPa and the closest value of yield strength for In-RAFMS is at -120°C. Thus, the tensile response for F82H at -100°C was generated with the tensile response of In-RAFMS at -120°C with $\sigma_0 = 575$ MPa for F82H. The mesh of 1T and 0.4T CT geometries are shown in Figure 10.2.

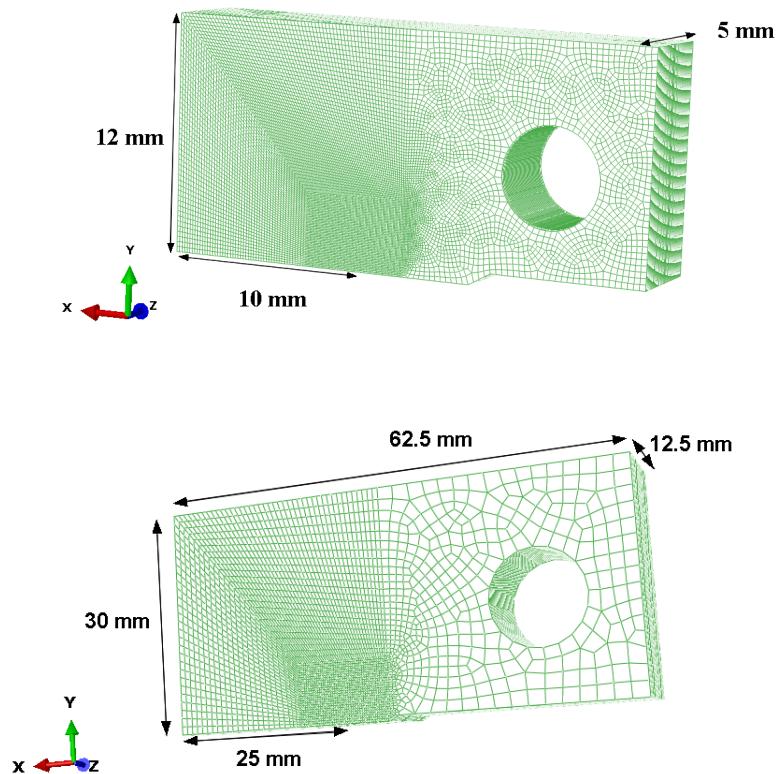


FIGURE 10.2: Quarter symmetric models of (a) 0.4T CT geometry for LC condition and (b) CT 1T geometry modelled for F82H steel as HC condition

The Weibull stress was calculated with the same post processing method described in Section 3.1. Both HC and LC conditions were meshed with 20 noded serendipity elements and the FE analysis was carried out using incremental plasticity.

10.3.3 Finite element analysis of Mod-9Cr-1Mo steels

The HC dataset of P91 corresponded to 10×10 standard charpy geometry and LC to 0.16 T CT with dimensions of 1T CT geometry and thickness of 4mm. The HC dataset

comprised 15 data and LC comprised 20 data. The calibration temperature was chosen to be -110°C . Few of the tests, which were carried out at -100°C were also used for calibration. The mesh technique for 0.16 T CT and 10×10 standard charpy specimen were similar to the meshes for F82H and In-RAFMS with quarter symmetry.

The tensile data used for FE analysis for In-RAFMS, F82H and P91 steel models are shown in Figure 10.3.

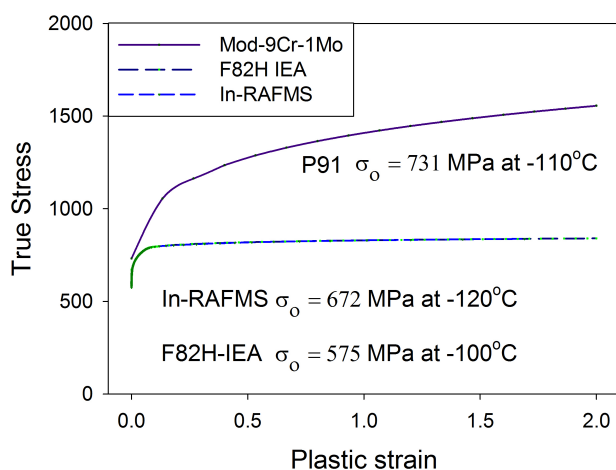


FIGURE 10.3: Tensile behaviour of In-RAFMS at -120°C , F82H at -100°C and P91 at -110°C extrapolated to 2.0 strain used for FE modelling. (The tensile property of F82H at -100°C is generated using the yield strength reported in literature and tensile property of In-RAFMS at -120°C .)

10.4 Results

10.4.1 Calibration of Weibull slope: In-RAFMS

The dataset obtained by quasi-static fracture tests using ASTM E1921 used for Weibull calibration are shown in Figure 10.4 with the rank probabilities. The LC dataset corresponds to 0.2T TPB specimens and HC corresponds to 0.4T CT side grooved specimens.

The difference in constraint can be easily realized from Figure 10.4. The dataset was filtered to assure $M \geq 100$ for HC dataset. It has been suggested that calibration of Weibull slope with trial values of m and K_{min} should be done only with huge dataset by

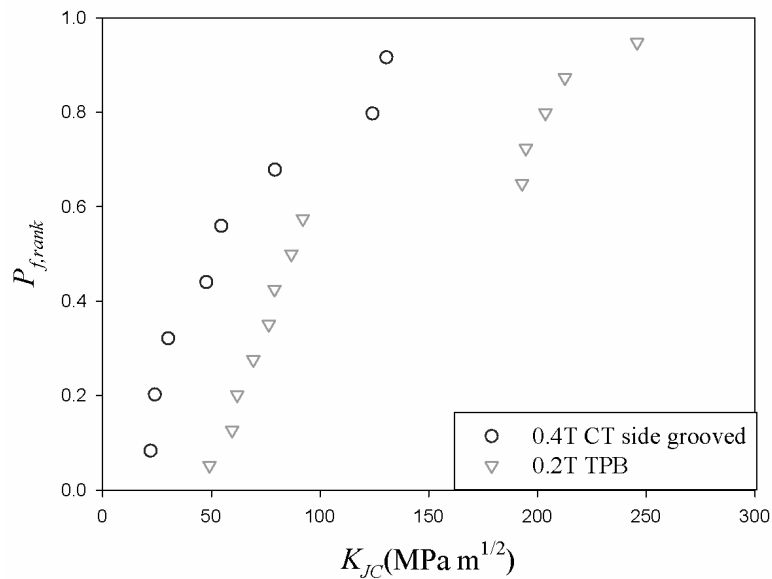


FIGURE 10.4: Rank probability of HC (0.4T CT side grooved) and LC (0.2T TPB) datasets of In-RAFMS

Gao et al. (2006), however, in this work m and K_{min} both calibration is attempted and m at $K_{min} = 20$ is used as calibrated value of m . The error obtained against trial value of m and K_{min} is shown in Figure 10.5.

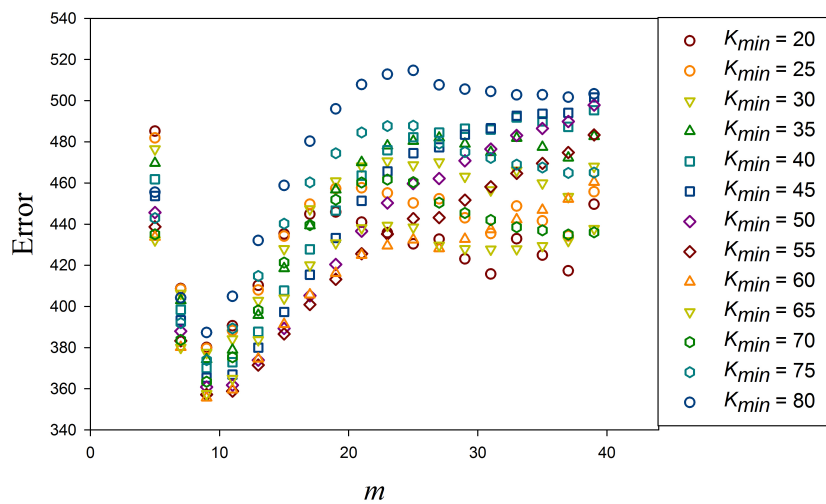


FIGURE 10.5: Error calculated using Eq.(10.5) for trial values of m and K_{min} used on fracture data of In-RAFMS

It can be visualized from Figure 10.5 that the error defined by Eq.(10.5) gets minimized for all trial values of K_{min} at $m = 9$. The minimum error was found at $K_{min} = 60 \text{ MPa m}^{1/2}$, however, as discussed earlier due to the smaller dataset, the K_{min} of $20 \text{ MPa m}^{1/2}$ is used in the investigations on In-RAFMS further. The g -function for increasing m

values for HC and LC models are shown in Figure 10.6(a). The increasing Weibull slope appears to increase the g -function for both HC and LC models. It can be inferred from Eq.(10.4)) that the g -function apart from the specimen thickness B is a direct function of σ_W . Therefore, for LC model due to the relaxation of stresses at the crack tip resulting from loss of constraint, the g -function is usually lower than that for HC model at same K_{JC} . The smaller σ_W resulting in smaller g -function can be realized for m of 9 in Figure 10.6(b).

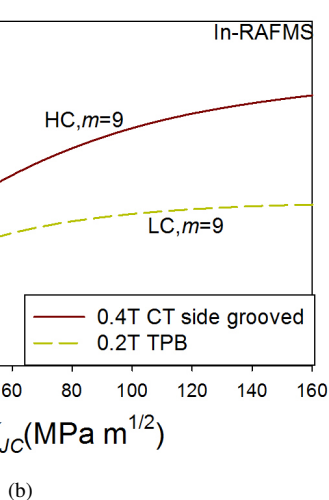
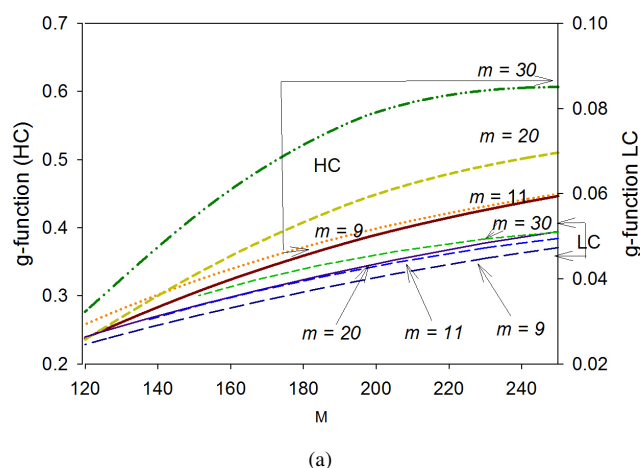


FIGURE 10.6: (a) The behaviour of g -function for HC and LC models at different m values and (b) σ_W behaviour for HC and LC dataset of In-RAFMS at $m = 9$

10.4.2 Calibration of Weibull slope:F82H

The dataset of F82H from the work of Sokolov and Tanigawa (2007) has very few data at single temperature for both 1T CT and 0.4T CT. Maximum number of data are available at -100°C. Five data for 1T CT specimen geometry and 6 data for 0.4T CT geometry were selected for calibration of Weibull slope. The dataset is shown in Table 10.1. The rank probability for the HC and LC datasets are shown in Figure 10.7

TABLE 10.1: Dataset from Sokolov and Tanigawa (2007) used for Weibull calibration.

$K_{JC,HC}$ 1T CT	Validity	$K_{JC,LC}$ 0.4T CT	Validity
111.7	1	81	1
96.6	1	161.3	1
173.4	1	92.9	1
96.4	1	135.1	1
131.5	1	116.8	1
		25.5	0

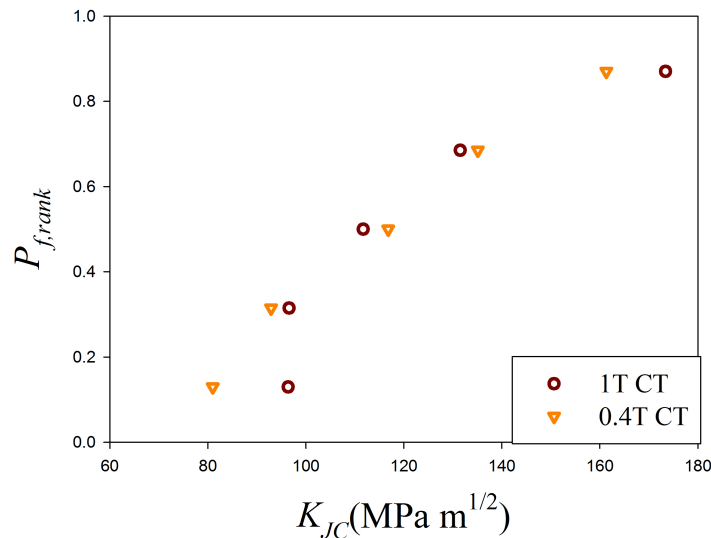


FIGURE 10.7: Rank probability of HC (1T CT) and LC (0.4T CT) dataset for F82H-IEA showing no constraint difference

The dataset shows almost no constraint difference as appearing from Figure 10.7. Also, the dataset is too small for calibration of Weibull slope. Nevertheless, this dataset was used for calibration of Weibull slope for F82H, just to know if it falls close to the one obtained for In-RAFMS. The error obtained by attempting Weibull slope calibration for F82H is shown in Figure 10.8 for same range of trial values of m and K_{min} .

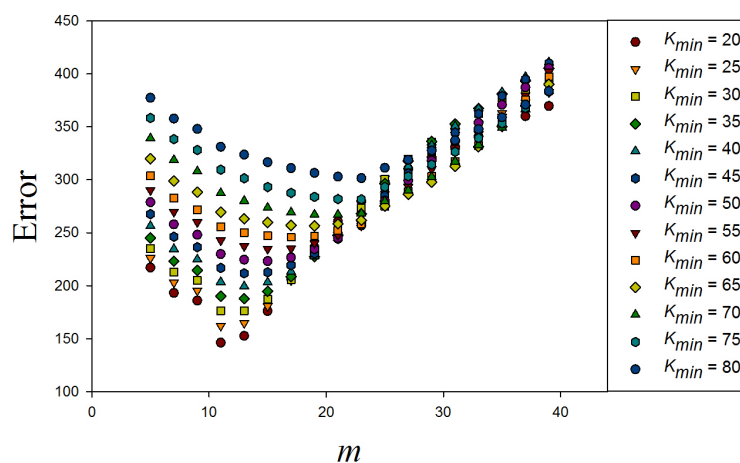


FIGURE 10.8: Error values obtained for trial values of m and K_{min} for F82H-IEA

In case of F82H as shown in Figure 10.8, the error minimizes for higher values of m when K_{min} is higher. The minimum error of all is obtained at $K_{min} = 20 \text{ MPa m}^{1/2}$ and $m = 11$. Although, it would be too erroneous to conclude that m for F82H is 11, still the certainty for calibrated m for In-RAFMS can be said to be obtained due to the close value with that of F82H.

10.4.3 Calibration of Weibull slope: Mod-9Cr-1Mo

The dataset of P91 fracture tests for HC and LC conditions consist of 15 data and 20 data respectively as shown in Figure 10.9 with the rank probabilities. For P91 HC and LC conditions the error minimization calculations were performed with a narrower range of trial values of m (in the range of 5 to 35) and K_{min} (in the range of 20 to 60). The error values are plotted in Figure 10.10.

10.4.4 Master Curve analysis of In-RAFMS at different loading rates

The multi-temperature MC analysis of In-RAFMS specimens tested in quasi-static condition resulted in T_0 of -123°C by 0.2T TPB dataset and -120°C by 0.4T CT dataset . The Master Curve plot for quasi-static condition is shown in Figure 10.11.

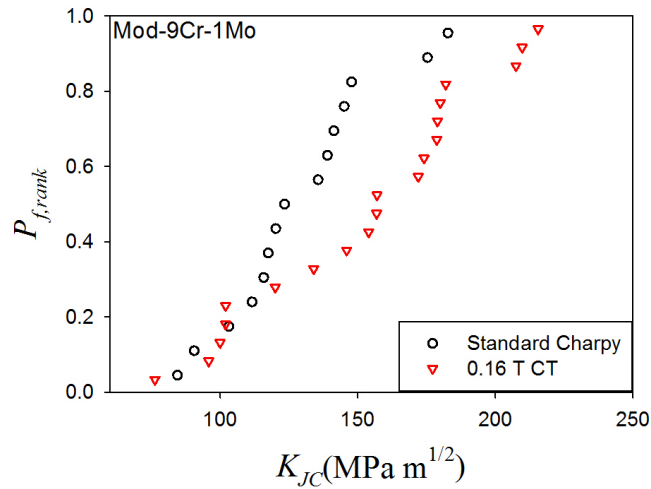


FIGURE 10.9: Rank probabilities of test data obtained on P91 steel for 10×10 standard charpy as HC and 0.16T CT as LC conditions

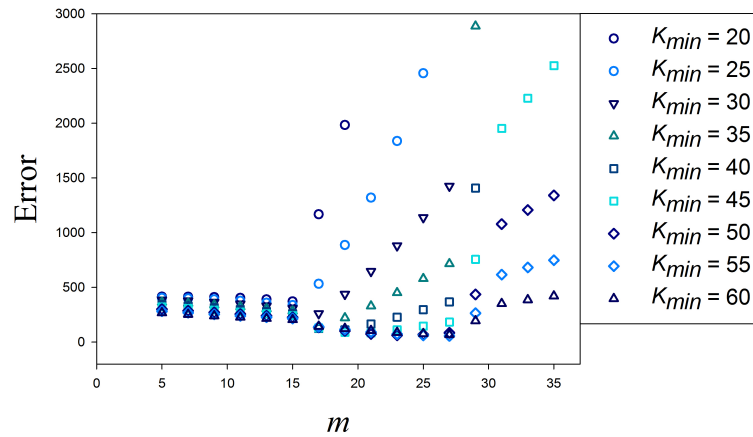


FIGURE 10.10: Error values obtained for trial values of m and K_{min} for Mod-9Cr-1Mo steel

At the higher actuator speeds, i.e. at dK/dt in range of $250 \text{ MPa m}^{1/2}\text{s}^{-1}$ to $370 \text{ MPa m}^{1/2}\text{s}^{-1}$ for 100 mm/min and 650 to $1450 \text{ MPa m}^{1/2}\text{s}^{-1}$ for 1000 mm/min , the T_0 was found to be -95°C and -90°C , respectively. The Master Curve plots corresponding to tests carried out at higher loading rates are shown in Figure 10.12.

The effect of loading rate described by Wallin (1997) on T_0 , estimates the shift ΔT_0 as shown in Figure 10.13 in, which the variation of T_0 obtained in this work is compared with the prediction obtained by correlation given by Wallin as in Eq.(10.1).

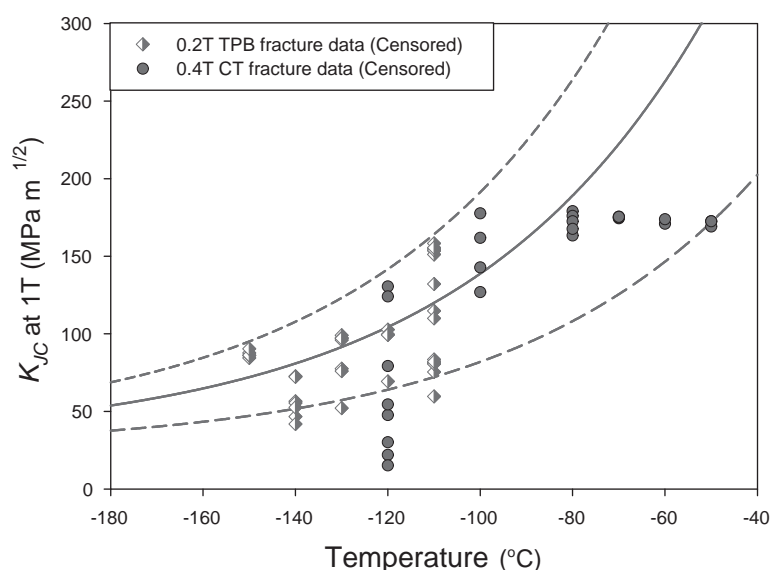


FIGURE 10.11: Master curve of In-RAFMS with $T_0 = -120^\circ\text{C}$ with scatter of 0.2T TPB and 0.4T CT datasets

10.5 Discussions

10.5.1 Calibrated cleavage failure probability distribution for ferritic/martensitic steels

The calibrated m values as discussed in earlier section for three grades of ferritic/martensitic steels were used to find cleavage failure probability according to Eq.(9.6). The cleavage failure probabilities for In-RAFMS, Mod-9Cr-1Mo and F82H steels for both HC and LC datasets are shown in Figure 10.14 (a) to (c) respectively. The experimental data plotted with rank probability is mostly covered in the boundaries of cleavage failure probability obtained with $\pm 5\%$ of σ_U for In-RAFMS. For Mod-9Cr-1Mo dataset, the cleavage failure probability obtained numerically shows closer predictions at higher K_{JC} for HC dataset. This is not the case for LC dataset for P91 steel. For F82H, on the other hand, no conclusion of constraint difference can be made. Still the numerical prediction shows good accuracy for the calibrated value of m for the small dataset used.

The prediction of cleavage failure probability is not very close to the experimental results, probably due to the plastic strain contribution, which is neglected in the Weibull stress analyses used in this work and also by others (Gao et al., 2006; Wasiluk et al.,

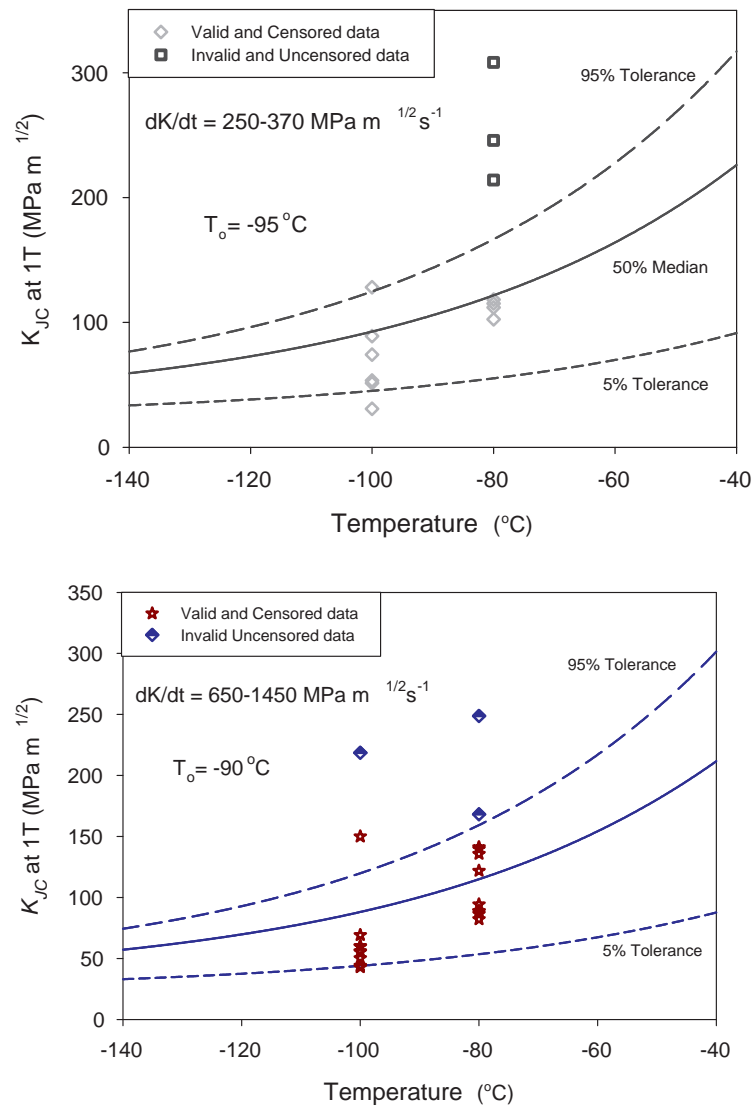


FIGURE 10.12: Master curves of 0.4T standard charpy specimens dataset of In-RAFMS tested at (a) 100 mm/min and (b) 1000 mm/min of actuator speed

2006). In the pioneer work by Beremin et al. (1983b), the effect of plastic strain was studied on the cleavage failure probability. The formation of micro-cracks in reference volume V_0 must vary for different geometry of specimens, size and temperature, which contributes to the sluggishness or abrupt initiations of micro-cracks. For the same geometry of notched tensile specimens at -196°C , (Beremin et al., 1983b) has reported a rupture strain of 15% and 69%, which resulted in average rupture stress of 1127 and 1485 MPa, respectively.

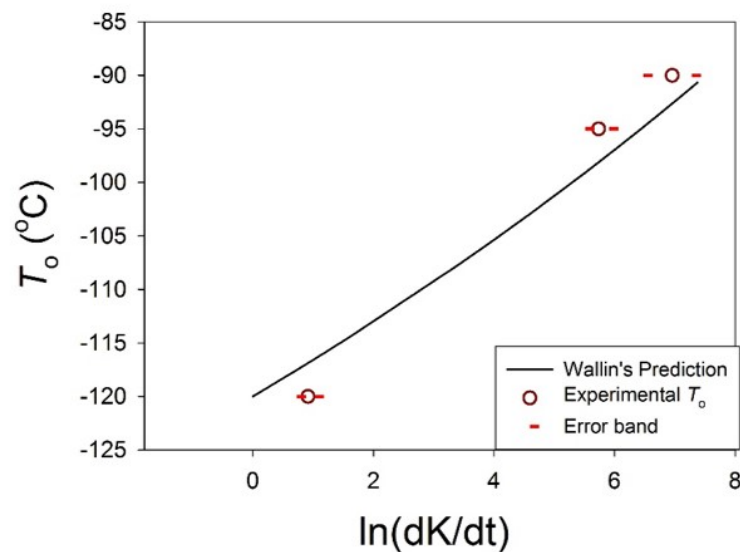


FIGURE 10.13: Shift in reference transition temperature T_0 of In-RAFMS with increasing loading rate with the prediction of Wallin according to Eq.(10.1)

In the recent work by [Ruggieri et al. \(2015\)](#), the impact of plastic strain on cleavage failure probability is extensively studied with different form of functions used for inserting the effect of plastic strain in Beremin's model (Chapter 2). Though, with different forms of plastic strain functions, close values of results can be obtained, the development of an unequivocal form of function needs both more experimental studies with larger datasets as well as analytical or empirical support. The investigation on contribution of plastic strain function on cleavage failure probability distribution remains the scope for our future study. With the observations made in this study, it can be concluded that the experimental behaviour supports the numerical predictions for the calibrated values of m for In-RAFMS and P91 steels.

10.5.2 Effect of loading rate on fracture behaviour

The experimental results obtained from the fracture tests conducted on In-RAFMS shows that the T_0 obtained at various strain rates were in accordance with Wallins prediction. The Zener-Hollomon parameter based correlation suggested by Wallin is based on the heat of activation associated with the stress relaxation on loading at higher rates. Zener and Hollomon, in their work used the indirect method of measurement of effects

of loading rates on isothermal stress-strain response of the material, by accounting for the changes due to loading rate with that due to temperature.

It is well known that the effect of strain rate on plastic flow of material is equivalent to that induced by change in temperature (Zener and Hollomon, 1944). The same was observed in the tensile behaviour of In-RAFMS, as shown in the σ_{UTS}/σ_0 versus temperature plot for quasi-static loading shown in Figure 6.6 (b) in Chapter 6. The equivalent effect of decreasing σ_{UTS}/σ_0 with increasing strain rate is also shown for In-RAFMS in Figure 6.6 (b). The Zener-Hollomon strain rate parameter based correlation given by Wallin for shift in T_0 captures efficiently the experimental results for In-RAFMS. This also implies that the activation energy defined by Zener and Hollomon, remains constant in the range of loading rate investigated in this work. As the strain rate increases the macroscopic toughness for cleavage decreases causing the T_0 to shift at higher values. This can be explained further using dislocation mobility as the effects of decreasing temperature and increasing loading rate are equivalent. The toughness of steels is demonstrated by the mobility of dislocations in lattice, which decreases with decreasing temperature and increasing loading rate. The flow behaviour of BCC alloys has been found to have thermal and athermal part (Zerilli and Armstrong, 1987; EricksonKirk and EricksonKirk, 2006). Additionally, if the thermal activation energy described by Zener and Hollomon (1944) assumed to be constant in the tested conditions, the increase in loading rate would result in decreased dislocation movement, which in turn will decrease the toughness of the material. The effect of loading rate on cleavage failure probability comparison with experimental rank probability for 100 mm/min and 1000 mm/min actuator speeds are shown in Figure 10.15(a) and Figure 10.15(b) respectively.

The fracture tests data, statistical and Weibull analysis parameters are noted in Table 10.2.

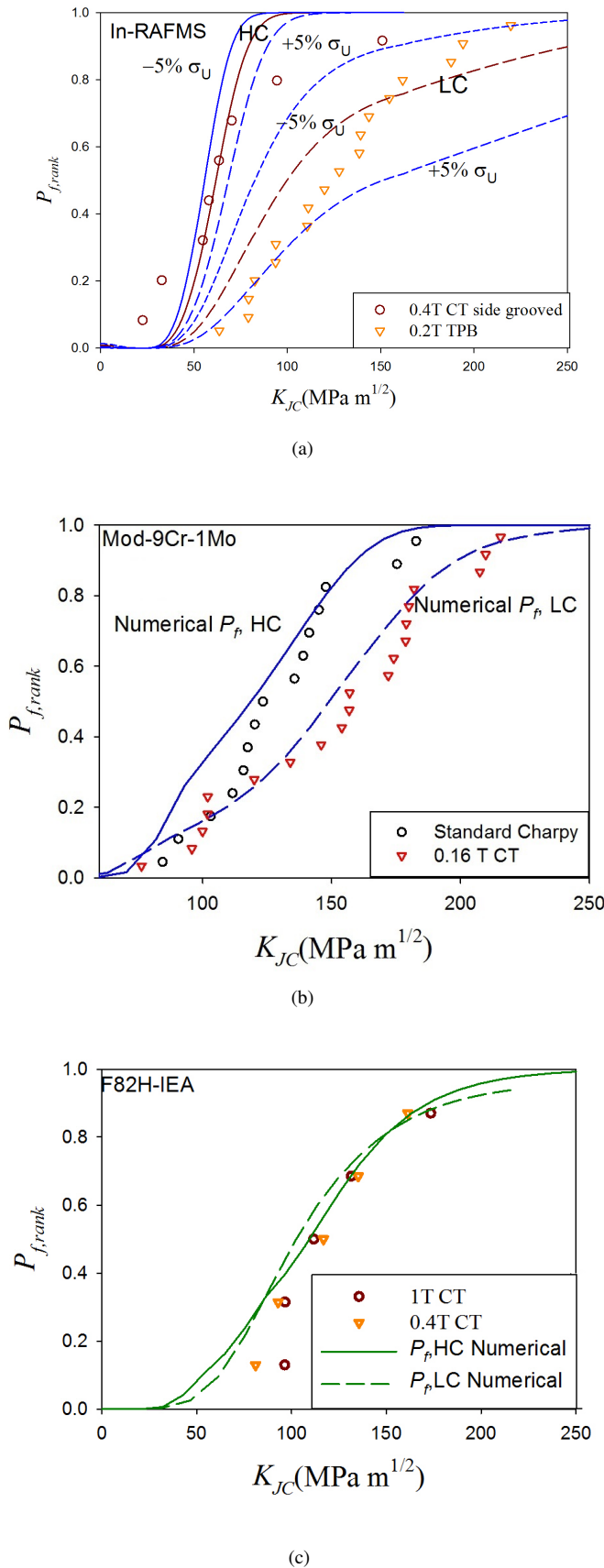
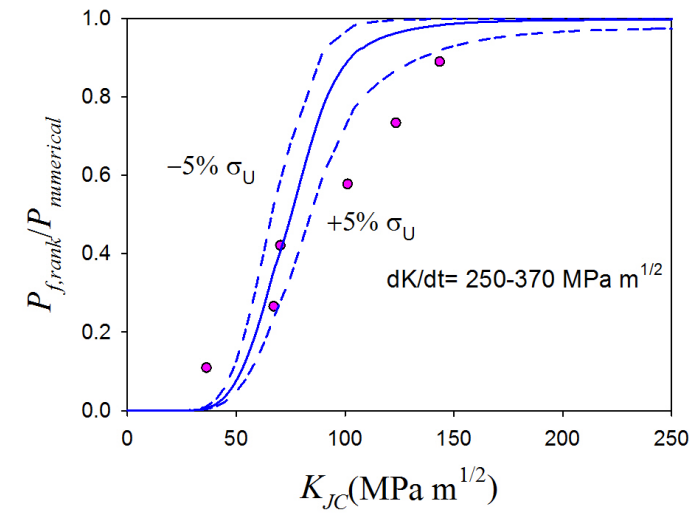
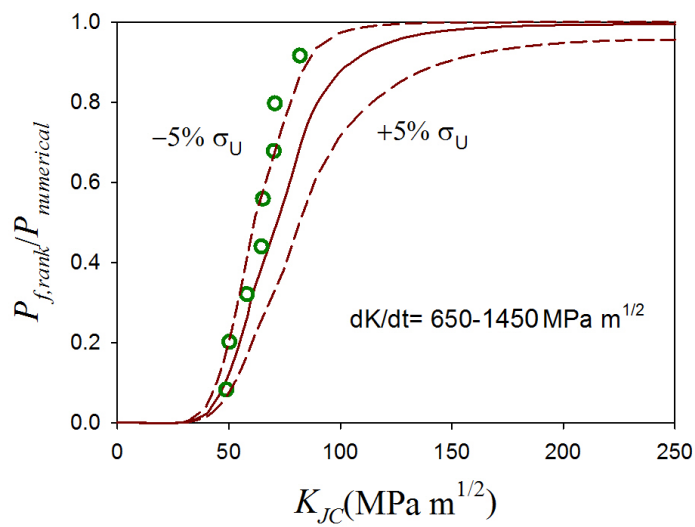


FIGURE 10.14: Cleavage failure probability with HC and LC datasets of (a) In-RAFMS (b) Mod-9Cr-1Mo and (c) F82H steels



(a)



(b)

FIGURE 10.15: Numerical prediction and experimental rank probabilities for fracture tests performed at (a) 100 mm/min and (b) 1000 mm/min actuator speed

TABLE 10.2: Numerical and statistical parameters of fracture test datasets.

	Total Tests (n_i)	Valid Tests (r_i)	T_o	(dK/dT) MPa m ^{1/2} s ⁻¹	σ_U (MPa)	σ_{W-min} (MPa)	ΔT_o by Eq. (10)	ΔT_o experimental	m at $K_{min} = 20$
In-RAFMS (HC)	26	14	-120°C	≤ 2	2900	1266	-	-	9
In-RAFMS (LC)	39	26	-123°C	≤ 2	2290	1183	-	-	9
P91 (HC)	25	15	-	≤ 2	2600	2150	-	-	15
P91 (LC)	32	20	-	≤ 2	2380	1790	-	-	15
F82H (HC)	5	5	-103°C	-	2992	1063	-	-	11
F82H (LC)	6	6	-103°C	-	2387	973	-	-	11
In-RAFMS Charpy	10	7	-95°C	250 -370	2990	1095	16.44 -17.48 °C	25 °C	9
In-RAFMS Charpy	18	8	-90°C	650 -1450	2952	1270	18.94 -20.96 °C	30 °C	9

The scaling parameter of Weibull's fit, σ_U , was found to be decreasing with the increase in loading rate. The shift in T_0 as well as in σ_U was larger when changing dK/dt from quasi-static loading rate of $2 \text{ MPa m}^{1/2}\text{s}^{-1}$ to $250\text{-}370 \text{ MPa m}^{1/2}\text{s}^{-1}$ in comparison to that for a change from $250\text{-}370$ to $650\text{-}1450 \text{ MPa m}^{1/2}\text{s}^{-1}$. The result therefore predicts that the σ_U behaviour is also similar to the behaviour of T_0 . Similar behaviour of σ_U was found by [Gao and Dodds Jr \(2005b\)](#); [Gao et al. \(2008, 2001\)](#). The scaling parameter decreased with increasing loading rate as the overall toughness of the material decreased. The load carrying capacity of the material is hampered as dislocation movement becomes difficult with increase in loading rate.

Another observation, which can be made from [Figure 10.14\(a\)](#), [Figure 10.15\(a\)](#) and [Figure 10.15\(b\)](#) that as the material toughness decreases with increase in loading rate the plastic strain impact appears to decrease. The numerical prediction comes closer to the experimental rank probability distribution from [Figure 10.14\(a\)](#) to [Figure 10.15\(b\)](#) with increasing loading rate. It can therefore be realized that the importance of plastic strain factor to assess the effect of loading rate also needs to be studied in detail to strengthen the cleavage failure probability predictions.

10.6 Conclusions

For the assessment of cleavage failure probability of ferritic/martensitic steels and to investigate the effect of loading rate on reference transition temperature T_0 along with cleavage failure probability, two grades of ferritic/martensitic steel using CT and TPB specimens were tested in DBT region. For the numerical prediction of cleavage failure probability, calibration of Weibull slope was carried out on HC and LC datasets of the two steels. Calibration of Weibull slope was also attempted on fusion reactor grade F82H steel, however, due to the reported inhomogeneity of the F82H dataset, the calibrated m may lack in accuracy.

The cleavage failure probability for In-RAFMS and P91 steels datasets, captures the experimental fracture behaviour to satisfactory extent. The prediction can be made

more accurate with an established plastic strain embedded in the calculation of cleavage failure numerical probability. The calibrated m value for In-RAFMS is found to be 9, and close in the range with other ferritic/martensitic steels analysed in this work and reported in Table 10.2.

The calibrated m value of In-RAFMS was used for assessment of fracture behaviour in DBT region at elevated loading rates. At 0.5 mm/min, 100 mm/min and 1000 mm/min of crosshead speeds the T_0 estimated are -120°C , -95°C and -90°C , respectively. It is found in the assessment that the probability of cleavage failure increases for a K_{JC} at higher loading rate and the shift in reference transition temperature T_0 is in accordance with correlation suggested by Wallin in Eq. (10.1).

Chapter 11

Master curve in upper region of DBT

The fracture behaviour of ferritic and ferritic martensitic steels in Ductile to Brittle Transition (DBT) region has been extensively studied in recent years and a probabilistic approach of master curve method is generally used to describe the fracture toughness of BCC steels in DBT region as a function of temperature. The assessment of cleavage failure probability however is still untouched in the upper region of ductile to brittle transition, although various extensions of master curve approach and various local approaches has been explored. Additionally, the geometry of specimens (CT and SE(B)) also adds up to the difficulties when cleavage failure is assisted with prior ductile tearing. In this chapter, the cleavage fracture is investigated in upper region of DBT and a modified master curve approach is presented, which can satisfactorily describe the fracture toughness as a function of temperature as well as amount of ductile tearing preceding cleavage. The methodology is explored for both CT and SE(B) geometries.

The results and findings presented in this chapter are published in:

Tiwari, Abhishek, R. N. Singh, and Per Ståhle. "Assessment of effect of ductile tearing on cleavage failure probability in ductile to brittle transition region." *International Journal of Fracture* (2017): 1-24.

and

Tiwari, Abhishek, R. N. Singh, Per Ståhle, and J. K. Chakravartty. "Master curve in upper region of ductile brittle transition: a modification based on local damage approach. *Procedia Structural Integrity* 2 (2016): 1553-1560.

11.1 Introduction

The approach of master curve and local approaches towards cleavage micro-mechanics has already been discussed earlier. The subject, which has remained untouched in this work is also the problem, which is not yet solved by the researchers of fracture community, is the problem of cleavage fracture in upper region of DBT. The phenomena of cleavage when associates itself with significant amount of DCG prior to it, the fracture toughness load-line displacement behaviour shows significant non-linearity violating SSY domain and therefore remains isolated from the conventional master curve approach or any other probabilistic approach to described cleavage failure probability.

The dataset, which comprises cleavage fracture with significant amount of prior DCG cannot be used for estimation of T_0 . The fracture behaviour therefore in upper region of DBT, which is a major part of DBT regime remains unanalysed and indescribable so far. In this Chapter the approach towards this part of DBT is dealt with.

11.1.1 Cleavage fracture in upper region of ductile to brittle transition

[Margolin et al. \(2003\)](#) has discussed this issue in detail by discussing three possibilities, which are

- Condition of cleavage fracture toughness measured at no prior ductile tearing to be equal to cleavage fracture toughness with prior DCG, which means there is no effect of prior DCG,
- Condition of cleavage fracture toughness at no prior ductile tearing to be $>$ cleavage fracture toughness with prior DCG, i.e. fracture toughness increases more steeply in upper DBT than master curve and
- Condition of cleavage fracture toughness no prior ductile tearing to be $<$ cleavage fracture toughness with prior DCG, i.e. fracture toughness increases less steeply in upper DBT than master curve.

In the work of Margolin et al. it was noticed that for general grade of ferritic steels the fracture toughness in upper DBT is much by the plastic strain and the third condition is observed. The same was experimentally observed by Tagawa et al. (2010), where the specimens of two different thickness to width ratios (B/W) were tested. Tagawa et al. concluded in their work that in upper region of DBT the cleavage failure probability scales with BK^2 rather than the master curve scaling of BK^4 .

Scibetta (Scibetta, 2010) brought out that for very low toughness materials the onset of DCG resulting in cleavage can occur prior to out of plane loss of constraint. It was also re-confirmed in the same study that the crack growth effectively increases the cleavage failure probability by resharping the crack tip and lower bound of DBT region is unaffected by such mechanisms.

The phenomena of cleavage failure with prior DCG has also been investigated by Moskovic (Doig and Moskovic, 1993; Moskovic, 2002; Burdekin et al., 1999) using log-normal distributions. The analytical contribution of sampled volume in case of prior DCG is studied by Bruckner and Munz (Bruckner and Munz, 1984). The study of Brückner and Munz and Wallin Wallin (1989a) on the probability of cleavage failure with prior DCG shows similar expressions as,

$$\ln\left(\frac{1}{1-P_f}\right) = \left(\frac{K}{K_0}\right)^4 \cdot \frac{D}{K_0^4} \int_0^{\Delta a} (f(\Delta a)^m) \partial(\Delta a) , \quad (11.1)$$

where $f(\Delta a)$ is a function of Δa and m has a value of 2 in Wallin's work and 4 in the work of Brückner and Munz. The parameter D is a function dependent on flow behaviour of the material and the position of maximum value of tensile stress ahead of crack tip. Wallin's expression of the form as shown in Eq.(11.1) assumes that the effective active volume grows with increased loading, whereas Brückner and Munz's expression assumes the active volume to be constant with crack growth. Wallin (Wallin, 1989a) simplified the probability of failure for very small prior DCG by a modified probability distribution as,

$$\ln\left(\frac{1}{1-P_f}\right)^{1/4} = \left(\frac{B_{nT}}{B_{1T}}\right)^{1/4} \left(\frac{K - K_{min}}{K_o - K_{min}}\right) \cdot \left(1 + 2\frac{\Delta a \sigma_{flow}^2}{K^2 \beta}\right)^{1/4}, \quad (11.2)$$

where $\beta = 3.5\left(\frac{K_{JC}}{\sigma_o}\right)^2$, is the distance from the crack tip to the boundary of the active volume and σ_{flow} is the average of ultimate tensile strength and Yield strength (σ_o). The simplification in the form of Eq.(11.2) was given by Wallin to avoid cumbersome integration of function of Δa and this form of equation was suggested to be valid for a small amount of Δa where K_{JC} versus Δa behaviour is flat.

With the discussion on master curve methodology and process of cleavage fracture in upper region of DBT, it is observed that the cleavage is generally preceded by significant amount of ductile tearing in upper region of DBT. The K_{JC} inevitably fails to single handedly describe the fracture toughness and master curve methodology cannot be used for describing the correlation of fracture toughness with temperature. The problem therefore arises with the dataset, which shows cleavage fracture and yet cannot be used straight away for probabilistic determination of its correlation with temperature. The conventional master curve methodology censors the dataset generated in upper DBT. Censoring the dataset in DBT region is a powerful tool to utilize the data, which do not fall into the validity window of the statistical model of master curve. The censoring scheme is schematically shown in Figure (11.1).

In case of MC approach another censoring method for loss of constraint is applied, which uses the ligament length and the flow properties of the tested sample and limits the toughness by a constraint parameter M is described in Chapter 2, Eq.(2.13). The value of $K_{JC,limit}$ is, according to Eq.(2.13), the fracture toughness, which sample would have achieved in SSY condition. The tested toughness value, i.e. $K_{JC,exp}$ is discarded from the analysis. This part of censoring is appreciated by the authors for constraint loss, however constraint correction methods (Tiwari et al., 2015; Gao and Dodds Jr, 2000) can be used to transform the invalid toughness values to a SSY equivalent values. The numerical correction and MC censoring are similar in nature and any of the method can be used.

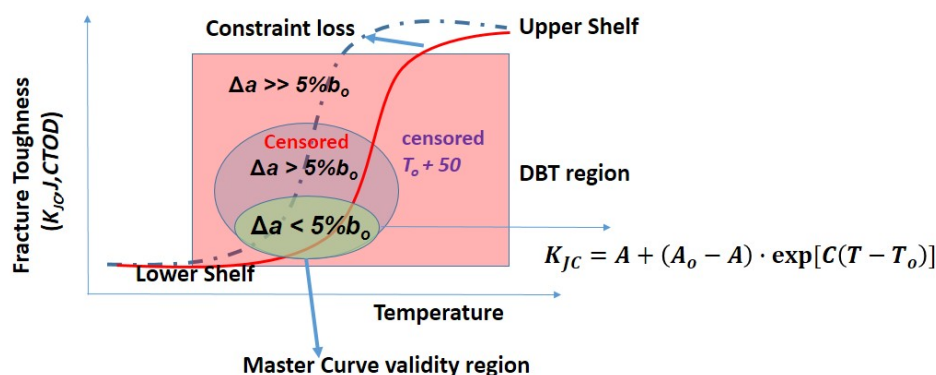


FIGURE 11.1: Schematic of validity criteria of datasets used in master curve method

The censoring where the data corresponding to cleavage failure with significant amount of ductile tearing is also appreciated as long as the analysis method is master curve approach. The real behaviour of upper region of DBT and utilization of dataset belonging to upper region of DBT in assessment of a transition temperature is missed by conventional methods. The question arises that whether the dataset in upper region of DBT can be dealt in a similar way and whether it would be possible to elevate the structural potential of a material, which might be under utilized by conventional conservative approaches.

The fracture toughness with temperature changes in upper DBT drastically due to the significant changes at the crack tip activities due to prior ductile tearing. Whether or not the master curve methodology holds good to certain extent is one of the question being investigated in this study. The answer to the question imposed by the event of cleavage preceded by ductile tearing is not very simple, however it is certain that the fracture toughness is not dependent on temperature only. The amount of ductile tearing significantly alters the behaviour of fracture toughness with temperature.

The objective of this work is to answer some of the questions if not all. The upper region of DBT is examined using existing approaches and works of other researchers and an important factor of constraint increment with DCG, which is missing in earlier studies of this subject, is incorporated.

In our approach, the cumbersome integration part of Eq.(11.1) is solved with an assumption that the materials resistance curve remains unchanged in the DBT region. This assumption is not far from reality for many of the tested materials. The approach to study the upper region of DBT is studied in this work by extending the master curve concept and incorporating the changes occurring due to prior ductile tearing. The conventional master curve is an extensively studied subject and has been proven to be a strong tool to measure reference transition temperature as a global parameter independent of specimen geometry, loading rate and type of loading. The analysis of upper region of DBT ought to complicate the simple master curve methodology but it is justifiable for the complex nature of fracture behaviour in this region of transition. It is not the objective of this work to create a cumbersome methodology. The work presented explores the upper region of DBT and efforts are made to make the fracture data available in upper region of DBT potent enough to determine T_0 , which otherwise may not be determined for a completely or partially invalid dataset.

11.2 Material datasets

For the assessment of effect of fracture behaviour in DBT region, the largest dataset is the *Euro Fracture* dataset. This dataset was created by testing 0.5T, 1T, 2T and 4T thick Compact Tension (CT) specimens at various laboratories across Europe on 22NiMoCr37 steel. The cumulative dataset contains test results conducted over many years. For the assessment of modification proposed in this work on cleavage failure probability, the dataset of 0.5T specimens are used as the dataset of 0.5T specimens contain most of the cleavage data affected by prior DCG.

Apart from Euro dataset, 0.4T CT specimen dataset and 0.2T SE(B) dataset of In-RAFMS were also used for assessment of effect of prior ductile tearing on cleavage fracture. The material and experimental details are provided in Chapter 4 and 5, respectively.

11.3 Cleavage with prior DCG

11.3.1 Increasing active volume with DCG

The volume as discussed above, which influences the cleavage event is the volume, which is under sufficient tensile stress and, which has deformed plastically. This volume is shown schematically in two dimension for a crack growth of Δa in Figure 11.2. It

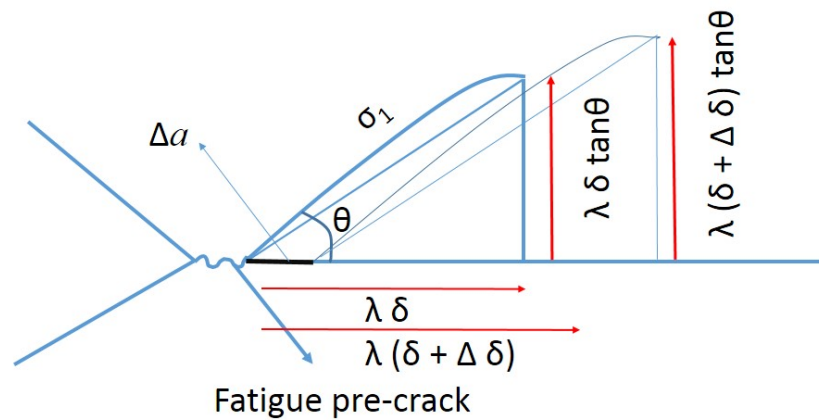


FIGURE 11.2: Schematic of increasing active volume with ductile tearing

is well studied that the maximum first principal stress is achieved at a distance of 2-4 times of Crack Tip Opening Displacement (CTOD) symbolized as δ . For a material this value of proportionality is constant in the range of 2-4 and therefore, for our calculation of increasing active volume it is assumed that the maximum first principal stress is achieved at a distance of λ times of CTOD. Similar to the derivation of Wallin, an arbitrary triangular area is considered as shown in Figure 11.2 for derivation. It is also assumed here that the stress field remains self-similar along the thickness. For initial condition of no crack growth, the active volume for the half symmetric crack tip as in Figure 11.2 would be

$$V = \frac{1}{2} \lambda \delta_i \cdot \lambda \delta_i \cdot B \tan \theta , \quad (11.3)$$

where B is the specimen thickness and δ_i is the initiation CTOD. It is a valid assumption made here that the scaling of the perpendicular and the base of the triangular region in Figure 11.2 remains unchanged with DCG (Wallin, 1989a). Thus, after a ductile through thickness crack growth of Δa the active volume would be

$$V = \frac{1}{2} \lambda(\delta + \Delta\delta) \cdot \lambda(\delta + \Delta\delta) \cdot B \tan \theta , \quad (11.4)$$

The scaling volume V_o as described by Wallin can be defined by the argument of BK^4 scaling with V_i as the active volume at the CTOD of δ_i as

$$V_o = V_i \frac{\delta_o}{\delta_i} . \quad (11.5)$$

The cleavage failure probability as a function of active volume can be described as

$$P_f = 1 - \exp\left[-\frac{\rho}{\rho_o} \cdot \frac{V - V_{min}}{V_o - V_{min}}\right] . \quad (11.6)$$

where ρ defines the number density of critical cleavage initiators taking part in micro-crack generation. Under the assumption of homogeneous distribution of cleavage initiators it is not unwise to state that ρ at any point of applied K will be same as ρ_o , only if there is no crack growth. The effect of crack growth on P_f will be discussed in section 11.3.2. For through thickness self similarity and for V_{min} to be zero, the cleavage failure probability can be simply defined as

$$P_f = 1 - \exp\left[-\frac{V}{V_o}\right] . \quad (11.7)$$

Using the expressions of V and V_o from Eq.(11.4) and Eq.(11.5) and ignoring the higher order terms, the probability of cleavage failure can be re-written as,

$$\ln\left(\frac{1}{1 - P_f}\right) = \frac{\delta^2}{\delta_o^2} \cdot \left(1 + 2\frac{\Delta\delta}{\delta}\right) . \quad (11.8)$$

By using the fact that CTOD is directly correlated to J and again transforming J to K , Eq.(11.5) can be re-written as,

$$\ln\left(\frac{1}{1-P_f}\right) = \frac{K^4}{K_0^4} \cdot \left(1 + 2\frac{(\Delta K)^2}{K^2}\right). \quad (11.9)$$

The derivation of increment in active volume is similar to that of Wallin and for more details the readers are referred to the work of Wallin (1989a). The expression however differs and is more simple in this case. Another simplification is incorporated by describing the K versus Δa correlation with K_i as the initiation fracture toughness as,

$$K = K_i + \phi(\Delta a)^m. \quad (11.10)$$

The K correlation with Δa as described above is used to replace ΔK from Eq.(11.9), which results in cleavage failure probability as,

$$\ln\left(\frac{1}{1-P_f}\right) = \frac{B_{nT}}{B_{1T}} \frac{K^4}{K_0^4} \cdot \left[1 + 2\frac{(\phi(\Delta a)^m)^2}{K^2}\right]. \quad (11.11)$$

11.3.2 Change in constraint with DCG

In the assessment of effect of ductile tearing on cleavage failure probability by Wallin as well as Brückner and Munz, the change in constraint associated with ductile crack growth was ignored. For a significantly smaller crack growth, this assumption does not result in much error, however, for a significant amount of ductile tearing as observed in upper region of DBT, the change in constraint needs to be addressed in the cleavage failure probability calculation.

As the crack grows, the sampled volume increases and the probability of cleavage failure increases. The initial ductile tearing may occur due to the overall increase in plasticity of material matrix or due to the constraint loss. Both result in increase in toughness values. As the crack advances, the constraint increases due to decreasing ligament length. In other words, the ductile tearing may start due to constraint loss or higher test temperature, which makes carbides less critical for unstable crack growth and tries to

achieve higher constraint by increasing a/W . However, if the carbide becomes critical for instability, cleavage occurs.

It is many a times doubted whether the change in constraint with advancing crack is positive i.e. constraint increases or negative i.e. decreases, despite numerous works in literature on both CT and SE(B) geometries in support of increment in constraint with DCG (Moattari et al., 2016; Varias, 1998; Yan and Mai, 1997; Ruggieri and Dodds Jr, 1996). The increment in constraint is attributed to the decreasing ligament length and to understand the effect in a very simple way one can take an imaginary ligament to be the reference frame. This imaginary ligament is assumed to be constant with growing crack. In reality however, the ligament will decrease and so will the ratio of ligament and thickness of the specimen. To keep this ratio same for imaginary ligament the thickness should increase. Therefore, a crack growth process can be viewed as a transition from a thinner to thicker specimen with decreasing ligament to thickness ratio. The importance of ρ in Eq.(11.6) is readily brought out as the change in constraint will change the effective distribution of inhomogeneities/carbides, which become critical for micro-crack initiation. Thus, the probability of cleavage fracture needs further modification to incorporate the changes occurring in $\frac{\rho}{\rho_0}$ with increasing constraint. It is already discussed by many researchers that for α number of carbides taking part in cleavage fracture directly, the condition of ductile tearing i.e. increasing plastic strain imposes a few of these carbides say α_0 to participate in micro-void coalescence. Therefore, only $\alpha - \alpha_0$ number of carbides remain available for next active volume for cleavage initiation as those taking part in micro-void coalescence cannot contribute to micro-crack nucleation and its dynamic propagation. The number of carbides taking part in micro-void coalescence depends on amount of plastic strain. The events taking place at the crack tip for a ductile matrix chronologically can be described as below.

- With applied loading the stresses at the crack tip increases and the crack tip deforms plastically. If the carbides in the active volume do not initiate micro-cracks the plastic strain continues to increase and the micro-void coalescence occurs as

it becomes difficult for the micro-crack generated by failed carbide to move into the matrix at lower stresses.

- The micro-voids subsequently grow and coalesce further to promote ductile tearing. Statistically it can be visualized that all the carbides may not participate in micro-void coalescence and some may participate in micro-cracks propagation into the matrix, which locally escalates the probability of cleavage according to Eq.(11.6).
- As the crack grows the volume ahead of crack tip consists of a region, which is elastically unloaded followed by a new active volume, which may take part in cleavage fracture and a region between these two where plastic strain is higher to promote nucleation, growth and coalescence of voids (Ruggieri and Dodds Jr, 1996).
- With the crack growth, the constraint ahead of the crack tip increases and the chances for carbides to contribute in micro-void coalescence decreases.

With the above discussion, it can be concluded that the increasing constraint can be used as a measure of change in ρ with respect to the initial distribution density of carbides. Generally for a growing crack the constraint is measured by a factor q also known as triaxiality parameter, which is defined as the ratio of hydrostatic stress component, σ_h and equivalent stress σ_{eq} (Ruggieri and Dodds Jr, 1996; Yan and Mai, 1997; Moattari et al., 2016)

As the constraint increases the material flow is restricted and the material around the carbide cannot increase its plastic strain easily in comparison to the matrix where constraint is less. With triaxiality ratio q as a measurement of constraint, a simple function can be defined to accommodate the effective increment in potential cleavage initiators. This increment should have a reference frame set at the initial testing condition and the number density of potential cleavage initiators should increase with increasing constraint due to Δa . This function is defined here by assuming a linear proportionality

between $\frac{\rho}{\rho_0}$ and corresponding triaxialities as,

$$\phi = \frac{q_f}{q_i}, \quad (11.12)$$

where q_f is the final triaxiality factor and q_i is the triaxiality factor before the ductile tearing starts. The linear approximation is inspired from the pioneer work of Argon et al. (Argon et al., 1975) and Beremin et al. (Beremin, 1981) where the stress based criteria for debonding of inclusions to form cavities is a function of $\sigma_h + \sigma_{eq}$, which can be rearranged to be a function of q as $\sigma_{eq}(1 + q)$. As the debonding of the inclusion is accelerated with increasing constraint for a system of carbides it would assist in dynamic propagation of micro-cracks into matrix and from one grain to another before the plastic strain limit for micro-void coalescence is reached.

With earlier discussion on increasing active volume calculation and triaxiality function, the cleavage failure probability can now be redefined with the increment in active volume and cleavage initiators with a function of q as,

$$\ln\left(\frac{1}{1 - P_f}\right) = \frac{B_{nT}}{B_{1T}} \left(\frac{q_f}{q_i}\right) \cdot \left(\frac{K - K_{min}}{K_0 - K_{min}}\right)^4 \cdot \left[1 + 2 \frac{(\phi(\Delta a)^m)^2}{K^2}\right]. \quad (11.13)$$

The maximum likelihood analysis of Eq.(11.13) is carried out using Eq.(2.10) and Eq.(2.11). The maximization of maximum likelihood parameter L is performed only with respect to T_0 as other variables of Eq.(11.13) are kept as in ASTM E1921, with $K_{min} = 20 \text{ MPa m}^{1/2}$. Detailed maximum likelihood analysis procedure for Eq.(11.13) is provided in Appendix A.3.

The temperature dependence of K_{JC} in modified master curve follows same behaviour as in conventional master curve described in Eq.(2.6). For a mean approximation of K_{JC} behaviour with ductile crack growth Δa , the dependency of K_{JC} with ductile tearing can be described as,

$$K_{JC,med} = A + (100 - A) \exp\{0.019(T - T_0)\} = K_{JC,ini} + \phi(\Delta a)^m. \quad (11.14)$$

where $K_{JC,ini}$ is the initiation fracture toughness and ϕ and m are the power law fitting

constants. The modified master curve therefore follows the correlation with Δa either coming out as a mean approximation from the experimental data or from the numerical prediction based on finite element analysis.

With the cleavage failure probability described in the form of Eq.(11.13), one can express the cleavage failure probability for two differently sized specimens, say of thickness nT and $1T$ where T denotes thickness in *inches*, with same amount of cleavage fracture probability as,

$$B_{nT} \cdot \frac{K_{nT}^4}{K_0^4} \cdot f(\Delta a) = B_{1T} \cdot \frac{K_{1T}^4}{K_0^4} \cdot f(\Delta a) . \quad (11.15)$$

It is required here to have a mean approximation of size independent $K_{JC} - \Delta a$ or a $K_{JC} - \Delta a$ correlation obtained by numerically analysing 1T reference thickness geometry. In this case the function dependent on DCG cancels out and size adjustment scheme of conventional master curve can be used for the proposed modification. In the formulation of Eq.(11.13) there is a function dependent on triaxiality also included in the probability expression. This function assuming it to be independent of other parameters will also cancel out for a size independent behaviour for same amount of DCG. The effect of plastic strain embrittlement on the triaxiality function is discussed in section 6, which supports the unchanged size adjustment scheme.

11.4 Numerical analyses

The numerical analysis to simulate prior ductile crack growth to cleavage, was carried out with ductile damage. The failure criteria of elements were ductile damage dependent. The load displacement response of the model was used to calculate K_{JC} by assuming cleavage to occur at each increment of crack. The finite element analyses of both CT and TPB geometries were performed for measurement of change in constraint with ductile tearing.

The plastic behaviour, using isotropic hardening following the true stress plastic strain response used as input, was implemented in VUMAT subroutine. The numerical solution followed full Newtonian non linear algorithm using explicit scheme. The mesh size was kept constant in the area of interest near the crack tip for volume calculation as the post processing for active volume calculation requires the elemental volume to be constant in the crack tip region (Tiwari et al., 2015). Twenty noded brick elements were used for both tensile specimen models as well as CT and TPB fracture models. The element size near crack tip was 0.15 mm in thickness direction and 0.2 mm in plane normal to crack front.

11.4.1 Ductile damage implementation

The ductile damage was introduced in the finite element analyses using Gurson, Tvergaard and Needleman (GTN) (Gurson, 1977; Tvergaard, 1982; Tvergaard and Needleman, 1984) model. The details of the ductile damage implementation is given in Chapter 5, section 5.2.2.

11.4.2 Calibration of GTN parameters

Initially it was required to justify that the user subroutine VUMAT was coded correctly. Therefore, the subroutine was compared with the ductile damage porous plasticity in-built in ABAQUS FEA package. The geometry of the tensile specimen modelled is shown in Figure 11.3(a) In Figure 11.3(b), the comparison of the engineering stress strain response of quarter symmetric three dimensional (3D) model of tensile specimen is shown. The calibration of GTN parameter and VUMAT with calibrated parameter is compared in Figure 11.3(b). The void volume fraction f^* at the centre of the quarter symmetric tensile model is also compared in Figure 11.3(c).

It can be realized from Figure 11.3(c) that the VUMAT coded was reasonably accurate. The reason for coding of ductile damage using VUMAT subroutine was preferred on

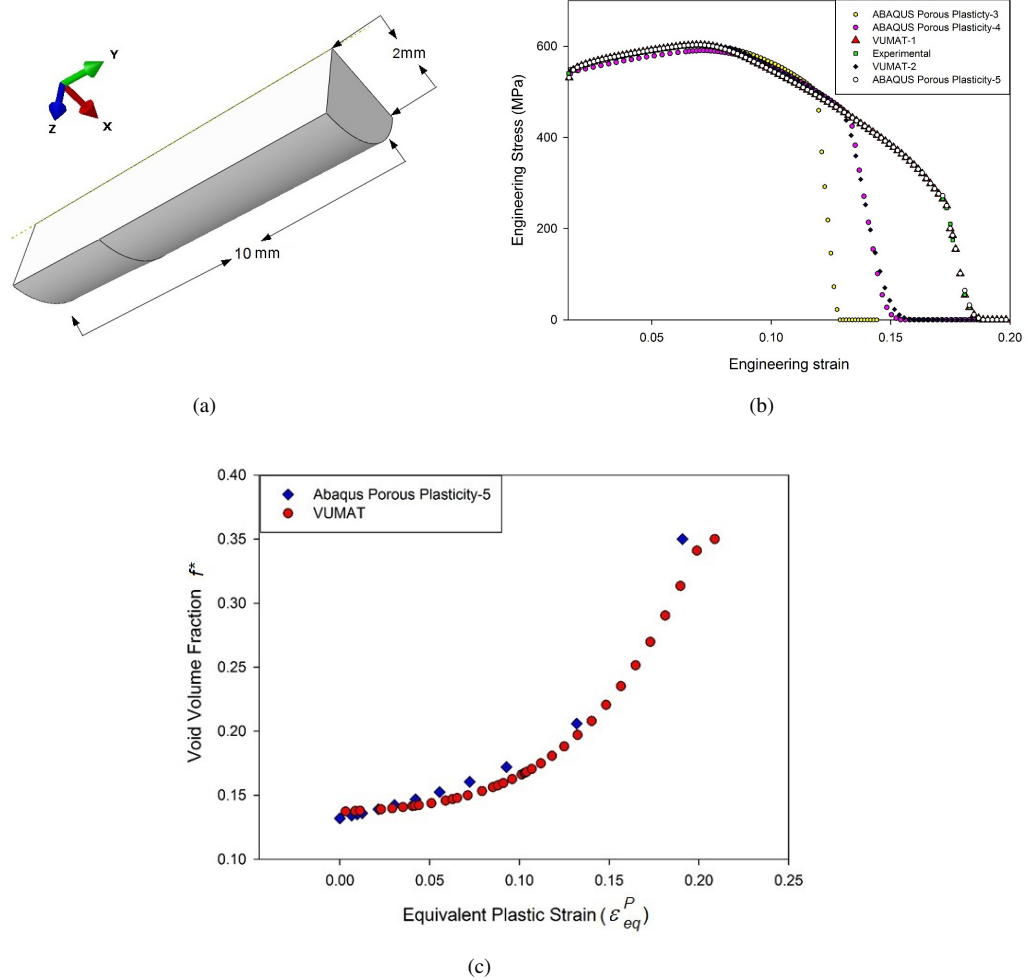


FIGURE 11.3: Implementation of ductile damage in FEM using VUMAT subroutine; (a) Geometry of quarter symmetric tensile specimen (b) Calibration of GTN parameters (c) Comparison of calibrated VUMAT with Abaqus porous plasticity

ABAQUS in-built porous plasticity, to have freedom in changing or removing nucleation or growth rate calculations if needed.

11.4.3 Finite element models of CT and TPB geometries

The GTN parameter calibration was carried out using ABAQUS in-built porous plasticity algorithm using 3D explicit 8 noded brick elements with $2 \times 2 \times 2$ Gaussian points. The initial trial of GTN parameters were taken from the work of [Stratil et al. \(2014\)](#) on Eurofer 97. The plasticity data were given in form of true stress-true plastic strain

extrapolated to a final plastic strain of 2. The plastic data used for modelling, corresponded to In-RAFMS tensile data tested at -110°C and -130°C . At these temperature many fracture specimens tested in three point bending revealed significant ductile crack growth prior to cleavage failure.

The mesh and boundary conditions with quarter symmetric specimen dimensions for CT and TPB geometries are discussed in Chapter 5. The GTN parameters for porous plasticity and VUMAT subroutine models used for calibration of -110°C tensile specimen response for In-RAFMS is shown in Table 11.1.

TABLE 11.1: Trials used for GTN parameter calibration for In-RAFMS tensile response at -110°C

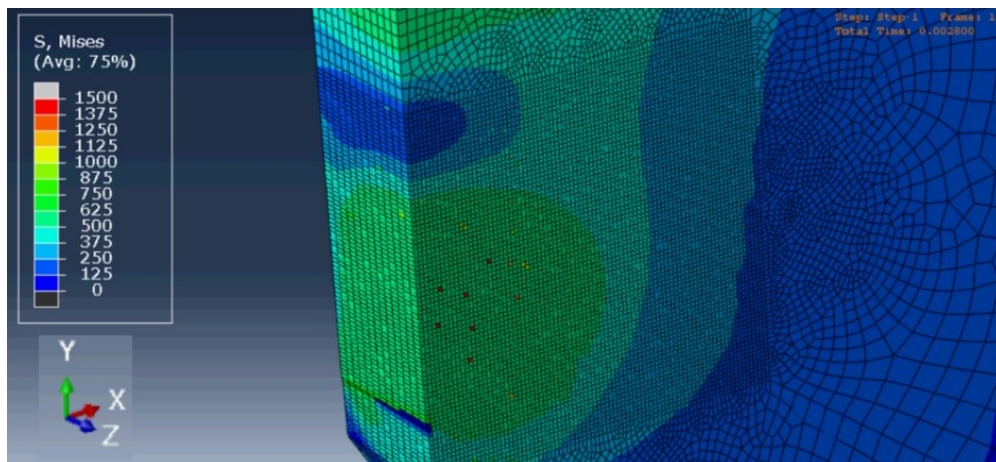
Tensile models	GTN Parameters						
	q_1	q_2	f_F	f_C	μ	σ_{std}	f_o
Abaqus porous plasticity-1	1.26	0.931	0.1	0.02	0.3	0.1	0.00088
Abaqus porous plasticity-2	1.26	0.931	0.17	0.01	0.3	0.1	0.00088
Abaqus porous plasticity-3	1.26	0.931	0.1	0.01	0.3	0.1	0.00088
Abaqus porous plasticity-4	1.06	0.931	0.29	0.1	0.3	0.1	0.00088
Abaqus porous plasticity-5	1.06	0.931	0.35	0.1	0.3	0.1	0.00088

Apart from the objective of obtaining change in constraint and fracture responses from the finite element models a qualitative study of increasing number density of carbides taking part in cleavage fracture with increasing DCG was also performed on SE(B) geometry by assigning linear elastic properties for small number of elements, chosen pseudo-randomly using computer code. The increasing stresses on these elements simulating elastic response while matrix deforms plastically confirms increasing $\frac{\rho}{\rho_0}$ as depicted with continuous crack growth in Figure 11.4.

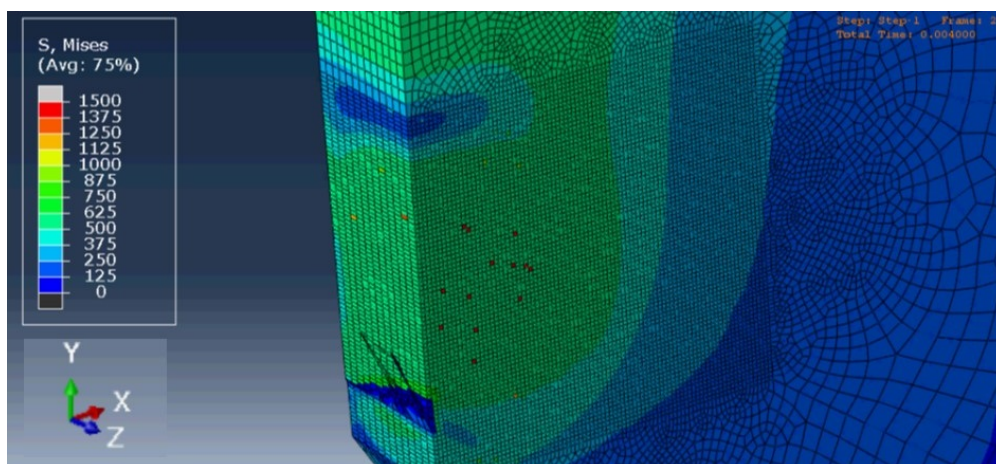
For the application of modified master curve formulation on Euro fracture data, three test temperatures were chosen to investigate the effect of plastic strain in terms of void volume fraction at failure and embrittlement in terms of true stress logarithmic strain response. The three test temperatures, 0°C , -20°C and -60°C were chosen as at 0°C and

-20°C, most of the data were affected by prior DCG and at -60°C many conventionally valid data were available for comparison of conventional and modified master curve.

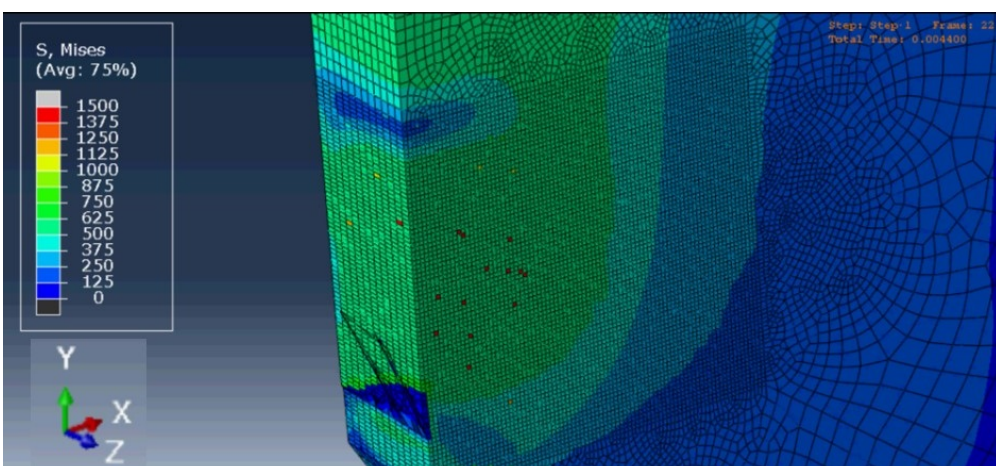
The 22NiMoCr37 steel tensile data were obtained from [Heerens and Hellmann \(2002\)](#). The true stress strain behaviour of 22NiMoCr37 steel used for FE analyses is shown in [Figure 11.5 \(a\)](#).



(a)



(b)



(c)

FIGURE 11.4: Pseudo-randomly distributed elastic elements showing effect of constraint on criticality of carbides (a) Onset of DCG and carbides, (b) $\Delta a = 0.2mm$, (c) $\Delta a = 0.4mm$

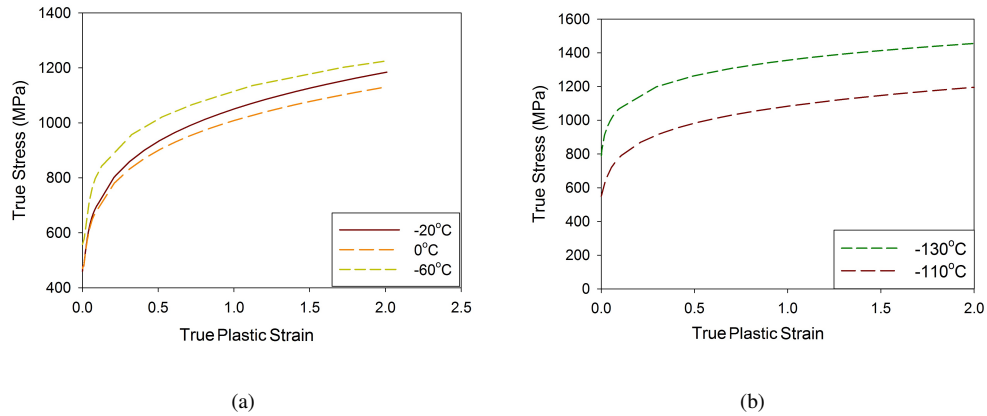


FIGURE 11.5: True stress plastic strain response extrapolated to 2 for (a) 22NiMoCr37 and (b) In-RAFMS steel

The true stress plastic strain response used for finite element analyses of In-RAFMS at -110 and -130°C are shown in Figure 11.5 (b). The GTN parameters for 22NiMoCr37 steel used for modelling ductile crack growth were calibrated using load displacement response. The tensile load displacement response for 22NiMoCr37 steel was obtained from <ftp://ftp.gkss.de/pub/eurodataset> and the final point was assumed to be the failure point. The calibrated GTN parameters for 22NiMoCr37 steels and In-RAFMS are shown in Table 11.2.

TABLE 11.2: Calibrated GTN parameters used for ductile crack growth modelling for In-RAFMS and 22NiMoCr37 steels

Euro Fracture Data Material (22NiMoCr37 Steel)									
Test Temperature	YS	UTS	f_o	σ_{std}	GTN parameters				
					μ	q_1	q_2	f_c	f_F
0	470	621	0.009	0.1	0.3	1.35	0.931	0.08	0.12
-20	476	640	0.008	0.1	0.3	1.05	0.78	0.1	0.15
-60	509	670	0.008	0.15	0.3	1.35	0.931	0.08	0.12
In-RAFMS									
Test Temperature	YS	UTS	f_o	σ_{std}	GTN parameters				
					μ	q_1	q_2	f_c	f_F
-110	560	710	0.00088	0.1	0.3	1.06	0.931	0.1	0.1
-130	790	951	0.00088	0.1	0.3	1.01	0.95	0.1	0.15

11.5 Results

Finite element modelling of CT and TPB geometries with GTN damage made it possible to calculate the change in triaxiality factor q with Δa . The behaviour of changing q with crack length to specimen width ratio for the CT and TPB models are shown in Figure 11.6 (b).

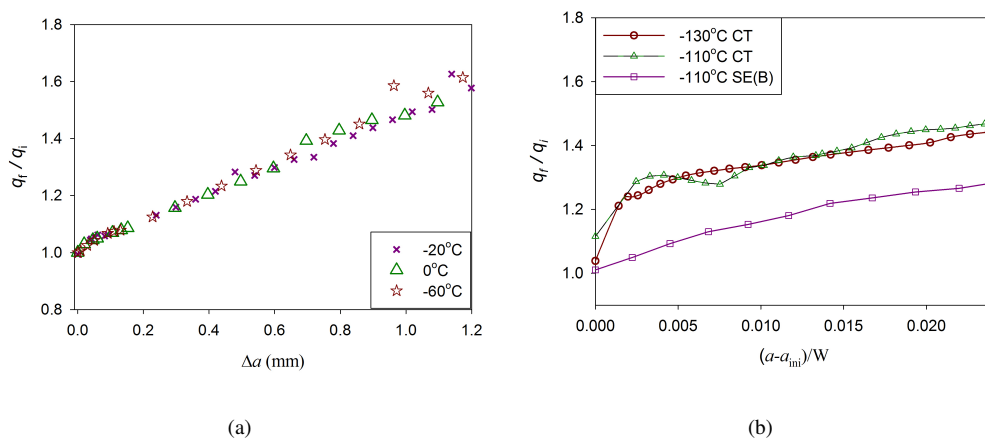


FIGURE 11.6: Triaxiality ratio q_f/q_i at different temperatures for (a) 0.5 T CT 22NiMoCr37 steel, (b) 0.4 T CT In-RAFMS steel

Similar behaviour was observed for the material of Euro fracture data, i.e. DIN 22NiMoCr37. The behaviour of triaxiality function for 22NiMoCr37 steel at three different temperature obtained by modelling 0.5T CT geometry is shown in Figure 11.6 (a).

The qualitative finite element results to visualize effect of increment in potential cleavage initiators is shown in Figure 11.4, where as the ductile crack grows more numbers of pseudo-randomly selected elements feel higher stresses, confirming the effect of increasing constraint on $\frac{\rho}{\rho_0}$.

The increasing active volume with ductile tearing for TPB and CT side grooved models are shown in Figure 11.7.

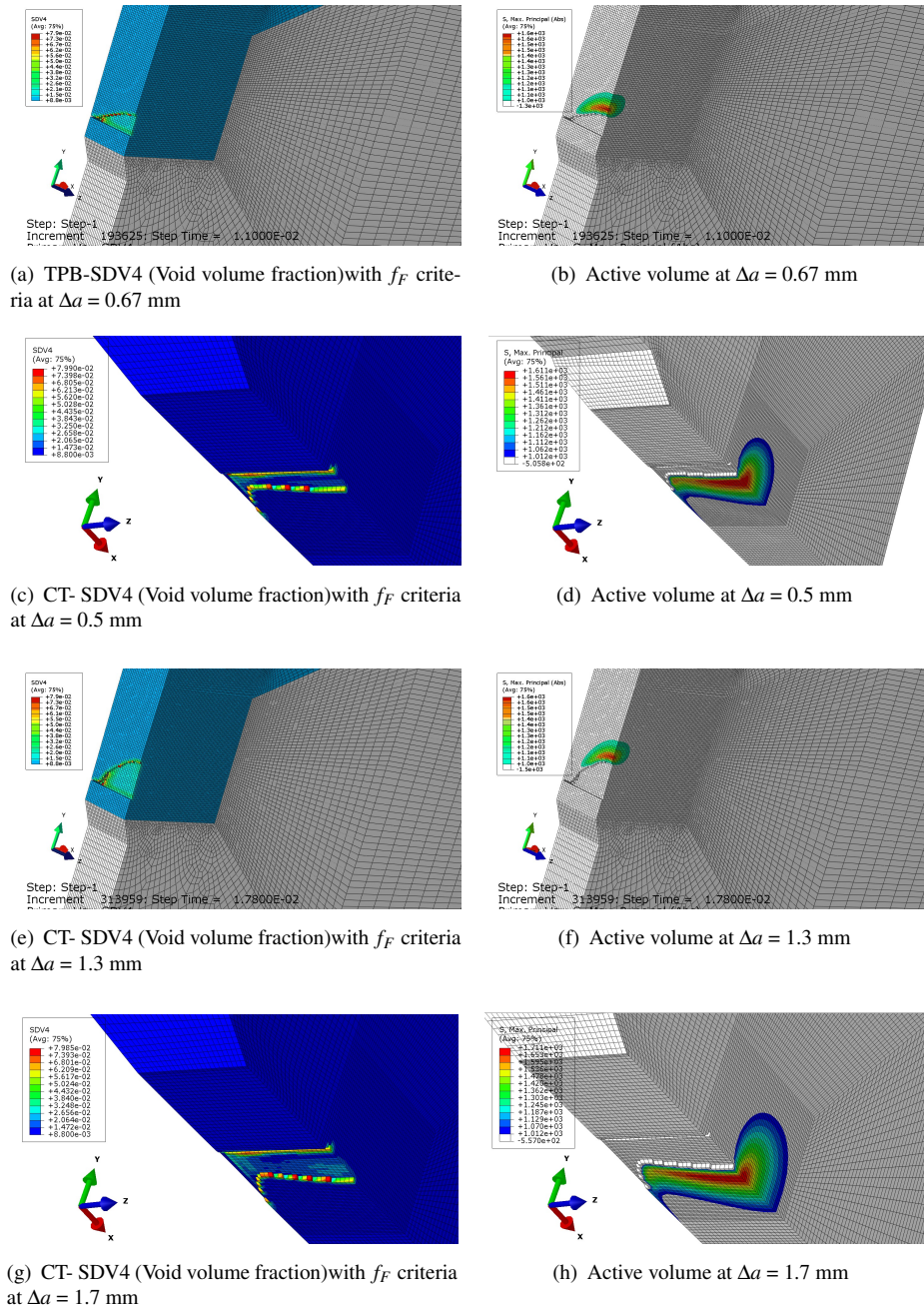


FIGURE 11.7: Ductile tearing based on GTN ductile damage in 0.4T CT side grooved and 0.2T TPB geometries modelled with material parameters corresponding to -110°C for In-RAFMS

The modified master curve analyses were performed on different datasets as discussed earlier using Eq.(11.13) with a partial censoring approach. As discussed in section Chapter 2, the conventional master curve applies two fold of censoring on the fracture data. The censoring to avoid contribution in non-linearity of load-displacement behaviour due to ductile tearing is avoided in modified master curve analysis. Any data showing ductile tearing is treated valid and only those data, which showed no DCG and

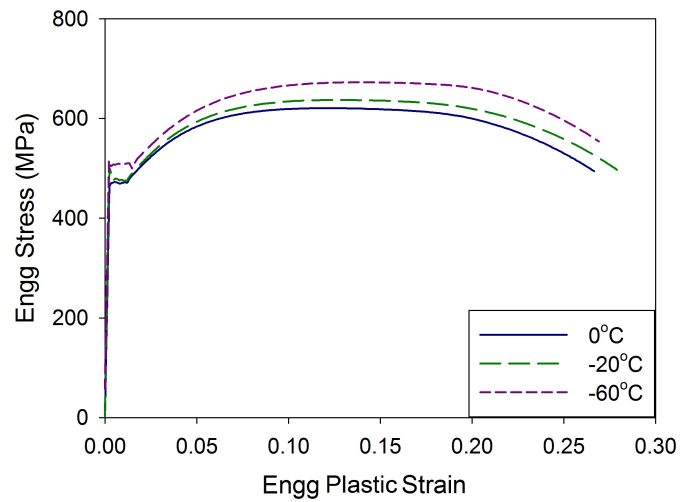
crossed the criteria of $K_{JC,limit}$ based on out of plane constraint loss, were censored. This approach of single fold censoring increases the validity window of conventional master curve and expands it to upper region of DBT. The results of master curve analyses on different datasets are discussed below.

11.5.1 Euro fracture data

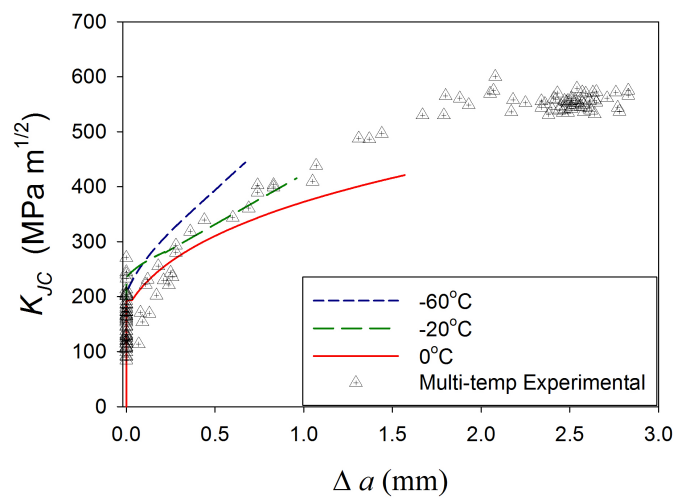
The Euro fracture dataset of 0.5T CT specimen shows ductile crack growth as high as 2.54 mm. The K_{JC} versus Δa behaviour for 0.5T CT dataset and one obtained at 0°C, -20°C and -60°C by finite element analyses are shown in Figure 11.8 (b).

The dataset does not show much variation in the behaviour in the temperature region of -60°C to 0°C for 0.5T CT specimens. The correlations obtained in form of Eq.(11.10) were used for maximum likelihood analysis of modified master curve.

The reference transition temperatures for dataset affected by Δa is analysed using Eq.(11.13) is expected to shift lower due to increasing $K_{JC,med}$. This behaviour as a result of modified master curve analysis is shown in Figure 11.9 (a). The comparison is shown by further categorizing the dataset in three sections. The first section includes dataset with $\Delta a < 1$ mm, the second section with Δa varying in range of 1.2 mm to 1.45 mm and the third section with $\Delta a > 1.45$ mm. The change in T_o , as discussed earlier can be predicted by Eq.(11.14), which is compared with the modified master curve results in Figure 11.9 (b).



(a)



(b)

FIGURE 11.8: (a) Engineering Stress-strain response 22NiMoCr37 steel tensile specimens and (b) $K_{JC} - \Delta a$ response of 0.5T CT Euro data

11.5.2 In-RAFMS data

The fracture tests performed on In-RAFMS comprised 26 tests on 0.4T CT specimens and 39 tests on 0.2T TPB specimens in the range of test temperature from -50°C to -150°C . The finite element based K_{JC} versus Δa behaviour calculation was carried out for

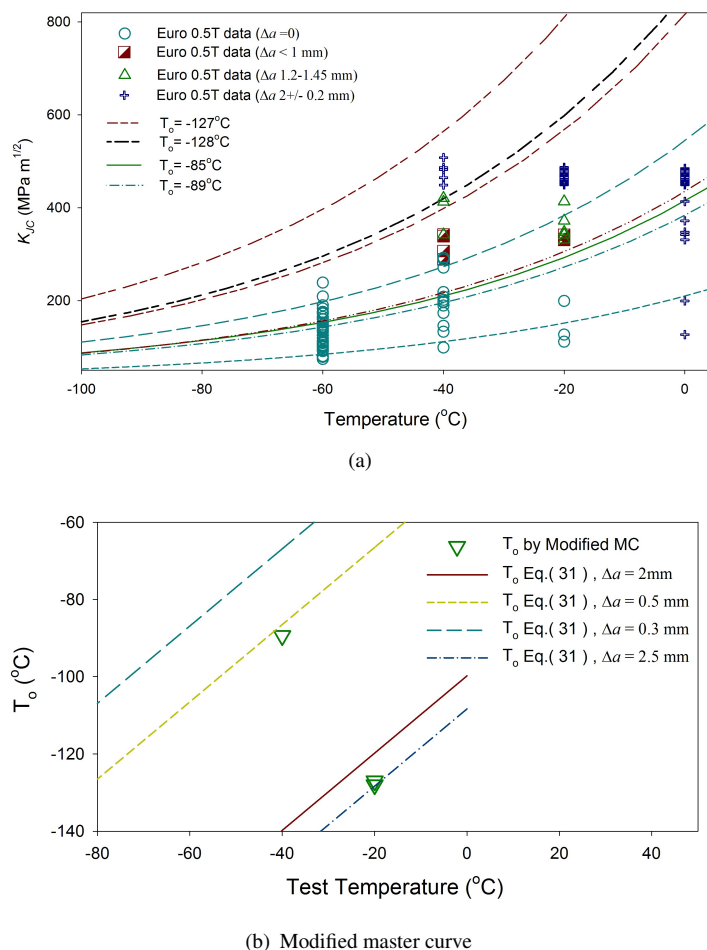


FIGURE 11.9: (a) Modified master curve and conventional master curve for 0.5T CT Euro fracture dataset and (b) comparison with predictions obtained from Eq. (31)

-110°C and -130°C. The engineering stress-strain behaviour is shown in Figure 11.10 (a). The K_{Jc} versus Δa behaviour of In-RAFMS dataset is shown in Figure 11.10 (b), where finite element results obtained at -110°C and -130°C are also compared. The TPB specimen experimental data was inconclusive to give a K_{Jc} versus Δa correlation. Therefore, the correlation obtained from CT specimen dataset was used for modified master curve analysis.

The modified and conventional master curve results for In-RAFMS are shown in Figure 11.11 (a) and Figure 11.11 (b) for CT and TPB datasets, respectively. The T_0 values obtained from conventional and modified master curve methods for CT dataset are -120°C and -123.5°C respectively. On the other hand for TPB dataset the conventional and modified master curve analyses resulted in T_0 values of -123°C and -140°C.

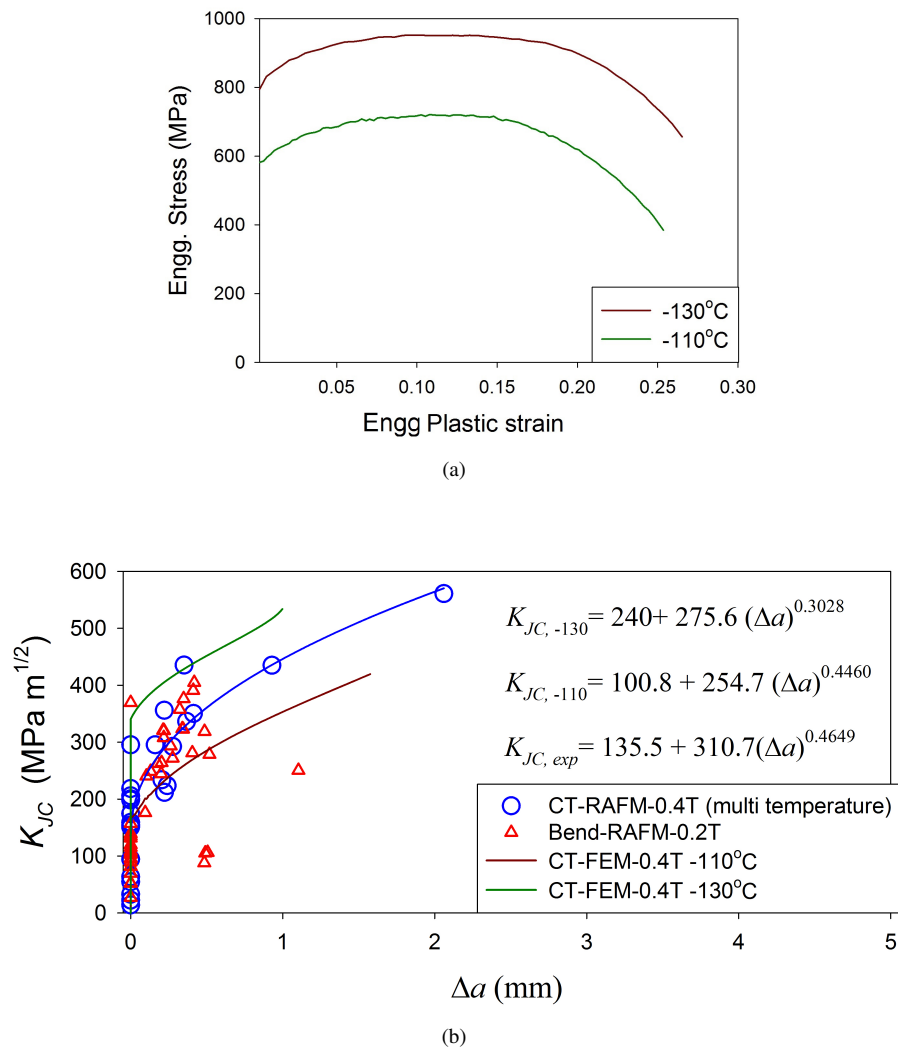


FIGURE 11.10: (a) Engineering stress strain response In-RAFMS and (b) K_{JC} versus Δa behavior of In-RAFMS obtained from experimental CT and TPB datasets and finite element analyses

The larger difference in the results of TPB dataset is attributed to the fact that more number of data in case of TPB were affected by prior DCG in comparison to CT dataset. Although the amount of ductile tearing was more in case of CT specimens due to the higher test temperatures but more datasets with smaller amount of DCG were involved in the TPB dataset. Another reason, which had an effect on modified master curve analysis was the differences in triaxiality function in comparison to CT.

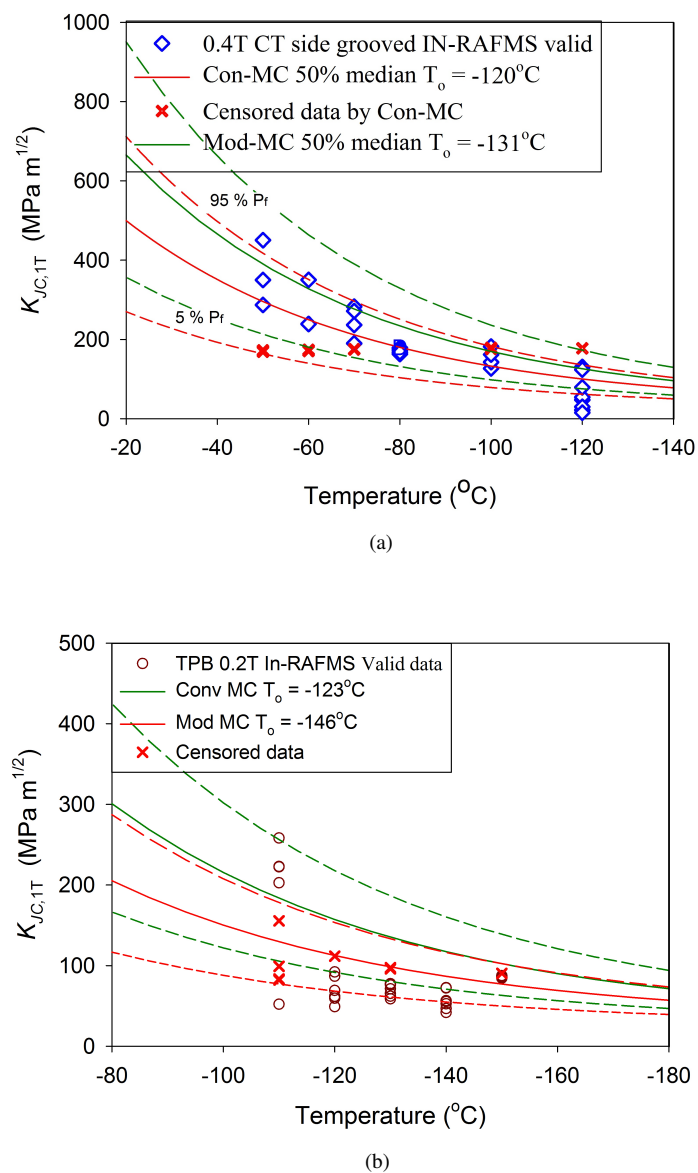


FIGURE 11.11: (a) Conventional and modified master curves 0.4T CT and (b) 0.2T TPB datasets of In-RAFMS steel

11.6 Discussion

The modified cleavage failure probability derived from conventional master curve methodology when applied on selected datasets shows a greater potential of utilizing the cleavage data with prior DCG. The modification based on incremental active volume and constraint helps in estimation of reference transition temperature, T_0 from the conventionally invalid dataset. The approach described to incorporate the effect of prior DCG

on cleavage failure probability by Wallin is compared with the rank probability and proposed correction by present authors in Figure 11.12.

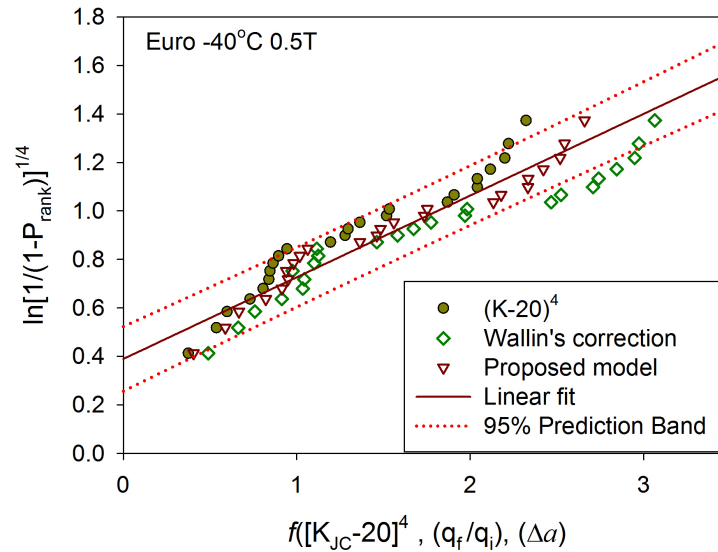


FIGURE 11.12: Comparison of conventional, Wallin's and proposed formulation with rank probability obtained for 0.5T CT Euro fracture data at -40°C

The unique correlation of active volume scaling with functions of K_{JC} , Δa , and triaxiality is shown in Figure 11.13. It can be seen from Figure 11.13 that on a semi-log scale for functions of K_{JC} , Δa , and triaxiality, the volume shows two different dependencies for proposed formulation described by Eq.(11.13). The slope changes a little later from the initiation of DCG and follows the scaling to the maximum DCG simulated at -110°C and -130°C . Wallin's DCG correction also shows similar trend but the behaviour changes at larger DCG.

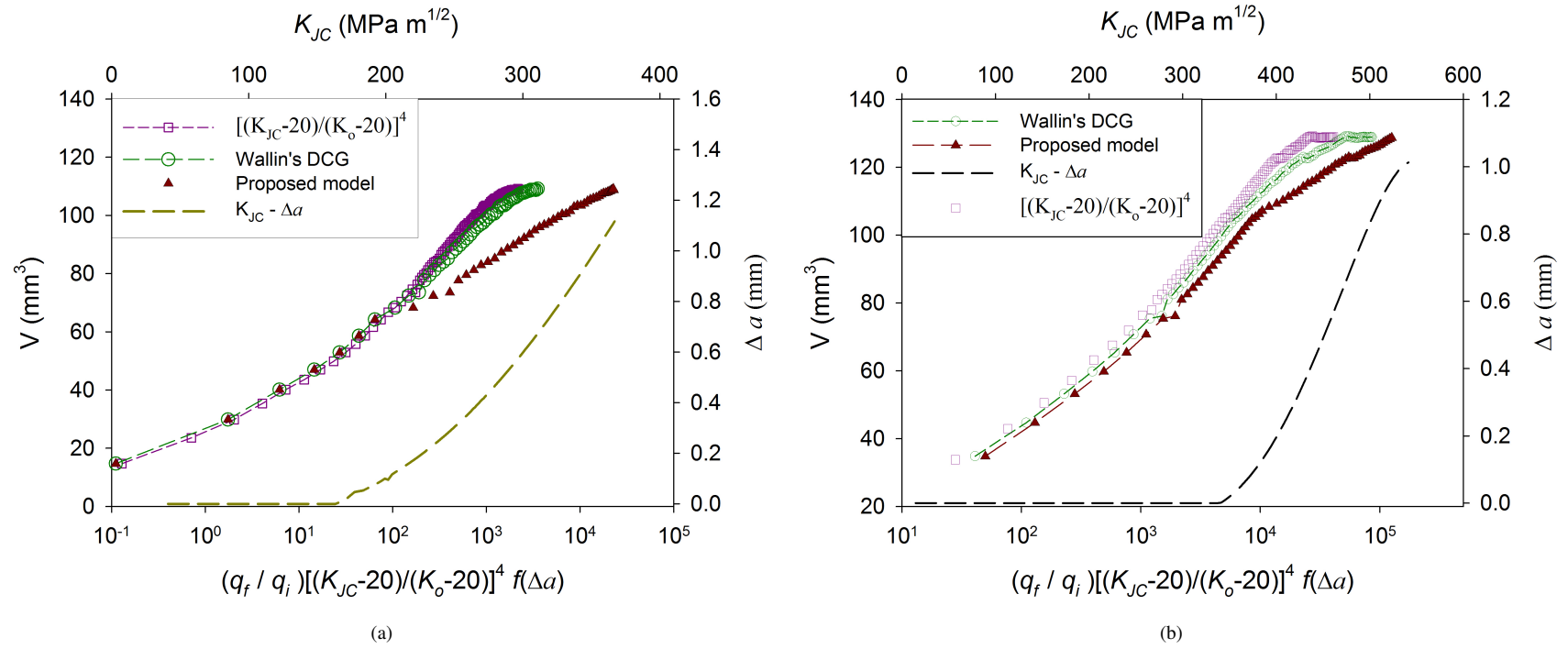


FIGURE 11.13: Comparison of scaling of Active volume with conventional, Wallin's correction and proposed model of this work for (a) -110°C and (b) -130°C

11.6.1 Effect of plastic strain and embrittlement

Various investigations on the effect of prior DCG on cleavage fracture probability, exploring the subject using local approaches (Moattari et al., 2016; Margolin et al., 2003; Ruggieri and Dodds Jr, 1996; Sobotka and Dodds, 2014) as well as global approaches (Bruckner and Munz, 1984; Moskovic, 2002; Tagawa et al., 2010; Scibetta, 2010; Wallin, 1989a) converge to demonstrate that the probability of cleavage fracture increases with increasing amount of prior ductile tearing in a cleavage fracture, except Margolin et al. (2003). In Margolin et al. (2003) work a heat treated condition simulating irradiation hardening was analysed using local approach and it was demonstrated that for embrittled condition the probability of cleavage fracture decreased. The increasing probability of cleavage fracture originates from the facts such as increasing active volume and constraint causing increasing numbers of potential cleavage initiators as discussed in sections 3.1 and 3.2. However, a decreasing cleavage fracture probability needs mechanism based explanation as it seems difficult that for a work hardening material the cleavage failure probability will decrease.

In the formulation proposed in this work in form of Eq.(11.13), scope of decreasing fracture probability exists if a decreasing constraint is realized with ductile tearing. The effect of embrittlement as well as plastic strain defining ductile failure is analysed by simulating -110°C and -130°C conditions on In-RAFMS and 0°C , -20°C and -60°C conditions on 22NiMoCr37 steel. The engineering stress strain behaviour of 22NiMoCr37 steel shown in Figure 11.8 (a) when compared to the behaviour of $K_{JC} - \Delta a$ response in Figure 11.8 (b), it is revealed that the initiation of ductile tearing depends on the failure strain. The failure strain visible from the engineering stress strain behaviour predicts that the failure void volume fraction will be achieved for 0°C and -60°C earlier to that for -20°C . The effect of work hardening is also reflected in the $K_{JC} - \Delta a$ response. Similar behaviour can be observed for In-RAFMS in Figure 11.10. It is evident, therefore, that the effect of differences in work hardening and plastic failure strain is taken care for by including the $K_{JC} - \Delta a$ in form of Eq.(11.10).

To study the effect of plastic failure strain and embrittlement on triaxiality function, the q_f/q_i response for In-RAFMS and 22NiMoCr37 steels at different temperatures is shown in Figure 11.6 (a) and Figure 11.6 (b), respectively. For CT geometry the q_f/q_i ratio was not found to change much except in the initiation point, which is dependent on failure void volume fraction. However, sub-sized TPB showed a different response for q_f/q_i ratio in comparison to CT specimens. This behaviour was expected due to different amount of constraints associated with the geometries.

For 22NiMoCr37 the q_f/q_i ratio was found to be similar for 0°C and -60°C and differs at higher amount of DCG for -20°C. The failure void volume fraction does not have an effect on the amplitude of q_f/q_i ratio rather the effect is realized in the position of onset of ductile tearing. The work hardening also does not change the q_f/q_i ratio for smaller amount of DCG but appears to cause differences at larger DCG. This behaviour may be attributed to the increasing q_i for materials or conditions with higher work hardening.

The comparison of conventional master curve with modified master curve for all the datasets shows that the two approaches give same result at no ductile crack growth. As the ductile tearing increases the transition temperature realized from that dataset goes lower, which thereby increases the $K_{JC,med}$. This is due to the fact that for more numbers of data showing significant DCG the probability of cleavage failure shifts towards lower temperatures.

The potential of modification made for master curve to be applicable in upper region of DBT can be realized in Table 11.3.

The modification in cleavage failure probability proposed in this work does not take care of the change in constraint due to thickness i.e. out of plane loss of constraint, which may increase the $K_{JC,med}$ significantly. Therefore, the approach of partial censoring is applied, which is to censor the datasets having $K_{JC,1T} > K_{JC,limit}$. Any data showing any measurable amount of DCG is treated valid.

TABLE 11.3: Comparison of T_0 obtained from modified and conventional MC for different datasets

Datasets	No. of Tests	Test temperatures	T_0 Conventional	T_0 Modified
In-RAFMS (0.5T CT)	26 14 valid	-50,-60,-70,-80,-100, -120°C	-120°C	-131°C
In-RAFMS (0.2T TPB)	39 26 valid	-110,-120,-130,-140,-150°C	-123°C	-146°C
Euro data 0.5T CT $\Delta a = 0$	53	-60°C	-85°C	-85°C
Euro data 0.5T CT $\Delta a < 1$ mm	59 53 valid	-40,-60°C	-85°C	-89°C
Euro data 0.5T CT Δa 1.2-1.45 mm	61 53 valid	-20, -40,-60°C	-85°C	-127°C
Euro data 0.5T CT Δa 2±0.5 mm	58 0 valid	-40,-60°C	T_0 Not possible	-128°C

11.7 Conclusions

The phenomena of cleavage fracture preceded by ductile tearing is studied in detail and investigated by a proposed modification of the master curve method, which is based on the increasing active volume and constraint with ductile tearing. The methodology analyses the cleavage fracture data with single fold censoring unlike conventional master curve by revalidating the data showing any significant amount of ductile crack growth in the DBT region and ending in cleavage fracture mode. The modified master curve method is applied on existing databases and also on the dataset of newly developed In-RAFM steel for its applicability in upper region of DBT. The question raised in the introductory section to understand the complex behaviour of cleavage fracture in upper region of DBT where preceding Δa alters the conventionally modelled behaviour of fracture toughness with temperature is answered to certain extent by the proposed methodology. The fracture toughness is described as a function of temperature as well as the ductile crack growth. The modified master curve estimates the T_0 for a dataset in upper DBT and the estimated T_0 lowers as the amount of DCG and number data affected by DCG increases.

Chapter 12

Summary and conclusions

In this work, the master curve methodology was used to investigate and characterize the fracture behaviour of In-RAFMS in DBT region. Simultaneous efforts were made to not only characterize the fracture behaviour of In-RAFMS but also to challenge the approach itself beyond the limits of validity and assumptions. Required corrections based on numerical calculations as well as analytical understanding were implemented on the probabilistic approach to address the problem of DBT where competing failure mechanisms decide the fracture mode. More than the material aspect, it may seem in this work that the approach is challenged, however the compatibility of the approach beyond its limits are judged by the dataset of the material in question.

The master curve method inherently suffers with the evergreen constraint loss problem of fracture mechanics due to its assumption of self-similar stress field at the crack tip. The problem is magnified owing to involvement of statistical analyses as individual data shows variation in constraint at crack tip. This difference causes a variation in local temperature felt by the specimen, local strain rate as well as local micro-mechanisms.

It also comes out as a known fact and an observation in this work that changes in parameters such as loading rate, thickness, type of loading and material properties all result in changes in crack tip stress fields, which can be quantified as a change in temperature or loading rate or constraint. The effect of changing any parameter is equivalent to change in other. The parametric studies in this work was carried out with In-RAFMS as the main material of investigation with comparative studies on similar grade of P91 steel. The study included the effect of loss of constraint due to change in size of the specimen with constant crack depth and also due to change in crack depth with constant size of the specimens. The effect of loading rate and effect of specimen geometry (CT and SE(B)) were also examined on both In-RAFMS and P91 steels.

A novel method of constraint quantification using triaxiality ratio was studied both experimentally and numerically using finite element calculations. This was named **Weibull Triaxiality**. Another novel approach towards assessment of probability of cleavage failure in upper region of DBT, was established by extending the conventional master curve method. The mechanisms, which were not included in conventional master curve approach were analytically examined and included in modified master curve approach proposed in this work. The method was justified on existing largest dataset of *Euro Fracture data* as well as on the newly developed dataset of In-RAFMS.

The constraint assessment on both out of plane constraint loss as well as in plane constraint loss, using finite element method and experimental justification showed that the active volume ahead of the crack tip can be used efficiently to describe the loss of constraint. The method not only quantifies the loss of constraint but also comes out to be a tool to correct the lower constraint fracture toughness value to an equivalent SSY condition. Although, active volume does not describe the micro-mechanical stress concentration in the specimen like Weibull stress does, yet it clearly separates the differences, which occur due to dimension or crack depth. This method of constraint scaling is pronounced in this work as $\sigma^* - V^*$ approach.

Another type of constraint quantification pronounced as Weibull Triaxiality is developed in this work. It has been shown that Weibull Triaxiality (q_W) efficiently captures the micro-mechanical constraint distribution in active volume and thus it is ranked higher than Weibull stress as well as active volume. A proposal to embed (q_W) in the cleavage failure probability is also discussed however complete understanding of this parameter remains in the scope in future.

The Weibull stress (σ_W) method is used to calibrate the Weibull modulus m as a material property and later it has been used for assessment of loading rate on the master curve methodology and reference transition temperature T_0 . The conclusions from the work are summarized as following.

- **Loss of constraint** The conventional master curve analysis of 0.2T TPB specimens of In-RAFMS resulted in a T_0 of -123°C. The small specimen do not show

a self similar stress field at crack front and therefore the master curve assumption of BK^4 scaling does not work. This violation of SSY condition can be corrected numerically by transforming the volume deformed under a non-SSY condition to an equivalent SSY condition, which is described as $\sigma^* - V^*$ approach. The numerical correction based on $\sigma^* - V^*$ approach resulted in a T_0 of -123°C of -109°C .

The in plane constraint loss assessment by testing specimen of same dimension with varying crack depths showed an expected behaviour of increasing T_0 from lowest value of -125°C for crack depth of 0.3 to 0.44 to highest of -99°C for crack depth of 0.65 to 0.7. The approach of $\sigma^* - V^*$ again showed good potential to scale the differently constrained conditions to SSY condition and a T_0 of -100°C was obtained for all data transformed to a/W of 0.5. The in plane change in constraint also showed that the standard deviation increased for shallower crack depths, which indicated that as the dataset moves away from high constraint condition more uncertainty is induced in the estimation of T_0 .

- **Tension vs Bending** The two popular loading schemes of fracture mechanics impose different amount of triaxiality along the crack front. This is then magnified with the in plane or out of plane constraint effects as discussed above. CT and TPB specimens of In-RAFMS as well as P91 steels re-confirmed the effect and proved once again that CT specimens should be preferred for T_0 estimation as it always shows more triaxiality in comparison to bending. The bending scheme may have other benefits such as quick setting up while testing and advantage of using load line displacement for K_{JC} measurement but it also induces errors associated with the benefits. The side grooved CT specimens of In-RAFMS showed the constraint to be higher than not only 0.4T TPB but also 0.2T TPB specimens. The 10% side grooving shows added benefit of self-similar stress field, which was proven by FEA and use of novel constraint measurement tool developed as Weibull Triaxiality.

- **Loading rate** The experimental results on the dataset of In-RAFMS at three different loading rates showed an expected systematic increase in T_0 with increasing loading rate. The Weibull stress analysis was used to predict the cleavage failure probability numerically. This method required a numerical parameter, which is also a material property to be calibrated. For In-RAFMS this material property known as Weibull modulus was found to be 9. The Weibull modulus for P91 was also calibrated for the first time and was found to be 15. The numerical prediction of Weibull stress analysis does not show very good agreement with the experimental results. This behaviour is attributed to the effect of plastic strain, which causes violation of constant numbers of cleavage initiators in the active volume. The reasoning is supported experimentally as for higher loading rate datasets the Weibull stress based numerical predictions were better than that for quasi-static condition. As a higher strain imposes more triaxiality the possibility of cleavage initiators turning into void nucleation sites decreases.

The changes in T_0 with loading rate was in accord with Zener-Hollomon based loading rate correction proposed by Wallin. The correlation is accurate enough to predict the shift in T_0 in the tested range of loading rate.

- **Cleavage preceded by ductile tearing** The event was analytically modelled and a contribution due to change in constraint with ductile tearing, mostly ignored by previous researchers, was considered in the mathematical model. It was found that this modification expands the validity window of master curve approach and predicts T_0 for a dataset completely invalid for conventional method.

The modified master curve shows that by discarding/censoring the cleavage events with prior DCG, conventional master curve is unable to estimate the true potential of the material and over conservative results are obtained by following conventional master curve with censoring of DCG affected cleavage events.

Chapter 13

Future scope of work

The event of cleavage fracture is modelled in this work using Beremin's model, $\sigma^* - V^*$, and Weibull triaxiality corrected Beremin's model. All these models and also the concept of master curve is based on the assumption of randomly distributed cleavage initiators. However, it was shown in the SEM micrographs in Chapter 6, in Figures 6.3 and 6.4 that ferritic/martensitic grade steels show a quantifiable pattern of cleavage initiating carbides. Therefore, it seems appealing to develop a mathematical model of cleavage fracture which can utilize the information of carbide position. The method based on specific distribution of carbides can also be used for next generation RAFM grade, in which oxides are being used for strengthening the alloy.

A recent study by [Lei \(2016a,b\)](#); [Qian et al. \(2017\)](#), has shown that the axioms of probability theory are violated in the basic formulation of Beremin's model. By the same researchers new local approach is developed and calibrated for ferritic steels. Simultaneously, effect of plastic strain which was a part of initial works of Beremin was neglected by major research groups across the globe while modelling cleavage fracture. Therefore, a systematic study on the effect of plastic strain with a new local or non-local approach towards cleavage fracture may be interesting.

To make the numerical prediction closer to the mesoscale material response, a crystal plasticity based formulation for prediction of cleavage failure probability may prove to be better than the conventional local approaches. Further, it is a real concern that a non-local approach towards cleavage fracture formulation does not exist and any work in this direction would surely be appreciated.

Appendix A

Appendix-A

A.1 Maximum likelihood analysis: conventional master curve

As described in Chapter 2, the probability of cleavage fracture is described as,

$$P_f = 1 - \exp\left[-\frac{B_{nT}}{B_{1T}} \left(\frac{K_{JC} - K_{min}}{K_o - K_{min}}\right)^4\right], \quad (\text{A.1})$$

The probability density function and survival function to find maximum likelihood parameters are described as,

$$f_i = \frac{dP_f}{dK_{JC}}, \quad (\text{A.2})$$

$$S_i = \exp\left[-\left(\frac{K_{JC(i)} - K_{min}}{K_o - K_{min}}\right)^{1/4}\right], \quad (\text{A.3})$$

where index i refers to the individual data analysed at each test temperature. The maximum likelihood parameter is described as

$$L = \prod_{i=1}^N f_i^{\delta_i} \cdot S_i^{1-\delta_i}. \quad (\text{A.4})$$

For conventional master curve the maximization of ML parameter is obtained only with respect to reference transition temperature T_o , which gives f_i as,

$$\frac{\partial P_f}{dK_{JC}} = 4 \frac{(K_{JC} - K_{min})^3}{(K_o - K_{min})^4} \exp\left[-\left(\frac{K_{JC} - K_{min}}{K_o - K_{min}}\right)^4\right], \quad (\text{A.5})$$

and survival function S_i as,

$$S_i = \exp\left[-\left(\frac{K_{JC} - K_{min}}{K_o - K_{min}}\right)^4\right]. \quad (\text{A.6})$$

The maximum likelihood parameter is then described as,

$$L = \prod_{i=1}^N \left(4 \frac{(K_{JC} - K_{min})^3}{(K_o - K_{min})^4} \right) \exp\left[-\left(\frac{K_{JC} - K_{min}}{K_o - K_{min}}\right)^4\right]^{\delta_i} \cdot \left(\exp\left[-\left(\frac{K_{JC} - K_{min}}{K_o - K_{min}}\right)^4\right]\right)^{1-\delta_i}, \quad (\text{A.7})$$

which simply becomes,

$$L = \prod_{i=1}^N \left(4 \frac{(K_{JC} - K_{min})^3}{(K_o - K_{min})^4} \right)^{\delta_i} \exp\left[-\left(\frac{K_{JC} - K_{min}}{K_o - K_{min}}\right)^4\right], \quad (\text{A.8})$$

The maximization of L with respect to T_o is easier when Eq.(A.7) is changed to logarithmic form as $\frac{\partial(\ln L)}{\partial T_o}$. As the only function which is dependent on T_o in Eq.(A.8) is K_o by the relation given as,

$$K_o - K_{min} = \frac{1}{(\ln 2)^{1/4}} \{(30 - K_{min}) + 70 \exp[C(T - T_o)]\}. \quad (\text{A.9})$$

The partial derivative is first obtained w.r.t. K_o as,

$$\frac{\partial(\ln L)}{\partial K_o} = \left(4 \frac{(K_{JC} - K_{min})^4}{(K_o - K_{min})^5} - \frac{4}{(K_o - K_{min})} \right) \cdot \frac{\partial K_o}{\partial T_o}. \quad (\text{A.10})$$

The partial derivative w.r.t. K_o is ,

$$\frac{\partial K_o}{\partial T_o} = \frac{1}{(\ln 2)^{1/4}} \{-C \times 70 \exp[C(T - T_o)]\}. \quad (\text{A.11})$$

Replacing $\frac{\partial K_o}{\partial T_o}$ and K_o from Eq.(A.10) with $\ln(2)^{1/4}$ as 0.9124, K_{min} as 20 MPa m^{1/2} and C as 0.019°C⁻¹ gives ,

$$\frac{\partial(\ln L)}{\partial T_o} = 0 = \frac{\frac{\partial K_o}{\partial T_o}}{(11 + 77 \exp[0.019(T - T_o)])^5} + \frac{\frac{\partial K_o}{\partial T_o} (K_{JC} - K_{min})^4}{(11 + 77 \exp[0.019(T - T_o)])^5}. \quad (\text{A.12})$$

Eq.(A.12) has to be performed for each experimental value after censoring and it takes the summation as described in Eq.(A.6). The T_o is obtained by trial of different values which results in summation of Eq.(A.12) as zero.

A.2 Maximum likelihood analysis: Bimodal master curve master curve for upper DBT

The maximum likelihood analysis of bimodal master curve is more complicated in comparison to conventional as apart from two reference transition temperatures another unknown parameter p_a exists. The probability of cleavage fracture for a bimodal distribution is described as,

$$P_f = 1 - p_a \exp\left[-\left(\frac{K_{JC} - K_{min}}{K_{o,1} - K_{min}}\right)^4\right] - (1 - p_a) \exp\left[-\left(\frac{K_{JC} - K_{min}}{K_{o,2} - K_{min}}\right)^4\right], \quad (\text{A.13})$$

The probability density function as $\frac{\partial P_f}{\partial K_{JC}}$ takes the form,

$$\begin{aligned} \frac{\partial P_f}{\partial K_{JC}} = & 4p_a \frac{(K_{JC} - K_{min})^3}{(K_{o,1} - K_{min})^4} \exp\left[-\left(\frac{K_{JC} - K_{min}}{K_{o,1} - K_{min}}\right)^4\right] + \\ & 4(1 - p_a) \frac{(K_{JC} - K_{min})^3}{(K_{o,2} - K_{min})^4} \exp\left[-\left(\frac{K_{JC} - K_{min}}{K_{o,2} - K_{min}}\right)^4\right], \quad (\text{A.14}) \end{aligned}$$

and the survival function is described as,

$$S_i = p_a \exp\left[-\left(\frac{K_{JC} - K_{min}}{K_{o,1} - K_{min}}\right)^4\right] + (1 - p_a) \exp\left[-\left(\frac{K_{JC} - K_{min}}{K_{o,2} - K_{min}}\right)^4\right], \quad (\text{A.15})$$

The rest of the procedure remains same as for conventional master curve except that, instead of one equation for one reference transition temperature two equations for $T_{o,1}$ and $T_{o,2}$ are solved for. The dependence of $T_{o,1}$ and $T_{o,2}$ on $K_{o,1}$ and $K_{o,2}$ is described as,

$$K_{o,1} = \frac{1}{\ln(2)^{1/4}} (A + (100 - A) \exp[C(T - T_{o1})]), \quad (\text{A.16})$$

$$K_{o,2} = \frac{1}{\ln(2)^{1/4}} (A + (100 - A) \exp[C(T - T_{o2})]). \quad (\text{A.17})$$

A.3 Maximum likelihood analysis: Modified master curve for upper DBT

The modified master curve as described in Chapter 11 describes the cleavage failure probability as,

$$\ln\left(\frac{1}{1-P_f}\right) = \left(\frac{q_f}{q_i}\right) \cdot \left(\frac{K-K_{min}}{K_o-K_{min}}\right)^4 \cdot \left[1 + 2\frac{(\phi(\Delta a)^m)^2}{K^2}\right]. \quad (\text{A.18})$$

In the present form the maximum likelihood analysis is more complicated and therefore, a simple assumption that the initiation fracture toughness is a constant¹ is applied and the probability can then be re-written as,

$$\ln\left(\frac{1}{1-P_f}\right) = \left(\frac{q_f}{q_i}\right) \cdot \left(\frac{K-K_{min}}{K_o-K_{min}}\right)^4 \cdot \left[1 + 2\frac{(\phi(\Delta a)^m)^2}{K_i^2}\right]. \quad (\text{A.19})$$

After this simplification the probability density function becomes,

$$\frac{\partial P_f}{\partial K_{JC}} = 4\frac{(K_{JC}-K_{min})^3}{(K_o-K_{min})^4} \exp\left[-\left(\frac{K_{JC}-K_{min}}{K_o-K_{min}}\right)^4\right] \left(\frac{q_f}{q_i}\right) \left[1 + 2\frac{(\phi(\Delta a)^m)^2}{K_i^2}\right], \quad (\text{A.20})$$

and the survival function becomes,

$$S_i = \exp\left[-\left(\frac{K_{JC}-K_{min}}{K_o-K_{min}}\right)^4\right] \left(\frac{q_f}{q_i}\right) \left[1 + 2\frac{(\phi(\Delta a)^m)^2}{K_i^2}\right]. \quad (\text{A.21})$$

The triaxiality function and function dependent on DCG which describes the increasing active volume remain independent of K_o and T_o and therefore, the rest of the procedure for T_o determination is same as that for conventional master curve.

¹The details about importance of initiation fracture toughness in modified master curve is detailed in Chapter 11

Appendix B

Appendix-B

All the fracture data generated in this thesis are listed in this section. The unit of fracture toughness parameter K_{JC} and all other forms of this parameter is **MPa m^{0.5}**, and the unit of temperature is always °C.

B.1 Fracture data of 0.4T SEB specimen of In-RAFMS

TABLE B.1: Fracture data of 0.4T SEB specimen of In-RAFMS

Sample Id.	b_0 (mm)	Δa (mm)	a/W	Temp (°C)	YS (MPa)	K_{JC} (MPa m ^{0.5})	$K_{JC,limit}$ (MPa m ^{0.5})	validity	Censored	$K_{JC,IT}$ (MPa m ^{0.5})
HS-1	7.64	4.72	0.62	-100	490	191.98	168.47	1	Non-Test	
HS-5	9.5	0.99	0.52	-100	490	96.59	187.91	1	96.58	80.91
K-4	10.87	0	0.46	-110	507	69.86	204.43	1	69.86	59.65
K-6	10.97	0	0.45	-110	507	187.9	205.35	1	187.9	153.53
K-9	10.56	0	0.47	-110	507	96.68	201.44	1	96.68	80.98
1	8.93	0	0.55	-110	507	139.24	185.29	1	139.24	114.83
6	9.14	0	0.54	-110	507	161.02	187.47	1	161.02	132.15
2	9.01	0	0.55	-110	507	133.23	186.09	1	133.24	110.05
4	8.91	0	0.55	-110	507	209.53	185.08	0	185.08	151.29
7	9.36	0	0.53	-110	507	272.87	189.7	0	189.7	154.96
10	9.25	0	0.54	-110	507	323.52	188.59	0	188.59	154.08
3	9.79	0	0.51	-110	507	394.08	194.05	0	194.05	158.42
5	9.45	0	0.53	-110	507	408.26	190.6	0	190.6	155.67
8	9.45	0	0.53	-110	507	166.37	190.6	1	166.37	136.4
9	9.45	0	0.53	-110	507	96.25	190.6	1	96.25	80.64

Sample id	b_o (mm)	Δa (mm)	a/W	Temp (°C)	YS (MPa)	K_{JC} (MPa m ^{0.5})	$K_{JC,Limit}$ (MPa m ^{0.5})	validity	Censored at M = 30	$K_{JC,1T}$ censored
10	9.25	0	0.54	-110	507	323.52	188.59	0	188.59	154.08
3	9.79	0	0.51	-110	507	394.08	194.05	0	194.05	158.42
5	9.45	0	0.53	-110	507	408.26	190.6	0	190.6	155.67
8	9.45	0	0.53	-110	507	166.37	190.6	1	166.37	136.4
9	9.45	0	0.53	-110	507	96.25	190.6	1	96.25	80.64
I-9	11.1	0	0.45	-120	675.4	124.02	238.47	1	124.02	102.72
J-9	10.48	0	0.47	-120	675.4	82.07	231.62	1	82.07	69.36
K-10	10.47	0	0.47	-120	675.4	120.23	231.61	1	120.23	99.71
K-7	11.15	0	0.44	-120	675.4	119.68	239.01	1	119.68	99.27
E1	9.99	0.01	0.5	-120	675.4	116.11	226.24	1	116.11	96.43
E2	10.57	1.13	0.47	-120	675.4	144.84	232.61	1	144.84	119.28
E3	9.88	0.23	0.51	-120	675.4	221.34	224.99	1	221.34	180.12
E4	9.51	0.98	0.52	-120	675.4	101.92	220.64	1	101.92	85.15
E13	9.77	0.45	0.51	-130	750	84.58	235.79	1	84.58	71.36
E21	9.76	0.49	0.51	-130	750	114.22	235.54	1	114.22	94.93

Sample id	b_o (mm)	Δa (mm)	a/W	Temp (°C)	YS (MPa)	K_{JC} (MPa m ^{0.5})	K_{JC,limit} (MPa m ^{0.5})	validity	Censored at M = 30	K_{JC,1T} censored
W1	9.95	0.09	0.5	-130	750	147.62	237.89	1	147.62	121.49
W2	9.54	0.96	0.52	-130	750	114.17	232.88	1	114.17	94.89
W3	10.6	1.2	0.47	-130	750	116.22	245.54	1	116.22	96.52
W4	9.96	0.09	0.5	-130	750	127.16	237.93	1	127.16	105.22
W5	10.24	0.48	0.49	-130	750	127.04	241.34	1	127.04	105.13
B1	10.34	0	0.48	-120	675.4	139.44	230.17	1	139.44	114.99
B2	9.96	0.09	0.5	-120	675.4	133.16	225.79	1	133.16	109.99
B3	9.83	0.33	0.51	-120	675.4	162.65	224.41	1	162.65	133.45
B4	10.32	0.64	0.48	-120	675.4	131.97	229.87	1	131.95	109.03

B.2 Fracture data of 0.4T CT specimens of In-RAFMS

TABLE B.2: Fracture data of 0.4T CT specimens of In-RAFMS

Sample id	b_0	Δa	Temp °C	YS MPa	K_{JC} MPa m ^{0.5}	$K_{JC,limit}$	Validity	Censored $K_{JC,xT}$	Censored $K_{JC,1T}$
507S B5	10.9	2.06	-50	413	560.97	184.75	0	211.77	172.51
50B8	13.75	0.22	-50	413	356	207.51	0	207.51	169.12
60B3	13.56	0.35	-60	428	435.34	209.75	0	209.75	170.9
60D0	14.04	0.16	-60	428	295.4	213.43	0	213.43	173.83
70B2	13.54	0.28	-70	447	292.4	214.22	0	214.22	174.46
70B7	13.61	0.41	-70	447	350.29	214.78	0	214.78	174.9
70D1	13.7	0.21	-70	447	233.89	215.48	0	215.48	175.46
50D2C1	11.64	0.93	-50	413	435.09	190.93	0	211.77	172.51
70D4	13.69	0.37	-70	447	336.36	215.37	0	215.37	175.37
120B4	14.27	0	-120	765	22.51	270.37	1	22.51	22
100B6	13.79	0	-100	490	154.41	226.37	1	154.41	126.89
100B9	12.82	0.24	-100	490	223.72	218.23	0	218.23	177.65
100D7	13.71	0	-100	490	174.38	225.69	1	174.38	142.77
120S0	13.07	0	-120	765	54.75	258.67	1	54.75	47.63
80c2	14.05	0	-80	454	295.37	219.96	0	219.96	179.02
80d8	13.45	0	-80	454	200.24	215.21	1	200.24	163.34
120c4	13.08	0	-120	765	158.95	258.79	1	158.95	130.5
s1-120	14.91	0	-120	765	63.42	276.34	1	63.42	54.53
120s3	14.03	0	-120	765	150.88	268.05	1	150.88	124.08
120s2	13.98	0	-120	765	94.46	267.59	1	94.47	79.22
5s 120	14.23	0	-120	765	32.73	269.91	1	32.73	30.13
120s50	14.51	0	-120	765	14.01	272.56	1	14.01	15.24
80-C5	13.57	0	-80	454	218.52	216.13	0	216.13	175.98
80S4	13.4	0.22	-80	454	211.77	214.77	1	211.77	172.51
S8	14.55	0	-80	454	205.62	223.77	1	205.62	167.62

B.3 Fracture data of 0.4T SEB specimens of In-RAFMS at different loading rates

TABLE B.3: Fracture data at 100 mmpm actuator speed

	0.2T(5×10)	a_0	a/W	K_{JC}	Temp	$K_{JC,IT}$	$K_{JC,limit}$	Validity
	Specimen Id	(mm)		(MPa m ^{0.5})	°C	(MPa m ^{0.5})	(MPa m ^{0.5})	
100 mmpm	s1	4.96	0.50	310.20	-80.00	214.07	166.95	0
	s2/s7	5.31	0.53	36.30	-100.00	30.90	164.12	1
	s4	5.23	0.52	450.99	-80.00	308.22	162.41	0
	s5	5.67	0.57	123.30	-100.00	89.08	157.72	1
	x6	5.50	0.55	357.70	-80.00	245.83	157.64	0
	x2	5.77	0.58	143.44	-80.00	102.55	152.86	1
	1	4.37	0.44	70.25	-100.00	53.60	179.69	1
	s10	4.21	0.42	67.20	-100.00	51.56	182.33	1
	u2	4.55	0.46	101.13	-100.00	74.25	176.86	1
	u10	4.24	0.42	21.61	-100.00	21.08	181.80	1

TABLE B.4: Fracture data at 1000 mmpm actuator speed

	0.4T(10x10)	a_0	a/W	K_{JC}	Temp	$K_{JC,1T}$	$K_{JC,Limit}$	Validity
	Specimen Id	(mm)		(MPa m ^{0.5})	°C	(MPa m ^{0.5})	(MPa m ^{0.5})	
1000 mmpm	R29	4.52	0.45	98.32	-80	172.69	141.43	1
	R30	4.54	0.45	206.2	-80	172.44	141.23	0
	R32	4.07	0.4	106.54	-80	179.69	146.99	1
	R33	4.63	0.46	113.55	-80	171.03	140.11	1
	R34	4.69	0.46	106.49	-80	170.12	139.38	1
	R35	4.97	0.49	307.51	-80	165.55	135.75	0
	R48	4.61	0.46	170.77	-80	171.36	140.37	1
	RR1	4.42	0.44	103.8	-80	174.32	142.73	1
	RR2	4.56	0.45	148.14	-80	172.13	140.98	1
	R26	4.48	0.44	81.89	-100	185.08	151.28	1
	R31	4.52	0.45	48.82	-100	184.34	150.69	1
	R38	4.47	0.44	50.24	-100	185.23	151.4	1
	R39	3.84	0.38	70.17	-100	195.43	159.51	1
	R42	4.56	0.45	70.66	-100	183.74	150.22	1
	R43	4.58	0.45	269.53	-100	183.45	149.99	0
	R46	4.55	0.45	64.61	-100	183.95	150.38	1
R47	4.38	0.43	65.27	-100	186.66	152.54	1	
R49	4.99	0.49	58.07	-100	176.24	144.26	1	

B.4 Fracture data of 0.2T SEB specimens of In-RAFMS at different crack depths

TABLE B.5: Fracture data with a/W in range of 0.29 to 0.34

	Sr No	a/W	Temp (°C)	K_{JC} (MPa m ^{0.5})	$K_{JC,1T}$ (MPa m ^{0.5})	YS (MPa)	$K_{JC,Limit}$ (MPa m ^{0.5})	$K_{JC,1T,Limit}$ (MPa m ^{0.5})	Validity
Gr-1	1	0.19	-140	98.21	72.30	871	163.97	116.28	1
	3	0.32	-140	95.94	70.78	871	150.30	107.13	1
	4	0.29	-140	52.83	41.96	871	152.96	108.91	1
	5	0.25	-140	369.66	253.83	871	157.43	111.91	0
	6	0.35	-110	376.34	258.30	506	111.71	81.33	0
	7	0.32	-110	334.38	230.24	506	114.14	82.96	0
	8	0.35	-110	266.94	185.14	506	112.09	81.58	0
	9	0.34	-130	158.92	112.90	750	137.37	98.49	0
	10	0.32	-140	73.05	55.48	871	150.25	107.10	1
	11	0.33	-140	59.97	46.73	871	148.39	105.86	1
	12	0.33	-140	68.83	52.65	871	148.31	105.80	1
	13	0.31	-140	52.74	41.90	871	151.30	107.81	1
	14	0.32	-150	116.45	84.50	891	151.42	107.89	1
	15	0.32	-150	118.73	86.02	891	151.36	107.84	1

TABLE B.6: Fracture data with a/W in range of 0.35 to 0.44

	Sr No	a/W	Temp (°C)	K_{JC} (MPa m ^{0.5})	$K_{JC,1T}$ (MPa m ^{0.5})	YS (MPa)	$K_{JC,Limit}$ (MPa m ^{0.5})	$K_{JC,Limit,1T}$ (MPa m ^{0.5})	Validity
Gr-2	1	0.42	120	82.57	61.85	675.4	121.72	88.03	1
	2	0.43	120	63.54	49.12	675.4	120.67	87.32	1
	3	0.39	130	96.54	71.19	750	131.19	94.36	1
	4	0.43	130	78.03	58.81	750	127.38	91.81	1
	5	0.40	130	82.97	62.11	750	130.78	94.08	1
	6	0.37	-110	323.58	223.01	506	109.72	80.00	0
	7	0.39	-130	103.75	76.01	750	131.83	94.79	1
	8	0.37	-130	139.92	100.19	750	134.19	96.36	0
	9	0.39	-130	208.05	145.75	750	132.04	94.93	0
	10	0.37	-130	188.02	132.36	750	134.29	96.43	0
	11	0.39	-140	74.64	56.54	871	142.24	101.75	1
	12	0.37	-140	98.78	72.68	871	144.80	103.46	1
	13	0.41	-150	118.97	86.19	891.4	141.04	100.95	1
	14	0.44	-110	131.66	94.67	506	103.42	75.78	0
	15	0.45	-110	293.20	202.70	506	102.81	75.38	0

TABLE B.7: Fracture data with a/W in range of 0.46 to 0.55

	Sr No	a/W	Temp (°C)	K_{JC} (MPa m ^{0.5})	$K_{JC,1T}$ (MPa m ^{0.5})	YS (MPa)	$K_{JC,Limit}$ (MPa m ^{0.5})	$K_{JC,Limit,1T}$ (MPa m ^{0.5})	Validity
Gr-3	1	0.51	120	119.87	86.78	675.4	112.09	81.59	0
	2	0.52	120	93.70	69.29	675.4	110.52	80.54	1
	3	0.52	120	294.56	203.61	675.4	111.10	80.92	0
	4	0.52	120	127.78	92.08	675.4	111.21	80.99	0
	5	0.52	130	331.35	228.21	750	117.19	84.99	0
	6	0.51	130	106.29	77.71	750	118.51	85.88	1
	7	0.49	130	105.28	77.03	750	120.35	87.11	1
	8	0.48	130	87.99	65.47	750	121.13	87.63	1
	9	0.53	-120	104.33	76.39	675.4	109.52	79.87	1
	10	0.49	-130	68.11	52.17	750	120.26	87.04	1
	11	0.54	-130	106.14	77.60	750	114.39	83.12	1
	12	0.54	-130	89.90	66.74	750	114.39	83.12	1

TABLE B.8: Fracture data with a/W in range of 0.56 to 0.69

	Sr No	a/W	Temp (°C)	K_{JC} (MPa m ^{0.5})	$K_{JC,1T}$ (MPa m ^{0.5})	YS (MPa)	$K_{JC,Limit}$ (MPa m ^{0.5})	$K_{JC,1T,Limit}$ (MPa m ^{0.5})	Validity
	1	0.60	-120	281.19	194.67	675.4	100.87	74.08	0
	2	0.60	-120	278.57	192.92	675.4	101.43	74.46	0
	3	0.59	-120	69.69	53.23	675.4	103.02	75.52	1
	4	0.63	-120	115.27	83.71	675.4	97.82	72.04	0
	5	0.59	-110	264.03	183.19	508	88.90	66.08	0
	6	0.62	-130	108.84	79.41	750	104.48	76.49	0
	7	0.62	-130	139.30	99.78	750	103.44	75.80	0
	8	0.56	-130	120.09	86.94	750	111.46	81.16	0
	9	0.55	-150	153.81	109.48	891.4	123.27	89.06	0
	10	0.55	-110	318.77	219.80	508	93.59	69.21	0
	1	0.67	-110	320.44	220.91	508	79.80	59.99	0
	2	0.65	-120	307.98	212.58	675.4	94.26	69.66	0
	3	0.65	-130	135.22	97.05	750	99.65	73.27	0
	4	0.67	-110	390.87	268.02	506	79.84	60.02	0
	5	0.65	-110	94.96	70.13	506	81.67	61.24	0
Gr-4	6	0.64	-130	81.63	61.22	750	101.36	74.41	1
	7	0.64	-110	102.99	75.50	506	82.94	62.09	0
	8	0.64	-110	250.45	174.11	506	83.66	62.57	0
	9	0.64	-130	240.38	167.38	750	100.96	74.14	0
	1	0.58	-120	357.69	245.82	675.4	103.24	75.67	0
	2	0.64	-110	272.01	188.53	506	82.80	62.00	0
	3	0.61	-110	176.25	124.49	506	86.63	64.56	0
	4	0.63	-110	244.45	170.10	506	83.80	62.67	0
	5	0.59	-130	52.02	41.41	750	107.51	78.52	1
	6	0.56	-120	108.25	79.01	690	107.04	78.21	0
	7	0.60	-130	27.34	24.91	750	107.23	78.34	1
	8	0.69	-110	157.23	111.77	506	77.57	58.50	0
	9	0.63	-110	248.61	172.88	506	83.69	62.59	0
	B1	0.53	-140	93.99	69.48	871	124.22	89.70	1
	B2	0.55	-140	103.31	75.71	871	121.84	88.10	1
	B3	0.59	-130	157.90	112.22	750	107.35	78.41	0
	E4	0.58	-130	90.17	66.93	750	109.71	79.99	1
	M7	0.61	-140	79.96	60.10	871	114.02	82.87	1

B.5 Fracture data of 1T CT specimens of P91 steel

TABLE B.9: Fracture data of 1T CT specimens of P91 steel

Sample id	b_0	Δa	a_0	a/W	K_{JC}	$K_{JC,Limit}$	Temp
	(mm)	(mm)	(mm)		(MPa m ^{0.5})	(MPa m ^{0.5})	(°C)
P4	21.49	0.34	28.51	0.57	278.17	362.81	-60
P7	22.90		27.10	0.54	193.87	378.18	-70
P9	23.61		26.39	0.53	149.69	384.05	-70
P15	24.10		25.90	0.52	136.80	387.99	-70
P16	23.41		26.59	0.53	184.83	378.67	-60
P18	23.20	0.37	26.80	0.54	229.90	376.97	-60
P19	24.22		25.78	0.52	212.37	385.12	-60
P1	26.95		23.05	0.46	29.27	406.28	-60
P2	25.62		24.38	0.49	180.67	396.13	-60
P3	26.28		23.72	0.47	213.78	401.21	-60
P11	26.35		23.65	0.47	192.25	405.73	-70
P5	26.82		23.18	0.46	73.11	409.32	-70
P6	25.35		24.65	0.49	34.41	397.88	-70
P8	25.30		24.70	0.49	201.57	393.65	-60

B.6 Fracture data of 0.4T standard charpy specimens of P91 steel

TABLE B.10: Fracture data of 0.4T standard charpy specimens of P91 steel

Sample id	b_0	Δa	a_0	a/W	K_{JC}	$K_{JC,Limit}$	Temp
	(mm)	(mm)	(mm)		(MPa m ^{0.5})	(MPa m ^{0.5})	(°C)
A1	4.82		5.18	0.52	225.93	170.42	-100
A2	5.00	0.10	5.00	0.50	241.97	173.47	-100
A3	4.92		5.08	0.51	145.09	174.50	-110
A6	5.03	0.09	4.97	0.50	219.42	176.33	-110
K4	4.98		5.02	0.50	84.56	175.48	-110
P1	4.95		5.05	0.51	200.54	174.94	-110
P2	5.08		4.92	0.49	141.37	177.18	-110
R1	4.67	0.33	5.33	0.53	332.35	167.76	-100
R2	4.84	0.11	5.16	0.52	237.77	170.65	-100
R4	5.00		5.00	0.50	190.43	175.78	-100
R6	4.88	0.35	5.12	0.51	135.66	171.35	-100
T3	4.93		5.07	0.51	179.56	174.71	-110
T4	4.70	0.26	5.30	0.53	314.85	168.16	-100
T21	4.82		5.18	0.52	195.83	170.32	-100
P3	5.07		4.93	0.49	120.26	177.05	-110
R3	4.89		5.11	0.51	175.37	173.93	-110
B4	4.89		5.11	0.51	182.79	171.60	-100

Appendix C

Appendix-C

Engineering drawing of test specimens

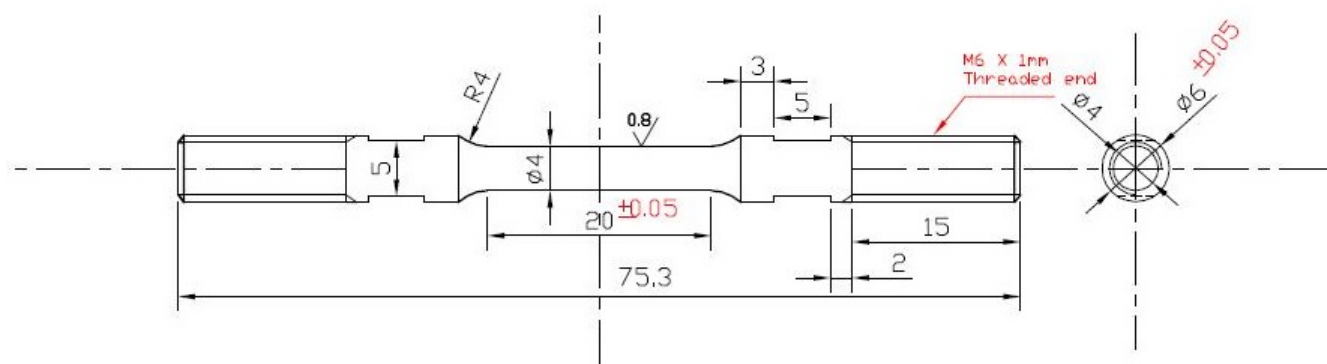


FIGURE C.1: Fabrication drawing of M6 tensile specimens)

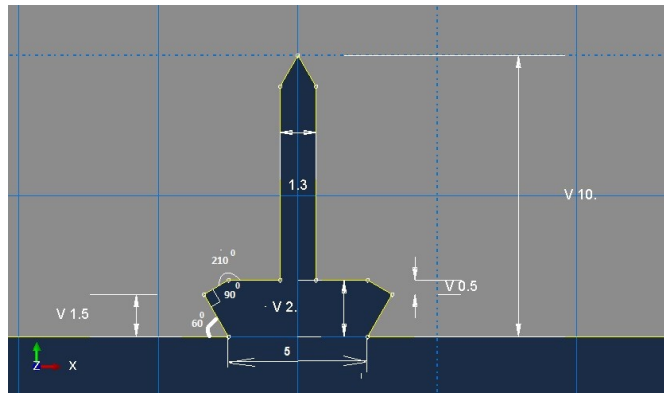


FIGURE C.3: Notch dimension of SE(B) 0.4T specimen)

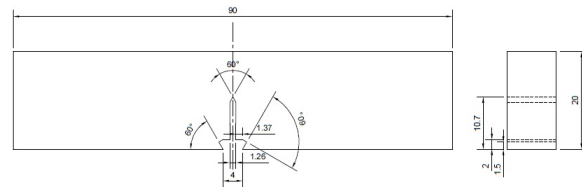


FIGURE C.4: Fabrication drawing of 0.4T SE(B) specimen

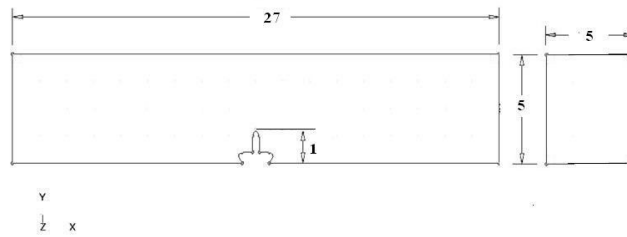


FIGURE C.5: Fabrication drawing of 0.2T SE(B) specimen

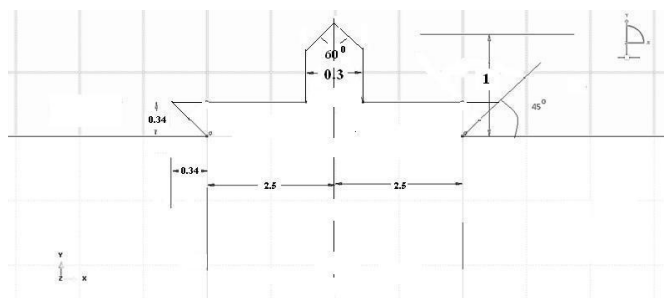


FIGURE C.6: Notch dimension of 0.4T SE(B) specimen

Bibliography

- Abe F., Kern T.-U., Viswanathan R. (2008) Creep-resistant steels. Elsevier
- Anderson T. L. (2005) Fracture Mechanics: Fundamentals and Applications, Third Edition. Taylor & Francis, New York, NY
- Andersson J.-O., Helander T., Höglund L., Shi P., Sundman B. (2002) Thermo-calc & dictra, computational tools for materials science. Calphad 26(2):273–312
- Andrews K. (1965) Empirical formulae for the calculation of some transformation temperatures. J Iron Steel Inst 203(7):721–727
- Argon A., Im J., Safoglu R. (1975) Cavity formation from inclusions in ductile fracture. Metallurgical Transactions A 6(4):825–837
- Banerjee S. (2014) Overview of indian activities on fusion reactor materials. Journal of Nuclear Materials 455(13):217 – 224, DOI <http://dx.doi.org/10.1016/j.jnucmat.2014.06.009>, proceedings of the 16th International Conference on Fusion Reactor Materials (ICFRM-16)
- Beremin F. (1981) Cavity formation from inclusions in ductile fracture of a508 steel. Metallurgical Transactions A 12(5):723–731
- Beremin F., Pineau A., Mudry F., Devaux J.-C., D'Escatha Y., Ledermann P. (1983a) A local criterion for cleavage fracture of a nuclear pressure vessel steel. Metallurgical transactions A 14(11):2277–2287
- Beremin F. M., Pineau A., Mudry F., Devaux J.-C., D'Escatha Y., Ledermann P. (1983b) A local criterion for cleavage fracture of a nuclear pressure vessel steel. Metallurgical Transactions A 14(11):2277–2287, DOI 10.1007/BF02663302
- Bhowmik S., Sahoo P., Acharyya S., Chattopadhyay J., Dhar S. (2012) Application and comparative study of the master curve methodology for fracture toughness characterization of 20mnmoni55 steel. Materials and Design 39:309 – 317, DOI <http://dx.doi.org/10.1016/j.matdes.2012.02.050>
- Bhowmik S., Sahoo P., Acharyya S. K., Dhar S., Chattopadhyay J. (2015) Evaluation and effect of loss of constraint on master curve reference temperature of 20mnmoni55 steel. Engineering Fracture Mechanics 136:142 – 157, DOI <http://dx.doi.org/10.1016/j.engfracmech.2015.01.022>
- Bonad R., Mueller P., Sptig P. (2008) Fracture toughness behavior in the ductilebrittle transition region of the tempered martensitic eurofer97 steel: Experiments and modeling. Engineering Fracture Mechanics 75(13):3985 – 4000, DOI <https://doi.org/10.1016/j.engfracmech.2008.01.016>
- Bonadé R., Mueller P., Spätig P. (2008) Fracture toughness behavior in the ductile–brittle transition region of the tempered martensitic eurofer97 steel: Experiments and modeling. Engineering fracture mechanics 75(13):3985–4000
- Bonadé R. A. (2006) Constitutive behavior and fracture properties of tempered martensitic steels for nuclear applications

- Bromberg J. (1982) *Fusion: Science, Politics, and the Invention of a New Energy Source*. MIT Press
- Bruckner A., Munz D. (1984) Scatter of fracture toughness in the brittle-ductile transition region of a ferritic steel. *ASME, PVP 92*:105–113
- Burdekin F., Lidbury D., Moskvic R. (1999) On the onset of upper shelf transition temperature behaviour in ferritic steels. *International journal of pressure vessels and piping 76(13)*:875–877
- Chaudhuri P., Kumar E. R., Sircar A., Ranjithkumar S., Chaudhari V., Danani C., Yadav B., Bhattacharyay R., Mehta V., Patel R., Vyas K., Singh R., Sarkar M., Srivastava R., Mohan S., Bhanja K., Suri A. (2012) Status and progress of indian {LLCB} test blanket systems for {ITER}. *Fusion Engineering and Design 87(78)*:1009 – 1013, DOI <http://dx.doi.org/10.1016/j.fusengdes.2012.02.062>, tenth International Symposium on Fusion Nuclear Technology (ISFNT-10)
- Daniel J. (2012) Fusion energy production by deuterium particle injection
- Danon A., Alamo A. (2002) Behavior of eurofer97 reduced activation martensitic steel upon heating and continuous cooling. *Journal of nuclear materials 307*:479–483
- Daum E., Ehrlich K., Schirra M. (1997) Proceedings of the second milestone meeting of European laboratories on the development of ferritic/martensitic steels for fusion technology. Tech. rep., FIZ Karlsruhe
- Delorenzi H., Shih C. (1983) 3-d elastic-plastic investigation of fracture parameters in side-grooved compact specimen. *International Journal of Fracture 21(3)*:195–220
- Dodds Jr R. H., Anderson T. L., Kirk M. T. (1991) A framework to correlate a/w ratio effects on elastic-plastic fracture toughness (J_c). *International Journal of Fracture 48(1)*:1–22
- Doig P., Moskvic R. (1993) The influence of competing fracture mode on the ductile to brittle transition temperature. *Engineering fracture mechanics 46(3)*:529–535
- Donald E. McCabe K. W. John G. Merkle (2005) *An Introduction to the Development and Use of the Master Curve Method*. ASTM International
- Dowling A. R., Lidbury D. P. G. (2000) Local approach modelling of constraint contributions to the ductile to brittle transition. In: Hirsch P., Lidbury D. (eds) *Fracture, Plastic Flow and Structural Integrity, Proceedings of the 7th Symposium, Technical Advisory Group on Structural Integrity of Nuclear Plant*
- E1921 A. (2013) E 1921 standard test method for determination of reference temperature, T_0 , for ferritic steels in the transition range
- Eldis G. T. (1977) A critical review of data sources for isothermal transformation and continuous cooling transformation diagrams. *Hardening Concepts with Applications to Steel* pp. 126–157
- EricksonKirk M., EricksonKirk M. (2006) An upper-shelf fracture toughness master curve for ferritic steels. *International Journal of Pressure Vessels and Piping 83(8)*:571 – 583, DOI <http://dx.doi.org/10.1016/j.ijpvp.2006.05.001>

- Faleskog J., Gao X., Shih C. F. (1998) Cell model for nonlinear fracture analysis–i. micromechanics calibration. *International Journal of Fracture* 89(4):355–373
- Gao X., Dodds Jr R. H. (2000) Constraint effects on the ductile-to-brittle transition temperature of ferritic steels: a weibull stress model. *International Journal of Fracture* 102(1):43–69
- Gao X., Dodds Jr R. H. (2005a) Loading rate effects on parameters of the weibull stress model for ferritic steels. *Engineering Fracture Mechanics* 72(15):2416 – 2425, DOI <http://dx.doi.org/10.1016/j.engfracmech.2005.03.001>
- Gao X., Dodds Jr R. H. (2005b) Loading rate effects on parameters of the weibull stress model for ferritic steels. *Engineering Fracture Mechanics* 72(15):2416 – 2425, DOI <http://dx.doi.org/10.1016/j.engfracmech.2005.03.001>
- Gao X., Dodds Jr R. H., Tregoning R., Joyce J. A. (2001) Weibull stress model for cleavage fracture under high-rate loading. *Fatigue & Fracture of Engineering Materials & Structures* 24(8):551–564
- Gao X., Zhang G., Srivatsan T. (2006) A probabilistic model for prediction of cleavage fracture in the ductile-to-brittle transition region and the effect of temperature on model parameters. *Materials Science and Engineering: A* 415(12):264 – 272, DOI <http://dx.doi.org/10.1016/j.msea.2005.09.098>
- Gao X., Joyce J. A., Roe C. (2008) An investigation of the loading rate dependence of the weibull stress parameters. *Engineering Fracture Mechanics* 75(6):1451 – 1467, DOI <http://dx.doi.org/10.1016/j.engfracmech.2007.07.007>
- Gurson A. L. (1977) Continuum theory of ductile rupture by void nucleation and growth: Part i yield criteria and flow rules for porous ductile media. *Journal of engineering materials and technology* 99(1):2–15
- Hasegawa K., Chen Z.-C., Nishimura K., Ikeda K. (2009) Determination of true stress-strain curves of sheet metals in post-uniform elongation range. *MATERIALS TRANSACTIONS* 50(1):138–144, DOI 10.2320/matertrans.P-MRA2008838
- Heerens J., Hellmann D. (1999) Fracture toughness of steel in the ductile to brittle transition regime. Final Report, Measurement and Testing Programme Contract MAT1-CT-940080
- Heerens J., Hellmann D. (2002) Development of the euro fracture toughness dataset. *Engineering Fracture Mechanics* 69(4):421–449
- Hibbitt, Karlsson, Sorensen (1998) ABAQUS/standard: User's Manual, vol 1. Hibbitt, Karlsson & Sorensen
- IAEA (2001a) Final Report of the ITER EDA. No. 21 in ITER EDA Documentation Series, INTERNATIONAL ATOMIC ENERGY AGENCY, Vienna
- IAEA (2001b) Summary of the ITER Final Design Report. No. 22 in ITER EDA Documentation Series, INTERNATIONAL ATOMIC ENERGY AGENCY, Vienna
- IAEA (2009) 1631. master curve approach to monitor fracture toughness of reactor pressure vessels in nuclear power plants. International Atomic Energy Agency

- Ioltukhovskiy A., Leontyeva-Smirnova M., Kazennov Y., Medvedeva E., Tselishchev A., Shamardin V., Povstyanko A., Ostrovsky S., Dvoryashin A., Porollo S., et al. (1998) Influence of operation conditions on structure and properties of 12% cr steels as candidate structural materials for fusion reactor. *Journal of nuclear materials* 258:1312–1318
- Jayakumar T., Mathew M., Laha K. (2013) High temperature materials for nuclear fast fission and fusion reactors and advanced fossil power plants. *Procedia Engineering* 55:259 – 270, DOI <http://dx.doi.org/10.1016/j.proeng.2013.03.252>, 6th International Conference on Creep, Fatigue and Creep-Fatigue Interaction
- Joyce J., Tregoning R. (2005a) Determination of constraint limits for cleavage initiated toughness data. *Engineering fracture mechanics* 72(10):1559–1579
- Joyce J., Tregoning R. (2005b) Determination of constraint limits for cleavage initiated toughness data. *Engineering fracture mechanics* 72(10):1559–1579
- Kim B. J., Kasada R., Kimura A., Wakai E., Tanigawa H. (2013) Application of master curve method to the evaluation of fracture toughness of f82h steels. *Journal of Nuclear Materials* 442(1):S38–S42
- Klimenkov M., Materna-Morris E., Möslang A. (2015) Boron effect on the microstructure of 9% cr ferritic–martensitic steels. *Journal of Nuclear Materials* 462:280–288
- Klueh R. (2005) Elevated temperature ferritic and martensitic steels and their application to future nuclear reactors. *International Materials Reviews* 50(5):287–310
- Knott J. (1995) The transition from fibrous fracture to cleavage fracture. *International journal of pressure vessels and piping* 64(3):225–234
- Koers R. W., Braam H., Bakker A. (2013) Investigation into the effect of thickness on three- and four-point single edge notch bend specimens using two- and three-dimensional elastic-plastic stress analyses. In: ICF7, Houston (USA) 1989
- Koppenhoefer K. C., Dodds Jr R. H. (1997) Loading rate effects on cleavage fracture of pre-cracked CVN specimens: 3-d studies. *Engineering Fracture Mechanics* 58(3):249 – 270, DOI [http://dx.doi.org/10.1016/S0013-7944\(97\)00076-3](http://dx.doi.org/10.1016/S0013-7944(97)00076-3)
- Koppenhoefer K. C., Gullerud A. S., Ruggieri C., Dodds Jr R. H., Healey B. (1994) WARP3D: dynamic nonlinear analysis of solids using a preconditioned conjugate gradient software architecture. Tech. rep., University of Illinois at Urbana–Champaign
- Kung C., Rayment J. (1982) Examination of the validity of existing empirical formulae for the calculation of m /sub s /temperature. *Metall Trans, A;(United States)* 13(2)
- Kunitake T. (2001) Prediction of a_c sub 1, a_c sub 3 and m_s temperatures of steel by empirical formulas. *Netsu Shori(Journal of the Japan Society for Heat Treatment)(Japan)* 41(3):164–169
- Kunitake T., Ohtani H. (1969) Calculating the continuous cooling transformation characteristics of steel from its chemical composition. *SUMITOMO SEARCH*, NOV 1969,–2–, 18-21

- Kytka M., Brumovsky M., Falcnik M. (2011) Irradiation embrittlement characterization of the eurofer 97 material. *Journal of Nuclear Materials* 409(2):147–152
- Laha K., Saroja S., Moitra A., Sandhya R., Mathew M., Jayakumar T., Kumar E. R. (2013) Development of india-specific RAFM steel through optimization of tungsten and tantalum contents for better combination of impact, tensile, low cycle fatigue and creep properties. *Journal of Nuclear Materials* 439(1):41 – 50, DOI <http://dx.doi.org/10.1016/j.jnucmat.2013.03.073>
- Landes J., Shaffer D. (1980) Statistical characterization of fracture in the transition region. In: *Fracture Mechanics*, ASTM International
- Lei W.-S. (2016a) A cumulative failure probability model for cleavage fracture in ferritic steels. *Mechanics of Materials* 93:184–198
- Lei W.-S. (2016b) A statistical model of cleavage fracture in structural steels with power-law distribution of microcrack size. *Philosophical Magazine Letters* 96(3):101–111
- Li X.-G., Yan Q.-Z., Rong M., Wang H.-Q., Ge C.-C. (2010) First results of characterization of 9cr-3wvtitan low activation ferritic/martensitic steel. *Journal of Iron and Steel Research, International* 17(5):57–62
- Lucas G., Odette G., Matsui H., Mslang A., Spätig P., Rensman J., Yamamoto T. (2007) The role of small specimen test technology in fusion materials development. *Journal of Nuclear Materials* 367370, Part B:1549 – 1556, DOI <http://dx.doi.org/10.1016/j.jnucmat.2007.04.034>, proceedings of the Twelfth International Conference on Fusion Reactor Materials (ICFRM-12) Proceedings of the Twelfth International Conference on Fusion Reactor Materials (ICFRM-12)
- Lucon E., Scibetta M. (2011) Application of advanced master curve approaches to the euro fracture toughness data set. In: *Fatigue and Fracture Mechanics: 37th Volume*, ASTM International
- Margolin B., Kostylev V., Minkin A. (2003) The effect of ductile crack growth on the temperature dependence of cleavage fracture toughness for a rpv steel with various degrees of embrittlement. *International journal of pressure vessels and piping* 80(5):285–296
- Mathew M., Vanaja J., Laha K., Reddy G. V., Chandravathi K., Rao K. B. S. (2011) Tensile and creep properties of reduced activation ferriticmartensitic steel for fusion energy application. *Journal of Nuclear Materials* 417(13):77 – 80, DOI <http://dx.doi.org/10.1016/j.jnucmat.2011.01.058>, proceedings of ICFRM-14
- McMeeking R. (1977) Finite deformation analysis of crack-tip opening in elastic-plastic materials and implications for fracture. *Journal of the Mechanics and Physics of Solids* 25(5):357 – 381, DOI [http://dx.doi.org/10.1016/0022-5096\(77\)90003-5](http://dx.doi.org/10.1016/0022-5096(77)90003-5)
- Miernik J., Statham G., Fabisinski L., Maples C., Adams R., Polsgrove T., Fincher S., Cassibry J., Cortez R., Turner M., Percy T. (2013) Z-pinch fusion-based nuclear propulsion. *Acta Astronautica* 82(2):173 – 182, DOI <http://dx.doi.org/10.1016/j.actaastro.2012.02.012>, 7th {IAA} Symposium on Realistic Advanced Scientific Space Missions Aosta, Italy, July 2011

- Mishnev R., Dudova N., Kaibyshev R. (2016) Low cycle fatigue behavior of a 10cr–2w–mo–3co–nbv steel. *International Journal of Fatigue* 83:344–355
- Moattari M., Sattari-Far I., Bonora N. (2016) The effect of subcritical ductile crack growth on cleavage fracture probability in the transition regime using continuum damage mechanics simulation. *Theoretical and Applied Fracture Mechanics* 82:125–135
- Moitra A., Dasgupta A., Sathyanarayanan S., Sasikala G., Albert S., Saroja S., Bhaduri A., Kumar E. R., Jayakumar T. (2014) A study of fracture mechanisms in rafm steel in the ductile to brittle transition temperature regime. *Procedia Engineering* 86:258–263
- Moskovic R. (2002) Modelling of fracture toughness data in the ductile to brittle transition temperature region by statistical analysis. *Engineering fracture mechanics* 69(4):511–530
- Möslang A., Diegele E., Klimiankou M., Lässer R., Lindau R., Lucon E., Materna-Morris E., Petersen C., Pippan R., Rensman J., et al. (2005) Towards reduced activation structural materials data for fusion demo reactors. *Nuclear fusion* 45(7):649
- Mudry F. (1987) A local approach to cleavage fracture. *Nuclear Engineering and design* 105(1):65–76
- Mueller P., Spätig P., Bonad R., Odette G., Gragg D. (2009) Fracture toughness master-curve analysis of the tempered martensitic steel eurofer97. *Journal of Nuclear Materials* 386388:323 – 327, DOI <http://dx.doi.org/10.1016/j.jnucmat.2008.12.122>, fusion Reactor Materials Proceedings of the Thirteenth International Conference on Fusion Reactor Materials
- Murty K., Charit I. (2008) Structural materials for gen-iv nuclear reactors: Challenges and opportunities. *Journal of Nuclear Materials* 383(1):189–195
- Mythili R., Vanaja J., Laha K., Saroja S., Jayakumar T., Mathew M., Rajendrakumar E., et al. (2013) Microstructural modifications due to tungsten and tantalum in 9cr reduced activation ferritic martensitic steels on creep exposure. *Procedia Engineering* 55:295–299
- Nevalainen M., Dodds Jr R. H. (1996) Numerical investigation of 3-d constraint effects on brittle fracture in se (b) and c (t) specimens. *International Journal of Fracture* 74(2):131–161
- Neville D. (1988) On the distance criterion for failure at the tips of cracks, minimum fracture toughness, and non-dimensional toughness parameters. *Journal of the Mechanics and Physics of Solids* 36(4):443–457
- Odette G., He M. Y. (2000) A cleavage toughness master curve model. *Journal of nuclear materials* 283:120–127
- Oughton D. (2016) Societal and ethical aspects of the fukushima accident. *Integrated Environmental Assessment and Management* 12(4):651–653
- Parks D. (1992) Advances in characterization of elastic-plastic crack-tip fields. In: *Topics in Fracture and Fatigue*, Springer, pp. 59–98

- Petti J. P., Dodds Jr R. H. (2005) Calibration of the weibull stress scale parameter, u , using the master curve. *Engineering Fracture Mechanics* 72(1):91 – 120, DOI <http://dx.doi.org/10.1016/j.engfracmech.2004.03.009>
- Qian G., Gonzalez-Albuixech V., Niffenegger M. (2015) Calibration of beremin model with the master curve. *Engineering Fracture Mechanics* 136:15 – 25, DOI <http://dx.doi.org/10.1016/j.engfracmech.2015.02.003>
- Qian G., Lei W.-S., Niffenegger M. (2017) Calibration of a new local approach to cleavage fracture of ferritic steels. *Materials Science and Engineering: A* 694:10–12
- Qian X., Zhang S., Swaddiwudhipong S. (2011) Calibration of weibull parameters using the conventional mechanism-based strain gradient plasticity. *Engineering Fracture Mechanics* 78(9):1928 – 1944, DOI <http://dx.doi.org/10.1016/j.engfracmech.2011.03.010>
- Raju S., Ganesh B. J., Rai A. K., Mythili R., Saroja S., Mohandas E., Vijayalakshmi M., Rao K., Raj B. (2009) Measurement of transformation temperatures and specific heat capacity of tungsten added reduced activation ferriticmartensitic steel. *Journal of Nuclear Materials* 389(3):385 – 393, DOI <http://dx.doi.org/10.1016/j.jnucmat.2009.02.030>
- Rathbun H., Odette G., Yamamoto T., Lucas G. (2006) Influence of statistical and constraint loss size effects on cleavage fracture toughness in the transitiona single variable experiment and database. *Engineering Fracture Mechanics* 73(1):134 – 158, DOI <http://dx.doi.org/10.1016/j.engfracmech.2005.07.008>
- Rice J., Johnson M., Kanninen M., et al. (1970) *Inelastic behavior of solids*. McGraw-Hill, New York 641
- Ritchie R. O., Knott J. F., Rice J. (1973) On the relationship between critical tensile stress and fracture toughness in mild steel. *Journal of the Mechanics and Physics of Solids* 21(6):395–410
- Rosenwasser S., Miller P., Dalessandro J., Rawls J., Toffolo W., Chen W. (1979) The application of martensitic stainless steels in long lifetime fusion first wall/blankets. *Journal of Nuclear Materials* 85:177–182
- Ruggieri C., Dodds Jr R. H. (1996) A transferability model for brittle fracture including constraint and ductile tearing effects: a probabilistic approach. *International Journal of Fracture* 79(4):309–340
- Ruggieri C., Dodds Jr R. H. (2015) An engineering methodology for constraint corrections of elasticplastic fracture toughness part i: A review on probabilistic models and exploration of plastic strain effects. *Engineering Fracture Mechanics* 134:368 – 390, DOI <http://dx.doi.org/10.1016/j.engfracmech.2014.12.015>
- Ruggieri C., Jr R. D., Wallin K. (1998) Constraint effects on reference temperature, t_0 , for ferritic steels in the transition region. *Engineering Fracture Mechanics* 60(1):19 – 36, DOI [http://dx.doi.org/10.1016/S0013-7944\(98\)00001-0](http://dx.doi.org/10.1016/S0013-7944(98)00001-0)
- Ruggieri C., Savioli R. G., Dodds Jr R. H. (2015) An engineering methodology for constraint corrections of elasticplastic fracture toughness part ii: Effects of specimen

- geometry and plastic strain on cleavage fracture predictions. *Engineering Fracture Mechanics* 146:185 – 209, DOI <http://dx.doi.org/10.1016/j.engfracmech.2015.06.087>
- Sandim M., Farrão F., Oliveira V., Bredda E., Santos A., dos Santos C., Sandim H. (2015) Effect of tempering on the microstructure, electrical, and magnetic properties of eurofer-97 steel. *Journal of Nuclear Materials* 461:265–270
- Saunders N., Guo U., Li X., Miodownik A., Schillé J.-P. (2003) Using jmatpro to model materials properties and behavior. *JOM* 55(12):60–65
- Scibetta M. (2010) Effect of prior crack growth on cleavage fracture of low toughness precracked charpy specimens. *Journal of Nuclear Materials* 406(1):113–118
- SINTAP S. I. A. P. (1999) Final revision. EU-Brite Euram-Project, BE pp. 95–1462
- Slatcher S. (1986) A probabilistic model for lower-shelf fracture toughness theory and application. *Fatigue & Fracture of Engineering Materials & Structures* 9(4):275–289
- Smith E. (1966) Physical basis of yield and fracture. In: *Proc. Conf., Institute of Physics and Physical Society, Oxford, United Kingdom*, p. 36
- Sobotka J., Dodds R. (2014) Effects of steady ductile crack growth on cleavage fracture from three-dimensional, small-scale yielding simulations. *Engineering Fracture Mechanics* 127:211–225
- Sokolov M., Tanigawa H. (2007) Application of the master curve to inhomogeneous ferritic/martensitic steel. *Journal of Nuclear Materials* 367:587–592
- Spätig P., Bonad R., Odette G., Rensman J., Campitelli E., Mueller P. (2007) Plastic flow properties and fracture toughness characterization of unirradiated and irradiated tempered martensitic steels. *Journal of Nuclear Materials* 367:370, Part A:527 – 538, DOI <http://dx.doi.org/10.1016/j.jnucmat.2007.03.038>, proceedings of the Twelfth International Conference on Fusion Reactor Materials (ICFRM-12) Proceedings of the Twelfth International Conference on Fusion Reactor Materials (ICFRM-12)
- Stacey W. (2010) *Fusion: An Introduction to the Physics and Technology of Magnetic Confinement Fusion*. Wiley
- Steven W., Haynes A. (1956) The temperature of formation of martensite and bainite in low-alloy steels. *Journal of the Iron and Steel Institute* 183(8):349–359
- Stratil L., Siska F., Hadraba H., Dlouhy I. (2014) Modeling of ductile tearing for rafm steel eurofer97. *Procedia Materials Science* 3:1155–1160
- Sumpter J., Forbes A. (1993) *Constraint based analysis of shallow cracks in mild steel*. Abington Publishing(UK), p. 7
- T. M. (1972) *Tekko-zairyo-gaku*, chapter martensite. JikkyoSyuppan Corp in Japanese 43(1):4–11
- Tagawa T., Kayamori Y., Hira H. (2010) Statistical scatter of fracture toughness in the ductile–brittle transition of a structural steel. *Engineering Fracture Mechanics* 77(16):3077–3086

- Tamura I. (1970) Steel material study on the strength. Nikkan Kogyo Shinbun Ltd, Tokyo 40
- Tan L., Yang Y., Busby J. T. (2013) Effects of alloying elements and thermomechanical treatment on 9cr reduced activation ferritic–martensitic (rafm) steels. *Journal of Nuclear Materials* 442(1):S13–S17
- Tiwari A., Avinash G., Sunil S., Singh R., Ståhle P., Chattopadhyay J., Chakravartty J. (2015) Determination of reference transition temperature of in-rafms in ductile brittle transition regime using numerically corrected master curve approach. *Engineering Fracture Mechanics* 142:79 – 92, DOI <http://dx.doi.org/10.1016/j.engfracmech.2015.05.041>
- Tvergaard V. (1981) Influence of voids on shear band instabilities under plane strain conditions. *International Journal of Fracture* 17(4):389–407
- Tvergaard V. (1982) Influence of void nucleation on ductile shear fracture at a free surface. *Journal of the Mechanics and Physics of Solids* 30(6):399–425
- Tvergaard V., Needleman A. (1984) Analysis of the cup-cone fracture in a round tensile bar. *Acta metallurgica* 32(1):157–169
- Vanaja J., Laha K., Mythili R., Chandravathi K., Saroja S., Mathew M. (2012) Creep deformation and rupture behaviour of 9cr–1w–0.2 v–0.06 ta reduced activation ferritic–martensitic steel. *Materials Science and Engineering: A* 533:17–25
- Vanaja J., Laha K., Nandagopal M., Sam S., Mathew M., Jayakumar T., Kumar E. R. (2013) Effect of tungsten on tensile properties and flow behaviour of rafm steel. *Journal of Nuclear Materials* 433(1):412–418
- Varias A. (1998) Constraint effects during stable transient crack growth. *Computational Mechanics* 21(4-5):316–329
- Wallin K. (1984) The scatter in KIC-results. *Engineering Fracture Mechanics* 19(6):1085 – 1093, DOI [http://dx.doi.org/10.1016/0013-7944\(84\)90153-X](http://dx.doi.org/10.1016/0013-7944(84)90153-X)
- Wallin K. (1989a) The effect of ductile tearing on cleavage fracture probability in fracture toughness testing. *Engineering Fracture Mechanics* 32(4):523 – 531, DOI [http://dx.doi.org/10.1016/0013-7944\(89\)90186-0](http://dx.doi.org/10.1016/0013-7944(89)90186-0)
- Wallin K. (1989b) The effect of ligament size on cleavage fracture toughness. *Engineering Fracture Mechanics* 32(3):449 – 457, DOI [http://dx.doi.org/10.1016/0013-7944\(89\)90316-0](http://dx.doi.org/10.1016/0013-7944(89)90316-0)
- Wallin K. (1993) Irradiation damage effects on the fracture toughness transition curve shape for reactor pressure vessel steels. *International journal of pressure vessels and piping* 55(1):61–79
- Wallin K. (1997) Proc. conf. 'Recent Advances in Fracture' (R K Mahidhara, Ed). The Minerals, Metal and Materials Society of AIME pp. 171 – 181
- Wallin K. (1999) The master curve method: a new concept for brittle fracture. *International Journal of Materials and Product Technology* 14(2-4):342–354

- Wallin K. (2001) Quantifying t-stress controlled constraint by the master curve transition temperature T_0 . *Engineering Fracture Mechanics* 68(3):303 – 328, DOI [http://dx.doi.org/10.1016/S0013-7944\(00\)00067-9](http://dx.doi.org/10.1016/S0013-7944(00)00067-9)
- Wallin K. (2002) Master curve analysis of the euro fracture toughness dataset. *Engineering Fracture Mechanics* 69(4):451 – 481, DOI [http://dx.doi.org/10.1016/S0013-7944\(01\)00071-6](http://dx.doi.org/10.1016/S0013-7944(01)00071-6)
- Wallin K. (2003) Master curve implementation of the warm pre-stress effect. *Engineering Fracture Mechanics* 70(18):2587 – 2602, DOI [http://dx.doi.org/10.1016/S0013-7944\(03\)00064-X](http://dx.doi.org/10.1016/S0013-7944(03)00064-X)
- Wallin K. (2004) Warm pre-stress based pre-cracking criteria for fracture toughness testing. *Engineering Fracture Mechanics* 71(12):1737 – 1750, DOI [http://dx.doi.org/10.1016/S0013-7944\(03\)00245-5](http://dx.doi.org/10.1016/S0013-7944(03)00245-5)
- Wallin K. (2010a) Structural integrity assessment aspects of the master curve methodology. *Engineering Fracture Mechanics* 77(2):285 – 292, DOI <http://dx.doi.org/10.1016/j.engfracmech.2009.02.010>
- Wallin K. (2010b) Structural integrity assessment aspects of the master curve methodology. *Engineering Fracture Mechanics* 77(2):285–292
- Wallin K., Laukkanen A. (2008) New developments of the wallin, saario, törrönen cleavage fracture model. *Engineering Fracture Mechanics* 75(11):3367–3377
- Wallin K., Saario T., Torronen K., Forstén J., Törrönen K., Aho-Mantila I. (1986) Brittle fracture theory (wst model). *Reliability of Reactor Materials Fracture Mechanics*
- Wallin K., Planman T., Valo M., Rintamaa R. (2001) Applicability of miniature size bend specimens to determine the master curve reference temperature T_0 . *Engineering Fracture Mechanics* 68(11):1265 – 1296, DOI [http://dx.doi.org/10.1016/S0013-7944\(01\)00020-0](http://dx.doi.org/10.1016/S0013-7944(01)00020-0)
- Wallin K., Nevasmaa P., Laukkanen A., Planman T. (2004) Master curve analysis of inhomogeneous ferritic steels. *Engineering Fracture Mechanics* 71(1617):2329 – 2346, DOI <http://dx.doi.org/10.1016/j.engfracmech.2004.01.010>
- Wallin K., Pallaspuuro S., Valkonen I., Karjalainen-Roikonen P., Suikkanen P. (2015) Fracture properties of high performance steels and their welds. *Engineering Fracture Mechanics* 135:219 – 231, DOI <http://dx.doi.org/10.1016/j.engfracmech.2015.01.007>
- Wallin K. R. (2013) Distribution free statistical assessment of scatter and size effects in the euro fracture toughness data set. *Engineering Fracture Mechanics* 103:69 – 78, DOI <http://dx.doi.org/10.1016/j.engfracmech.2012.05.018>, advances in Failure Assessment Using Fracture and Damage Mechanics.
- Wang Y., Parks D. (1992) Evaluation of the elastic t-stress in surface-cracked plates using the line-spring method. *International Journal of fracture* 56(1):25–40
- Wasiluk B., Petti J. P., Jr. R. H. D. (2006) Temperature dependence of weibull stress parameters: Studies using the euro-material. *Engineering Fracture Mechanics* 73(8):1046 – 1069, DOI <http://dx.doi.org/10.1016/j.engfracmech.2005.11.006>

- Weibull W. (1951) Wide applicability. *Journal of applied mechanics* 103:293–297
- Wikipedia (2004) Fusion power — Wikipedia, the free encyclopedia. [Online; modified 17 October 2016,]
- Williams M. (1961) The bending stress distribution at the base of a stationary crack. *Journal of applied mechanics* 28(1):78–82
- Xiao X., Liu G., Hu B., Wang J., Ullah A. (2013) Effect of v and t_a on the precipitation behavior of 12% cr reduced activation ferrite/martensite steel. *Materials Characterization* 82:130–139
- Xu Y., Zhang X., Tian Y., Chen C., Nan Y., He H., Wang M. (2016) Study on the nucleation and growth of m 23 c 6 carbides in a 10% cr martensite ferritic steel after long-term aging. *Materials Characterization* 111:122–127
- Yan C., Mai Y. (1997) Effect of constraint on ductile crack growth and ductile-brittle fracture transition of a carbon steel. *International journal of pressure vessels and piping* 73(3):167–173
- Yoon K., Hall J., Van Der Sluys W., Higuchi M., Iida K. (2001a) Japanese fracture toughness data analysis using the master curve method. *ASME-PUBLICATIONS-PVP* 423:167–178
- Yoon K., Hall J., Van Der Sluys W., Higuchi M., Iida K. (2001b) Japanese fracture toughness data analysis using the master curve method. *ASME-PUBLICATIONS-PVP* 423:167–178
- Yu J., Huang Q., Wan F. (2007) Research and development on the china low activation martensitic steel (clam). *Journal of Nuclear Materials* 367:97–101
- Zener C., Hollomon J. (1944) Effect of strain rate upon plastic flow of steel. *Journal of Applied physics* 15(1):22–32
- Zerilli F. J., Armstrong R. W. (1987) Dislocation-mechanics-based constitutive relations for material dynamics calculations. *Journal of Applied Physics* 61(5):1816–1825
- Zilnyk K., Oliveira V. B., Sandim H. R. Z., Möslang A., Raabe D. (2015) Martensitic transformation in eurofer-97 and ods-eurofer steels: A comparative study. *Journal of Nuclear Materials* 462:360–367

Index

- $\sigma^* - V^*$ approach, 107
- $\sigma^* - V^*$ approach, 215
- Beremin's Model, 48
- Beremin's model, 156, 157
- Bimodal master curve, 41
- Calibration of Weibull parameters, 157, 159
- Cleavage failure probability, numerical predictions, 157
- Cleavage failure probability, Weibull stress, 156
- Cleavage, local approach, 46
- Constitutive equations of finite element analyses, 80
- Constraint loss, in plane, 122
- Constraint loss, out of plane, 104
- Euro fracture data, 113
- Fatigue pre cracking of fracture specimens, 73
- Ferritic/Martensitic steels, 49
- First wall, 24
- Fracture toughness measurement, 78
- Griffith's criteria, 47
- Griffith's criteria of cleavage fracture, 104
- Griffith's micro-cracks, 47
- GTN damage, 83
- Impact test, 77
- In-RAFMS, 49, 52
- ITER, 21
- ITER, phases of fusion reaction, 22
- MANET, 50
- Master Curve, 35
- Maximum likelihood analysis, 6, 38
- Mesh, finite element, 82
- mesh, finite element, 84
- Metallography, etchant, 77
- Micro-mechanics of cleavage fracture, 47
- Modified 9%Cr-1%Mo steels, 49
- Modified boundary layer model, 81
- Multi-modal master curve, 41
- Multi-temperature master curve, 96
- Objectives of the work, 27
- OPTIFIER, 50
- P91 steel, 49
- Phase diagram, In-RAFMS, 59
- Phase diagram, P91, 59
- Quarter symmetric boundary conditions, 108
- RAFMS, carbide fracture, 87
- RAFMS, comparison of different grades, 63
- RAFMS, damage, 87
- RAFMS, effect of alloying elements, 51
- RAFMS, heat treatment, 59
- RAFMS, Impact toughness, 86
- RAFMS, Lave phases, 65
- RAFMS, Ludwig fit, 93
- RAFMS, $M_{23}C_6$ and MX carbides, 65
- RAFMS, micro structure, 59, 65
- RAFMS, micro-cracks, 87
- RAFMS, Phase transformation, 59
- RAFMS, precipitates, 65
- RAFMS, tensile behaviour, 93
- RAFMS, voids, 87
- Random inhomogeneity analysis, 41
- RKR model, 48
- sensitivity analysis, 84
- Single-temperature master curve, 96
- SINTAP lower tail estimate, 41
- solver, finite element, 84
- SSY corrected T_o , 121
- T_{stress} , modified boundary layer model, 81
- Validity criteria, master curve, 35
- Void growth, 84
- Void nucleation, 84
- Void volume fraction, GTN model, porous plasticity, 84
- Weakest link theory, 36
- Weibull stress, 157, 158
- Weibull stress calculation, 165
- Weibull Triaxiality, 141, 215
- WST model, 48, 107
- Zener-Hollomon strain rate function, 156
- Zeta pinch, 21